

ENERGETIC AND HYDROLOGICAL RESPONSES
OF HADLEY CIRCULATIONS AND THE
AFRICAN SAHEL TO SEA SURFACE
TEMPERATURE PERTURBATIONS

Spencer Alan Hill

A DISSERTATION
PRESENTED TO THE FACULTY
OF PRINCETON UNIVERSITY
IN CANDIDACY FOR THE DEGREE
OF DOCTOR OF PHILOSOPHY

RECOMMENDED FOR ACCEPTANCE
BY THE PROGRAM IN
ATMOSPHERIC AND OCEANIC SCIENCES

Adviser: Dr. Yi Ming

September 2016



Spencer Alan Hill, 2016

© by Spencer Alan Hill. This dissertation is licensed under the Creative Commons Attribution 4.0 International License. To view a copy of this license, visit <http://creativecommons.org/licenses/by/4.0/>.

Abstract

Tropical precipitation is linked through the moist static energy (MSE) budget to the global distribution of sea surface temperatures (SSTs), and large deviations from the present-day SST distribution have been inferred for past climates and projected for global warming. We use idealized SST perturbation experiments in multiple atmospheric general circulation models (AGCMs) to examine the hydrologic and energetic responses in the zonal mean and in the African Sahel to SST perturbations. We also use observational data to assess the prospects for emergent constraints on future rainfall in the Sahel.

The tropical zonal mean anomalous MSE fluxes in the NOAA Geophysical Fluid Dynamics Laboratory (GFDL) AM2.1 AGCM due to SST anomalies caused by either historical greenhouse gas or aerosol forcing primarily occur through the time-mean, zonal mean (Hadley) circulation. Away from the Intertropical Convergence Zone (ITCZ), this largely stems from altered efficiency of the Hadley circulation energy transport, i.e. the gross moist stability (GMS). A thermodynamic scaling-based estimate that relates GMS change to the local climatological moisture and temperature change relative to the ITCZ captures most of the qualitative GMS responses. It also yields a heuristic explanation for the well known correlation between low-latitude MSE fluxes and the ITCZ latitude.

Severe Sahelian drying with uniform SST warming in AM2.1 is eliminated when the default convective parameterization is replaced with an alternate. The drying is commensurate with MSE convergence due to suppressed ascent balanced by MSE divergence due to increased dry advection from the Sahara. These qualitative energetic responses to uniform warming are shared by five other GFDL models and ten CMIP5 models, although they do not translate into quantitative predictors of the Sahel rainfall response. Climatological values and interannual variability in observations and reanalyses suggest that drying in AM2.1

is exacerbated by an overly top-heavy ascent profile and positive feedbacks through cloud radiative properties. Simulations with patterned SST anomalies suggest a major role for mean SST variations in discrepancies among models and potentially in observed decadal variations of Sahelian precipitation.

Acknowledgments

Taking me on as an undergraduate summer intern and then as a graduate student, I cannot overstate the influence of Yi Ming on my scientific development and life. I expected that my PhD adviser would provide scientific guidance, which Yi did in spades, but I had no idea that person would also become a dear friend. I will forever cherish Yi's unwavering support, generosity, and simply all the fun we had together.

My wife Alyssa was ceaseless in her love and support over the past five years – I simply could not have done this without her – but, much more importantly, she has widened my gaze beyond science to worlds of beauty, joy, love, and adventure (not to mention delicious food). My close friends and family – Hills, Bricklins, Phalons, and the rest – were beyond compare in their love and support.

My PhD committee – Leo Donner, Isaac Held, and Ming Zhao – consistently improved my research through their thoughtful questions and ideas. In particular, Isaac identified loose ends in my thinking at several critical junctures.

It was a privilege to be affiliated with the NOAA Geophysical Fluid Dynamics Laboratory and the Princeton AOS Program. I am grateful for stimulating conversations with (among many others) professors Stephan Fueglistaler, Gabriel Lau and Gabriel Vecchi; postdocs Alexei Belochitski, Alexis Berg, Massimo Ballasina, Tom Flannaghan, Martin Jucker, and Tim Merlis; fellow students Andrew Ballinger, Spencer Clark, Nick Lutsko, Sam Potter, and Zhaoyi Shen; and summer intern Jane Smyth. Anna Valerio made administrative issues a breeze and was always a joy to talk with. I will always cherish the camaraderie of my six classmates: Junyi Chai, Jaya Khana, Todd Mooring, Geeta Persad, Jeff Strong, and Hannah Zanowski. Danielle Schmitt provided vital help when I was a teaching assistant, and the Princeton McGraw Center for Teaching and Learning greatly improved my teaching.

My undergraduate education in the UCLA AOS and Mathematics departments prepared me well for graduate work. In particular, I thank AOS professors Robert Fovell, Alex Hall, Qinbin Li, Jonathan Mitchell, and David Neelin.

One of Yi's most valuable influences was encouraging and facilitating me to present our work widely at conferences and meetings. Through this travel, I had the pleasure of meeting and conversing with many bright scientists, their ideas ultimately feeding back on my research: among others, Bill Boos, Simona Bordoni, Natalie Burls, Michael Byrne, Dargan Frierson, Ben Lintner, Jonathan Mitchell, David Neelin, Olivier Pauluis, Jack Scheff, and Martin Singh. Jonathan Mitchell and his group generously accommodated me during an extended visit back to UCLA.

I relied heavily on open-source software: the Python programming language, the Numpy, Scipy, matplotlib, and xarray Python packages, the Zotero reference manager, the Git version control system, the Emacs text editor and its org-mode package, and the Flexible Modeling System (FMS) developed by the GFDL Modeling Services group. Spencer Clark, Fanrong Zeng, Larry Horowitz, Erik Mason, and Sergey Malyshев provided invaluable technical help.

The NOAA Hollings scholarship funded my summer internship with Yi Ming as an undergraduate. The Princeton/NOAA Cooperative Institute for Climate Science funded the first two years of my PhD, and a Department of Defense National Defense Science and Engineering Graduate fellowship funded the subsequent three.

Chapter 2 is joint work with Yi Ming and Isaac Held. Chapter 3 is joint work with Yi Ming, Isaac Held, and Ming Zhao. Chapters 4 and 5 are joint work with Yi Ming.

Contents

Abstract	iii
Acknowledgments	v
1 Introduction	1
1.1 Motivations	1
1.2 Theoretical underpinnings	2
1.3 Zonal mean energetics and precipitation	7
1.4 Energetics and precipitation for tropical land and the Sahel	10
1.5 Thesis roadmap	15
2 Zonal mean energy transports and ITCZ movements	18
Abstract	18
2.1 Introduction	19
2.2 Methodology	21
2.3 Results	24
2.4 Discussion	44
2.5 Summary	47
Acknowledgments	48
2.A Calculation of meridional energy flux, mass flux, and gross moist stability . .	49
3 Sahel rainfall and moist static energy budget response to uniform warming	52
Abstract	52
3.1 Introduction	53
3.2 Methodology	55

3.3	Precipitation and surface climate	57
3.4	Moist static energy budget in the control simulations	60
3.5	Moist static energy budget responses to SST warming	66
3.6	Disentangling control climate and convective processes	76
3.7	Discussion	81
3.8	Summary	84
	Acknowledgments	85
3.A	Adjustment method for correcting imbalances in column tracer budgets . . .	86
3.B	Computational procedure used for each term in the moist static energy budget	88
4	Towards emergent constraints on Sahel rainfall	91
	Abstract	91
4.1	Introduction	92
4.2	Methodology	94
4.3	GFDL and CMIP5 model results	99
4.4	Observations and reanalyses	115
4.5	Discussion	123
4.6	Summary	125
	Acknowledgments	126
5	Sahel rainfall: beyond uniform 2 K	127
	Abstract	127
5.1	Introduction	128
5.2	Localized SST perturbations	128
5.3	Responses to SST spatial patterns	132
5.4	Simulations of 20th century variations	141
5.5	Discussion	145
	Acknowledgments	147

6 Conclusions	148
6.1 Summary	148
6.2 Implications, limitations, and future work	152
Bibliography	186

Chapter 1

Introduction

1.1 Motivations

Precipitation in Earth’s Tropics varies with the global distribution of sea surface temperatures (SSTs) and with the flows of energy through the coupled atmosphere-ocean-land climate system. Large variations in both SSTs and tropical precipitation have been inferred for Earth’s past and projected for anthropogenic climate change, but general circulation models (GCM) disagree even in sign on future rainfall changes in many tropical regions [e. g. *Collins et al.*, 2013]. The present-day distribution of precipitation in the Tropics is relied on by sizable fractions of Earth’s species and the human population – the finance minister of India once described Indian monsoon rainfall as the country’s “real Finance Minister” [*Indo-Asian News Service*, 2010] – and this adds societal urgency to the scientific challenge of constraining future changes.

This thesis investigates SST-forced tropical precipitation variations in two contexts – in the zonal average and in the Sahel region of Africa – using the atmospheric budget of moist static energy (MSE) to elucidate the relevant physical mechanisms. This introductory chapter reviews the fundamental theoretical underpinnings of the tropical SST-precipitation-MSE budget relationships (Section 1.2), summarizes the state of understanding of these fields in the zonal mean (Section 1.3) and Sahelian (Section 1.4) contexts, and finally presents a roadmap for the remainder of the thesis (Section 1.5).

1.2 Theoretical underpinnings

1.2.1 Overall tropical thermal and hydrological structure

A fundamental property of the free troposphere in Earth’s Tropics is a vertical thermal profile that is nearly moist adiabatic and horizontally homogeneous. Within convecting regions, the moist adiabatic structure results from the tendency of moist convection to rapidly consume any convective available potential energy (CAPE, i.e. the integral of buoyancy of a parcel adiabatically lifted from the boundary layer to its level of neutral buoyancy), which through convective mixing relaxes the environmental lapse rate towards a moist adiabat. This is the well-known convective quasi-equilibrium (CQE) constraint [*Arakawa and Schubert, 1974*]. The horizontal homogeneity results from the smallness of the Coriolis parameter in the Tropics: with planetary rotation projecting weakly in the local horizontal near the equator, horizontal temperature and geopotential gradients cannot be sustained and instead are rapidly flattened by gravity waves. This is the well-known weak-temperature gradient (WTG) constraint [e.g. *Sobel et al., 2001*].

Oceanic convection is tightly linked to the underlying SSTs: a warmer surface tends to drive stronger convection through large surface fluxes of latent and sensible enthalpy [e.g. *Neelin and Held, 1987; Sobel, 2007*]. As such, on climatic timescales convective precipitation is largely restricted to regions warmer than some threshold SST [that depends on tropical-mean SST, c.f. *Johnson and Xie, 2010; Sobel, 2010*]. The combined CQE, WTG, and SST-based constraints thus cause the overall tropical tropospheric thermal structure to be largely determined by the SSTs aggregated over convecting regions [*Sobel et al., 2002; Flannaghan et al., 2014*].

1.2.2 Effect of tropical SST variations on precipitation

Alterations to the tropical SST field will therefore alter the distribution of convection and the thermal structure of the tropical troposphere.¹ Conceptually, any SST perturbation may be decomposed into a mean (i. e. uniform) component without spatial structure and a spatial pattern component with zero mean. For the spatial pattern component, a straightforward result based on the above considerations is that convection tends to be enhanced where SSTs are warmed relative to other regions.² This occurs, for example, in the central and eastern equatorial Pacific in response to local SST warming during El Niño events [e. g. *Su and Neelin*, 2002] and in simulations of global warming in regions where SSTs warm in excess of the tropical mean SST warming [e. g. *Vecchi and Soden*, 2007; *Xie et al.*, 2010; *Ma and Xie*, 2012; *Chadwick et al.*, 2013]. Conversely, moist convection is generally suppressed where SSTs cool relative to neighboring regions or, in the case of global scale perturbations, relative to the tropical mean.

For the uniform component, the precipitation response involves more subtle balances among multiple countervailing factors, and as a result depends more on climatological factors. Global mean precipitation and evaporation increase with global mean surface temperature at $\sim 2\% \text{ K}^{-1}$ in modern and paleoclimate [*Back et al.*, 2013] contexts.³ Because the bulk of Earth's precipitation occurs in the tropics, this $\sim 2\% \text{ K}^{-1}$ rate also holds for the tropics in isolation. Because relative humidity over ocean does not vary greatly with warming [*Held and Soden*, 2000; *O'Gorman and Schneider*, 2008; *Romps*, 2014], atmospheric water vapor

¹The direct, i. e. non-surface-temperature-mediated, effects of forcing agents on tropical precipitation is an active area of research. For greenhouse gases and absorbing aerosols, this “fast” response can be appreciable relative to the slower SST-mediated response [e. g. *Ming et al.*, 2010; *Bony et al.*, 2013]. Nevertheless, we focus exclusively in this thesis on SST-mediated precipitation variations.

²A rich literature focused on the momentum budget of the oceanic boundary layer emphasizes SST horizontal gradients in driving near-surface convergence necessary for convection [*Lindzen and Nigam*, 1987]. We focus throughout this thesis on the energy budget-based framework; see *Sobel* [2007] for comparison of the two classes of theories.

³Although the short atmospheric residence time of water vapor requires that global mean precipitation and evaporation be equal, this $\sim 2\% \text{ K}^{-1}$ rate of increase has been separately interpreted based on atmospheric energetics constraining precipitation [e. g. *Allen and Ingram*, 2002] and surface energetics constraining evaporation [e. g. *O'Gorman and Schneider*, 2008].

increases with global mean temperature at the roughly exponential rate set by the Clausius-Clapeyron relationship between the saturation vapor pressure of water and temperature (ignoring the pressure dependence). At Earth-like temperatures, this rate is $\sim 7\% \text{ K}^{-1}$. All else equal, this increase in water vapor at a rate proportional to the climatology acts to enhance the existing gradients in moisture and MSE. This behavior, applied to the column moisture budget, yields the ubiquitous thermodynamic scaling or “rich-get-richer” mechanism for the precipitation response to mean warming [Mitchell *et al.*, 1987; Chou and Neelin, 2004; Held and Soden, 2006]: preferential moistening of climatological convecting regions enhances precipitation in these locations at the expense of precipitation in non-convecting regions.

Although thermodynamic scaling captures the gross zonal mean precipitation and precipitation minus evaporation ($P - E$) changes in many contexts, quantitative discrepancies are generally appreciable at many latitudes, the more so that the imposed perturbation has appreciable spatial structure [Boos, 2011; Back *et al.*, 2013]. In the zonal mean, the position of the Intertropical Convergence Zone (ITCZ) is also sensitive to global scale energy flows [Kraus, 1977a,b] not accounted for by thermodynamic scaling.⁴ Deviations tend to be even worse on a regional basis, and over land the theory is not physically justified due to surface hydrological constraints (discussed further below). In terms of societal impacts, the latter is especially problematic. These complicating physical factors are best understood through a more careful consideration of the attendant energetics, and we therefore formally present the MSE budget before considering its manifestation in the zonal mean and semi-arid land contexts and the respective links to ITCZ and Sahel rainfall variations.

⁴Some studies [e.g. Nicholson, 2009], preferring a literal interpretation of the term “convergence zone”, use ITCZ to refer to the location of maximum low-level convergence and “tropical rainbelt” for the location of maximum precipitation. The two features are not necessarily co-located, with the precipitation maximum in some contexts occurring equatorward of the convergence maximum [e.g. Hastenrath and Lamb, 1977].

1.2.3 The moist static energy budget

The column-integrated MSE budget succinctly encapsulates the energetics of tropical circulations in both transient and time-mean contexts. Denoting MSE by h , then $h \equiv c_p T + gz + L_v q_v - L_f q_i$, where c_p is the specific heat of air at constant pressure, T is temperature, g is the gravitational constant, z is geopotential height, L_v is the latent heat of vaporization of water, q_v is specific humidity, L_f is the latent heat of fusion of water, and q_i is specific mass of ice. MSE therefore comprises potential energy and sensible and latent enthalpy while neglecting kinetic energy. Denoting column-mass integrals with curly brackets ($\{\cdot\} \equiv \int_0^{p_s} \cdot \frac{dp}{g}$, where p_s is surface pressure), time-averages with overbars, and deviations from the time-average with primes, the time-mean, column-integrated MSE budget may be expressed as

$$\frac{\partial}{\partial t} \{\bar{\mathcal{E}}\} + \{\bar{\mathbf{u}} \cdot \nabla_p \bar{h}\} + \left\{ \bar{\omega} \frac{\partial \bar{h}}{\partial p} \right\} + \nabla \cdot \{\bar{h}' \bar{\mathbf{u}}'\} \approx \bar{F}_{\text{net}}, \quad (1.1)$$

where $\mathcal{E} \equiv c_v T + gz + L_v q_v - L_f q_i$ is total internal energy, c_v is the specific heat of air at constant volume, \mathbf{u} is horizontal velocity, ∇_p is the horizontal divergence operator at constant pressure, and F_{net} is the net energetic forcing. F_{net} comprises top-of-atmosphere (TOA) and surface radiative fluxes (R_t and R_s , respectively) and surface turbulent fluxes of sensible (H) and latent enthalpy ($L_v E$, where E is evaporation; all signed positive directed into the atmosphere):

$$F_{\text{net}} \equiv L_v E + H + R_t + R_s. \quad (1.2)$$

Notably, convective diabatic moistening and heating terms that appear (often with large magnitude) at individual levels must cancel in the column integral, one of the key draws of (1.1). Conceptually, energetic input into the atmospheric column through its upper and lower boundaries (\bar{F}_{net}) must be balanced by some combination of column-integrated time-mean horizontal MSE advection ($\{\bar{\mathbf{u}} \cdot \nabla_p \bar{h}\}$, typically dominated by the large-scale rotational flow), column-integrated time-mean vertical MSE advection ($\{\bar{\omega} \partial_p \bar{h}\}$, inherently due to the divergent flow), and column-integrated transient eddy MSE flux divergence ($\nabla \cdot \{\bar{h}' \bar{\mathbf{u}}'\}$), less

any change in column-integrated total internal energy ($\partial_t \{\bar{\mathcal{E}}\}$).⁵

Strictly speaking, MSE is not a conserved quantity, and several other approximations are inherent in (1.1) both in MSE as the thermodynamic tracer⁶ and in how the column budget is formed⁷. But for our purposes (1.1) constitutes a sufficiently accurate encapsulation of atmospheric energetics.

The classical picture of a tropical convecting region [*Neelin and Held, 1987*] comprises positive net energetic forcing balanced by the time-mean divergent circulation, $\bar{F}_{\text{net}} \approx \{\bar{\omega} \partial_p \bar{h}\}$: convergence of mass and MSE in the boundary layer, deeply penetrating moist convection, and convective outflow near the tropopause that diverges mass and more MSE than is converged in the boundary layer. Under these conditions, for a given F_{net} , precipitation depends on the efficiency of the column-integrated MSE flux divergence per unit low-level mass convergence, i. e. the gross moist stability (GMS) – the less efficient convection is at diverging MSE, the more mass must be circulated, thereby increasing the precipitation – as well as the amount of water vapor converged per unit low-level mass convergence [i. e. the gross moisture

⁵The time-averaged energy storage term ($\partial_t \bar{\mathcal{E}}$) is often neglected, but it can be non-negligible in the context of sub-annual time-averages as well as in the difference between climate states (both of which are of interest in this thesis).

⁶See *Neelin* [2007] and *Romps* [2015] for relevant discussion. An exhaustive accounting of atmospheric thermodynamics in terms of the dry entropy budget is presented by *Romps* [2008]. The solid water phase is often neglected in MSE; its inclusion is sometimes specified via the term “frozen MSE” [e. g. *Peters et al.*, 2008]. But the latent enthalpy released by freezing ice can appreciably enhance convective parcel buoyancy [e. g. *Romps and Kuang*, 2010; *Seeley and Romps*, 2016], and including the ice phase adds little conceptual or computational difficulty.

⁷As noted by *Trenberth* [1991], this expression of the column budget makes the following approximations:

- The surface pressure advection term due to the Leibniz integral rule (c. f. his Equation 8b) is neglected:

$$\nabla \cdot \int_0^{p_s} h \mathbf{u} \, dp = \int_0^{p_s} \nabla_p \cdot h \mathbf{u} \, dp + h_s \mathbf{u}_s \cdot \nabla p_s,$$

where h_s and \mathbf{u}_s are MSE and horizontal wind at the surface.

- The water vapor contribution to the total atmospheric mass is neglected by using the approximate continuity equation $\partial_p \omega + \nabla \cdot \mathbf{u} \approx 0$. The more accurate expression includes the net diabatic source of water vapor as the right hand side, since conversions to or from the vapor phase alter the total mass of gas present.
- The assumed $\omega = 0$ bottom boundary condition neglects surface pressure variations:

$$\omega_s = \frac{\partial p_s}{\partial t} + \mathbf{u}_s \cdot \nabla p_s$$

stratification, c. f. *Neelin and Held*, 1987]. Conversely, for a given GMS and gross moisture stratification, precipitation will increase with increasing F_{net} , as the divergent circulation that drives convection must ramp up in order to balance the energetic forcing. This is also complicated by cloud radiative feedbacks: deep convective cumulus towers generally trap more longwave radiation than they reflect shortwave radiation, countering the circulation’s overall MSE divergence and thereby reducing its effective GMS [Bretherton *et al.*, 2006; Raymond *et al.*, 2009].

However, the first baroclinic MSE profile typical of the tropics (minimum in the mid-troposphere) renders the MSE divergence by the divergent circulation sensitive to the depth of the convection – if sufficiently shallow, the divergent circulation actually converges MSE in the column integral. On the timescale of a convective life-cycle, this transport of moisture and MSE into the free troposphere by shallow convection conditions the column for subsequent deep convection [e. g. Wu, 2003; Inoue and Back, 2015]. On climatic timescales, this must be balanced by MSE divergence through some combination of transient eddies and the time-mean horizontal flow [e. g. Back and Bretherton, 2006; Bretherton *et al.*, 2006].

1.3 Zonal mean energetics and precipitation

Earth absorbs more solar radiation in the tropics than at high latitudes, driving atmospheric circulations that transport energy poleward.⁸ This zonal mean energy transport is more readily understood by examining MSE fluxes rather than flux divergences. Neglecting the storage term and zonally integrating (1.1) yields the time-mean, column-integrated, zonally integrated MSE budget,

$$\int_0^{2\pi} \frac{\partial}{\partial \phi} (\{\bar{h}\bar{v}\} \cos \phi) \, d\lambda = \int_0^{2\pi} \bar{F}_{\text{net}} a \cos \phi \, d\lambda, \quad (1.3)$$

⁸Less some notational differences, much of this section is taken from Section 1 of Hill *et al.* [2015], © American Meteorological Society. Used with permission.

where a is planetary radius, ϕ is latitude, λ is longitude, and v is meridional velocity. Denoting zonal averages with square brackets, integrating (1.3) meridionally from either pole (where the meridional wind vanishes; we choose the South Pole) to each latitude ϕ gives

$$2\pi a \cos \phi \{ [\bar{h}v] \} = \int_{-\pi/2}^{\phi} \int_0^{2\pi} \bar{F}_{\text{net}} a^2 \cos \hat{\phi} d\lambda d\hat{\phi}, \quad (1.4)$$

where $\hat{\phi}$ denotes the variable of integration. This is an expression for the total atmospheric meridional MSE flux at each latitude, commonly referred to as atmospheric heat transport (AHT). This transport manifests through the mean meridional circulation (MMC), stationary eddies, and transient eddies:

$$[\bar{h}v] = \underbrace{[\bar{h}][\bar{v}]}_{\text{MMC}} + \underbrace{[\bar{h}^* \bar{v}^*]}_{\text{stationary eddies}} + \underbrace{[\bar{h}'v']}_{\text{transient eddies}}, \quad (1.5)$$

where asterisks denote deviations from the zonal mean, i. e. $h^* \equiv h - [h]$.⁹

In the tropics, the mean meridional circulation consists of the two Hadley cells. These Hadley circulations – which broadly comprise near-equatorial ascent, poleward flow aloft, descent in the subtropics, and equatorward near-surface flow – commonly arise in planetary climates, e. g. on Venus and Titan [Mitchell, 2008] and motivated some of the earliest modern climate studies [Halley, 1686; Hadley, 1735]. The modern perspective on Hadley circulations combines CQE with dynamical theories of angular momentum-conserving overturning circulations [Schneider, 1977; Held and Hou, 1980; Hou and Lindzen, 1992; Plumb and Hou, 1992] and posits near-surface meridional energetic gradients as the fundamental driver of monsoon circulations [Emanuel, 1995, 2007].¹⁰ The convergence of moist air underlying the ascending branch of the Hadley cells generates the ITCZ, which in the CQE framework occurs just

⁹The transient eddy term is occasionally [e. g. Marshall *et al.*, 2013] further separated into zonal-mean and zonally asymmetric components, i. e. $[\bar{h}'v'] = [\bar{h}'][\bar{v}'] + [\bar{h}^*v^*']$, but the first LHS term (the “transient overturning circulation”) is generally negligible on Earth.

¹⁰This contrasts with the emphasis on surface thermal gradients central to the traditional land-sea contrast perspective on monsoons [e. g. Webster, 1987], which agrees less well with observations and modeling results [Hurley and Boos, 2013].

equatorward of the local maximum of subcloud MSE [*Privé and Plumb, 2007*] (although the two can separate in planetary contexts with sufficiently slow rotation rate, c. f. *Faulk et al. [2016]*).

The Hadley cells are the largest contributors to AHT in the deep tropics and primarily flux energy poleward, the large winter cell spanning across the equator and including a flux from the summer to the winter hemisphere. As a result, meridionally asymmetric energy perturbations – e. g. the Northern Hemisphere-centric anthropogenic aerosols or asymmetric feedbacks to the more uniform greenhouse gas forcing – can push the inner boundary of the Hadley cells, and with it the ITCZ, farther away from the energy deficient hemisphere [e. g. *Kang et al., 2008, 2009; Ming and Ramaswamy, 2011; Chiang and Friedman, 2012; Frierson and Hwang, 2012; Schneider et al., 2014*]. However, this framework for energetically-forced ITCZ displacements is hamstrung by radiative feedbacks accompanying the circulation response that can exceed the original forcing in magnitude [*Kang et al., 2009; Voigt and Shaw, 2015; Shekhar and Boos, 2016*]; constraining these feedbacks *a priori* has proven difficult. Recent quantitative approaches [*Bischoff and Schneider, 2014, 2015*] to the ITCZ energetic framework are an important theoretical advance (although they rely on a linearization of the ITCZ position with respect to the equator, whereas in planetary contexts with sufficiently slow rotation rate the ITCZ can migrate seasonally all the way to either pole [*Faulk et al., 2016*]) and compare well with observed seasonal and interannual ITCZ excursions [*Adam et al., 2016a,b*].

Moreover, the energetic framework for the Hadley circulation perturbations neglects variations in the transport efficiency, i. e. the Hadley cell GMS. But in some idealized GCM simulations, GMS can be the dominant term, causing the energetic framework to fail qualitatively [*Merlis et al., 2013a*]. Understanding the role of the GMS variations in forced ITCZ movements in a more realistic modeling setting is therefore a key focus of Chapter 2 of this thesis.

1.4 Energetics and precipitation for tropical land and the Sahel

1.4.1 Land surface dynamics

Inherent differences between land and ocean include (in rough order of importance for the questions of interest) heat capacity, surface hydrology, albedo, topography, surface roughness, and vegetation dynamics. For either surface type, the surface energy budget may be written

$$C \frac{\partial T_s}{\partial t} = -R_s - H - L_v E - \nabla \cdot \mathbf{F}_{\text{sub}}, \quad (1.6)$$

where C is the surface heat capacity, T_s is surface temperature, and $\nabla \cdot \mathbf{F}_{\text{sub}}$ is the sub-surface energy flux divergence. (1.6) states that surface temperature responds (at a rate set by its heat capacity) to the net convergence of energy through sub-atmospheric transports and through the boundary with the atmosphere.

For ocean, surface heat capacity depends on the depth of the well-mixed surface layer: $C = \rho_w c_w D$, where ρ_w is water density, c_w is the specific heat capacity of water, and D is the mixed-layer depth. Ocean currents can produce large divergences or convergences of energy, and for sufficiently deep ocean mixed layers, energy storage can be appreciable on seasonal or longer timescales. Poleward ocean heat transport cools the tropical oceans, thereby favoring continental convection at low latitudes, but can also weaken the Hadley circulation by necessitating less atmospheric poleward energy transport [Chou *et al.*, 2001]. Both sensible and latent enthalpy fluxes follow the well-known bulk aerodynamic formulas. For sensible enthalpy, $H = c_p \rho c_H |\mathbf{u}_s| (T_s - T_a)$, where T_a is the near-surface atmospheric temperature, ρ is air density, $|\mathbf{u}_s|$ is surface wind speed, c_H is a transfer coefficient that depends on surface roughness. For evaporation, $E = \rho c_E |\mathbf{u}_s| (q_s^* - q_a)$, where q_s^* is the saturation specific humidity at the surface, q_a is the near-surface specific humidity, and c_E is the transfer coefficient. Thus, all else equal, warming of SSTs at fixed relative humidity increases both sensible and

latent enthalpy fluxes into the atmosphere.

For land, there is no appreciable sub-ground horizontal energy flux, and the ground heat capacity is sufficiently small that the net surface energy flux is negligible for the monthly and longer timescales of interest: $\bar{R}_s + \bar{H} + L_v \bar{E} \approx 0$. The net column energy flux therefore reduces to the top-of-atmosphere radiative flux: $\bar{F}_{\text{net}} \approx \bar{R}_t$. The resulting absence of surface fluxes from the column MSE budget over land does not mean that they are irrelevant – a surface with a large downward radiative flux balanced by large upward latent and sensible enthalpy fluxes can be expected to induce more convective precipitation than one where each of the individual surface fluxes is small. However, this partitioning is further complicated by surface hydrology limitations on evaporation.

Provided the sensible enthalpy flux is non-negative (computed using the same bulk formula as for ocean), the net downward radiative flux constitutes an upper limit on evaporation [although in very hot climates in an idealized GCM the sensible enthalpy flux can become negative, c. f. *O’Gorman and Schneider*, 2008]. The net surface radiative flux divided by L_v is therefore referred to as the potential evaporation: $E_{\text{pot}} \equiv -R_s/L_v$.¹¹ Because sub-ground horizontal moisture transport is negligible on spatial scales larger than individual catchments, evaporation cannot exceed precipitation (P) on climatic timescales: $\bar{P} - \bar{E} \geq 0$. As such, the source of liquid water from precipitation provides another upper bound on evaporation. The relative importance of the energy and moisture limitations to evaporation are well captured by the Budyko relationship [e. g. *Lintner et al.*, 2015], which provides empirical functions for the value of E as a function of E_{pot} and P : starting from $P = 0$ to $P \gg E_{\text{pot}}$, evaporation increases almost linearly with precipitation in much of the moisture-limited ($P < E_{\text{pot}}$) regime, before asymptoting towards E_{pot} once in the energy-limited ($P > E_{\text{pot}}$) regime.

Semi-arid regions are generally firmly in a moisture-limited evaporative regime, causing surface temperature and precipitation to be anti-correlated: reduced precipitation engenders

¹¹We use the term “evaporation” over land as a shorthand for evapotranspiration, the latter encompassing both direct evaporation from the surface and transpiration of water from vegetation. In the literature, potential evapotranspiration (PET) is computed in numerous ways in order to account empirically for biophysical factors that affect evapotranspiration beyond the energy limitation [e. g. *Scheff and Frierson*, 2014].

reduced evaporation, causing the surface to warm up in order to regain energy balance through compensating changes in longwave emission and sensible enthalpy flux. This reduces the near-surface relative humidity, which may amplify the drying by inhibiting convective precipitation reaching the surface through entrainment of drier air [*Derbyshire et al.*, 2004; *Bretherton et al.*, 2006] and increased re-evaporation of raindrops before reaching the surface [*Gentine et al.*, 2013]. Concomitant cloud cover loss may further amplify the drying by allowing more shortwave radiation to reach the surface, necessitating further surface warming in order to regain energy balance [*Tanaka et al.*, 1975; *Charney et al.*, 1977; *Chou et al.*, 2001]. (The arguments all apply with sign reversed for the case of a positive precipitation anomaly.) At the same time, heating of overlying parcels by a hot surface will increase their buoyancy; at the mesoscale, moist convection in the Sahel occurs preferentially over dry patches, as horizontal advection of moist parcels over the hot surface triggers moist convection [*Taylor et al.*, 2011].

1.4.2 Tropical land precipitation variations

Under global warming, surface warming is land-amplified in both transient and equilibrium contexts [*Byrne and O’Gorman*, 2013; *Byrne and O’Gorman*, 2013], a straightforward result of CQE dynamics. Combined with modest global mean and ocean-mean relative humidity change, this land-amplified warming causes relative humidity over land to decrease. Largely as a result, terrestrial aridity (defined e.g. as the ratio of precipitation to potential evapotranspiration), generally increases at low- and mid-latitudes [*Scheff and Frierson*, 2014; *Sherwood and Fu*, 2014; *Scheff and Frierson*, 2015]. As such, in global warming simulations changes to precipitation and surface temperature over tropical land are anti-correlated [*Chadwick*, 2016], and most of the land regions that warm more than the global land average are semi-arid regions in which precipitation has decreased [*Berg et al.*, 2014].

Many of the mechanisms that limit the extent of continental convection relative to the area of positive energetic forcing (which generally extends much farther poleward) were

developed using the intermediate-complexity Quasi-equilibrium Tropical Circulation Model (QTCM) [*Chou et al.*, 2001; *Chou and Neelin*, 2001, 2003]. Of central importance in this thesis is the “ventilation” mechanism, wherein horizontal advection of low MSE (cool and/or dry) air inhibits moist convection. Mechanisms of tropical precipitation responses to warming (including rich-get-richer behavior) were also developed from QTCM simulations [*Neelin et al.*, 2003; *Chou and Neelin*, 2004]. Of central importance in this thesis is the “upped ante” mechanism, wherein increased tropical dry static stability inhibits convection where moisture convergence does not increase sufficiently, in particular on convective margins due to inflow acting on the enhanced moisture gradient.

1.4.3 The Sahel

The Sahel is the transitional region between the Sahara Desert and the savannas of West Africa and northern equatorial Africa. The majority of its annual mean precipitation occurs during the northward excursion of the ITCZ in boreal summer [e.g. review by *Nicholson*, 2013], which manifests in the region’s west as the West African Monsoon [e.g. *Nie et al.*, 2010] and in its east as a northward shift of continental convection. Despite this effect of the continental geometry, the Sahelian precipitation and many other surface climate markers are to first order zonally symmetric spanning the continent’s full width.¹² Being, by definition, a transitional zone, the Sahel climate varies rapidly in the meridional, but on average it is squarely semi-arid. Because of its strong surface temperature-precipitation-evaporation relationship, the Sahel it is considered a “hot-spot” for land-atmosphere coupling [*Koster et al.*, 2004]. The positive energetic forcing criterion for moist convection is acute for the Sahel, due to its location on the southern border of the Sahara Desert: the latter’s high surface albedo limits shortwave absorption, high temperatures promote longwave emission, and lack of water vapor limit longwave absorption, collectively leading to vanishing or even negative

¹²Modest zonal asymmetries in precipitation include local maxima in the far west and east [*Cook*, 1997], the latter being common to continental convection zones [*Cook*, 1994; *Chou et al.*, 2001] but further localized by the topography of the Ethiopian Highlands.

net forcing values [*Charney*, 1975; *Chou and Neelin*, 2003]. The ventilation mechanism manifests prominently in the northern Sahel as northerly flow of dry Saharan air [*Zhang et al.*, 2008; *Nie et al.*, 2010; *Nicholson*, 2013].

The hydroclimate of the African Sahel varies markedly on interannual to millennial timescales. Most notoriously, a severe drought spanned from the late 1960s to the mid 1980s [*Tanaka et al.*, 1975; *Nicholson*, 1985; *Gallego et al.*, 2015]. Though initially ascribed to local overgrazing by livestock triggering a vegetation-surface albedo-precipitation desertification feedback [*Charney*, 1975; *Charney et al.*, 1975], AGCMs run with fixed vegetation and the observed timeseries of SSTs generally capture the drought and other observed decadal-scale Sahel rainfall variations [*Folland et al.*, 1986; *Giannini et al.*, 2003], leading to the effects of SST patterns becoming the primary research focus [e.g. review by *Rodríguez-Fonseca et al.*, 2015].¹³

GCM end-of-21st century projections of Sahel rainfall range from severe drying to even greater wettening [e.g. *Biasutti*, 2013], a spread that has not improved over the past two generations of the Coupled Model Intercomparison Project (CMIP), CMIP3 and CMIP5 [e.g. Figure 11 of *Rodríguez-Fonseca et al.*, 2015]. GCMs also project widely varying spatial patterns of SST change [e.g. Figure 12 of *Zhao et al.*, 2009], leading to arguments that this is the source of the Sahel rainfall spread. But model-dependent responses to imposed SST anomalies [*Rodríguez-Fonseca et al.*, 2015, and references therein] and non-stationary relationships between Sahel rainfall and various SST indices both in models [e.g. *Lough*, 1986; *Biasutti et al.*, 2008; *Losada et al.*, 2012] and observations [*Gallego et al.*, 2015] have led to continuing disagreement regarding the most important ocean basin or SST pattern, with Atlantic [e.g. *Zhang and Delworth*, 2006], Indian [e.g. *Lu*, 2009], and Arctic [*Park et al.*,

¹³Vegetation feedbacks still figure centrally in interpretations [e.g. *Hales et al.*, 2006] of the onset of the African Humid Period of \sim 14.8–5.5 ka, wherein abundant rainfall and vegetation spanned the Sahel and most of the Sahara [e.g. *Shanahan et al.*, 2015], although how rapidly this “Green Sahara” state arose relative to its root cause of orbital precession-induced increases in summer insolation is contested [*deMenocal et al.*, 2000; *Kröpelin et al.*, 2008a,b; *Brookin and Claussen*, 2008]. Also, interannual variations are typically amplified and agreement with observations improved when vegetation is made dynamic [e.g. *Zeng et al.*, 1999; *Giannini et al.*, 2003]. And, based on AGCM simulations, *Dong and Sutton* [2015] attribute the observed recovery from drought since the 1980s primarily to direct forcing by increasing greenhouse gases rather than SSTs.

2015] SSTs separately posited as being fundamental.

1.4.4 Emergent constraints

Given the longstanding lack of guidance from GCM future simulations regarding the future fate of the Sahelian hydroclimate, an attractive alternative is to search for emergent observational constraints – i. e. some present-day observable (and observed) quantity that correlates across GCMs with their precipitation response in future simulations, which can therefore be compared to real-world observational values to rule out the projected change in those models that sit outside the likely observational range of the predictor [nicely discussed by *Caldwell et al.*, 2014]. To be truly credible, an emergent constraint also requires a clear physical mechanism that gives rise to the correlation between the control quantity and the response. Such attempts have been made for snow albedo feedback with global warming based on the present-day seasonal cycle feedback [*Hall and Qu*, 2006] and equilibrium climate sensitivity based on tropospheric relative humidity [*Fasullo and Trenberth*, 2012]. But to our knowledge, this has not been formally attempted for the Sahel rainfall response.

1.5 Thesis roadmap

In this thesis, we use idealized SST perturbation experiments in comprehensive AGCMs to investigate the linkages between precipitation and the MSE budget in response to imposed changes to the SST field – both its mean and its spatial pattern. Chapter 2 focuses on the zonal mean; we use the NOAA Geophysical Fluid Dynamics Laboratory AM2.1 AGCM to examine the annual cycle of zonal mean energy transport, Hadley cell strength, Hadley cell GMS, and movements of the ITCZ, both in a present-day control setting and in response to the mean and spatial pattern components of historical anthropogenic forcing agents. Hadley cell GMS anomalies generally constitute either the majority or at least a sizable fraction of the anomalous meridional energy transport in the cell centers, which we interpret through

the effects of thermodynamic scaling acting on climatological near-surface MSE gradients. Near the ITCZ, this vehicle for GMS changes is less efficient, which constitutes a heuristic explanation for the tight link between low-latitude MSE fluxes and the ITCZ position.

Chapters 3-5 focus on the Sahel. Through uniform 2 K SST warming simulations in AM2.1 (Chapter 3), both in its standard configuration and a new configuration utilizing an alternative convective parameterization, we highlight those processes most relevant to its well-documented pronounced drying response. In so doing, we quantify its climatological and perturbation MSE budget, using a new adjustment method to correct spurious imbalances in column tracer budgets. The SST warming acts to enhance the prevailing MSE difference between the Sahel and the Sahara Desert, and thereby the dry advection into the Sahel. But in AM2.1 with the alternate convective parameterization, these drying influences are overcome by the large-scale wettening influences of global SST warming, flipping the severe precipitation decrease in the default AM2.1 to a modest increase. We argue that the strengths of these competing drying and wettening effects depend in part on properties of the climatological circulation, rather than purely on the convective processes irrespective of the large-scale state.

By extending this analysis to uniform SST warming simulations in other GFDL models and CMIP5 models (Chapter 4), we find this overall picture to be robust, and precipitation decreases with uniform warming in fourteen of seventeen models analyzed. However, attempts to turn the robust qualitative signals into a quantitative emergent constraint are complicated by differing strengths of the relevant correlations across the GFDL models as compared to across the CMIP5 models. But reanalysis vertical velocity profiles and observations of covariances of cloud radiative variations with precipitation suggest mechanisms in AM2.1 that exacerbate the drying response to SST warming in a manner inconsistent with observations.

Through various additional simulations in GFDL AGCMs and further comparison to observations (Chapter 5), we refine the interpretation of the results in Chapters 3 and 4 and

provide insight on several other outstanding questions regarding relationships between SSTs and rainfall in the Sahel. These include 20th century simulations in GFDL AGCMs which suggest a non-negligible influence by variations in the global-mean SST on 20th century decadal-scale rainfall in the Sahel. Finally, Chapter 6 closes with summary of the results and discussion of their implications, limitations, and prospects for future work.

Our use of idealized SST perturbation experiments in comprehensive AGCMs provides a bridge between idealized models in which much of the relevant theory has been derived (e.g. the QTCM [*Neelin and Zeng, 2000*] and the *Frierson et al. [2006]* moist idealized GCM) and fully coupled GCMs (and the real world) in which such idealized SST perturbations are not feasible.

Chapter 2

Zonal mean energy transports and ITCZ movements

Abstract

Anthropogenically forced changes to the mean and spatial pattern of sea surface temperatures (SSTs) alter tropical atmospheric meridional energy transport throughout the seasonal cycle – in total, its partitioning between the Hadley cells and eddies, and, for the Hadley cells, the relative roles of the mass flux and the gross moist stability (GMS). We investigate this behavior using an atmospheric general circulation model forced with SST anomalies caused by either historical greenhouse gas or aerosol forcing, dividing the SST anomalies into two components: the tropical mean SST anomaly applied uniformly, and the full SST anomalies minus the tropical mean.

For greenhouse gases, the polar-amplified SST spatial pattern partially negates enhanced eddy poleward energy transport driven by mean warming. Both SST components weaken winter Hadley cell circulation and alter GMS. The Northern Hemisphere-focused aerosol cooling induces northward energy flux anomalies in the deep tropics, which manifest partially via strengthened northern and weakened southern Hadley cell overturning. Aerosol-induced GMS changes also contribute to the northward energy fluxes. A simple thermodynamic scaling qualitatively captures these changes, though it performs less well for the greenhouse gas simulations. The scaling provides an explanation for the tight correlation demonstrated in previous studies between shifts in the Intertropical Convergence Zone position and cross-

equatorial energy fluxes.

2.1 Introduction

As described in Chapter 1, the general circulation of Earth's atmosphere effects transport of energy from the tropics to higher latitudes that manifests through the Hadley cells, stationary eddies, and transient eddies, and the dominance of the Hadley cell energy transport in the deep tropics causes the Intertropical Convergence Zone (ITCZ) position to be sensitive to meridional energy gradients.¹ Both the total tropical atmospheric energy transport and its partitioning among these flow components vary with the seasonal cycle [e. g. *Trenberth and Stepaniak*, 2003]. Stationary eddy transports are also primarily poleward, and transient eddy poleward fluxes are large in autumn and winter, increasing in magnitude moving away from the equator. The dynamics controlling the Hadley cells' strength and extent is also seasonal, the winter cell adhering more closely to the classical angular momentum conserving models [e. g. *Held and Hou*, 1980], but with eddy stresses strongly affecting the circulation in the equinoctial and summer cells and the poleward flank of the winter cell [e. g. *Salmon et al.*, 2001; *Walker and Schneider*, 2005; *Merlis et al.*, 2013a].

The fluxes of energy and mass by the Hadley cells are linked via the gross moist stability (GMS). As the Hadley cells overturn, their upper and lower branches transport energy in opposite directions, so that the net meridional energy flux depends on their degree of compensation [*Held and Hoskins*, 1985]. This compensation depends on two factors: the rate of mass circulation (known as the mass flux) and the meridional energy flux per unit mass flux, which is the GMS. Symbolically at a given latitude ϕ ,

$$F_{\text{HC}}(\phi) = \Psi_{\text{max}}(\phi) \Delta_{\text{HC}}(\phi), \quad (2.1)$$

¹Less some notational differences, some introductory material used in Chapter 1, and a few new clarifying comments, this chapter is a direct reproduction of *Hill et al.* [2015], © American Meteorological Society. Used with permission.

where F_{HC} is the energy flux by the Hadley cells, Ψ_{max} the mass flux, and Δ_{HC} the GMS. This expression in fact defines GMS as the ratio of the Hadley cell energy flux to the mass flux;² in this sense GMS can be thought of as the efficiency of meridional energy transport by the Hadley cells.

It follows from (2.1) for sufficiently small perturbations that fractional changes in these quantities are related by

$$\frac{\delta F_{\text{HC}}(\phi)}{F_{\text{HC}}(\phi)} = \frac{\delta \Psi_{\text{max}}(\phi)}{\Psi_{\text{max}}(\phi)} + \frac{\delta \Delta_{\text{HC}}(\phi)}{\Delta_{\text{HC}}(\phi)}. \quad (2.2)$$

Merlis et al. [2013a] show that, at the Hadley cell centers in an intermediate complexity aquaplanet model forced by orbital precession changes, GMS can overcompensate for the imposed meridional energy imbalance, such that the fractional mass and energy flux changes are of opposite sign. *Merlis et al.* [2013a] also find the GMS response to be captured by a simple approximation by *Held* [2001] relating GMS to the surface meridional MSE gradient.

Meridional ITCZ shifts manifest as a spin-up of the cell in the energy excessive hemisphere and a spin-down in the energy deficient one. If GMS change compensates for some of the induced energy imbalance, then by (2.2) the mass circulation response – and with it the ITCZ shift – will be weaker. Yet prior studies have found changes in the ITCZ position to be tightly correlated with anomalous atmospheric energy transport at the equator [*Frierson and Hwang*, 2012; *Donohoe et al.*, 2013], suggesting a modest role for GMS change in and of itself near the cells’ shared equatorward border.

Several other recent studies have investigated GMS in the context of meridional energy transports and movement of the ITCZ [e.g. *Frierson*, 2007; *Kang et al.*, 2009; *Kang and Held*, 2011; *Merlis et al.*, 2013b,c], but all use zonally symmetric aquaplanet models (or with a simple zonally symmetric continent in *Merlis et al.* [2013b]), often with simplified

²The HC subscript on the gross moist stability term is meant to emphasize that the energy flux is by the Hadley cells only. The analogous quantity that also includes eddy energy transports is known as “total GMS” [e.g. *Kang et al.*, 2009]. Moreover, gross moist stability can be defined in other ways than the zonal-mean, meridional flux form we use here, such as using the flux divergence [e.g. *Neelin and Held*, 1987] or vertical velocity profile [e.g. *Chou et al.*, 2009], in which cases it is a function of both longitude and latitude.

treatments of radiation, convection, and other relevant processes. The behavior of tropical moist stability in global warming has also been studied more generally, with stability changes fundamental to the “upped-ante” and “rich-get-richer” mechanisms of *Neelin et al.* [2003] and *Chou and Neelin* [2004].

These considerations compel us to study how anthropogenically forced changes to the SST field – both its mean and its spatial pattern – alter the tropical meridional energy flux throughout the seasonal cycle in a comprehensive atmospheric general circulation model (AGCM). Section 2.2 and Appendix 2.A describe our methodology. Section 2.3 presents the results of these prescribed SST simulations and a thermodynamic scaling for GMS change that builds on the ideas of *Held* [2001]. Discussion and summary follow in Sections 2.4 and 2.5, respectively. We view these simulations as a bridge between the aforementioned idealized aquaplanet simulations and fully coupled GCMs (or the real world) in which such a decomposition of surface conditions into mean and spatial pattern components is not feasible.

2.2 Methodology

2.2.1 Prescribed SST experiments

We first create SST anomalies representative of the effects of either forcing agent using the experiments of *Ming and Ramaswamy* [2009] with the Geophysical Fluid Dynamics Laboratory (GFDL) AM2.1 AGCM [*GFDL Atmospheric Model Development Team*, 2004; *Delworth et al.*, 2006], 2° latitude \times 2.5° longitude resolution, coupled to a 50 meter mixed-layer (or “slab”) ocean. The AGCM accounts for aerosol-cloud interactions via a prognostic cloud droplet number concentration scheme for shallow cumulus and stratiform clouds that depends on local aerosol concentrations [*Ming et al.*, 2006, 2007]. A control case with pre-industrial atmospheric composition is perturbed with pre-industrial to present day anthropogenic burdens of either well-mixed greenhouse gas or aerosols. We run the pre-industrial control, present day greenhouse gases, and present day aerosol cases to equilibrium, averaging the

annual cycle of SSTs over model years 61–80 to produce a climatological SST annual cycle. We then subtract the control from the perturbation SSTs to obtain an SST anomaly field for each forcing agent.

Next, we add these SST anomalies to observed climatological SSTs from the NOAA Optimal Interpolation dataset [Reynolds *et al.*, 2002] over 1981–1999, again retaining an annual cycle. These SST fields along with observed climatological sea ice are then used to drive AM2.1, with the same annual cycle repeated each year. This yields a control case and greenhouse gas and aerosol perturbation cases. The AGCM is run for 17 years, the first year discarded as spin-up and results averaged over the subsequent 16. Results averaged over the first 8 years or subsequent 8 years of the averaging period are largely similar to results using all 16. Unless otherwise noted, all subsequent discussion of results are for the prescribed SST experiments.

Two additional simulations for each forcing agent isolate the roles of changes to the mean and spatial pattern of SSTs. In the first, the annual mean SST change averaged over the tropics (+2.0 K for greenhouse gases, −1.1 K for aerosols; tropics defined as 30°S–30°N) is added to the climatology at every ocean gridpoint and timestep.³ In the second, this tropical mean SST change is subtracted from the full SST anomaly field at each ocean gridpoint before being added to the climatology. These experiments thus represent the mean temperature change and spatial pattern components, respectively. *Ma and Xie* [2012] perform an analogous decomposition into mean and spatial pattern components in the CAM3 AGCM in their analysis of circulation and precipitation responses to anthropogenic forcing.

The near-zero tropical mean temperature change in the spatial pattern simulations negates changes in specific humidity induced via the Clausius-Clapeyron relation. Changes in annual and tropical mean water vapor path are −0.1 and −0.2 kg m^{−2} for the spatial pattern cases of greenhouse gases and aerosols, respectively, compared to +6.9 and −3.2 kg m^{−2} for the mean temperature change components and +6.7 and −3.4 kg m^{−2} for the full perturbation

³By coincidence of the tropical mean greenhouse gas warming being just over 2 K (2.04 K), the mean warming case is essentially identical to commonly run “plus 2 K” or “Cess” uniform SST warming simulations.

cases. In this sense, the mean and spatial pattern cases can be roughly thought of as the “thermodynamic” and “dynamic” components of the total response to the anomalous SSTs. The atmosphere responds quite linearly to the mean/spatial pattern decomposition, in that for all quantities analyzed the response to the full perturbation roughly equals the sum of the responses in the corresponding mean temperature change and spatial pattern cases (shown below for the energy flux).

2.2.2 Treatment of direct radiative forcing and surface fluxes

The atmospheric composition in all prescribed SST experiments is present day. Therefore, any differences in the climate response stem solely from differences in the imposed SST fields, and fast atmospheric adjustments (in particular by clouds) to the forcing agent are only incorporated to the extent that they affect the SST field in the original slab-ocean experiments. Nevertheless, the total atmospheric energy flux, mass flux, and GMS are to first order identical in the mixed layer ocean-AM2.1 and prescribed SST configurations (not shown), suggesting that fast atmospheric adjustments that do not imprint onto the SST field are of secondary importance for the large scale energetic response. The mixed layer ocean simulations include prescribed ocean surface flux adjustments as standard to mimic ocean heat transport. There are no prescribed surface fluxes in the prescribed SST simulations.

Altered atmospheric MSE transport is not the sole possible means of adjustment to an imposed meridionally asymmetric forcing: ocean heat transport or local radiative adjustments (e.g. via clouds) are feasible alternatives and are recognized to affect the ITCZ position (and hence the cross-equatorial energy flux) [e.g. *Kang et al.*, 2008, 2009; *Frierson and Hwang*, 2012; *Frierson et al.*, 2013; *Marshall et al.*, 2013]. Also, as demonstrated by *Yoshimori and Broccoli* [2008] and *Frierson and Hwang* [2012], cross-equatorial energy transports are ultimately tied to the TOA radiative imbalance between the hemispheres, for which the hemispheric mean surface temperature is a good, but not perfect, indicator. *Kang and Held* [2011] demonstrate SSTs to be a similarly imperfect proxy for surface energy

fluxes in driving tropical precipitation anomalies. Our focus on atmospheric MSE transports and framing of the energy transports and precipitation as responding to SST perturbations should be interpreted with these caveats in mind.

Appendix 2.A details how the energy flux, mass flux, and gross moist stability are calculated, including the partitioning of the energy flux among the MMC, stationary eddy, and transient eddy terms, a simple adjustment based on mass balance considerations applied in the MMC energy flux computation, and the sensitivity of the energy flux calculations to the height of the vertical integral.

2.3 Results

2.3.1 Surface temperature

Figure 2.1 shows the annual mean latitude-longitude pattern of surface air temperature change for the full and spatial pattern perturbation cases of each forcing agent. Tight coupling of the ocean and near-surface atmosphere cause these values over ocean to be nearly identical to the imposed SSTs (not shown), except for high latitude locations where the prevailing meteorology decouples the atmosphere from the surface. Table 2.1 lists the global mean, tropical mean, and Northern Hemisphere (NH) minus Southern Hemisphere (SH) annual mean surface air temperature responses for each perturbation simulation. Warming by greenhouse gases and weaker cooling by aerosols are evident (+2.6 and -1.6 K global mean, respectively), as are the polar amplified spatial pattern of the greenhouse gases and the aerosol-induced cooling of the NH relative to the SH (NH and SH mean change are +2.7 and +2.4 K respectively for greenhouse gases and -2.0 and -1.1 K for aerosols).

Figure 2.1 also shows the annual cycle of the zonal mean surface air temperature change for both full cases. The weakest changes occur in the Arctic during NH summer, when melting ice and snow peg surface temperature to the freezing point. Both also have their maximum magnitudes in the Arctic winter, as the prevailing near surface inversion inhibits

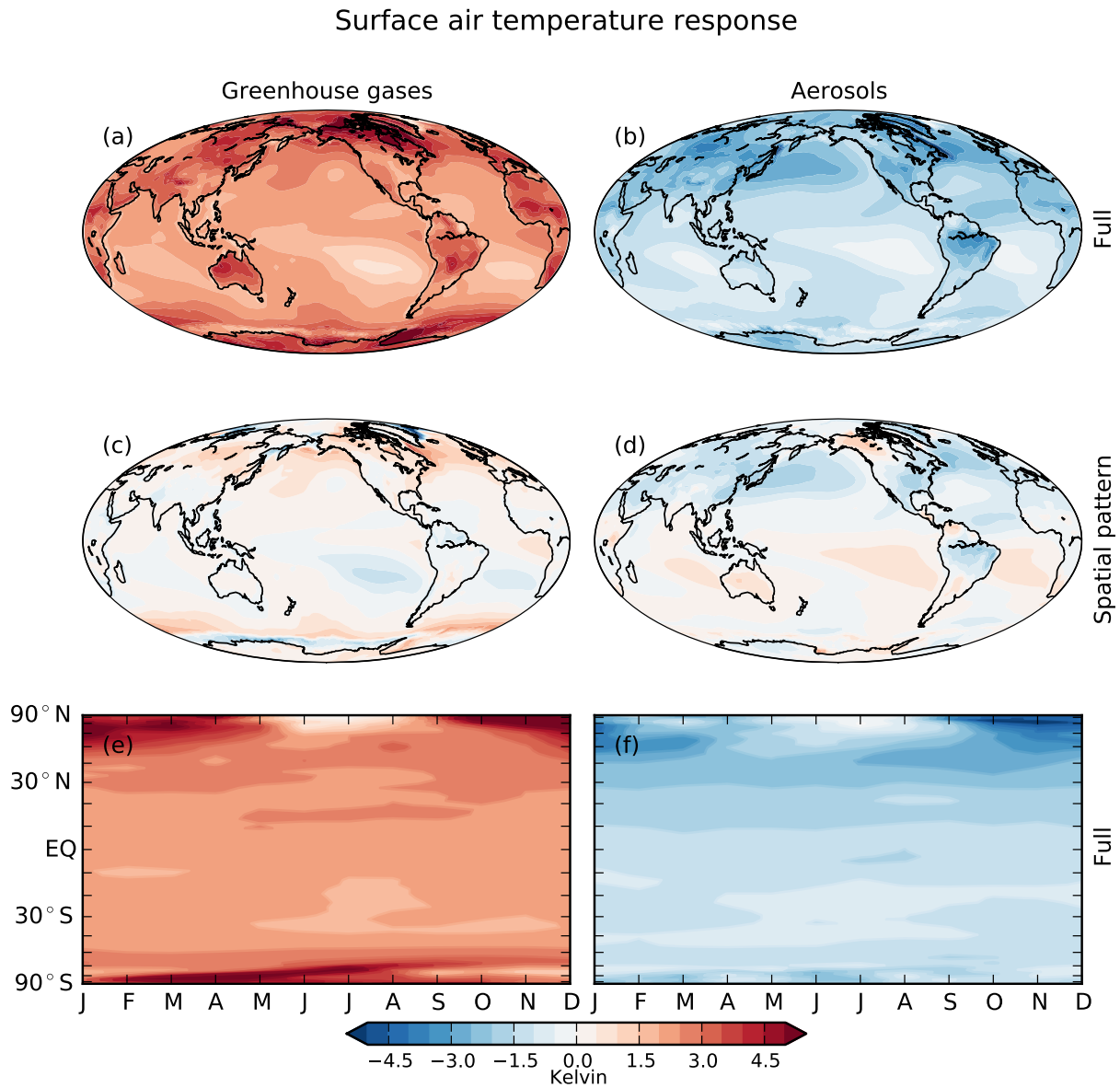


Figure 2.1: Surface air temperature response for the prescribed SST experiments: annual mean for (a) greenhouse gases, (b) aerosols, (c) greenhouse gases spatial pattern, and (d) aerosols spatial pattern, and the annual cycle of their zonal mean for (e) greenhouse gases and (f) aerosols. The vertical axis in panels (e) and (f) is $\sin \phi$ to be proportional to Earth's fractional surface area at each latitude.

Table 2.1: Annual mean surface air temperature anomaly (in K) for the global mean, the tropics (30°S – 30°N), and the northern hemisphere minus the southern hemisphere in the full, mean, and spatial pattern simulations for greenhouse gases and aerosols.

	Globe	Tropics	NH–SH
Greenhouse gases			
Full	2.6	2.3	0.3
Mean	2.3	2.3	0.1
Spatial pattern	0.1	–0.1	0.2
Aerosols			
Full	–1.6	–1.3	–0.9
Mean	–1.3	–1.3	–0.1
Spatial pattern	–0.3	–0.1	–0.7

turbulent fluxes, thereby forcing the energetic anomalies to be shed via changes in longwave emission [e.g. *Boé et al.*, 2009; *Lesins et al.*, 2012]. This results in seasonal variations in the NH high latitude surface temperature response of \sim 6 K for greenhouse gases and \sim 4 K for aerosols, in contrast to \lesssim 1 K in the tropics for either forcing agent.

2.3.2 Energy flux

Figure 2.2 shows the annual cycle of the monthly mean meridional energy flux in total and for the three flow components in the control experiment. Outside \sim 20°S–20°N, transport is poleward in both hemispheres year-round, reaching peak magnitudes near 7 PW in the mid-latitudes in early winter. The Hadley cells contribute up to \sim 3 PW in mid- to late winter of either hemisphere. Stationary eddies contribute up to \sim 3 PW to the poleward transport in the NH mid-latitudes in winter, but their contribution in the tropics is weaker. Transient eddies contribute more than 5 PW to the poleward energy transport in autumn and winter over much of the mid-latitudes, with spillover of up to 4 PW extending through the tropics.

Grey curves in this and subsequent figures indicate the locations of the Hadley cell boundaries, calculated as the zero crossings of the 500 hPa meridional mass streamfunction, linearly interpolating between the grid latitudes at which the streamfunction changes sign. As *Dima*

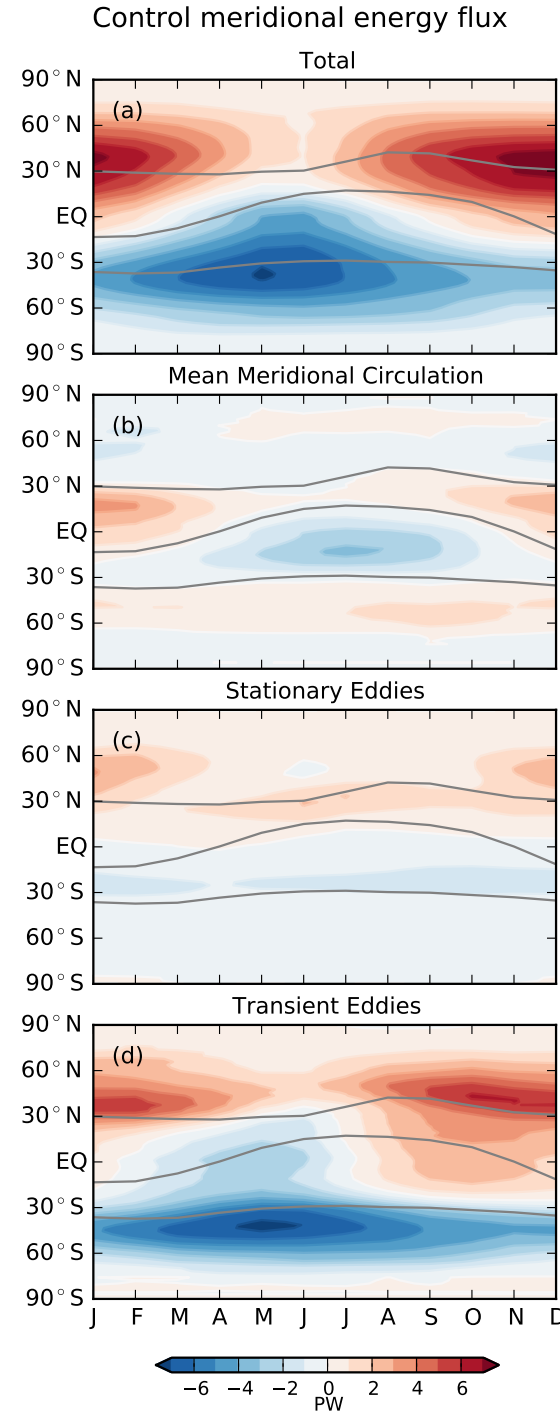


Figure 2.2: Annual cycle of northward energy flux in the prescribed SST control simulation in color contours: (a) its total, and contributions from (b) the mean meridional circulation, (c) stationary eddies, and (d) transient eddies. Appendix 2.A describes how these are calculated. Grey curves denote the positions of the Hadley cells' boundaries as defined by the zero crossings of the meridional mass streamfunction at 500 hPa. Because the flux calculations incorporate surface area, no $\sin \phi$ spacing is necessary on the vertical axis.

and Wallace [2003] demonstrate for reanalysis data, the two cells smoothly vary throughout the year between equinoctial and solstitial patterns (rather than displaying “square wave” behavior dominated by the solstitial cell as has sometimes been posited).

Figure 2.3 shows the total anomalous energy flux and the contributions of each flow component for the full greenhouse gas and aerosol experiments; the overlaid Hadley cell boundaries are of the perturbation run. Greenhouse gases mostly increase poleward transport, with maximum magnitudes ~ 0.4 PW. This is driven by eddies, with stationary eddies contributing northward anomalies over much of the NH tropics and transient eddies enhancing poleward energy transport over most of the extratropics. In contrast, the Hadley cells tend to oppose this enhanced poleward transport, contributing southward anomalies in the NH winter cell up to -0.6 PW and northward anomalies in the SH winter cell up to $+0.4$ PW. These anomalous cross-equatorial fluxes likely stem from the seasonally reversing anomalous meridional temperature gradient: the minimum in Arctic warming and concurrent relative maximum Antarctic warming in boreal summer induce a northward cross-equatorial energy transport, and vice-versa for austral summer.

Aerosols yield northward anomalies in the deep tropics year-round. They are centered on the equator, reach $+0.7$ PW in the SH winter cell, and occur almost exclusively via the Hadley cells. Interestingly, in the NH they are strongest in summer when Arctic cooling is minimum, rather than winter when the meridional gradient in temperature change is largest. Outside this region of strong northward anomalies, the picture is generally reduced poleward flux, with equatorward anomalies in either hemisphere. Stationary eddies contribute substantially to this weakening in the SH tropics, while transient eddies drive the extratropical response.⁴

Some latitudes and months exhibit pronounced re-partitioning among the flow components despite weak change in the total flux. For example, the strongest anomalies in any field are for the aerosol transient eddies in February in the NH mid-latitudes, with values reaching

⁴Though MSE flux anomalies by eddies in the deep tropics are weak in our simulations, the possible significance of eddy MSE fluxes there cannot in general be discounted – Figure 2.2 demonstrates this for the climatology [see also Peters *et al.* 2008].

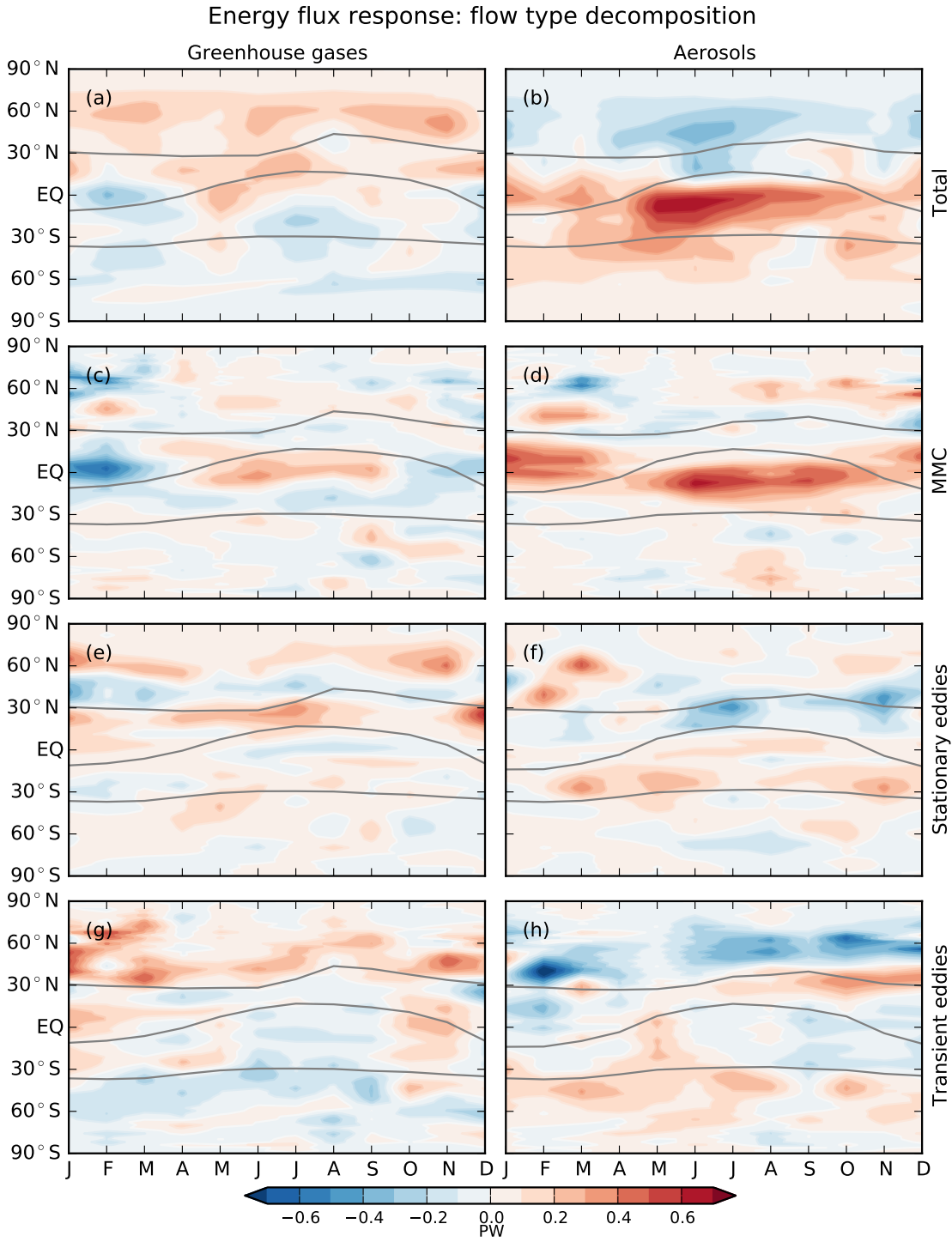


Figure 2.3: Annual cycle of the anomalous northward atmospheric energy transport for the full (left column) greenhouse gas and (right column) aerosol simulations, (a,b) in total and by each flow component: (c,d) the mean meridional circulation, (e,f) stationary eddies, and (g,h) transient eddies. Overlaid grey curves mark the locations of the Hadley cells' boundaries in the perturbation simulation, as defined by the zero crossings of the meridional mass streamfunction at 500 hPa.

–0.8 PW. However, moderate northward anomalies in both the MMC and stationary eddy fields compensate, yielding only a –0.1 PW anomaly in the total flux.

Figure 2.4 shows the change in total atmospheric energy transport for the mean and spatial pattern cases of each forcing agent and their sum. For greenhouse gases, these components generally oppose each other. The mean warming enhances poleward energy transport via increased poleward moisture transport (not shown) [*Manabe and Wetherald, 1975; Held and Soden, 2006; Hwang and Frierson, 2010*], with magnitudes near 0.3 PW for much of the year in the subtropics. In contrast, the polar amplified spatial pattern reduces the meridional temperature gradient, thereby weakening the poleward flux. The former effect being stronger than the latter in this case, the net result is enhanced poleward energy transport that is weaker than the mean warming case [*Caballero and Langen, 2005*].

Aerosol mean cooling weakens the poleward energy flux by more than 0.2 PW at most latitudes/months via the same moisture flux mechanism (albeit with opposite sign) as the greenhouse gas mean warming case. Meanwhile, the aerosol spatial pattern drives the strong northward anomalies (up to +0.7 PW) in the deep tropics apparent in the full case. These anomalies are strongest just poleward of the Hadley cells' interior boundary in either hemisphere. Thus the mean and spatial pattern effects buttress one another in the southern Hadley cell but oppose each other in the northern cell, resulting in the full aerosol case in northward anomalies that peak in the SH winter cell just south of the cells' shared border.

Combining these two decompositions – into MMC/stationary eddy/transient eddy components of the energy flux and into mean/spatial pattern of SSTs – the following picture emerges: greenhouse gas warming enhances poleward energy transport mostly through eddies, an effect that is partially negated by the weakened meridional temperature gradient. Meanwhile, the aerosol spatial pattern of relative NH cooling induces northward anomalies in the deep tropics that occur via the Hadley cells and that are superimposed on reduced poleward energy transport due to the mean cooling. Comparing the sum of the mean and spatial pattern components (Figure 2.4e,f) to the full case (Figure 2.3a,b) reveals that the

Energy flux response: mean/spatial pattern decomposition

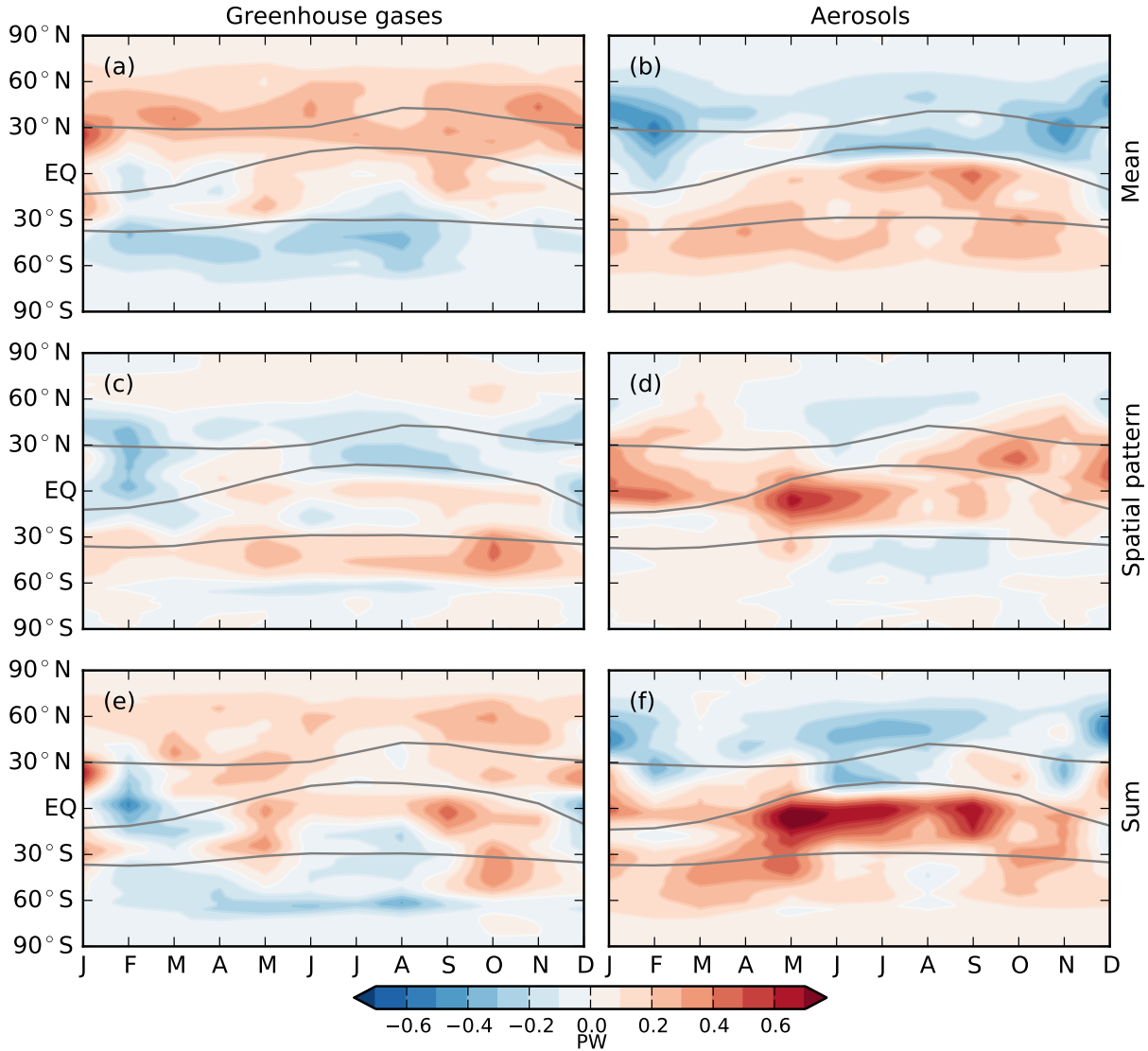


Figure 2.4: As in Figure 2.3, but for anomalous total northward atmospheric energy transport as defined by (2.10) for the (top row) uniform temperature change simulation, (center row) spatial pattern simulation and (bottom row) their sum. The grey curves denote the Hadley cell borders (a–d) in the perturbation simulation and (e,f) the average of their values in the uniform and spatial pattern simulations. The borders are determined by the zero crossings of the meridional mass streamfunction at 500 hPa.

response is quite linear to the imposed decomposition for either forcing agent.

2.3.3 Mass flux

That the Hadley cells contribute non-negligibly for greenhouse gases and substantially for aerosols to the anomalous energy flux justifies analysis of the relative roles of both the mass flux and gross moist stability, starting with the mass flux Ψ_{\max} . We define Ψ_{\max} conventionally (see Appendix 2.A) as the signed maximum magnitude of the Eulerian mean meridional streamfunction Ψ at each latitude, such that positive values correspond to northward flow aloft as in the NH cell. Ψ_{\max} is therefore climatologically the same sign as the energy flux F_{HC} .

Figure 2.5 shows the mass flux annual cycle in the control for 45°S - 45°N . Values peak in the winter cells and are strongly seasonal in the deep tropics, ranging from $15 \times 10^{10} \text{ kg s}^{-1}$ in January to $-24 \times 10^{10} \text{ kg s}^{-1}$ in July. This seasonality weakens moving towards the subtropics: at $30^{\circ}\text{S}/\text{N}$ the mass flux is of the same sign year-round, with an annual range of $\sim 4 \times 10^{10} \text{ kg s}^{-1}$.

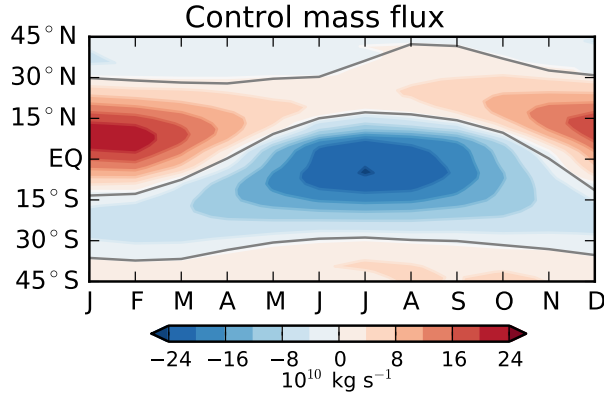


Figure 2.5: Annual cycle of the mass flux, Ψ_{\max} , in the control simulation for 45°S - 45°N , defined as the signed maximum magnitude of the meridional mass streamfunction at each latitude, where the streamfunction Ψ is defined as standard by (2.11). Positive values, as in the NH cell, denote northward flow in the upper branch of the overturning circulation. Overlaid grey curves denote the boundaries of the Hadley cells defined based on the zero crossings of Ψ at 500 hPa.

Figure 2.6 shows the mass flux response annual cycle in the six perturbation experiments.

Changes of substantial magnitude are bounded by the extent of the Hadley cells interior boundary seasonal migration, $\sim 15^{\circ}\text{S}$ – 15°N , hinting that the Hadley circulation responds primarily via alterations to its interior boundary location. For greenhouse gases the interior boundary moves southward April through September and northward otherwise, while for aerosols it moves southward year-round – both of these responses are consistent the sign of the mass flux changes in that simulation over most of the year.

For greenhouse gases, the mass flux anomalies vary seasonally as to oppose the climatology, in the northern winter cell up to $-5.4 \times 10^{10} \text{ kg s}^{-1}$ and in the southern winter cell up to $3.6 \times 10^{10} \text{ kg s}^{-1}$. *Kang et al.* [2013] likewise see weakening of both winter cells in a 40-member ensemble of the CCSM4 GCM subject to A1B emissions scenario radiative forcing (which is dominated by increased greenhouse gas concentrations).

By coincidence, the mass flux responds similarly to the mean warming and spatial pattern components of greenhouse gas SSTs, both acting primarily against the climatology. For mean warming, we expect the total convective mass flux to decrease because the specific humidity increases faster with temperature than the precipitation [*Knutson and Manabe*, 1995; *Held and Soden*, 2006]. If not constrained by other factors, one expects the mean meridional overturning mass flux to participate in this reduction, as seen here. (Being equatorward of 15° latitude, the large changes in seasonal Hadley cell mass flux are unlikely constrained by eddy momentum fluxes through the small-Rossby number zonal force balance between eddy momentum fluxes and Coriolis force.) For the polar amplified spatial pattern, the reduced meridional temperature gradient necessitates weaker poleward energy fluxes as discussed above. This is partly accomplished in the deep tropics via a weakening of the mass flux in the winter cell. The net result of these mechanisms is a stronger weakening of the circulation in total for greenhouse gases than for either the mean or spatial pattern component alone.

Aerosols induce strong anomalies nearly year-round in the deep tropics, with maximum values in January through March near $+6 \times 10^{10} \text{ kg s}^{-1}$. These reinforce the climatology in the NH cell but counteract it in the SH cell and are co-located with the strong northward

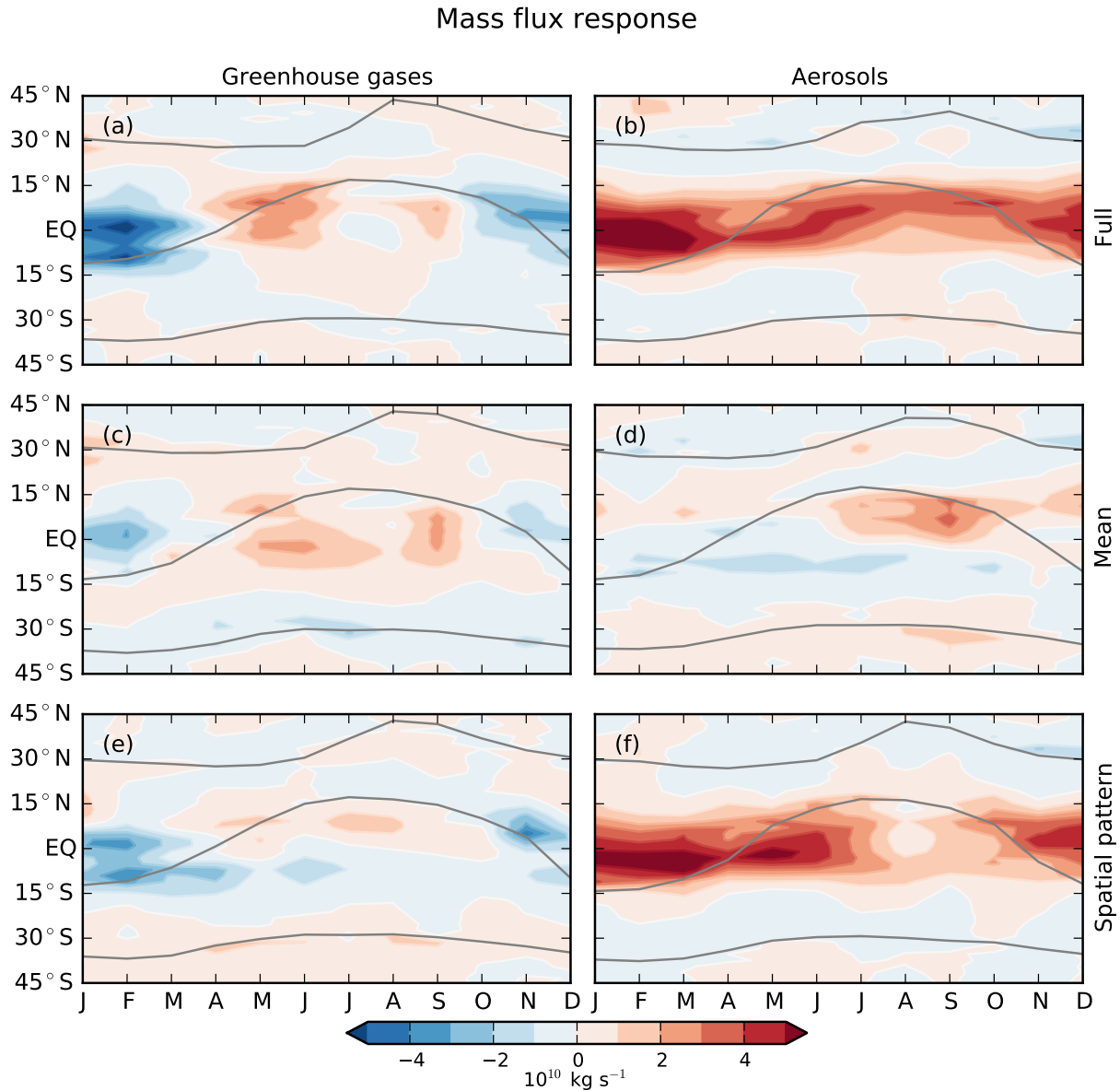


Figure 2.6: Annual cycle of the mass flux response for 45°S - 45°N in the (left column) greenhouse gas and (right column) aerosol (top row) full, (middle row) uniform temperature change, and (bottom row) spatial pattern cases. Overlaid grey curves mark the locations of the Hadley cells' boundaries in the perturbation simulation, as defined by the zero crossings of the meridional mass streamfunction at 500 hPa.

energy flux anomalies (Figure 2.3). In other words, the spin up of the NH cell enhances the climatological northward energy flux, while the spin down of the SH cell weakens the climatological southward energy flux in that cell. Both cases yield anomalous northward energy fluxes.

The mean cooling contributes weakly to this pattern, with substantial anomalies (up to $-3.4 \times 10^{10} \text{ kg s}^{-1}$) only in July through September just south of the Hadley cells' shared border. The mean cooling of aerosols does not spin-up the circulation in a scaled mirror image of the greenhouse gas mean warming; that is, the mass flux changes with uniform SST change are not symmetric about zero. This behavior is still under investigation. *Wyant et al. [2006]* demonstrate asymmetric tropical changes in both shortwave and longwave cloud radiative forcings in plus-2K and minus-2K experiments conducted in AM2.1, attributing them to differing condensate responses in ascent regions. Interestingly, they find no such asymmetry in another AGCM (namely NCAR CAM3.0).

Nevertheless, the mean temperature change component contributes only weakly to the total aerosol mass flux response. Instead, the spatial pattern component drives the northward anomalies. This is consistent with the net northward energy flux anomalies (Figure 2.3(b)) being driven by the spatial pattern simulation as well (Figure 2.4(d)), as discussed previously.

2.3.4 Gross moist stability

As detailed in Appendix 2.A, we use a definition of GMS that includes only the Hadley cell contribution to the meridional energy flux, in order to understand the Hadley cell energy flux changes that dominate the total transport change for aerosols and the anomalous cross-equatorial MSE fluxes for greenhouse gases that oppose the enhanced poleward energy transport by eddies.

2.3.4.1 Theory

We start with a simple estimate for GMS made by *Held* [2001] (hereafter H01). GMS as defined by (2.12) is a meridional flow-weighted difference between upper and lower level MSE [*Neelin and Held*, 1987]. In the limit of equal magnitude mass flow confined to one upper and one lower boundary layer, the mass flux weighting drops out and this simplifies to the upper minus lower level MSE. At the ITCZ, deep convection homogenizes MSE vertically. Additionally, the weak temperature gradient dynamical constraint in the free troposphere horizontally homogenizes temperature and geopotential fields aloft. Together these imply that the surface MSE at the ITCZ sets the MSE field aloft throughout the tropics, and therefore GMS at a given latitude within the Hadley cells depends on the difference between surface MSE values locally and at the ITCZ:

$$\Delta_{\text{HC}}(\phi) \approx h_{\text{ITCZ}} - h(\phi), \quad (2.3)$$

where the subscript ITCZ denotes the value at the latitude of the ITCZ and all variables refer to surface values.

H01 further simplifies by noting that geopotential is zero at the surface and writing $q = \mathcal{H}q_s$, where \mathcal{H} and q_s are the near-surface relative humidity and saturation specific humidity respectively, such that $h = c_p T + L_v \mathcal{H}q_s$. Then, neglecting meridional variations in \mathcal{H} , GMS becomes

$$\Delta_{\text{HC}}(\phi) \approx \left(c_p + L_v \bar{\mathcal{H}} \left. \frac{dq_s}{dT} \right|_{\mathcal{H}} \right) (T_{\text{ITCZ}} - T(\phi)), \quad (2.4)$$

where $\bar{\mathcal{H}}$ is the tropical mean near-surface relative humidity and $dq_s/dT|_{\mathcal{H}}$ is the change in saturation specific humidity with respect to temperature at a fixed relative humidity, as governed by the Clausius-Clapeyron relation. (2.4) states that GMS is determined solely by the meridional profile of surface temperatures and the tropical mean surface relative

humidity. While H01 is concerned with the climatological annual mean GMS, (2.3) and (2.4) are easily modified to represent GMS changes, e.g. between perturbation and control experiments. *Merlis et al.* [2013a] do so using (2.3), finding it to be a useful approximation of the GMS response to orbital precession in an idealized aquaplanet GCM (their Fig. 9).

We do likewise for our simulations but using a modified form of (2.4). Variations of relative humidity with latitude in the tropics for a given climate tend to exceed those at a given latitude in response to a climate perturbation. For example, annual and zonal mean relative humidity at 2 m above the surface varies by $\sim 15\%$ from the equator to 30° in either hemisphere in our control simulation, whereas the maximum magnitude change at a given tropical latitude from the control to any perturbation simulation is $\sim 1\%$. Therefore, we retain meridional variations in relative humidity and instead assume that specific humidity obeys the familiar thermodynamic scaling relation, i.e. $\delta q/q = \alpha \delta T$, where $\alpha = 7\% \text{ K}^{-1}$ represents the fractional increase in saturation vapor pressure with temperature via Clausius-Clapeyron. With these alterations, the GMS change is given by

$$\delta \Delta_{\text{HC}}(\phi) = (c_p + \alpha L_v q_{\text{ITCZ}}) \delta T_{\text{ITCZ}} - (c_p + \alpha L_v q(\phi)) \delta T(\phi), \quad (2.5)$$

where δ denotes the difference between two climate states. Rearranging terms reveals the condition governing the sign of GMS change (the two equalities can be replaced with $>$ or $<$):

$$\delta \Delta_{\text{HC}}(\phi) = 0 \iff \frac{\delta T(\phi)}{\delta T_{\text{ITCZ}}} = \frac{c_p + \alpha L_v q_{\text{ITCZ}}}{c_p + \alpha L_v q(\phi)}. \quad (2.6)$$

Presumably $q_{\text{ITCZ}} > q(\phi)$, and therefore the right hand side of the second equality in (2.6) is strictly greater than unity. Thus for GMS to remain constant, the magnitude of surface temperature change locally must exceed that at the ITCZ to an extent that depends on the existing specific humidity difference between them. Figure 2.7 shows this ratio $\delta T(\phi)/\delta T_{\text{ITCZ}}|_{\delta \Delta_{\text{HC}}=0}$ for the control experiment. As zonal mean specific humidity decreases monotonically away from the ITCZ into the subtropics (not shown), the temperature change

ratio increases monotonically, reaching ~ 1.6 near the poleward boundaries of either Hadley cell.

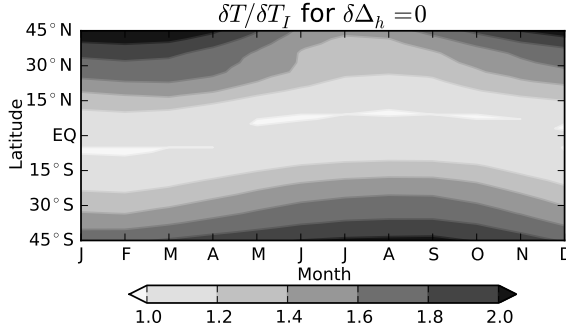


Figure 2.7: Based on (2.6), the ratio of near-surface temperature change at the given latitude and at the intertropical convergence zone (ITCZ) necessary for GMS change to be zero. 925 hPa values of q and T taken from the control simulation are used. The ITCZ latitude is taken as the latitude of maximum zonal mean precipitation, linearly interpolated between model grid points to where $\partial P/\partial\phi = 0$.

For the particular case of a uniform δT , (2.5) reduces to $\delta\Delta_{\text{HC}}(\phi) = \alpha L_v(q_{\text{ITCZ}} - q(\phi))\delta T$. Again assuming $q_{\text{ITCZ}} > q(\phi)$, the sign of the GMS change depends solely on the sign of δT . Uniform warming increases, and uniform cooling decreases, GMS at all latitudes outside the ITCZ, with the magnitude of the change increasing with the magnitude of the temperature change and moving towards the subtropics (we discuss the accuracy of this simple picture below). Given that climatologically GMS also increases meridionally away from ITCZ, this behavior in the case of uniform warming can be thought of as another manifestation of “rich-get-richer” behavior [Chou and Neelin, 2004; Held and Soden, 2006; Chou *et al.*, 2009]: the “stable get stabler” (taking liberty to define “the stable” as all latitudes outside the ITCZ).

2.3.4.2 Results

Figure 2.8 shows the annual cycle of GMS in the control simulation. All GMS plots absorb a $1/c_p$ factor as standard to get units of K and have values outside of the Hadley cells masked. Overlaid in the blue dotted curve is the ITCZ location, defined as the latitude of maximum zonal mean precipitation, linearly interpolated from the model grid to the point

where $\partial P/\partial\phi = 0$. The control GMS qualitatively adheres to the H01 picture, being near zero following the boundary separating the Hadley cells and increasing polewards. However, the ITCZ is usually displaced equatorward from that border by several degrees latitude; such equatorward displacement has been attributed in past studies to the streamfunction meridional gradient maximum also being displaced equatorward [see Figure 9 of *Donohoe et al.*, 2013]. Thus GMS at the ITCZ is generally positive ($\gtrsim 4$ K), contradicting the assertion by (2.3) that $\Delta_{\text{HC}} = 0$ at the ITCZ.

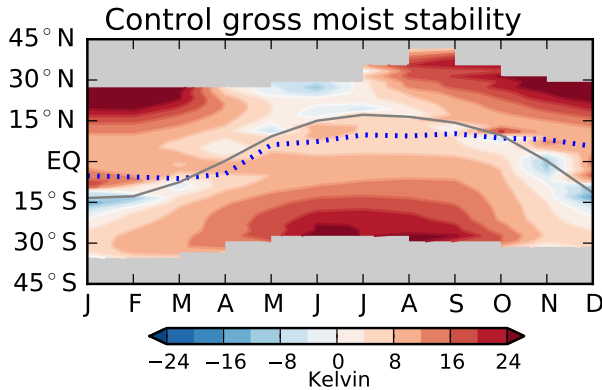


Figure 2.8: Annual cycle of gross moist stability $\Delta_{\text{HC}}(\phi)$ in the control simulation. Positive values indicate that the net meridional energy flux is in the same direction as the flow in the upper branch, as occurs in the Hadley cells. Values outside the Hadley cells are masked, as the primary concern is with tropical energy fluxes and since the underlying dynamics differ markedly for the Hadley and Ferrel cells. The dotted blue line denotes the ITCZ location, taken as the latitude of maximum zonal mean precipitation, linearly interpolated between model grid points to where $\partial P/\partial\phi = 0$. GMS has been divided by c_p in this and all subsequent plots as standard to get units of K.

We discuss the GMS responses of the aerosol simulations first, being simpler than those of the greenhouse gas cases. Figure 2.9 shows the GMS response for the three aerosol cases (left column) and their corresponding estimates using (2.5) (right column). Values within 6° latitude of the Hadley cells' interior border on either side are masked out for the full calculation, as it becomes problematic near where the mass flux goes to zero. The theoretical estimate uses values at 925 hPa. Despite its simplicity, (2.5) captures the qualitative behavior throughout the seasonal cycle in each simulation. For the full and spatial pattern cases, GMS decreases in the southern Hadley cell and increases in the northern cell for most of the year.

For the uniform cooling simulation, the estimate features nearly monotonically decreasing GMS moving meridionally away from the convection zone. The actual response to uniform cooling (Figure 2.9(c)) also predominantly features reductions, but with notable exceptions in the NH summer cell and over much of the year for $\sim 20^{\circ}\text{-}30^{\circ}\text{S}$.

The spatial pattern component can also be understood via the theoretical estimate. Because the reduction in zonal mean surface temperature increases northwards, GMS will decrease at latitudes south of the ITCZ and increase at latitudes north based on (2.6). This response yields an anomalous northward MSE transport that acts against the imposed cooling of the NH relative to the SH. So as was the case with the MSE flux, the aerosol mean cooling and spatial pattern components reinforce each other in the southern Hadley cell and counteract each other in the northern cell, resulting in generally weaker GMS increases in the northern cell than decreases in the southern cell for the full aerosol case. This pattern of destructive vs. constructive interference can also be seen in Table 2.2, which lists for each month in the full aerosol simulation the change in F_{HC} and the fractional changes in F_{HC} , Ψ_{max} , and Δ_{HC} at the latitude ϕ_{max} of the maximum magnitude of Ψ_{max} , which is essentially the center of the stronger Hadley cell. In the SH cell, more than half of the energy flux fractional change occurs via GMS, while the converse holds in the NH cell.

Figure 2.10 shows the GMS response for the three greenhouse gas cases and their corresponding (2.5) estimates. (2.5) captures the qualitative behavior of GMS in the spatial pattern case: in the southern cell, slight decreases just south of the interior border most of the year and mild increases year-round south of $\sim 15^{\circ}\text{S}$ and, in the northern cell, mild decreases most of the year. This behavior is essentially a weakened mirror image of the aerosol spatial pattern case, as the zonal mean surface temperature response increases (becomes more positive) nearly monotonically moving northward throughout the tropics. It acts to produce anomalous southward energy flux anomalies in either cell, consistent with the slight warming of the NH relative to the SH (Table 2.1).

The GMS responses to the full and uniform warming greenhouse gas cases are of compa-

Gross moist stability response: aerosols

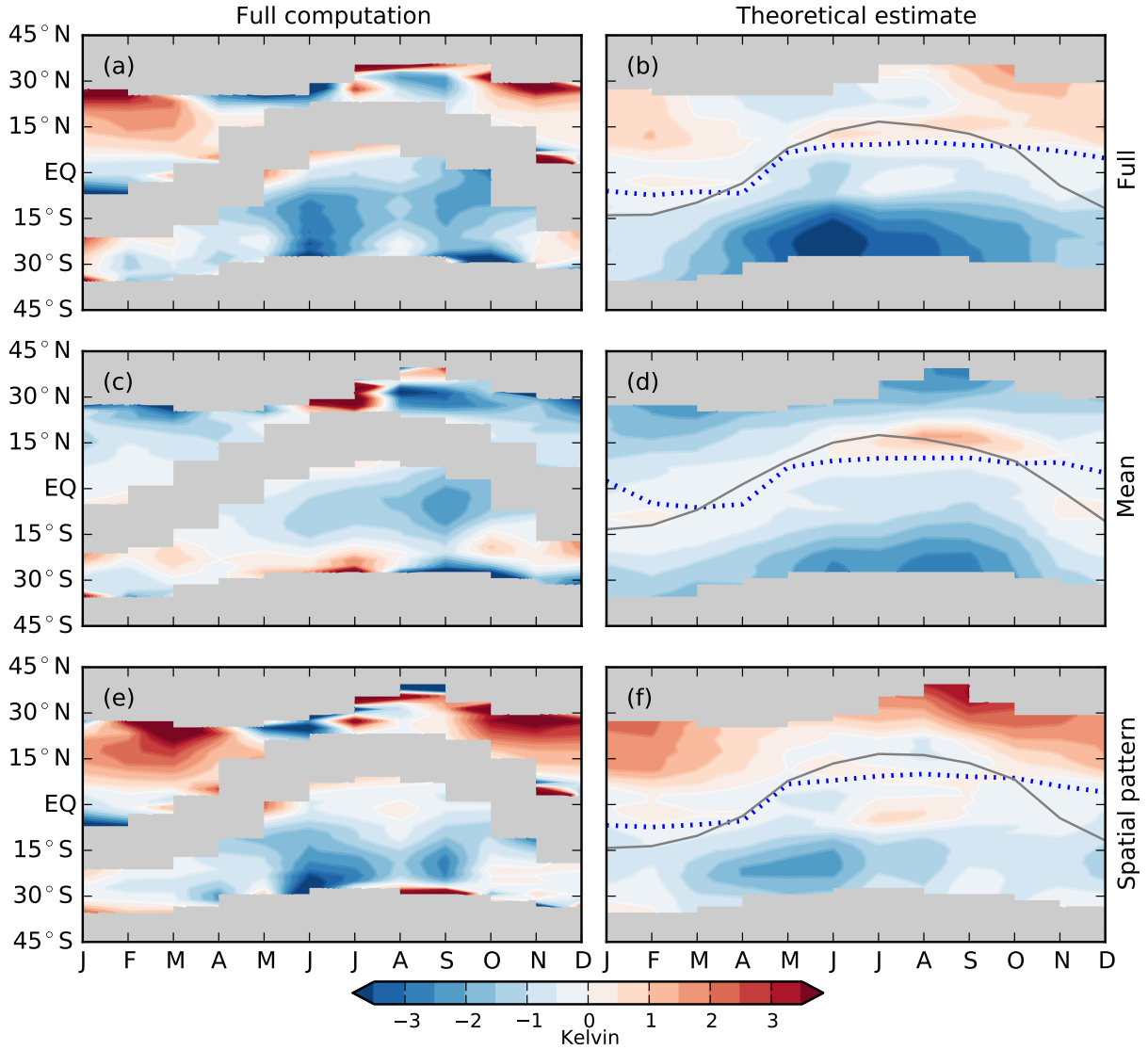


Figure 2.9: Annual cycle of the gross moist stability response to the aerosol (top row) full, (middle row) uniform temperature change, and (bottom row) spatial pattern cases, as computed using (left column) the full GMS calculation of (2.12) and (right column) the theoretical estimate (2.5). Values outside the Hadley cells are masked in all panels, and values within 6° latitude of the Hadley cells' interior border (indicated by the thin grey curve in the right panels) on either side are also masked out in the left column, as the GMS calculation becomes problematic near where the mass flux goes to zero. The Hadley cell boundaries are for the perturbation simulations, as defined by the zero crossings of the meridional mass streamfunction at 500 hPa. The dotted blue line denotes the ITCZ location in the perturbation simulation, taken as the latitude of maximum zonal mean precipitation, linearly interpolated between model grid points to where $\partial P/\partial\phi = 0$.

Gross moist stability response: greenhouse gases

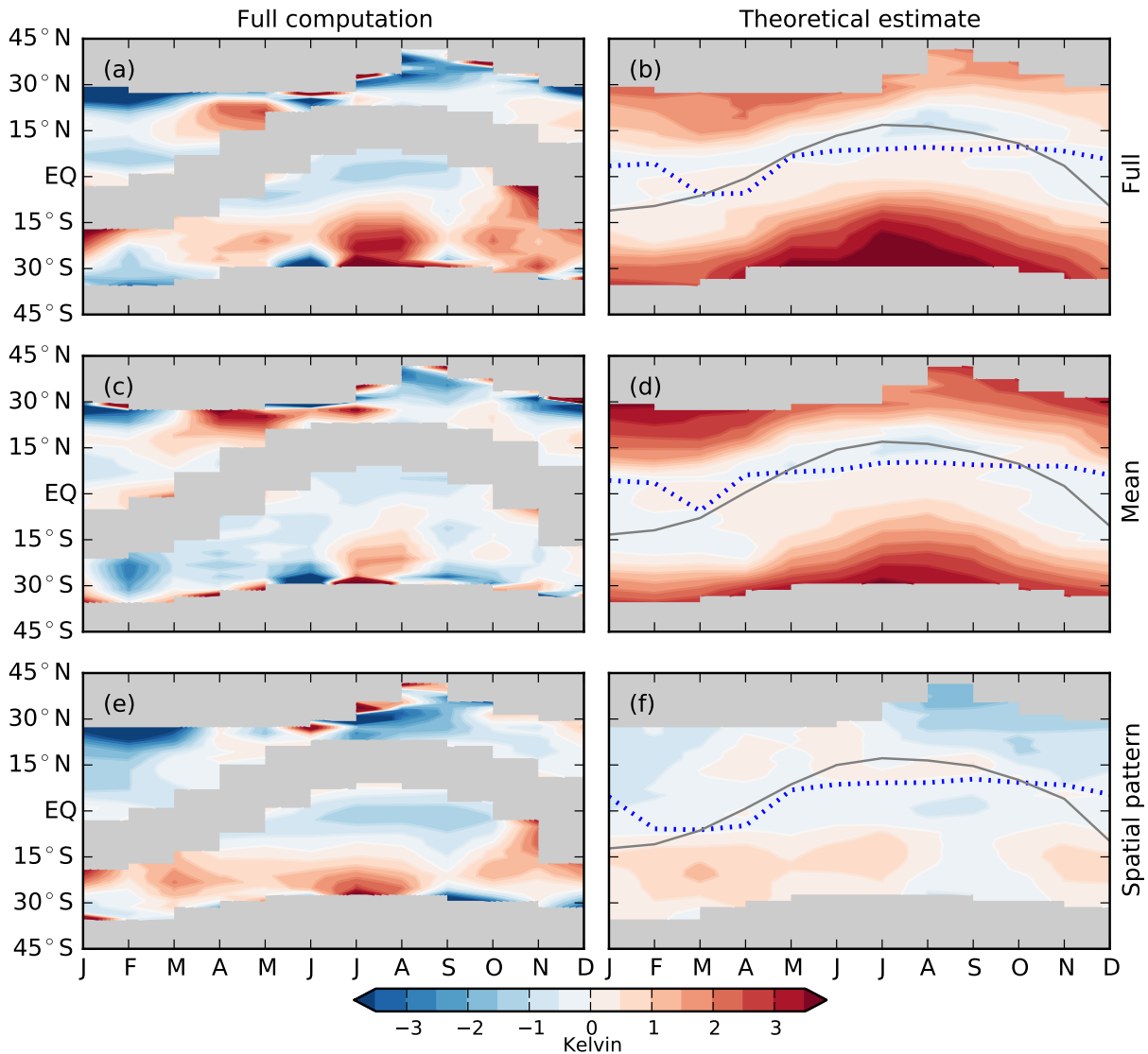


Figure 2.10: As in Figure 2.9, but for the greenhouse gas simulations.

Table 2.2: Columns from left to right: month, the latitude of the maximum magnitude of the mass streamfunction (in degrees and denoted ϕ_{\max}) in the control simulation, the northward MSE flux by the Hadley cell at the latitude ϕ_{\max} in the control simulation (in PW), and the fractional changes in the full aerosols simulation from the control at ϕ_{\max} of the Hadley cell energy flux, mass flux, and gross moist stability. The months begin in April rather than January so that the periods when the southern hemisphere (April to October) or northern hemisphere (November to March) cell are strongest are each continuous within the table.

Month	ϕ_{\max}	$F_{\text{HC}}(\phi_{\max})$	$\frac{\delta F_{\text{HC}}}{F_{\text{HC}}}(\phi_{\max})$	$\frac{\delta \Psi_{\max}}{\Psi_{\max}}(\phi_{\max})$	$\frac{\delta \Delta_{\text{HC}}}{\Delta_{\text{HC}}}(\phi_{\max})$
4	-13.1	-1.12	-0.14	-0.02	-0.11
5	-9.1	-1.68	-0.20	-0.07	-0.14
6	-5.1	-2.21	-0.27	-0.13	-0.17
7	-5.1	-2.71	-0.21	-0.07	-0.14
8	-5.1	-2.65	-0.17	-0.07	-0.11
9	-5.1	-2.19	-0.23	-0.08	-0.17
10	-7.1	-1.12	-0.32	-0.07	-0.26
11	15.2	1.80	0.10	0.09	0.01
12	11.1	2.09	0.21	0.17	0.03
1	9.1	2.53	0.22	0.16	0.05
2	7.1	2.19	0.20	0.15	0.04
3	9.1	1.48	0.28	0.16	0.10

rable magnitude to the corresponding aerosol simulations but noisy, with (2.5) doing a much poorer job than for the spatial pattern or for the three aerosol cases. Note that GMS response to the uniform warming case is the only field featuring substantial variations between the two 8 year averaging subperiods mentioned previously (not shown).

Two factors contribute to this discrepancy. First, MSE increases aloft at the ITCZ are smaller than at the surface year-round due to slight increases in boundary layer relative humidity (not shown), leading to an overestimate of GMS change when estimating the upper level change in MSE at the ITCZ using the surface change at fixed relative humidity. Second, the weak temperature gradient approximation is imperfect; increases in MSE aloft are maximum in each month near the equator and become smaller monotonically moving poleward, albeit weakly (not shown). Combined, these effects lead to a more positive prediction of GMS change when using surface MSE differences (i. e. (2.5)) rather than local vertical MSE differences. Why these assumptions fail only in response to greenhouse gas full or uniform SSTs remains an open question.

2.4 Discussion

2.4.1 Implications of GMS change for forced ITCZ shifts

(2.5) states that changes in GMS depend only on two fields: the climatological near-surface specific humidity, and the anomalous surface temperature. Both quantities have some finite scale of meridional variations – Fig. 1(e) and (f) roughly indicate this for surface temperature anomalies. At latitudes sufficiently far away from the ITCZ, the differences relative to the ITCZ of either field can be substantial, and hence GMS can vary via thermodynamic scaling. But there exist latitudes that are too near the ITCZ to experience substantial differences in either field relative to their values at the ITCZ. As such, (2.5) states that GMS will not vary substantially at these latitudes by simple thermodynamic scaling behavior. As a result, anomalous energy fluxes must manifest exclusively via anomalous circulation, consistent with large mass flux changes being confined to the latitudes near the ITCZ (Figure 2.6).

We speculate that this explains why the ITCZ position has been found to be so tightly correlated with atmospheric energy transport at the equator [e.g. *Frierson and Hwang*, 2012; *Donohoe et al.*, 2013]: near the equator, dynamical shifts of moisture convergence are the only practical means by which to substantially alter the energy transport. Moreover, latitudes near the energy transport zero-crossing can undergo a change in sign of the net energy flux (from southward to northward or vice versa). This can only be accomplished by a shift of the Hadley cells' border; increasing or decreasing the energy transport efficiency does not change the sign.

2.4.2 Interpreting our GMS results

Our estimate could be reconciled with the nonzero GMS at the ITCZ by forbidding GMS anywhere from dropping below its value at the ITCZ. Despite its imperfect column MSE homogenization, we still expect the intense convection within the ITCZ to communicate sur-

face conditions to the free troposphere more effectively than other regions [Sobel *et al.*, 2002] and thus set the baseline energetic stratification of the tropics. This baseline GMS value is likely model-dependent – see *Merlis et al.* [2013a] for further discussion of the decomposition of GMS into meridionally varying and uniform components and what sets the GMS value at the ITCZ.

That the actual GMS values drop below the value at the ITCZ near the cell edge does not seriously detract from this modification, since the computed changes in this region appear unphysical. As mentioned above, diagnosing the change in GMS as defined in (2.12) in a finite resolution model becomes difficult near the cell boundary where both its numerator and denominator go to zero, resulting in large unphysical dipoles. Definitions of GMS in terms of vertical velocity and MSE profiles [e.g. *Chou and Neelin*, 2004; *Chou et al.*, 2009] avoid this technical pitfall; however such measures lose the explicit, simple dependence on the MSE and mass fluxes that make (2.12) especially useful for our purposes.

Our neglect of zonal asymmetries is likely problematic. The deep tropical precipitation distribution possesses strong zonal asymmetries throughout the annual cycle [e.g. *Hu et al.*, 2007]. Presumably the local stability is nearly zero within local convection zones, but zonally averaging combines these with larger stability values of any non-convective regions at the same latitude. Any double ITCZ structure, such as in the eastern Pacific, certainly complicates the energetics, as nicely distilled by *Bischoff and Schneider* [2015]. The application of the *Bischoff and Schneider* [2014, 2015] energetic framework for single and double ITCZs to reanalysis and observational data by *Adam et al.* [2016a,b] indicates that the ITCZ energetic framework largely works within zonally confined sectors as well as in the zonal mean. This raises the possibility, of performing our analysis separately on individual zonal sectors, i.e. computing the GMS of each monsoon and ITCZ region separately. This introduces some conceptual difficulties, however, in particular accounting for mass and MSE transport through the zonal boundaries.

Our framework of taking the MSE fluxes as externally imposed and then seeing how they

are partitioned between the mass flux and GMS is somewhat arbitrary. Particularly when eddy stresses are important in the momentum balance, the Hadley cell mass flux (and with it GMS) is not free to respond directly to an energetic perturbation [e. g. *Walker and Schneider*, 2005]. For the solsticial Hadley cell in which eddy stresses are small, the forced mass flux response can be thought of as slaved to the energy and GMS forced responses [*Merlis et al.*, 2013a]. But without a simple relationship between anomalous atmospheric energy transport and radiative forcing (due to complicating effects of local feedbacks and ocean transport) and with our GMS scaling being at best qualitatively accurate, constraining the circulation response to forcing remains elusive.

2.4.3 Prescribed SSTs

While using prescribed SSTs enables the useful decomposition into mean and spatially varying components, it also prohibits coupling of the atmosphere and ocean responses that are important in the real world. *Kang and Held* [2011] demonstrate that model Hadley cell responses to extratropical forcing can be sensitive to the details of the imposed SST profiles, which could stem in part from the GMS dependence on SSTs we have presented. We have not explored the sensitivity of the results to different SST patterns. SST anomalies were attained using a mixed-layer ocean-AGCM rather than a fully coupled atmosphere-ocean GCM, and prior studies have demonstrated important differences in the projected SST change with global warming between them [e. g. *Xie et al.*, 2010].

Though both the imposed SST anomalies and the resulting atmospheric responses we analyze correspond to equilibrium differences between distinct climate states, nothing precludes our framework from being applied in a transient setting. Given that our GMS theory works best for the spatial pattern cases, it may even do better, since presumably SST gradients will be even sharper.

In addition to the simulations already described, *Ming and Ramaswamy* [2009] also perform an experiment with the mixed-layer ocean-AM2.1 setup in which both forcing agents

are set to their present day values in the same simulation. Because aerosols counter some of the greenhouse gas-driven mean warming while still imprinting their spatial pattern of NH cooling relative to the SH (annual mean global, NH, and SH mean surface air temperature change are +0.6, +0.2, and +1.3 K, respectively), the responses of this simulation (not shown) are similar to the aerosol spatial pattern prescribed SST simulation.

2.5 Summary

Using the GFDL AM2.1 AGCM, we have explored how SST anomalies induced by historical anthropogenic emissions of either well-mixed greenhouse gases or aerosols affect the meridional transport of energy by the tropical atmosphere throughout the annual cycle. Complementary simulations in which either the tropical mean SST anomaly is applied at all ocean gridpoints or the full SST anomalies minus this tropical mean are applied clarify the relative roles of the mean vs. the spatial pattern of SSTs, which loosely translate to the thermodynamic and dynamic components of the forced response, respectively.

Greenhouse gases increase the poleward energy transport by eddies, an effect driven by the mean warming but somewhat negated by the polar amplified spatial pattern. Aerosols induce northward energy flux anomalies in the deep tropics via the Hadley cells, due to their spatial pattern of the NH cooling relative to the SH; this feature is superimposed on a weakening of poleward energy transport driven by the mean cooling.

The mass flux by the Hadley cells is weakened year-round by greenhouse gases, due at least in part to the overall tropical circulation slowdown mediated by the mean warming. This slowdown is concentrated in the equatorward sector of the winter cells. The NH-centric aerosol cooling spins up the SH cell and spins down the NH cell; both contribute to the anomalous northward energy flux. For both forcing agents, significant mass flux changes are confined to the latitude range bounded by the seasonal meridional migrations of the Hadley cells' interior border.

The Hadley cell gross moist stability – the ratio of the energy and mass fluxes – equivalently measures the difference between upper and lower level moist static energies. By an argument by *Held* [2001] assuming uniform column MSE at the ITCZ and throughout the tropical troposphere aloft, this is approximately equal to the difference between surface MSE values at the given latitude and at the ITCZ. Further assuming thermodynamic scaling of near surface moisture with temperature implies that uniform warming will increase, and uniform cooling will decrease, GMS moving meridionally away from the ITCZ. Overlaid on this mechanism in the aerosol case is a reduction in GMS to the south of the ITCZ and an increase to the north due to the cooling increasing in magnitude northward. This yields northward energy flux anomalies year round that oppose the imposed NH cooling.

This simple scaling captures the qualitative behavior of the aerosol simulations and the greenhouse gas spatial pattern case but does poorly for the full and mean greenhouse gas components. It predicts weak GMS change near the ITCZ in all cases and thus may explain why the mass flux changes are strong at these latitudes, or equivalently why the ITCZ position and the cross equatorial atmospheric energy transport are so tightly correlated as prior studies have demonstrated.

Acknowledgments

We thank Leo Donner, Gabriel Lau, Tim Merlis, Dargan Frierson, Aaron Donohoe, Gabe Vecchi, Jonathan Mitchell, and J. David Neelin for insightful comments. Steve Garner and Mike Winton provided thoughtful reviews of an earlier draft, and comments from three anonymous reviewers greatly improved the paper. S.A.H. was funded first by the NOAA/Princeton University Cooperative Institute for Climate Science and later by the Department of Defense National Defense Science and Engineering Graduate Fellowship.

2.A Calculation of meridional energy flux, mass flux, and gross moist stability

All experiments are integrated on the model's native sigma vertical coordinate system and then interpolated to regular pressure levels as monthly means for analysis. This interpolation produces a small imbalance (a few percent) between the zonal-mean northerly and southerly mass flows that result in somewhat noisy behavior when trying to compute the MSE flux explicitly by integrating MSE times the meridional flow. As such, we introduce an *ad hoc* correction by defining an adjusted zonal mean meridional wind,

$$[\bar{v}]_{\text{adj}} \equiv [\bar{v}]_+ - [\bar{v}]_- \frac{\{[\bar{v}]_+\}}{\{[\bar{v}]_-\}}, \quad (2.7)$$

where $[\bar{v}]_+$ denotes southerly zonal mean wind (i. e. equal to $[\bar{v}]$ if $[\bar{v}] > 0$ and zero otherwise), $[\bar{v}]_-$ denotes northerly wind (defined conversely), and curly brackets denote a vertical mass-weighted integral, $\{\} \equiv \int dp/g$, where the integral extends over the depth of the column. Note that $\{[\bar{v}]_{\text{adj}}\} \equiv 0$, i. e. $[\bar{v}]_{\text{adj}}$ is strictly in mass balance.⁵

The mean meridional circulation component of the meridional MSE flux, i. e. the Hadley cell MSE flux $F_{\text{HC}}(\phi)$, is computed using this mass flux adjusted wind:⁶

$$F_{\text{HC}}(\phi) = 2\pi a \cos \phi \int_{p_{\text{top}}}^{p_{\text{sfc}}} [\bar{h}] [\bar{v}]_{\text{adj}} \, dp/g. \quad (2.8)$$

The adjustment removes the interpolation-based noise (not shown), and the resulting MSE flux compares well with the inferred total atmospheric flux (defined below) in the deep tropics where the Hadley cells are expected to dominate the energy transport.

⁵By typographical error, in *Hill et al.* [2015], the operator on the right hand side of this expression is, erroneously, addition, rather than subtraction. No results are affected by this.

⁶In *Hill et al.* [2015], the $2\pi a \cos \phi$ factor was inadvertently omitted in the expressions for the Hadley cell and stationary eddy meridional MSE fluxes [i. e. their (A2) and (A3)]. No results are affected by this. A formal Corrigendum correcting this and the sign error in their (A1) has been submitted for publication.

The stationary eddy component does not require any mass flux correction:

$$F_{\text{st. edd.}}(\phi) = 2\pi a \cos \phi \int_{p_{\text{top}}}^{p_{\text{sfc}}} [\bar{h}^* \bar{v}^*] \, dp / g. \quad (2.9)$$

We infer the total atmospheric energy transport by assuming steady state and thus relating the total atmospheric energy flux divergence to the top-of-atmosphere (TOA) and surface flux difference: $\nabla \cdot F_m = Q_{\text{TOA}} - Q_{\text{sfc}}$, where subscripts refer to TOA and surface fluxes, respectively, with downward defined as positive. We then integrate zonally and meridionally:

$$F_{\text{tot}}(\phi) = \int_{-\pi/2}^{\phi} \int_0^{2\pi} (Q_{\text{TOA}} - Q_{\text{sfc}}) a^2 \cos \phi \, d\lambda \, d\phi. \quad (2.10)$$

The transient eddy term is then taken as the residual of the total minus the time mean (i.e. the Hadley cells plus stationary eddies): $F_{\text{tr. edd.}}(\phi) = F_{\text{tot}}(\phi) - F_{\text{HC}}(\phi) - F_{\text{st. edd.}}(\phi)$. Because the total includes all energy while the explicit calculations include only MSE (neglecting kinetic energy), the transient eddy terms include any resulting residual. But presumably this residual term is small.

Another concern regarding the MSE flux by the Hadley cells is the vertical extent of the integral. While all of our conceptual analysis invokes tropospheric circulation only, integrating to the model top includes stratospheric flow. Though this circulation is weak and the densities low, large stability values due to the negative lapse rate and large MSE values due to the large geopotential term could result in non-negligible contributions to the net MSE flux. We test this effect by varying the vertical extent of the MSE flux integral (not shown). While the magnitude of the energy flux tends to reduce slightly by lowering the extent of the integral, the qualitative picture remains the same in either case. Also, since we are taking the transient eddy component as the residual of the total energy flux calculation – which implicitly includes the entire atmosphere – and the time mean component, moving the time mean integrals lower than the model top would lead to the transient eddy term being contaminated by the stratospheric time mean flow. We therefore integrate through

the depth of the model atmosphere.

For the mass flux Ψ_{\max} , we use the signed maximum magnitude value of the Eulerian meridional mass streamfunction at each latitude, where the streamfunction Ψ is defined as

$$\Psi(\phi, p) = 2\pi a \cos \phi \int_0^p [\bar{v}] \, dp / g. \quad (2.11)$$

The mass flux can also be obtained by integrating the adjusted meridional wind $[\bar{v}]_{\text{adj}}$ from the surface to the level where the integral attains its maximum magnitude. The results in either case are nearly identical, and so we choose the former, it being more conventional and simpler to calculate.

We calculate the gross moist stability, Δ_{HC} , as the ratio of the energy flux by the Hadley cells, $F_{\text{HC}}(\phi)$ to the mass flux, $\Psi_{\max}(\phi)$:

$$\Delta_{\text{HC}}(\phi) \equiv \frac{\int_{p_{\text{top}}}^{p_{\text{sfc}}} [\bar{h}] [\bar{v}]_{\text{adj}} \, dp / g}{\Psi_{\max}}. \quad (2.12)$$

Thus defined, Δ_{HC} is positive for a thermally direct circulation such as the Hadley cells. In all plots of Δ_{HC} or its theoretical approximations, we divide by c_p as standard in order to get units of K.

Chapter 3

Sahel rainfall and moist static energy budget response to uniform warming

Abstract

Rainfall in the African Sahel has varied markedly in the paleoclimate and modern observational records, and climate model projections of the semi-arid region's future rainfall span from severe drying to severe wetting. One of the strongest drying responses is generated by the NOAA Geophysical Fluid Dynamics Laboratory AM2.1 atmospheric general circulation model and occurs in response to ocean surface warming with or without spatial pattern. This study compares the Sahel's response to uniform 2 K sea surface temperature warming in AM2.1 using either its default convective parameterization, Relaxed Arakawa-Schubert (RAS), or an alternate, the University of Washington (UW) parameterization. The relevant mechanisms are then elucidated via the moist static energy (MSE) budget, for which closure in the column integral is enforced through an adjustment procedure.

Replacing RAS with UW causes the wet-season rainfall response to switch from a 40% decrease to a 6% increase. With either parameterization, the leading-order climatological region-mean budget comprises positive top-of-atmosphere radiative forcing balanced by MSE divergence via horizontal advection of dry, low-MSE air from the Sahara Desert. The latter is enhanced with oceanic warming due to prevailing MSE and moisture gradients throughout the tropics being enhanced. With RAS, this is balanced in the Sahel by anomalous MSE convergence through suppressed ascent. Under these conditions, in order to balance

a given horizontal MSE divergence, anomalous subsidence must be especially large in the mid-troposphere where the moist static stability is small, and at these levels the meridional MSE gradient magnitude is increased more in RAS than in UW. As such, for precipitation in UW the drying influences are overcome by the general wettening influences of mean ocean warming. This broad set of hydrological and energetic responses to SST warming persists across simulations with SSTs varied over a wide range. The implication is that both the convective processes themselves and the circulation characteristics they give rise to factor into the Sahel drying response in AM2.1.

3.1 Introduction

As described in Chapter 1, rainfall in the semi-arid Sahel is highly variable on climatic timescales and is sensitive to SST variations, but the physical understanding of its links to SSTs is incomplete, contributing to the vast spread in Sahel rainfall in GCM 21st century simulations.

Irrespective of the spatial signature, GCMs consistently project mean ocean surface warming [Collins *et al.*, 2013], and it has been argued that precipitation changes over tropical land in 21st century simulations are largely controlled by mean ocean warming [He *et al.*, 2014; Chadwick, 2016]. For the Sahel, while arguments appealing to changes in SST spatial patterns [e.g. Giannini *et al.*, 2013] would project no response to mean warming, CMIP3-era AGCMs perturbed with uniform 2 K SST warming exhibit rainfall responses in the Sahel ranging from modest to severe drying [Held *et al.*, 2005]. The severe drying response, in the NOAA Geophysical Fluid Dynamics Laboratory AM2.1 AGCM, drives comparable drying in 21st century simulations in its coupled atmosphere-ocean configuration, CM2.1. The drying in CM2.1 and its CMIP5-era descendant, ESM2M, are among the most severe drying responses of the CMIP3 [Held *et al.*, 2005] and CMIP5 [Biasutti, 2013] ensembles, respectively. The goal of this chapter, therefore, is to identify the physical mechanisms underlying

this drying response in AM2.1, as a first step towards assessing its plausibility as a real world response to mean ocean warming.

It can be reasonably expected that the convective parameterization shapes the Sahel’s drying response in AM2.1. How moist convection is represented fundamentally shapes the tropical circulation in comprehensive [Zhang, 1994] and idealized [Frierson, 2007] GCMs and alters the Sahelian annual cycle of precipitation in global [McCrary *et al.*, 2014] and regional [Marsham *et al.*, 2013; Im *et al.*, 2014; Birch *et al.*, 2014] AGCMs. Conceptually, the convective parameterization (or any other model component) can influence the response to warming through two orthogonal pathways [c. f. Mitchell *et al.*, 1987]. First, for a given control climate state, how do the convective processes as parameterized respond to the imposed perturbation? For example, supposing that the SST warming reduces tropospheric relative humidity, then, starting from the same control climate state, convection in a parameterization with substantial entrainment will be more inhibited by that drying than will that of a parameterization with weak entrainment. Second, for a given parameterization of convective processes, how does the regional climate response depend on the control state? The teleconnection mechanisms by which El Niño produces descent anomalies in remote regions differs depending on the existing circulation in those regions [Su and Neelin, 2002], and the “rich-get-richer” scaling response of $P - E$ to warming inherently depends on the existing distribution of $P - E$ [Mitchell *et al.*, 1987; Chou and Neelin, 2004; Held and Soden, 2006].

This distinction matters for efforts to assess the model response’s credibility through comparison with observations. If the drying response was found to depend on the convective parameterization over a wide range of climate states, subsequent efforts could focus on cloud resolving model and observational measures of the convective processes in question. Conversely, if the drying response was found to be sensitive to the control climate state irrespective of the convective formulation, then subsequent efforts could focus on comparison of the large-scale circulation characteristics with observations. But the convective parameterization’s fundamental role in the tropical circulation complicates the task of separating these

two pathways.

In this chapter, we use present-day control and uniform SST perturbation experiments in AM2.1, using either its standard convective parameterization or an alternate, to determine the processes underlying the Sahel’s drying response to warming. Following a description of the experimental design and model attributes (Section 3.2), we show that the precipitation and surface temperature responses in the warming experiments differ markedly between the two convective parameterizations (Section 3.3) – from severe drying and warming to modestly increased precipitation. The physical mechanisms behind this discrepancy are then diagnosed through the moist static energy (MSE) budget. The two convection schemes yield notable differences in the region’s MSE budget in the control simulation (Section 3.4), but the leading order balance is the same in either case. In contrast, the MSE budget response to SST warming differs fundamentally between the two (Section 3.5). By varying the SSTs over a wide range, we ultimately determine that the drying response in AM2.1 depends on both the character of the circulation and the formulation of the convective processes (Section 3.6). We conclude with discussion of the implications and limitations of these results (Section 3.7) and a final summary of the key findings (Section 3.8).

3.2 Methodology

AM2.1 [*GFDL Atmospheric Model Development Team*, 2004; *Delworth et al.*, 2006] uses a finite-volume, latitude-longitude dynamical core with 2° latitude $\times 2.5^\circ$ longitude horizontal resolution, 24 vertical levels extending to 10 hPa, prescribed monthly aerosol burdens, the LM2 land model [*Milly and Shmakin*, 2002], and the Relaxed Arakawa-Schubert (RAS) convective parameterization [*Arakawa and Schubert*, 1974; *Moorthi and Suarez*, 1992]. RAS represents moist convection as an ensemble of plumes originating from the boundary layer, each detraining cloudy air only at cloud top and entraining environmental air at all levels at a rate computed inversely based on their buoyancy and specified cloud top height. The

RAS implementation in AM2.1 uses the minimum-entrainment parameter of *Tokioka et al.* [1988], which prohibits convection that would otherwise have an entrainment rate lower than a specified minimum value that is inversely proportional to the boundary layer depth. In a deviation from *Tokioka et al.* [1988], this minimum-entrainment criterion is applied only for convective clouds extending vertically above 500 hPa, a choice made during AM2.1's development essentially for energy balance tuning purposes [*Held et al.*, 2007].

We create a modified version of AM2.1 by replacing RAS with the University of Washington (UW) parameterization [*Bretherton et al.*, 2004]. UW represents moist convection as a single bulk plume that entrains environmental air and detrains cloudy air at each level as it ascends, with entrainment inversely proportional to convective depth. This scheme has been used in other GFDL models, both in its original intended capacity as a shallow convective parameterization [AM3; *Donner et al.*, 2011] and as the parameterization for all convection [HiRAM; *Zhao et al.*, 2009; *Zhao*, 2014]. We use the same settings for UW as in its implementation in HiRAM, including a reduction in entrainment over land necessary to generate adequate convective continental precipitation; we use a value of 0.5 for this land-ocean entrainment ratio, the same as that used by HiRAM when run at this horizontal resolution [see Figure 1 and corresponding text of *Zhao et al.*, 2009]. The convective parameterization is the sole difference between the two model variants, and UW was chosen as the alternative parameterization based on expediency of coding and on preliminary results in the coarse resolution version of HiRAM that showed large Sahel rainfall differences compared to AM2.1. For the remainder of this chapter, we use the acronyms RAS and UW to refer to the respective model variants in addition to the parameterizations themselves.

We perform control and perturbation simulations in both RAS and UW. The control simulation comprises present-day climatological annual cycles of SSTs and sea ice repeated annually, the SSTs computed over 1981-1999 from the NOAA Optimal Interpolation dataset [*Reynolds et al.*, 2002]. In the perturbation simulation, 2 K is added uniformly to the SSTs. In order to focus exclusively on the role of SST warming, concentrations of greenhouse gases

and aerosols are fixed at present-day values in all simulations. The simulations span 31 years, with averages taken over the last 30. All values presented are averages over the peak rainy season, July through September. Region averages are based on land points within 10-20°N, 18°W-40°E, similar to that of *Held et al.* [2005].

We use data on the model’s native hybrid sigma-pressure coordinates [*Simmons and Burridge, 1981*] but postprocessed to a regular latitude-longitude grid, and this horizontal interpolation step is known to generate spurious mass and energy imbalances [despite retaining the native vertical coordinates, c. f. *Neelin, 2007*]. As such, in Appendix 3.A we present an adjustment method based on those of *Trenberth* [1991] and *Peters et al.* [2008] that imposes nearly exact closure of the column-integrated budgets of conserved tracers, and in Appendix 3.B we detail the computation procedures for all MSE budget terms, including the application of this adjustment method to MSE. The adjusted column MSE budget terms are computed using 3-hourly instantaneous data; other fields are computed from timeseries of monthly averages.

3.3 Precipitation and surface climate

The precipitation responses to 2 K SST warming in RAS and UW are shown in Figure 3.1, normalized by the Sahel region-mean precipitation in their respective control simulations (4.0 and 2.6 mm day⁻¹, respectively). Table 3.1 lists Sahel region-mean values of precipitation, surface temperature, and other surface climate fields. As documented by *Held et al.* [2005], rainfall decreases sharply over most of the Sahel in RAS, by 40% (1.7 mm day⁻¹) in the region average. This is part of a larger spatially coherent drying, with even greater precipitation decreases just to the east (over the southern Arabian Peninsula and Red Sea) and west (over the Atlantic Ocean). For context, precipitation reductions in excess of 4 mm day⁻¹ occur in several gridpoints within this band and nowhere else globally, and the global minimum of -7.4 mm day⁻¹ occurs just west of the Sahel. In sharp contrast, precipitation *increases*

modestly over most of the Sahel in UW, by 6% (0.2 mm day^{-1}) on average.

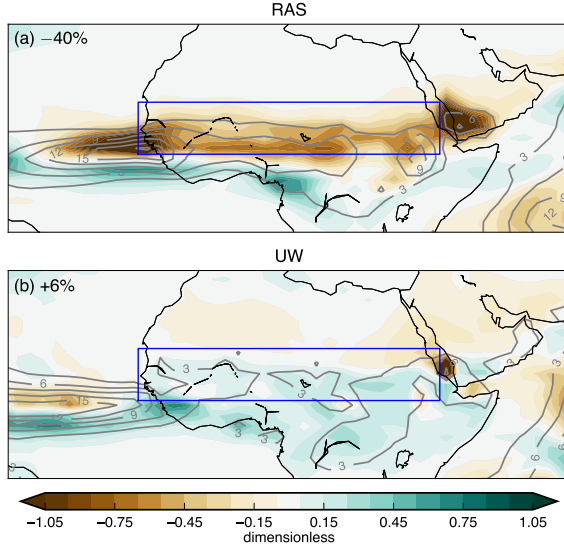


Figure 3.1: (Shaded contours) difference in precipitation between the uniform 2 K SST warming and present-day control simulations, normalized by the control simulation Sahel region-mean value and therefore unitless, and (grey contours) precipitation in the control simulation, with contours starting at 3 mm day^{-1} and with a 3 mm day^{-1} interval, in (a) RAS and (b) UW. In this and subsequent figures, blue boxes delineate the boundaries used to compute Sahel region-mean values, and values printed in the top-left of each panel are the Sahel region-mean values of the field in shaded contours (in this case the precipitation response).

The precipitation in the control simulations is also shown in Figure 3.1. In RAS, there is 74% more rainfall in the region than in UW (4.0 and 2.6 mm day^{-1} , respectively), mostly reflecting lower precipitation rates in UW in the southern Sahel. Precipitation is lower over most land in UW as compared to RAS, as the UW parameterization is less effective than RAS at generating continental convection (in contrast, precipitation is greater in UW over relatively shallow oceanic convection zones, such as the eastern Pacific ITCZ; not shown). Region-mean values of evaporation (E) are more similar than precipitation (P) in the control simulation (2.3 and 1.9 mm day^{-1} for evaporation in RAS and UW, respectively; Table 3.1). As a result, precipitation minus evaporation ($P - E$) is only 0.3 mm day^{-1} in UW in the control simulation, near the lower limit for a land region of zero. Nevertheless, $P - E$ does decrease slightly (by 0.1 mm day^{-1}), due to evaporation increasing more than precipitation.

Table 3.1: Sahel region-mean values of, from left to right: precipitation (mm day^{-1}), evaporation (mm day^{-1}), precipitation minus evaporation (mm day^{-1}), surface air temperature (K), and relative humidity 2 meters above the surface (percent) for the control simulation, 2 K SST warming simulation, and their difference, in both model variants. Parenthetical values for the precipitation, evaporation, and precipitation minus evaporation difference are the percentage change from the control simulation.

Model	Simulation	\bar{P}	\bar{E}	$\bar{P} - \bar{E}$	\bar{T}_s	$\bar{RH}_{2\text{m}}$
RAS	Control	4.0	2.3	1.7	300.9	64
	2 K	2.3	1.9	0.4	305.5	52
	2 K – Control	–1.7	–0.4	–1.3	+4.6	–12
		(–40%)	(–16%)	(–75%)		
UW	Control	2.6	2.4	0.3	299.5	59
	2 K	2.8	2.6	0.2	302.2	56
	2 K – Control	+0.2	+0.2	–0.1	+2.7	–3
		(+6%)	(+10%)	(–25%)		

In RAS, $P - E$ declines sharply with warming (by 1.3 mm day^{-1}).

Figure 3.2 shows the surface air temperature responses. Warming is land-amplified in both model variants. In RAS, the Sahel warms more than any other region worldwide. Warming exceeds 6 K over much of the Sahel, with a maximum of 9.0 K in the eastern Sahel; warming does not exceed 6 K in any location outside the region. Region-mean surface relative humidity reduces sharply, from 64% to 52% (Table 3.1). In contrast, Sahel surface warming is unexceptional in UW, with a region-mean of 2.7 K, and near-surface relative humidity decreases more modestly from 59 to 56% (Table 3.1).

To summarize, uniform 2 K SST warming in RAS causes severe reductions in precipitation and $P - E$, accompanied by intense surface warming and reduced relative humidity. The same perturbation in UW causes a more tepid response: modestly increased precipitation but slightly reduced $P - E$, surface warming comparable to neighboring regions, and modestly reduced relative humidity. The surface temperature and relative humidity responses in each case are consistent with expectations based on the surface dynamics of semi-arid land regions and theory for land responses to SST warming presented in Chapter 1, given the precipitation responses.

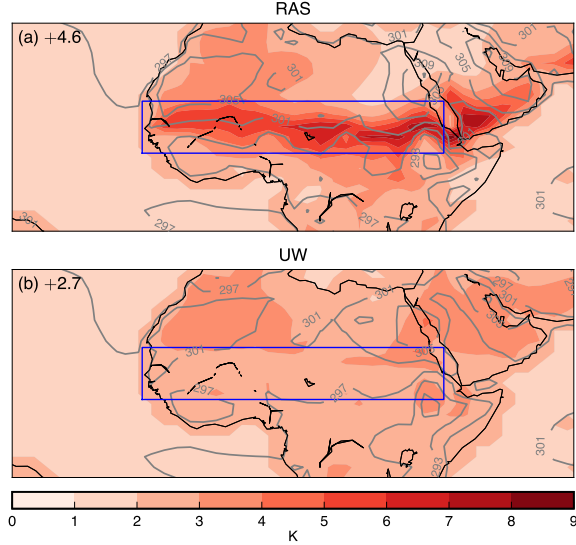


Figure 3.2: [Same as Figure 3.1, but for surface air temperature.] (Shaded contours) difference in surface air temperature between the uniform 2 K SST warming and present-day control simulations, in K, and (grey contours) surface air temperature in the control simulation, with contours values printed, in K, in (a) RAS and (b) UW.

3.4 Moist static energy budget in the control simulations

3.4.1 RAS

Figure 3.3 shows the column-integrated MSE budget terms in the control simulations. In and near the Sahel, the MSE budget varies markedly with latitude. The southern Sahel and equatorial Africa conform to the classical picture of tropical convecting regions: large energetic forcing [$\sim 100 \text{ W m}^{-2}$; Figure 3.3(a)] balanced primarily by MSE divergence by deep convection associated with the time-mean divergent circulation [Figure 3.3(e)].¹ Moving northward, while the energetic source term remains mostly positive within the Sahel, the convective term becomes steadily more negative, yielding net MSE convergence over most of the northern Sahel ($\sim 70 \text{ W m}^{-2}$), where presumably much of the convection is dry. These positive energetic inputs are balanced by large magnitude divergence of MSE by the time-mean horizontal flow [$\sim 100 \text{ W m}^{-2}$; Figure 3.3(c)].

¹Large horizontal and vertical advection values in the far southeastern Sahel stem from the topography of the Ethiopian highlands.

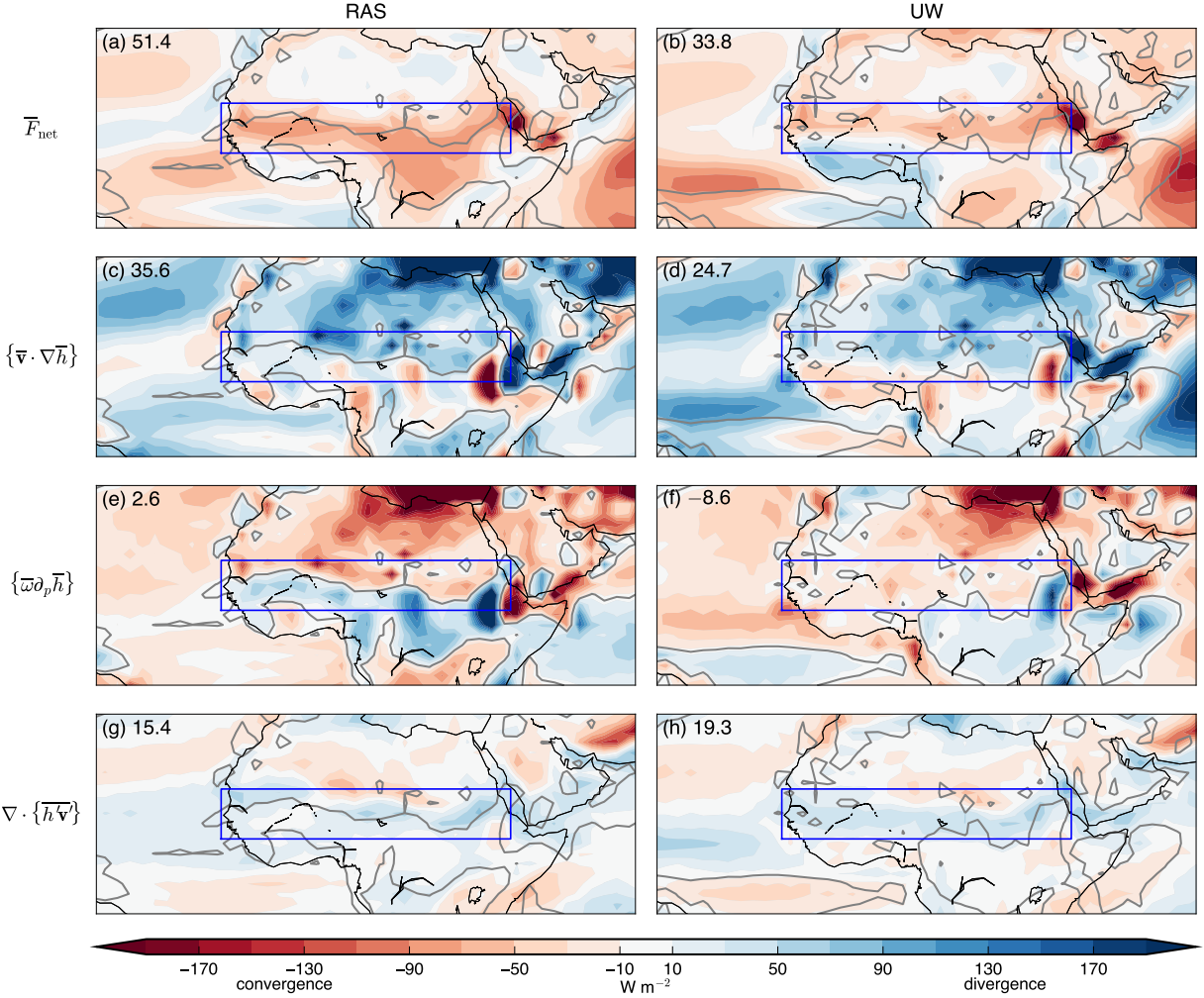


Figure 3.3: (Shaded contours) terms of the control simulation column-integrated MSE budget in (left column) RAS and (right column) UW, in W m^{-2} : (first row) net energetic forcing, (second row) time-mean horizontal advection, (third row) time-mean vertical advection, and (fourth row) eddy flux divergence. The colorbar corresponds to the three transport terms, for which red shades denote convergence (negative values), and blue shades divergence (positive values), of MSE. For the net energetic forcing term, the sign is opposite to the colorbar, with red shades denoting positive values and blue shades denoting negative values. With these conventions, for all terms red shades can be thought of as representing a gain, and blue shades a loss, of energy. The grey contour in all panels is the zero contour of the time-mean vertical advection. The storage term ($\partial_t \bar{\mathcal{E}}$) is omitted. It is the smallest magnitude term and does not factor into the response appreciably.

Figure 3.4 shows MSE and horizontal wind at two model levels, in the mid-troposphere and boundary layer, respectively, and Figure 3.5 shows the Sahel region-mean vertical profiles of the net energetic forcing and time-mean horizontal and vertical advection terms. In RAS, boundary layer MSE [Figure 3.4(b)] in the southern Sahel and equatorial Africa is high and fairly homogeneous, a structure that fuels deep convection while preventing horizontal MSE advection [Sobel, 2007]. The meridional MSE gradient is sharp in the northern Sahel, which is dominated by the meridional moisture gradient (the temperature gradient slightly counteracts this), and this is acted on by northerly winds to yield strong MSE divergence. Zonally, the largely westerly near-surface wind throughout the Sahel likely advects moisture from the western Sahel to the east, thereby contributing to the region's striking zonal symmetry despite the continental geometry discussed previously. In the mid-troposphere [Figure 3.4(a)], horizontal MSE gradients are weaker and the flow is more zonal and uniform than in the boundary layer, leading to little net horizontal MSE advection at this level. Consequently, the column-integrated horizontal MSE advection is dominated by the lower troposphere [Figure 3.5(b)] and by meridional (rather than zonal) advection (not shown).

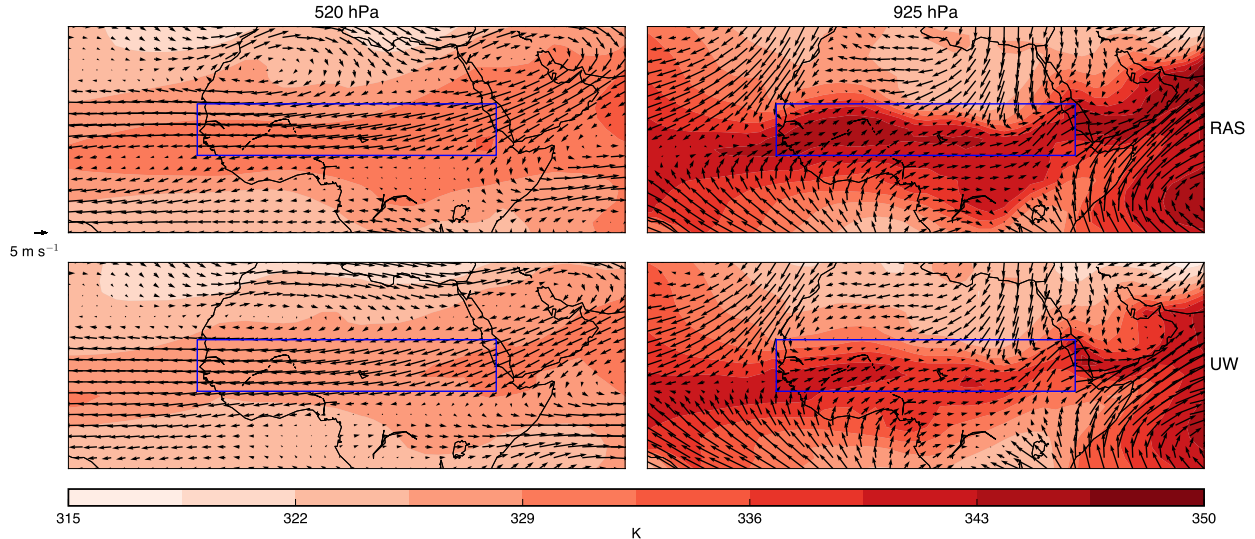


Figure 3.4: (Shaded contours) MSE in the control simulation, divided by c_p such that units are K, and (arrows) horizontal wind, in m s^{-1} , at the model levels corresponding roughly to (left column) 520 hPa and (right column) 920 hPa, in (top row) RAS and (bottom row) UW.

Largely opposing the time-mean horizontal circulation, the time-mean divergent flow [Figure 3.5(c)] converges MSE at lower levels and diverges it above. Figure 3.6 shows the region-mean profiles of vertical velocity and moist static stability. Ascent occurs throughout the troposphere and acts on positive values of moist static stability above ~ 700 hPa and negative values below, consistent with Figure 3.5(c).

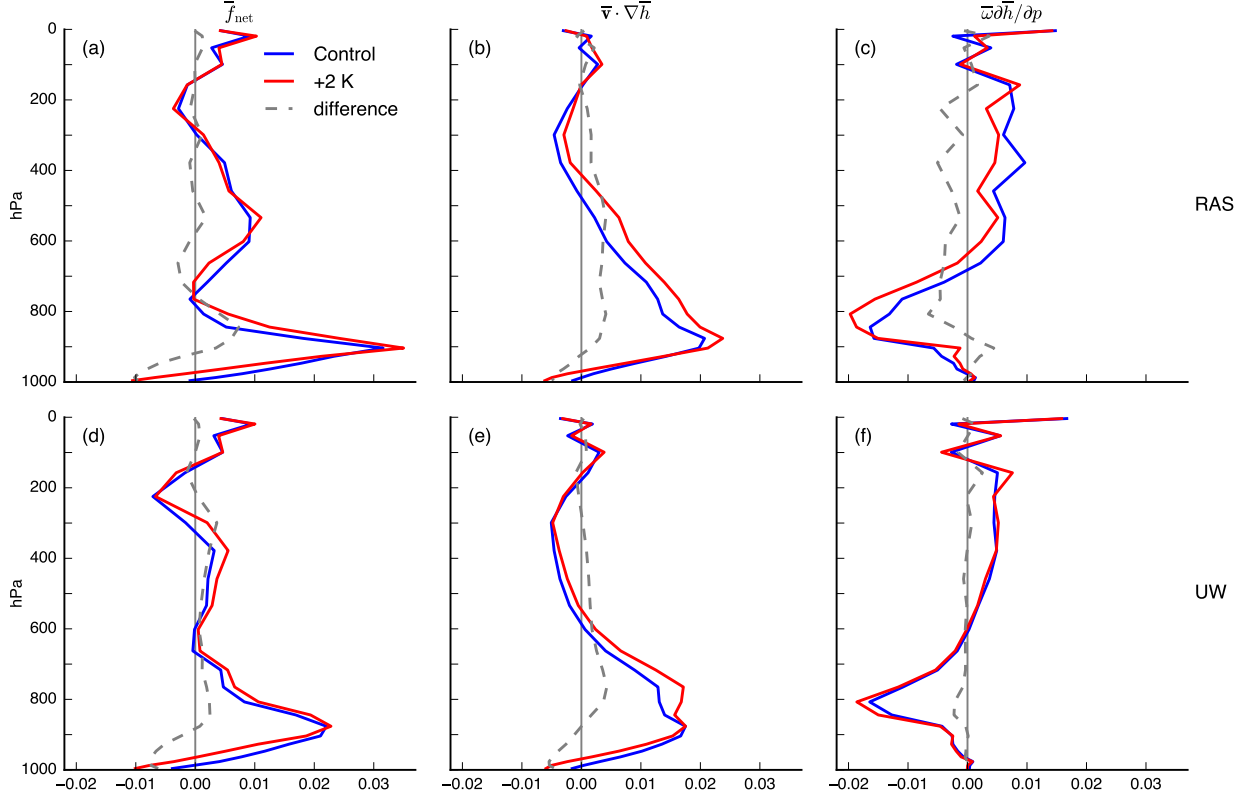


Figure 3.5: Sahel region-mean profiles of (left column) the net energetic forcing term, (middle column) time-mean horizontal MSE advection, and (right column) time-mean vertical MSE advection, for (blue curve) the control simulation, (red curve) the 2 K SST warming simulation, and (dashed grey curve) their difference, in (top row) RAS and (bottom row) UW, in $\text{J kg}^{-1} \text{Pa}^{-1}$. The advection terms are computed using monthly data with no column adjustment applied. Vertical advection is computed explicitly using model outputted \bar{w} and olh rather than as a residual.

Table 3.2 lists the Sahel region-mean column-integrated MSE budget terms. Because of the meridional cancellation of the time-mean vertical advection term, the leading order balance is of net energetic forcing (51.4 W m^{-2}) balanced by divergence of MSE by the time-mean horizontal circulation (35.6 W m^{-2}). Time-mean vertical advection contributes

only 2.6 W m^{-2} and transient eddies a non-negligible 15.4 W m^{-2} . The meridional dipole of the transient eddy MSE flux divergence [Figure 3.3(g)] presumably reflects northward moisture transport by African Easterly Waves, which track the sharp meridional gradient in soil moisture that spans the width of the Sahel [e.g. *Thorncroft et al.*, 2008, and references therein]. But the magnitudes are almost uniformly weaker than the other terms. The smallness of the region-mean budget residual of 0.3 W m^{-2} reflects the adjustment applied to impose near-exact closure. The overall meridional structure within the region of each MSE budget term and of precipitation is slightly tilted, northwest to southeast. This likely reflects the wettening effect of the West African Monsoon in the western Sahel, although there is also a zonal component with westerly onshore flow spanning the Sahel's western edge.

Table 3.2: Terms of the Sahel region-mean column-integrated MSE budget, in W m^{-2} , for the control simulation, 2 K SST warming simulation, and their difference, in both model variants.

Model	Simulation	\bar{F}_{net}	$\{\bar{\mathbf{u}} \cdot \nabla \bar{h}\}$	$\left\{ \bar{\omega} \frac{\partial \bar{h}}{\partial p} \right\}$	$\nabla \cdot \{\bar{h}' \mathbf{u}'\}$	$\frac{\partial \{\bar{\mathcal{E}}\}}{\partial t}$
RAS	Control	51.4	35.6	2.6	15.4	-1.9
	2 K	52.3	55.5	-13.2	12.6	-2.4
	2 K - Control	+0.9	+20.0	-15.9	-2.8	-0.4
UW	Control	33.8	24.7	-8.6	19.3	-1.5
	2 K	37.7	31.9	-11.1	18.4	-1.4
	2 K - Control	+3.9	+7.2	-2.4	-0.9	+0.0

3.4.2 UW

In UW, the column-integrated net energetic forcing [Figure 3.3(b)] spatial structure is similar to that of RAS, but within the Sahel values are generally smaller; the region-mean is 33.8 W m^{-2} . This arises from the cooler surface and more extensive low cloud cover in UW, which respectively yield less net emission of longwave radiation and less absorption of shortwave radiation (not shown). Divergence of MSE by horizontal advection spans most of the Sahel [Figure 3.3(d)], 24.7 W m^{-2} on average, yielding the same leading order region-

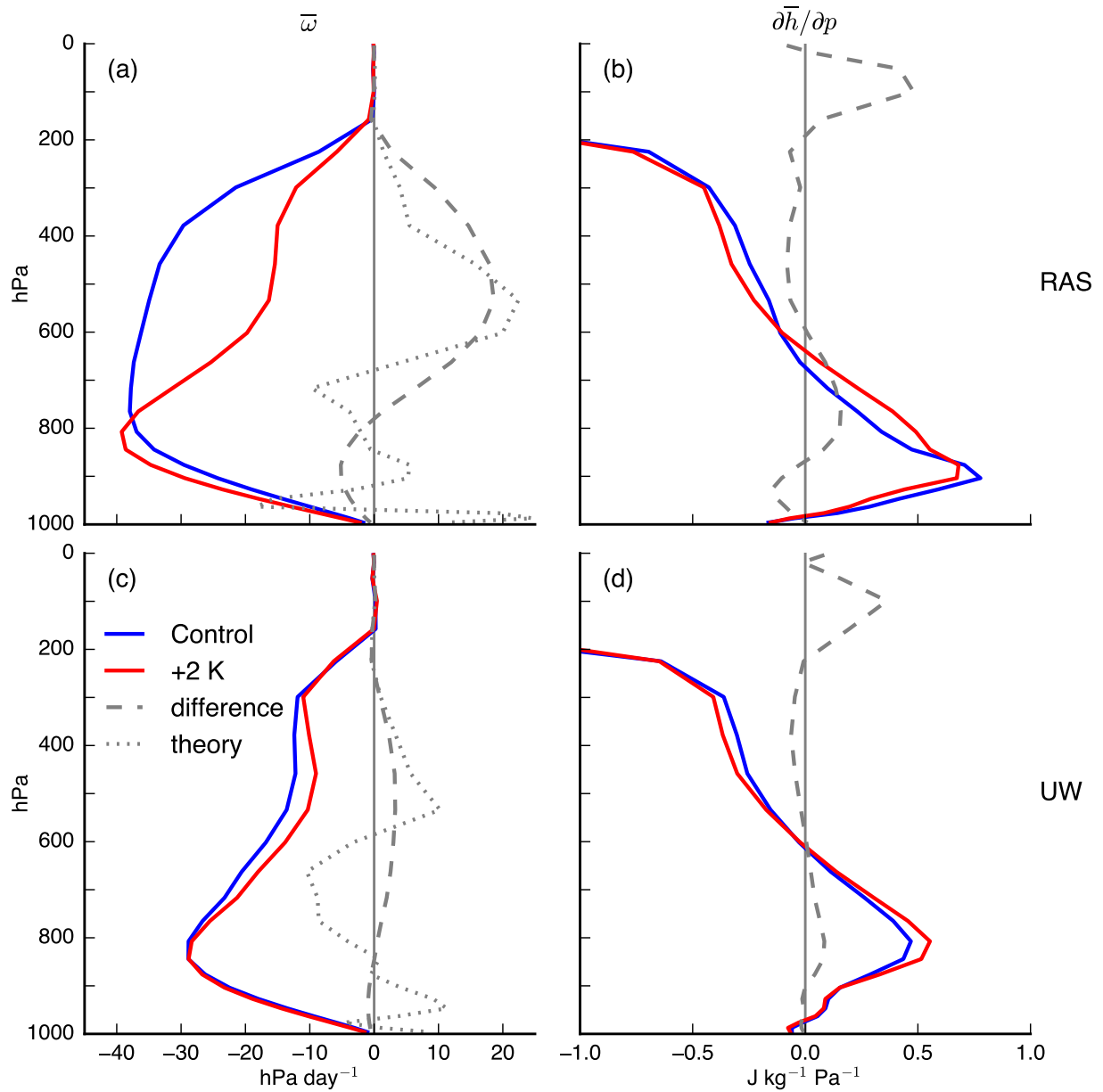


Figure 3.6: Sahel region-mean profiles of (left column) vertical velocity, in hPa day^{-1} , and (right column) moist static stability, in $\text{J kg}^{-1} \text{Pa}^{-1}$, for (blue curve) the control simulation, (red curve) the 2 K SST warming simulation, and (dashed grey curve) their difference, in (top row) RAS and (bottom row) UW. The dotted grey curve in (a) and (c) is the approximation for $\delta \bar{\omega}$ given by (3.1), computed at each gridpoint and month excluding where $|\partial_p \bar{h}| < 0.05 \text{ J kg}^{-1} \text{ Pa}^{-1}$ before temporally and regionally averaging.

mean balance as in RAS, $\bar{F}_{\text{net}} \approx \{\bar{\mathbf{u}} \cdot \nabla \bar{h}\}$. The horizontal flow is largely similar in both the mid-troposphere and boundary layer to RAS [Figure 3.4(b) and (d), respectively], but the meridional MSE gradient in the boundary layer is weaker in UW than in RAS. Modest MSE convergence in the mid-troposphere in UW arises from easterly wind acting on a modest zonal MSE gradient in the eastern Sahel.

Unlike RAS, convection is sufficiently shallow that vertical advection converges MSE in the column integral throughout nearly the entire Sahel [Figure 3.3(f)], 8.6 W m^{-2} in the region-mean. This discrepancy primarily stems from much weaker upper-tropospheric ascent in UW (Figure 3.6), an intuitive result in a convecting region given that UW is a less active parameterization than RAS. Also, contrary to classical expectation, vertical MSE advection does not track the near surface MSE maximum: the former is positive only within equatorial Africa, in which (unlike RAS) MSE values are low. The eddy flux divergence [Figure 3.3(h)] resembles that of RAS, with a region-mean value of 19.3 W m^{-2} divergence. The region-mean profiles of the net energetic forcing and time-mean advection terms [Figure 3.5(d)-(f)] are each qualitatively similar to their RAS counterparts, with vertical advection in UW reflecting shallower convection and associated overturning circulation.

3.5 Moist static energy budget responses to SST warming

In this section, we argue that the changes in the MSE budget that distinguish RAS from UW most importantly are in the mid-troposphere. The dominant change at these levels in RAS is increased MSE loss due to horizontal advection, driven primarily by the change in MSE gradients. This is balanced by anomalous mid-tropospheric subsidence and the resulting adiabatic warming, with little net energetic forcing response. Both the thermodynamic increase in the cooling due to horizontal advection and the dynamic increase in subsidence warming are smaller in UW.

3.5.1 RAS

Figure 3.7 shows the responses of each column-integrated MSE budget term to the +2 K SST perturbation, and Table 3.2 lists the Sahel region-mean responses and +2 K simulation values. In RAS, the largest responses are of the time-mean advection terms and occur primarily near and just north of the climatological $\{\bar{w}\partial_p\bar{h}\} = 0$ isoline that roughly bisects the Sahel. Specifically, MSE divergence by horizontal advection is strongly enhanced [Figure 3.7(c); region-mean $+20.0 \text{ W m}^{-2}$], balanced by anomalous MSE convergence by the time-mean divergent circulation [Figure 3.7(e); region-mean -15.9 W m^{-2}]. Based on the region-mean profiles of the anomalous advection terms shown in Figure 3.5, these column-integrated responses reflect consistent behavior throughout the free troposphere for both terms. The net energetic forcing [Figure 3.7(a); region-mean $+0.9 \text{ W m}^{-2}$] and eddy flux divergence [Figure 3.7(g); region-mean -2.8 W m^{-2}] responses are comparatively modest, comprising moderate magnitudes oriented in a meridional dipole that largely cancel in the region-mean. For eddies, this is primarily in the eastern Sahel and reflects the aforementioned local southward shifts of the temperature and moisture gradients. We next investigate the mechanisms that give rise to the leading-order balance between the anomalous time-mean advection terms.

Figure 3.6 shows Sahel region-mean profiles of the vertical velocity and moist static stability. Ascent is drastically reduced throughout the free troposphere and slightly enhanced in the boundary layer, which amounts to a severe shallowing of convection. This dominates over modest moist static stability responses, which we show by decomposing the response into dynamic, thermodynamic, and covariant components that arise respectively from the anomalous flow, from the anomalous MSE, and from the covariance of these two anomaly fields. The thermodynamic term includes the full response of MSE, i.e. it does not assume fixed-relative humidity. The Sahel region-mean profiles of these terms are shown in Figure 3.8 and column-integrated values in Figure 3.9. For vertical advection, the dynamic term is dominant throughout the free troposphere and in the column integral. In the northern Sahel,

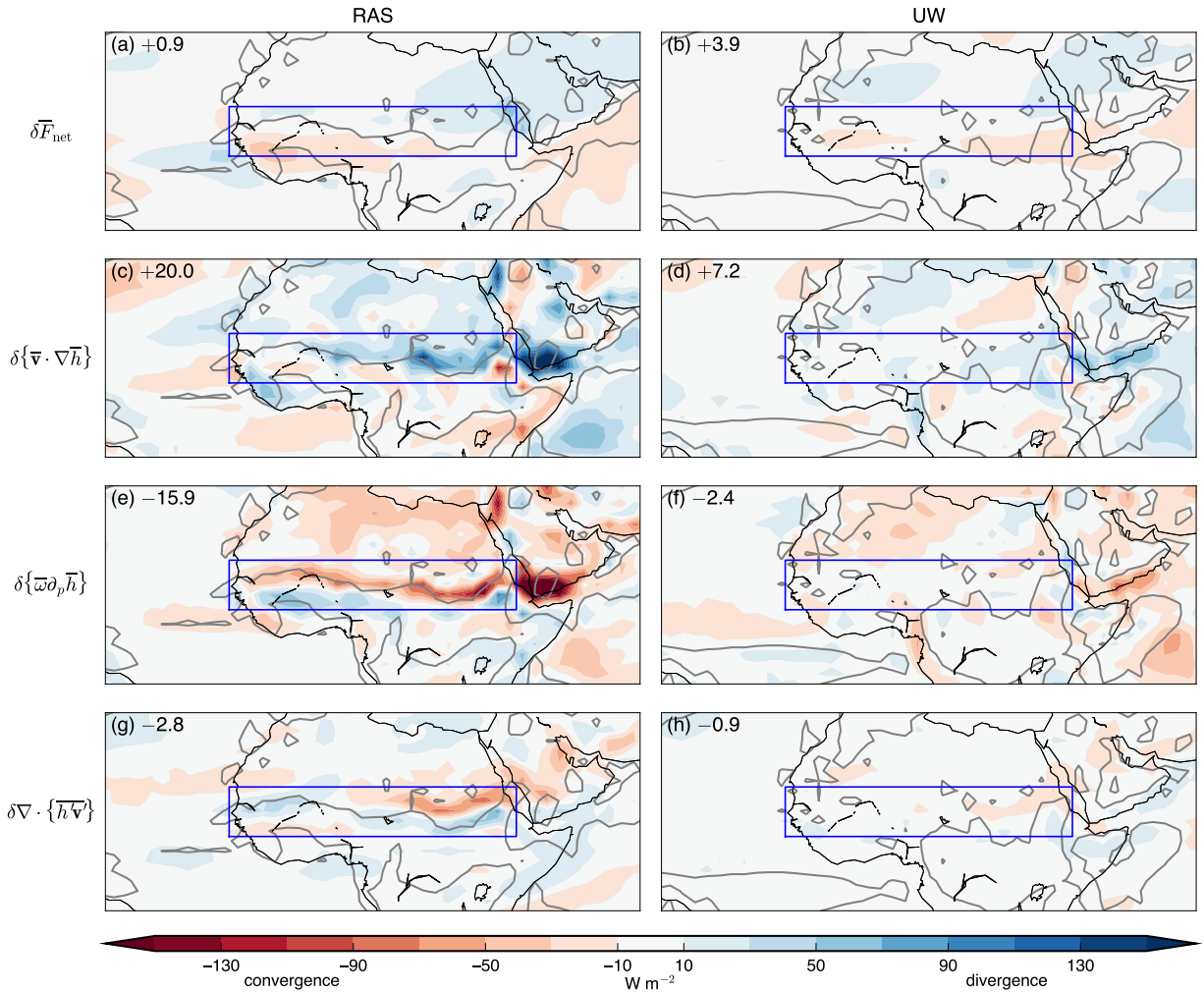


Figure 3.7: Same as Figure 3.3, but with shaded contours denoting the responses in the 2 K SST warming simulation. Note that the contour spacing is slightly smaller than in figure 3.3.

the combination of moderate anomalous ascent in the boundary layer, anomalous descent in the free troposphere, and reduced relative humidity and precipitation suggest increased dry convection. In the southwestern Sahel, MSE divergence through vertical advection actually increases, despite precipitation decreasing sharply [Figure 3.1(a)].

The time-mean horizontal MSE advection response in RAS primarily reflects the drying influence of an increased meridional MSE gradient spanning the Sahel. Figure 3.10 shows the responses of MSE and horizontal wind at the same mid-tropospheric and boundary layer levels shown in Figure 3.4. At both levels, MSE increases more in equatorial Africa than surrounding regions, including the Sahel and the Sahara Desert. This anomalous gradient predominantly reflects differential increases in water vapor that arise from mean warming. Figure 3.11 shows the control and response values of the column-integrated water vapor throughout the Tropics. As expected, relative humidity variations on a tropics-wide scale are modest (not shown), and thus column water vapor increases almost everywhere and generally more in regions where it is climatologically large.

The thermodynamic term dominates the region-mean anomalous MSE divergence in the free troposphere [Figure 3.8(a)] and yields column-integrated MSE divergence over most of the Sahel except the far west and east [Figure 3.9(a)] – we return to the boundary layer and northeastern Sahel responses further below. Combined with the dominance of the dynamic component of vertical advection in the free troposphere [Figure 3.8(b)] and a modest net energetic forcing term response above ~ 700 hPa [Figure 3.5(b)], the leading order balance at these levels is $\bar{\mathbf{u}} \cdot \delta \nabla \bar{h} \approx (\delta \bar{\omega}) \partial_p \bar{h}$. Rearranging this yields an approximate diagnostic for the anomalous ascent profile in the free troposphere:

$$\delta \bar{\omega} \approx -\frac{\bar{\mathbf{u}} \cdot \delta \nabla \bar{h}}{\partial_p \bar{h}}. \quad (3.1)$$

Figure 3.6(a) shows the anomalous vertical motion predicted by (3.1) for RAS. To avoid unphysical values near where the denominator vanishes, we exclude locations and months

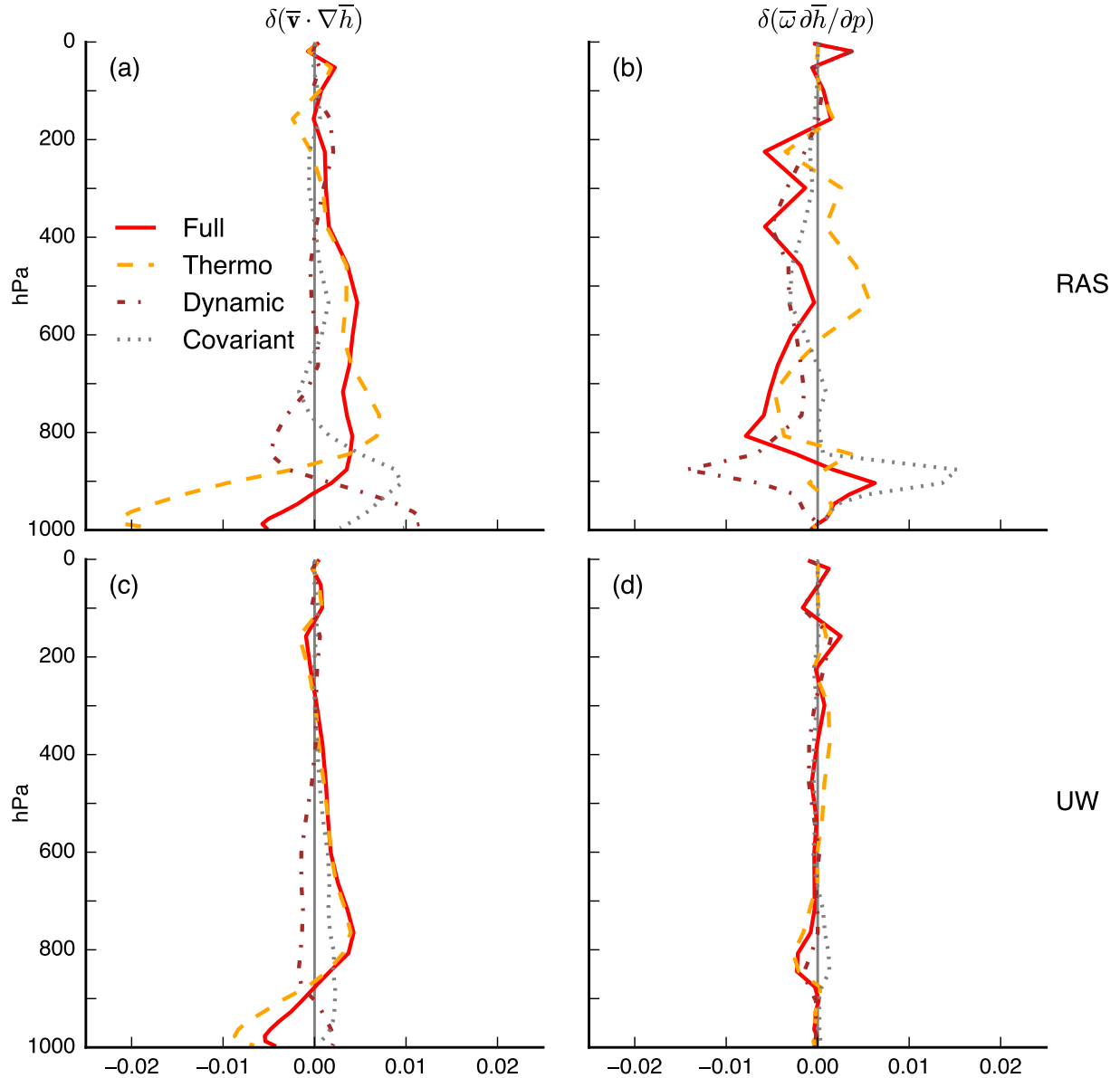


Figure 3.8: Profiles of Sahel region-mean values of the 2 K SST warming (red curves) full response and its decomposition into (dashed yellow curves) thermodynamic, (dash-dotted brown curves) dynamic, and (dotted grey curves) covariant components, for (left column) horizontal advection and (right column) vertical advection, in (top row) RAS and (bottom row) UW, in $\text{J kg}^{-1} \text{s}^{-1}$. For expediency, these computations are performed using monthly timeseries without the column budget adjustment, as detailed in Appendix 3.B.

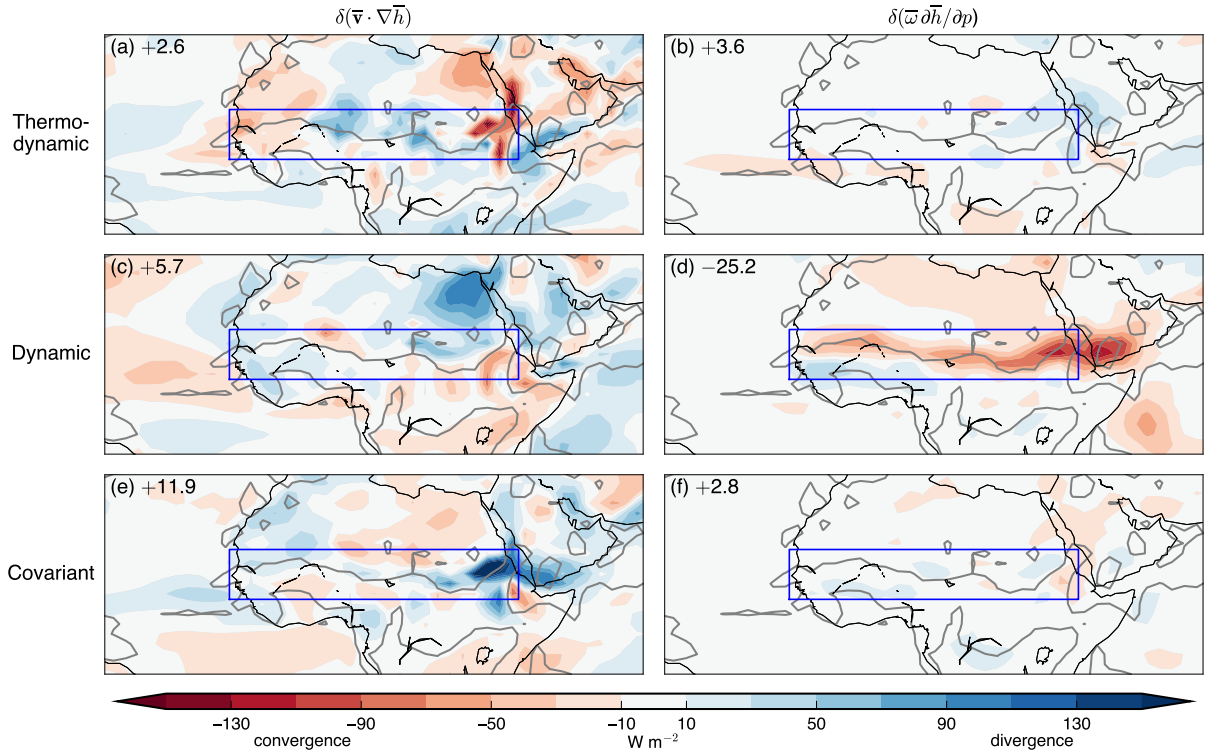


Figure 3.9: (Shaded contours) decomposition of the (left column) horizontal and (right column) vertical advection responses in the 2 K SST warming simulation into (top row) thermodynamic, (middle row) dynamic, and (bottom row) covariant components. All panels are for RAS. Grey contour is the same as in Figure 3.3.

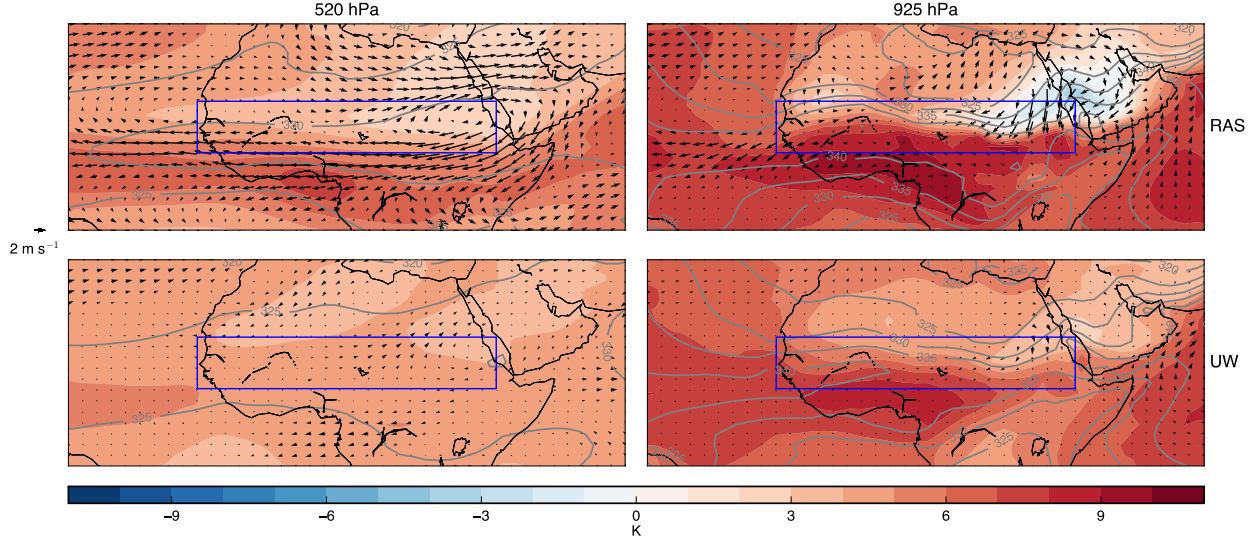


Figure 3.10: (Same as Figure 3.4, but for the response in the 2 K SST warming simulation.) (Shaded contours) Responses to 2 K SST warming of MSE, divided by c_p such that units are K, and (arrows) horizontal wind, in m s^{-1} , at the model levels corresponding roughly to (left column) 520 hPa and (right column) 920 hPa, in (top row) RAS and (bottom row) UW. Note the difference in wind scale compared to Figure 3.4.

where $|\partial_p \bar{h}| < 0.05 \text{ J kg}^{-1} \text{ Pa}^{-1}$ before temporally and regionally averaging; the value of 0.05 was chosen subjectively to provide the best fit. The approximation captures the overall free tropospheric behavior, including the anomalous descent peak in the mid-troposphere. Throughout the free troposphere, the horizontal advection anomaly is positive $[\delta(\bar{\mathbf{u}} \cdot \nabla \bar{h}) > 0$; Figure 3.8(a)] and the moist static stability is negative $[\partial_p \bar{h} < 0$; Figure 3.6(b)]. Therefore, anomalous descent ($\delta \bar{\omega} > 0$) is required for the budget to balance. In the mid-troposphere, the moist static stability approaches zero, and as such balancing the increased dry advection requires especially large anomalous descent. Suppressed convective precipitation is the straightforward hydrological consequence of this anomalous subsidence.

We now return to the horizontal MSE advection response in the boundary layer, which is dominated by the response in the northeastern Sahel. Clausius-Clapeyron scaling cannot account for the decreases in column-integrated water vapor in RAS spanning in this region – the only region worldwide where column water vapor decreases [Figure 3.11(a)]. This is coincident with large magnitudes in the covariant term of the horizontal advection

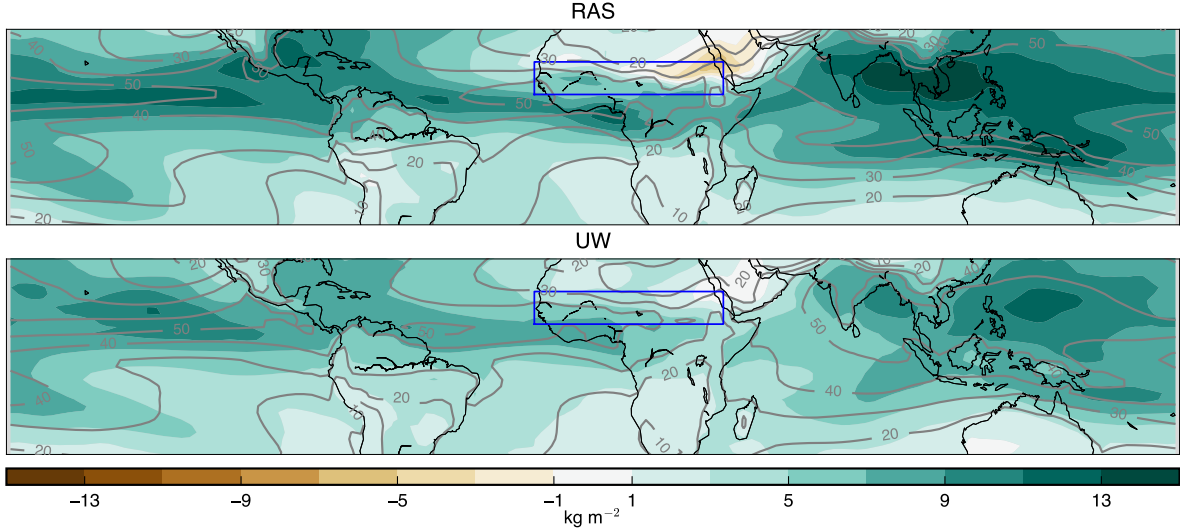


Figure 3.11: July-August-September column-integrated water vapor, in kg m^{-2} , in (grey contours) the control and (shaded contours) response to 2 K SST warming, in (top) RAS and (bottom) UW. The plotted domain is 30°S - 30°N , 180°W - 180°E .

response [Figure 3.9(e)] and anomalous MSE convergence from the thermodynamic component [Figure 3.9(a)]. In short, these large covariance values reflect a runaway drying and warming response: local surface warming [Figure 3.2(a)] caused by precipitation loss creates an anomalous heat low circulation [Figure 3.10(b)], whose boundary layer inflow is primarily northerly and thus imports even more dry Saharan air, amplifying the drying signal (the compensating mid-tropospheric anti-cyclonic outflow can be seen in Figure 3.10(a)]. The thermodynamic term behavior locally reflects climatological boundary layer flow from the southwest [Figure 3.4(a)] acting on the anomalous MSE gradient. Combining the thermodynamic and covariant components locally, the increased meridional MSE gradient ultimately drives the drying as in the rest of the northern Sahel.

As an aside, we note that over the region of intense drying over the northern flank of the Atlantic ITCZ, the column MSE budget response is actually mild and of a different character compared to that of the Sahel. Therefore, it should not be thought of as simply an westward, oceanic extension of the Sahel response, despite the shared sign of the precipitation response (at least in terms of the energetics).

In summary, increases in water vapor that roughly scale with their climatological values creates an anomalous MSE gradient spanning from equatorial Africa to the Sahara Desert, which acted on by climatological northerly wind dries out the Sahel. This inhibits moist convection and its attendant precipitation, and the resulting convective shallowing generates anomalous MSE convergence that largely balances the horizontal signal. In the northeastern Sahel, this overall mechanism effectively runs away, due to the drying-induced surface warming creating an anomalous heat low circulation: the resulting northerly inflow of dry air amplifies the original suppression of rainfall. This mechanism of the increased moisture gradient generating anomalous free tropospheric subsidence is essentially an extension of the upped-ante mechanism described in Chapter 1 [*Chou and Neelin, 2004*].²

3.5.2 UW

Like RAS, the largest term in the Sahel region mean anomalous column MSE budget is the time-mean horizontal advection (7.2 W m^{-2} ; Table 3.2). The profiles of both anomalous time-mean advection terms in UW – and their contributions from the thermodynamic, dynamic, and covariant terms – resemble smaller-magnitude versions of their RAS counterparts [Figures 3.5, 3.6, 3.10, and 3.8], including the dominance of the thermodynamic component of the anomalous horizontal advection in the free troposphere. Being much smaller in UW than RAS, it requires less compensating subsidence and thus poses a smaller drying influence, most notably in the mid-troposphere, where, like RAS, moist static stability is smallest and therefore ascent must be largest to generate a given vertical MSE advection value. Therefore, understanding the difference in the mid-tropospheric MSE gradient responses is crucial.

Figure 3.12 shows the control, +2 K, and response profiles in RAS and UW of the Sahel region-mean meridional MSE gradient, as well as zonal wind and meridional wind. Whereas

²An analogous extension of an existing, boundary-layer-focused theory in order to account for tropospheric dryness is performed by *Shekhar and Boos [2016]*, who find that the well-known estimate for the location of the ITCZ as the latitude of the maximum near-surface MSE [*Privé and Plumb, 2007*] is improved if the maximum of MSE averaged upwards to 500 hPa is used instead.

the horizontal wind fields are largely similar across RAS and UW and respond modestly, the meridional MSE gradient is enhanced more in RAS than in UW at most levels, including the mid-troposphere. Moreover, it is climatologically larger in magnitude near the surface in RAS and extends deeper into the free troposphere – zero crossings in the respective model variants are ~ 300 and ~ 450 hPa. These features lead to the following hypothesis: because of deeper climatological convection in the Sahel and equatorial Africa in RAS, the additional water vapor generated by the SST warming is communicated over a greater tropospheric depth in RAS than in UW within convecting regions. This causes the increase in the mid-tropospheric MSE gradient in the Sahel to be greater in RAS, and therefore requires greater anomalous subsidence.

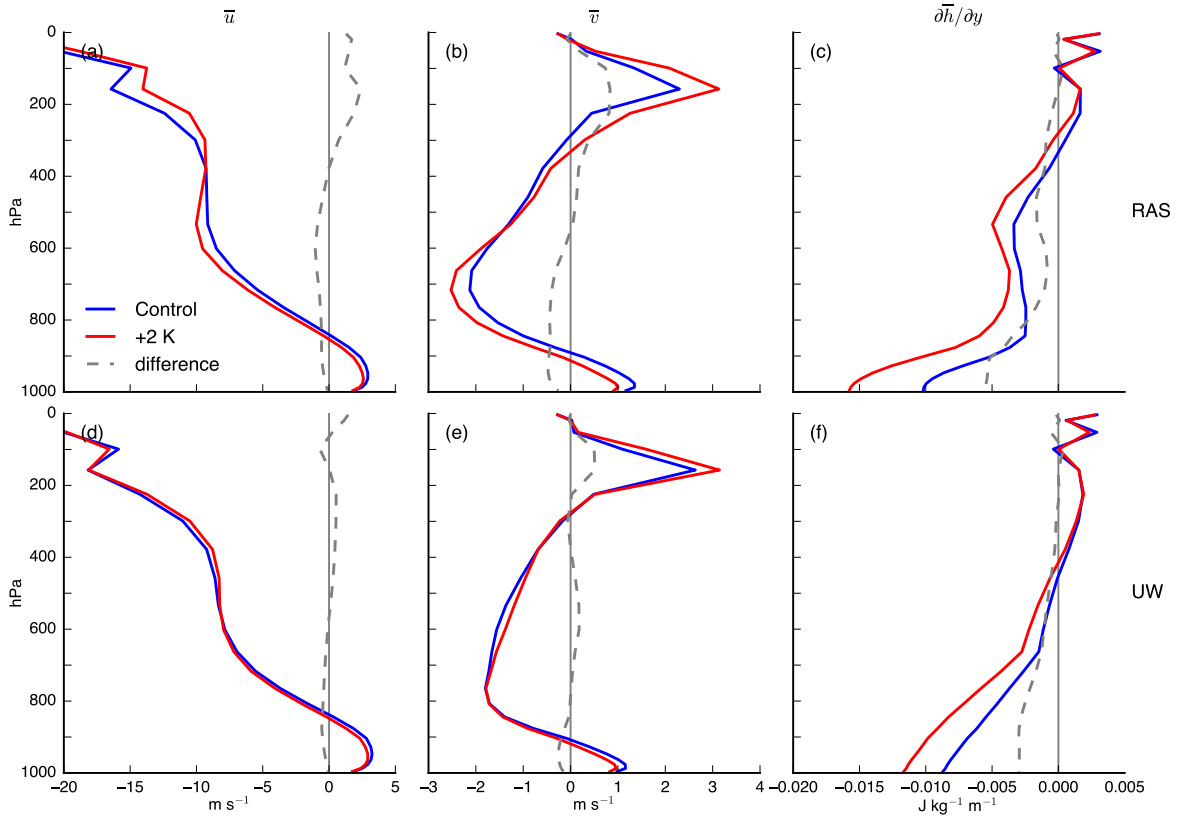


Figure 3.12: Sahel region-mean profiles of (left column, in m s^{-1}) zonal wind, (center column, in m s^{-1}) meridional wind, and (right column, in $\text{J kg}^{-1} \text{m}^{-1}$) meridional MSE gradient, in (top row) RAS and (bottom row) UW.

One complicating factor is the role of the net energetic source term, which responds

weakly in the free troposphere in RAS but not in UW [Figure 3.5(a,d)]. Figure 3.6(c) shows the anomalous vertical motion predicted by (3.1) applied to UW, for which it generally does a poor job, including excessive anomalous subsidence in the free troposphere. At these levels in UW, the net energetic source term largely balances the anomalous horizontal advection, thereby necessitating less sinking.

3.6 Disentangling control climate and convective processes

In convecting regions throughout the tropics, column water vapor increases less in UW than it does in RAS (Figure 3.11), and this does not scale with their climatological differences: averaged over the tropics (30°S - 30°N), column water vapor increases by 9.4 and $8.5\% \text{ K}^{-1}$ of imposed SST warming in RAS and UW, respectively (control simulation values are 35.4 and 34.1 kg m^{-2}). This is broadly consistent with the mechanism just presented in Section 3.5, given that ascent profiles in convecting regions are generally more top-heavy in RAS than in UW (not shown). However, this does not rule out a role of the convective processes themselves. For example, *Zhao* [2014] makes arguments of relevance regarding how entrainment will respond to warming in each scheme. In RAS, each plume's entrainment rate is computed inversely based on the plume's buoyancy and its specified cloud top height. To the extent that buoyancy increases with global warming [*Singh and O'Gorman*, 2013] this will lead to increased entrainment with warming, a drying influence – especially to the extent that this increase in buoyancy is concentrated in the upper troposphere [*Seeley and Romps*, 2015]. Conversely, in UW entrainment is proportional to convective depth. Given the general expectation for increased convective depths with warming [*Singh and O'Gorman*, 2012], this will reduce entrainment, a wettening influence. Given its relative dryness, changes in entrainment with warming would be especially influential in the Sahel.

To better separate the influences of the convective processes and the mean state, we perform additional uniform SST perturbation simulations in RAS and UW with magnitudes ± 2 ,

± 4 , ± 6 , ± 8 , and ± 10 K. In RAS, we also perform ± 0.25 , ± 0.5 , ± 1 , ± 1.5 , ± 3 K, and -15 K simulations. This generates a wide range of climates with each convective parameterization. If the precipitation varies similarly overall across the simulations with either convective parameterization, the large-scale climate state can be deemed the dominant factor. Conversely, if the precipitation response varies between RAS and UW appreciably over this range, the convective processes themselves are playing a central role. This systematic generation of a wide range of climate states is a common experimental design in idealized modeling contexts, including cloud resolving models, idealized moist GCMs [*O’Gorman and Schneider, 2008*], and GCM radiative-convective equilibrium simulations in various geometries [e.g. *Held et al., 2007; Merlis et al., 2016*]. Each simulations is 31 years, the first discarded as spin-up, and all fields are computed on model-native coordinates using monthly data without any MSE budget adjustments.

Figure 3.13 shows Sahel region-mean precipitation as a function of various other Sahel region-mean quantities in these wide SST range simulations in RAS, with each simulation’s color corresponding to the imposed SST perturbation. We restrict attention to those features directly relevant to the precipitation and MSE budget responses at present-day and warmer temperatures; future work will return to these simulations to consider some other interesting features, in particular why the Sahel hydrological response to SSTs tapers off sharply at roughly 1.5 K cooler and 1.5 K warmer than present-day.

Near present-day SSTs, Sahel precipitation varies linearly and rapidly with global mean SST and local surface temperature [Figure 3.13(a)], with an average rate of -1.1 mm day $^{-1}$ per K of imposed SST warming. Except for the very large magnitude SST simulations, evaporation scales linearly with precipitation (not shown), such that $P - E$ largely tracks P [Figure 3.13(b)]. Precipitation also varies linearly with the column-averaged relative humidity, which decreases almost monotonically and dramatically with SST over the full range of simulations (from 63 to 44%) [Figure 3.13(c)], and positively with column-averaged cloud fraction and omega [Figure 3.13(d) and (e)]. Given the precipitation response, all of these

relationships conform to basic physical expectations.

In terms of the MSE budget, precipitation varies monotonically with the average meridional MSE gradient (which becomes more negative with SST warming) [Figure 3.13(f)], column-integrated horizontal MSE advection (more positive with SST warming) [Figure 3.13(g)], and column-integrated vertical MSE advection (more negative with SST warming) [Figure 3.13(h)]. These relationships support the notion that precipitation in the Sahel is inhibited through interactions with the Sahara desert. In contrast, the region-mean net TOA radiation is non-monotonic both with precipitation and the imposed SST warming [Figure 3.13(i)]; the mechanisms behind this are discussed in Chapter 4.

For reasons still under investigation in UW, precipitation is non-monotonic with SST, decreasing with SST in the range -10 to -4 K and increasing with SST in all warmer simulations. In contrast, $P - E$ – like nearly all other fields – varies monotonically with SSTs over the full range of simulations. As such, the relationships between $P - E$ and other fields align much better with those of RAS and with physical expectations than if precipitation is used. As such Figure 3.14, which otherwise repeats Figure 3.13 for UW, uses $P - E$ as the vertical axis rather than precipitation. (Since, as mentioned, evaporation linearly scales with precipitation in RAS over nearly the entire range, the same substitution makes little difference in that model variant.)

Sahel $P - E$ in UW spans 0-1.3 mm day⁻¹ across all of the simulations, less than half of the 0-3.5 mm day⁻¹ range in RAS, but generally adheres to physical expectations: it decreases with the Sahel-Sahara MSE difference and with horizontal MSE advection, and it increases with vertical MSE advection, relative humidity, ascent, and cloud fraction. (Like RAS, the net energetic forcing behavior is less straightforward.) The curvature of several of the UW fields also loosely resembles that of the RAS control and warmer simulations, though in RAS these appear more as two distinct regimes (UW does not exhibit curvature akin to the cold simulation regime in RAS). These include surface temperature, the meridional MSE gradient, and horizontal MSE advection. The fields over which the range of variation differs

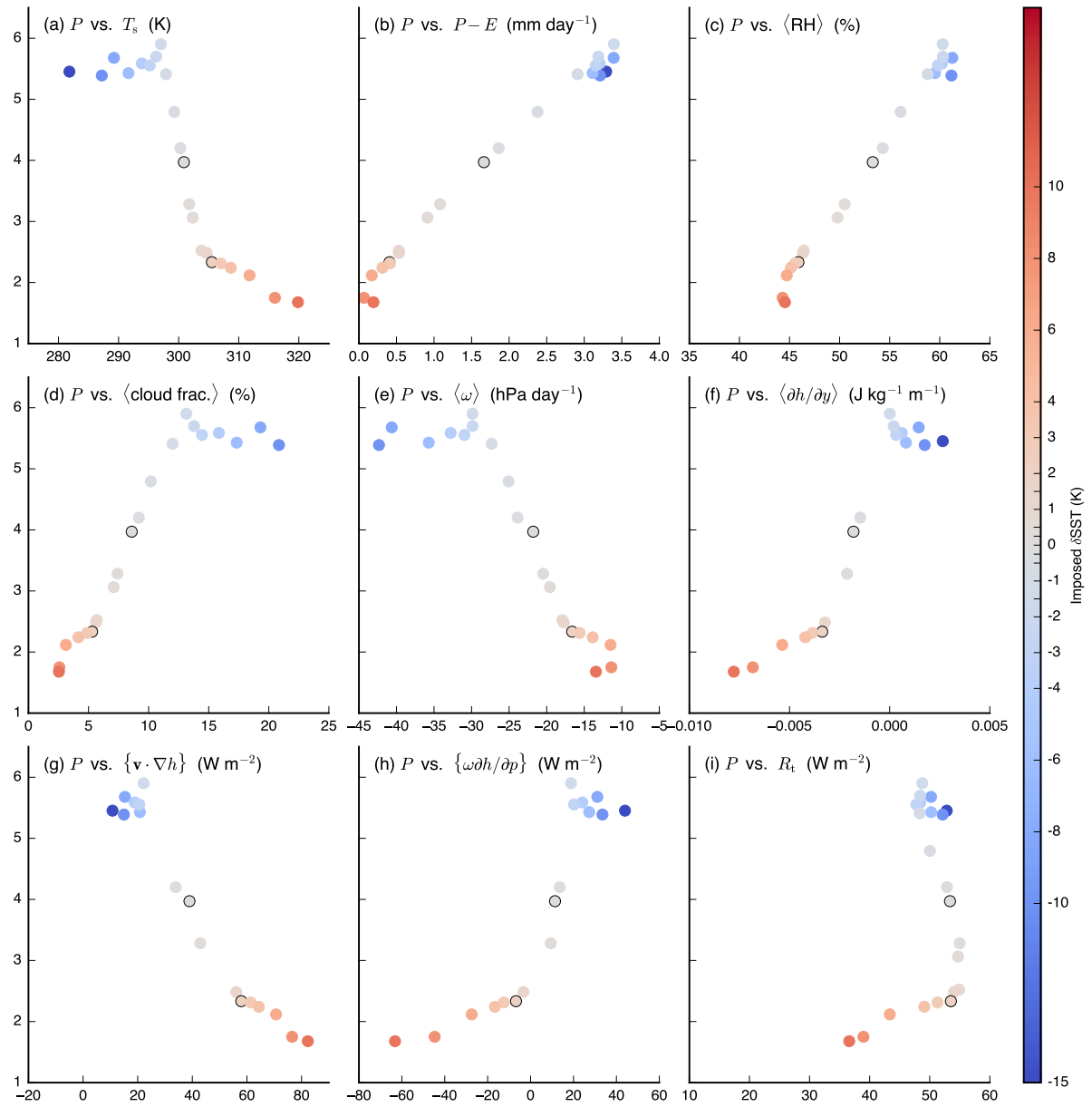


Figure 3.13: Sahel region-mean precipitation as a function of various other Sahel region-mean quantities in simulations in RAS over which the uniform SST perturbation is varied from -15 to $+10$ K. Each dot represents one simulation, with their color signifying the imposed SST perturbation according to the colorbar. The control and $+2$ K simulations are outlined in black for ease of reference. Precipitation is on the vertical axis in all panels, in mm day $^{-1}$. The quantity on the horizontal axis is printed at the top of the axis, along with its units. Angle brackets denote column averages, and curly brackets denote column integrals.

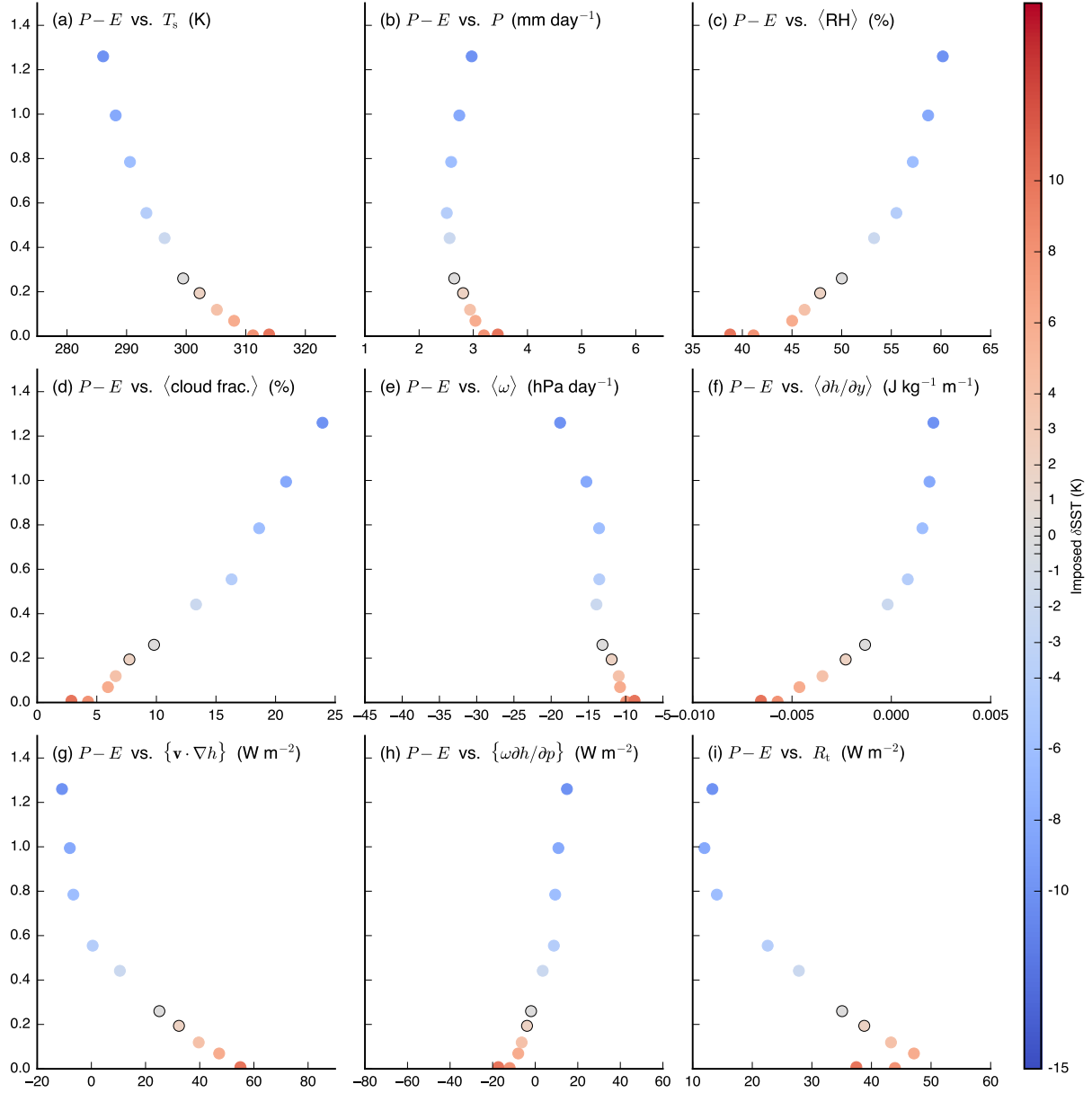


Figure 3.14: (Same as Figure 3.13, but for UW) $P - E$ in simulations in UW over which the uniform SST perturbation is varied from -10 to $+10$ K. Each dot represents one simulation, with their color signifying the imposed SST perturbation according to the colorbar. The control and $+2$ K simulations are outlined in black for ease of reference. $P - E$ is on the vertical axis in all panels, in mm day^{-1} . The quantity on the horizontal axis is printed at the top of the axis, along with its units. Angle brackets denote column averages, and curly brackets denote column integrals. The horizontal span of each panel is identical to the corresponding one in Figure 3.13.

most between RAS and UW are the vertical velocity and the vertical MSE advection: the latter ranges by over 100 W m^{-2} in RAS vs. less than 40 W m^{-2} in UW – but this is comparable to the difference in the range of $P - E$ variations.

All told, these wide SST range simulations indicate that the dominant influence on the Sahel with SST warming with either convective parameterization is the increased meridional moisture and MSE differences between the Sahel and the Sahara; acted upon by prevailing northerly flow this enhances the advection of dry air into the Sahel, thereby suppressing $P - E$. However, a given increase in horizontal dry advection generates greater anomalous descent and consequently anomalous MSE convergence by the divergent circulation in RAS than in UW. At least for the original control and $+2 \text{ K}$ simulation pair, we have already offered an explanation for this in terms of the horizontal advection in the mid-troposphere.

The major outstanding question, then, is why in UW precipitation increases over the range -4 to $+10 \text{ K}$ of simulations in the face of this extensive set of energetic and dynamical changes that would seem to promote drying, and why evaporation increases at an even faster rate with SSTs over this range, such that $P - E$ continues to decrease. As stated, for a semi-arid region, the expectation is for evaporation to scale with precipitation at some fractional rate, due to moisture limitations, which certainly occurs in RAS in the simulations with precipitation values spanning the same range of precipitation values in UW. This remains under investigation.

3.7 Discussion

More idealized simulations could aide in improving our understanding of these various processes and their interactions. In addition to an idealized GCM, a two-column, weak temperature gradient setting [c. f. *Shaevitz and Sobel, 2004*] with the subsidence column representing the Sahara Desert and the ascending column representing the Sahel, could comprise the optimal level of simplification. A conceptual two-box model could also prove useful.

Our results come to bear on some prior theoretical arguments. Despite the modest changes in moist static stability in our simulations, dry static stability does increase appreciably (not shown), and prior work has argued that increased upper tropospheric dry static stability with warming inhibits convection in the Sahel [Giannini, 2010]. We return to this in Chapter 5. While the correspondence in RAS between precipitation and the column relative humidity in the wide SST range simulations supports claims the latter is a dominant control on tropical precipitation [Raymond, 2000], in UW the opposite occurs. That drying and convective shallowing in RAS are accompanied by an increased magnitude (but negative) meridional MSE gradient is broadly consistent with the convective quasi-equilibrium perspective on monsoons, wherein overturning strength increases with this gradient. *Shaw and Voigt* [2015] find that, for both the monsoon seasonal progression in reanalysis data and the response to forcing in models, increases in the 925 hPa meridional equivalent potential temperature gradient are largely co-located with increases in ascent. In their analysis of the South Asian monsoon as simulated by CMIP5 models, *Boos and Hurley* [2013] demonstrate that the MSE difference between the monsoon region and the neighboring desert increases with warming, and that the modulation of that dry air advection (in their case by topography) strongly alters the monsoon circulation; these are consistent with our results.

One complicating factor regarding the wide SST simulations is that the wet season shifts later into the year as SSTs increase in both model variants (not shown). This is consistent with prior studies that indicate a robust delay in the Sahel rainy season onset in CMIP3 [Biasutti and Sobel, 2009; Seth *et al.*, 2010] and CMIP5 21st century simulations [Biasutti, 2013] and alterations by global warming to the annual cycles of tropical surface temperature and precipitation more generally [Dwyer *et al.*, 2012, 2014]. Nevertheless, repeating the analysis of the wide-SST range simulations with annual mean values does not alter the overall behavior (not shown). *Boos and Hurley* [2013] show that artificially truncating topography in South Asia, thereby enhancing low-MSE advection into the South Asian monsoon region, causes a delay in the monsoon annual cycle – consistent with our simulations in the sense

that horizontal low-MSE advection is enhanced and monsoon onset delayed with warming.

Although we have focused on the climatological convective depth, a few other differences between the two control climate states may also be important for the response to uniform SST warming. The expanse of large near-surface MSE values within the Sahel is larger magnitude, more widespread, and more continental in RAS than in UW. To the extent that prevailing MSE gradients are enhanced with warming [Boos and Hurley, 2013], this itself would lead to greater MSE increases in RAS than in UW. Another feature of potential relevance is the region of significantly negative \bar{F}_{net} in UW from the Gulf of Guinea coast to the Southern Sahel (local minima exceeding -70 W m^{-2}); in RAS there is also a negative patch but it is much smaller and smaller magnitude (Figure 3(a) and (b)). From the column MSE budget perspective, this region in UW is therefore highly unsuitable for convection, and so with warming convection in the Sahel is not drawn southward. In RAS, there is a strong dipole with precip and \bar{F}_{net} increasing in this region.

Numerous studies argue that warming of the Sahara Desert, by strengthening the Sahara Heat Low, increases the meridional pressure gradient from the Gulf of Guinea northward, thereby enhancing the monsoon flow into the Sahel [e.g. Biasutti *et al.*, 2009]. Such behavior, if it occurs, is not of central importance in these simulations. Although Saharan surface warming is modestly higher in UW than RAS, in both cases the anomalous boundary layer flow in the northern Sahel is northerly, opposite to the expectation if an anomalous heat low circulation centered in the Sahara Desert was dominant.

The character of the convection and MSE budget changes steadily in the meridional, and this complicates the interpretation of regional averages. Although averaged over the entire Sahel the meridional advection is a leading order term in the vertically integrated MSE and moisture budgets, within the more convective southern Sahel the canonical tropical convection zone balance exists between the source terms and the convergence. Conversely, in the north the convergence term is small and changes to the net energetic source/sink terms are balanced by horizontal advection. The $\{\bar{w}\partial_p\bar{h}\} = 0$ isoline is a convenient border sepa-

rating these regions. But the climatological precipitation distribution extends appreciably northward beyond this boundary, as do the reductions in precipitation with ocean warming, thereby limiting the utility of considering the northern and southern halves independently.

AM2.1's relatively coarse horizontal resolution likely prevents it from generating the mesoscale disturbances that in observations harbor the majority of time-mean Sahelian rainfall and also largely control decadal variability [Vellinga *et al.*, 2016]. At the same time, artificially suppressing transients does not appreciably alter the time-mean precipitation in one coarse AGCM [Cook, 1999]. From an impacts perspective, crop modeling suggests that the total rainy season rainfall, rather than any higher order statistics, drives changes to West African crop yields in the context of 21st century warming [Guan *et al.*, 2015].

Precipitation in GCMs that parameterize convection typically peaks at noon rather than in the early evening as observed, both in the Sahel [e. g. Marsham *et al.*, 2013] and elsewhere. This will affect the shortwave cloud radiative effect, since insolation is greatest near mid-day, shortwave reflection will be larger than if the convective clouds peaked in the evening. The smallness of the region-mean net energetic forcing response to 2 K SST warming in RAS relies in part on the cancellation between shortwave and longwave radiative responses, which could be influenced by this issue. We have not examined the diurnal cycle in our simulations.

3.8 Summary

Wet-season rainfall in the Sahel decreases by 40% in response to uniform 2 K SST warming in AM2.1 when the default, RAS convective parameterization is used but increases by 6% when the UW parameterization is used instead, a sensitivity we attempt to understand through the column-integrated MSE budget.

In both model variants, the present-day control simulation budget broadly comprises positive net energetic forcing balanced by horizontal advection of dry, low-MSE Saharan air into the northern Sahel and divergence of MSE by deep moist convection in the southern

Sahel, with additional region-mean MSE divergence from transient eddies. In RAS, the time-mean divergent circulation diverges MSE in the southern Sahel but converges MSE in the northern Sahel due to the convection shallowing moving northward, leading to a near-zero column mean MSE divergence through the divergent circulation. In UW, ascent is generally shallower, such that the divergent circulation converges MSE throughout the Sahel. Thus, in either case the region is far from the canonical tropical convecting zone balance between net energetic forcing and MSE divergence by the time-mean divergent circulation.

In RAS, the severe drying with SST warming is commensurate with strongly enhanced MSE divergence by horizontal advection and a shallowing of the convection. This leads to an expression for the anomalous vertical motion in the free troposphere in terms of the climatological moist static stability and the change in the meridional gradient of MSE. Changes in the MSE gradient are especially important in the mid-troposphere, where the moist static stability is small and therefore ascent must respond strongly to balance a given horizontal MSE advection anomaly. In UW, the horizontal MSE gradient is not enhanced as much in the mid-troposphere, as part of its overall weaker MSE budget response. Column water vapor increases throughout the deep tropics with 2 K SST warming at a higher rate in RAS than in UW, which contributes to the discrepancy in the meridional MSE gradient responses.

Varying SSTs over a wide range with either convective parameterization yields consistent energetic and $P - E$ responses but differing precipitation responses: the drying influences of the Sahara desert are steadily enhanced with warming, but in terms of precipitation in UW this is apparently overcome by the broader wettening influences in climatological convecting regions that accompany SST warming.

Acknowledgments

We thank Leo Donner for scientific guidance, Spencer Clark for guidance on computational procedures and Lucas Harris for guidance on numerical techniques and model conservation

properties. S.A.H. acknowledges discussions with other attendees of the “Monsoons: Past, Present and Future” workshop sponsored by the Ronald and Maxine Linde Center for Global Environmental Science in May 2015 that informed this work. S.A.H. was supported by a Department of Defense National Defense Science and Engineering Graduate Fellowship.

3.A Adjustment method for correcting imbalances in column tracer budgets

3.A.1 Motivation

The interpolation of GCM and reanalysis data from their model-native coordinates to regular latitude-longitude grids and/or pressure levels generates spurious imbalances in the budgets of mass and other conserved tracers [Trenberth, 1991]. This is especially true over land, where topography induces sharp gradients of surface pressure. As a result, commonly used finite-differencing methods for the derivatives in the flux divergence terms can yield residuals $>100 \text{ W m}^{-2}$ at individual grid points in the column MSE budget. Here we present a post-hoc adjustment method that rectifies these imbalances. It is effectively an extension of the dry mass budget adjustment method introduced by Trenberth [1991] and is similar to that of Peters *et al.* [2008]. Kidson and Newell [1977] also present a similar method for column mass using analysis data.

3.A.2 Adjustment procedure

Neglecting diffusion, the column-integrated budget of a conserved tracer, m , comprises time-tendency, flux divergence, and source terms:

$$\frac{\partial\{m\}}{\partial t} + \nabla \cdot \{m\mathbf{v}\} = S, \quad (3.2)$$

where curly brackets denote a mass-weighted column integral ($\{\}$) = $\int_0^{p_s} dp/g$, where p_s is surface pressure), S is the column-integrated source minus sink, and \mathbf{v} is the true horizontal wind such that this equality holds exactly. Using model-postprocessed data introduces a nonzero residual, R :

$$\frac{\partial \{m\}}{\partial t} + \nabla \cdot \{m \mathbf{v}_{\text{raw}}\} = S + R, \quad (3.3)$$

where \mathbf{u}_{raw} is the unadjusted horizontal wind, which we have assumed is the source of all error (rather than the time tendency or source terms). Let \mathbf{u}_{adj} be the adjustment applied to the wind, signed such that

$$\mathbf{v} = \mathbf{v}_{\text{raw}} - \mathbf{v}_{\text{adj}}, \quad (3.4)$$

Combining (3.3) and (3.4) yields

$$\nabla \cdot \{m \mathbf{v}_{\text{adj}}\} = R. \quad (3.5)$$

We assume that the adjustment is barotropic, such that it can be pulled out of the column integral. We also assume that the adjustment field is irrotational. This results in a system of two equations,

$$\begin{aligned} \nabla \cdot (\{m\} \mathbf{v}_{\text{adj}}) &= R \\ \nabla \times (\{m\} \mathbf{u}_{\text{adj}}) &= 0, \end{aligned} \quad (3.6)$$

which can be solved (e.g. using spherical harmonics) for the zonal and meridional components of the quantity $\{m\} \mathbf{u}_{\text{adj}}$. By subsequently dividing by $\{m\}$ to get \mathbf{v}_{adj} and, finally, using (3.4), we arrive at the adjusted wind \mathbf{v} that exactly satisfies the column budget expression (3.2).

3.A.3 Caveats

Importantly, this procedure will generate a horizontal wind field that yields closure of the specified source and time-tendency terms, whether or not such closure is physically justified. Most poignantly, if this were applied to the MSE budget using monthly-mean data, then the resulting adjusted monthly-mean circulation would exactly balance the energy storage and

net energetic forcing terms, with the likely false implication that transient eddies have no contribution.

While the resulting adjusted wind field is defined at each vertical level, the adjustment itself is barotropic and based on column-integrated terms, and closure is ensured only in the column-integral – not at each individual level.

3.B Computational procedure used for each term in the moist static energy budget

3.B.1 Column-integrated moist static energy flux divergence at each timestep

We apply two consecutive adjustments, first correcting column total mass (dry air plus water vapor), and then column energy. The column mass adjustment is based on the expression

$$\frac{\partial p_s}{\partial t} + \nabla \cdot \int_0^{p_s} \mathbf{u} dp = g(E - P). \quad (3.7)$$

This corrects for column mass imbalances exactly and largely ameliorates column energy imbalances. We then repeat this procedure, starting with these mass-adjusted winds, applied to the column MSE budget

$$\frac{\partial}{\partial t} \{\mathcal{E}\} + \nabla \cdot \{h\mathbf{u}\} = F_{\text{net}}, \quad (3.8)$$

with symbols all defined as in the main text. We apply this two-step adjustment to the horizontal wind field at each timestep of the post-processed model data. The column MSE flux divergence is then computed by forming the MSE fluxes ($h\mathbf{u}$), integrating them over the entire column ($\{h\mathbf{u}\}$), and then again using spherical harmonics to compute the divergence of the column integrals ($\nabla \cdot \{h\mathbf{u}\}$). This procedure yields the column-integrated MSE flux divergence in nearly exact balance with the column net energetic forcing and time-tendency at each 3 hourly timestep.

3.B.2 Partitioning total flux divergence into eddy and time-mean components

From this 3-hourly adjusted column flux divergence field, we separate the eddy and time-mean components as standard. Namely, the adjusted winds and all other original fields are averaged within each month, and the column flux divergence is re-computed using these fields to get $\nabla \cdot \{\bar{h} \bar{\mathbf{u}}\}$. The eddy component is then computed by subtracting the time-mean field from the full field: $\nabla \cdot \{\bar{h}' \bar{\mathbf{u}}'\} = \nabla \cdot \{\bar{h} \bar{\mathbf{u}}\} - \nabla \cdot \{\bar{h} \bar{\mathbf{u}}\}$.

3.B.3 Partitioning time-mean advection into horizontal and vertical components

We partition the total time-mean column flux divergence into horizontal and vertical advection components by 1) explicitly computing the horizontal advection at each level, 2) column-integrating, and 3) subtracting that integral from the time-mean to get the vertical advection as a residual. The level-by-level horizontal advection computation uses the time-series of adjusted, monthly-mean horizontal winds and second-order, upwind finite-differencing. Because the data is on the model-native hybrid pressure-sigma coordinates [Simmons and Burridge, 1981] while the budget equations require horizontal gradients on constant pressure surfaces, additional terms are required [Peters *et al.*, 2008]:

$$\nabla_p \bar{h} = \nabla_\eta \bar{h} + \frac{\partial \bar{h}}{\partial \eta} \nabla_p \eta = \nabla_\eta \bar{h} - \frac{\partial \bar{h}}{\partial \eta} \frac{b}{a' + b' \bar{p}_s \nabla_\eta \bar{p}_s}, \quad (3.9)$$

where the hybrid sigma-pressure model coordinates η are terrain-following near the surface and transition to constant pressure surfaces near the model top: $p(\eta, p_s) = a(\eta) + b(\eta)p_s$, where a and b do not vary horizontally or in time, $a' \equiv da/d\eta$, and $b' \equiv db/d\eta$ [Table 2 of *GFDL Atmospheric Model Development Team*, 2004].

3.B.4 Vertical advection at individual vertical levels

In order to examine the vertical profile of the budget terms, we also compute the time-mean vertical advection explicitly at each level using 2nd order upwind finite differencing. These are the quantities shown in all profile plots of time-mean advection. The sum of the two explicitly computed advection terms, column-integrated, exhibits a region-mean residual of $\sim 10 \text{ W m}^{-2}$ compared to the total time-mean flux divergence. But the overall character and spatial patterns of the column vertical advection is similar between the two methods.

This is why the total region-mean change differs modestly between the previously quoted value and the sum of the three response decomposition terms (-15.9 and -18.8 W m^{-2} , respectively). Similarly, to compute the decomposition terms only, for expediency the horizontal advection is computed using monthly averaged data, unadjusted. The results appear qualitatively insensitive to this choice.

3.B.5 Time tendency and source terms

Time tendencies are computed by first integrating the tracer over the column and then applying 2nd order centered finite differencing at each timestep. The source terms are outputted directly by the model and require no subsequent manipulation.

Chapter 4

Towards emergent constraints on Sahel rainfall

Abstract

Theoretical arguments and simulations in the NOAA Geophysical Fluid Dynamics Laboratory (GFDL) AM2.1 atmospheric general circulation model (AGCM) presented in Chapter 3 suggest that uniform SST warming causes increased advection of dry Sahara Desert air into the Sahel region of Africa, but the magnitude of this response and therefore whether it ultimately causes reduced Sahelian precipitation is sensitive to the convective parameterization. Chapter 3 further speculates on potential links between the dry advection response and properties of the regional column moist static energy (MSE) budget in the control simulation, which if verified would constitute the starting point toward an emergent observational constraint on the future behavior. We analyze uniform SST warming simulations performed in seven GFDL AGCM variants and in ten AGCMs performed as part of Phase 5 of the Coupled Model Intercomparison Project (CMIP5) in order to assess these theoretical and modeling aspects of generating an emergent observational constraint. We subsequently address several issues regarding the observational facet of developing an emergent constraint for forced Sahel rainfall changes.

Rainfall in the Sahel decreases with SST warming in 14 of the 17 models analyzed. In all 17 models, dry air advection into the Sahel is enhanced through an enhanced meridional MSE gradient, balanced energetically in part by anomalous subsidence. These results support the

notion that mean ocean warming acts to dry the Sahel through interactions with the Sahara Desert, although in a small minority of models this is overcome by the overall wettening influences of global warming on existing convecting regions.

Despite this qualitative consistency, given the sample sizes and considerations of model dependence, no unambiguously statistically significant correlations are identified between the precipitation response and any fields from the control simulations. Difficulties arise also on the observational side of developing an emergent constraint as satellite-based measures give different impressions of model credibility depending on the field examined. On the other hand, reanalyses suggest that relatively top-heavy ascent profiles that strongly drying models tend to exhibit are outside the observational range, and observations of precipitation and cloud radiative properties suggests that in AM2.1 an excessive positive cloud radiative feedback on precipitation changes is excessive.

4.1 Introduction

The simulations presented in Chapter 3 of uniform 2 K SST warming in the NOAA Geophysical Fluid Dynamics Laboratory (GFDL) AM2.1 atmospheric general circulation model (AGCM) using either the default, Relaxed Arakawa Schubert (RAS) convective parameterization or the University of Washington (UW) parameterization implicate an enhanced meridional MSE gradient spanning from central Africa to the Sahara desert as a key drying influence in the Sahel. This gradient is enhanced more with RAS than with UW, which Chapter 3 hypothesizes partly stems from deeper climatological convection in RAS being more effective at spreading the increased near-surface water vapor into the mid troposphere where the convection is especially sensitive to dry advection. However, precipitation responses to SST warming remain opposite-signed with RAS compared to with UW over a wide range of control SSTs and circulation characteristics, implying a direct role for convective processes themselves.

What are the hydrological and MSE budget responses in the Sahel in other models, and how do these relate to their respective control simulations? Pragmatically, this is aided by the availability of control and +2 K simulations performed in numerous other GFDL models. However, models from the same modeling institution typically share many components and are thus not truly independent [Masson and Knutti, 2011; Knutti *et al.*, 2013; Caldwell *et al.*, 2014], and it is therefore necessary to extend to non-GFDL AGCMs. The prescribed SST simulations performed as part of the Coupled Model Intercomparison Project 5th Phase (CMIP5) [Taylor *et al.*, 2012], which include present-day control and uniform 4 K SST warming simulations, are a natural resource in this regard.

Supposing links between the climatological fields and the response to uniform warming can be identified across models, it would mark the starting point toward an emergent observational constraint [e. g. Hall and Qu, 2006], i. e. an observable present-day quantity that correlates well across models with their responses to a perturbation (in this case, uniform SST warming). The next step would be to characterize Earth’s present-day circulation in the Sahel in order to compare to the model’s control values. But based on the demonstrated sensitivity in Chapter 3 of at least one model to its convective parameterization, the reliance of reanalyses products on a numerical model and convective parameterization is a cause for concern. Satellite observations of TOA radiative fluxes, which constitute for land regions the net column net energetic forcing term, are therefore a potentially attractive alternative for model comparison.

This chapter addresses these issues by extending the analyses from Chapter 3 to other GFDL and CMIP5 models and comparing them to observational and reanalysis data. After describing the GFDL and CMIP5 models and simulations and other methodological details (Section 4.2), we describe the results of uniform SST warming simulations in the GFDL and CMIP5 models (Section 4.3). Several aspects of the Sahel response to uniform warming are robust across the simulations and consistent with the overall dynamical and energetic arguments presented in Chapter 3: an enhanced meridional MSE gradient, anomalous subsi-

dence, and (except for AM2.1) reduced net energetic forcing. These lead to reduced rainfall in the Sahel in 4 of 7 GFDL AGCMs and 10 of 10 CMIP5 AGCMs analyzed. However, quantitative differences among the model responses, particularly for the CMIP5 ensemble, are sufficiently large that no statistically significant correlations are found between control simulation fields and the precipitation response to uniform SST warming.

Anticipating future refinements to these modeling and theoretical aspects of developing an emergent constraint, we also address the observational facet by examining in-situ, reanalysis, and satellite-based observational data for comparison with the model results (Section 4.4). Ascent profiles in reanalyses are generally bottom-heavy, while models with top-heavy ascent profiles are generally among those that dry the most with warming. Satellite-based measures are imperfect as emergent constraints due to the correlations between present-day Sahel TOA radiative fields and precipitation responses to SST warming being modest. We discuss the implications of these results for future research directions and the sources of spread among coupled models in Sahel rainfall in 21st century simulations (Section 4.5) and conclude with a final summary (Section 4.6).

4.2 Methodology

4.2.1 GFDL models and simulations

We examine present-day control and uniform 2 K simulations in the seven GFDL model variants listed in Table 4.1. AM2.1 is as described in Chapters 2 and 3; briefly, it features a finite-volume, ~ 200 km resolution, latitude-longitude dynamical core, 24 vertical levels extending to 10 hPa, the RAS convection scheme [Arakawa and Schubert, 1974; Moorthi and Suarez, 1992], prescribed monthly aerosol burdens, and the LM2 land model [Milly and Shmakin, 2002]. Both the standard AM2.1 and the variant from Chapter 3 that replaces RAS with the University of Washington convective parameterization [Bretherton *et al.*, 2004] are included in this chapter; they are referred to respectively as AM2.1 and AM2.1-UW for the

remainder of the thesis. AM3 [Donner *et al.*, 2011] features a finite-volume, \sim 200 km cubed-sphere dynamical core, 48 vertical levels extending to 1 hPa, the Donner deep [Donner, 1993; Donner *et al.*, 2001] and UW shallow [Bretherton *et al.*, 2004] convective parameterizations, comprehensive atmospheric chemistry, online interactive aerosols, a cloud microphysical parameterization that depends on aerosol burdens for stratiform clouds [Ming *et al.*, 2006, 2007], and the LM3 land model [Shevliakova *et al.*, 2009; Donner *et al.*, 2011]. HiRAM [Zhao *et al.*, 2009] features the same dynamical core as AM3 but with \sim 50 km horizontal resolution, 32 vertical levels extending to 10 hPa, the UW convection scheme for both deep and shallow convection (though with much convection treated at the grid scale), a relatively simple diagnostic cloud fraction scheme, the LM3 land model, and all other settings taken from AM2.1. Essentially, AM3 was developed from AM2.1 by increasing physical complexity but not resolution, and HiRAM was developed from AM2.1 by increasing resolution but not physical complexity.

The remaining three GFDL AGCMs are alternate-resolution versions of AM2.1, AM3, and HiRAM. AM2.5 [Delworth *et al.*, 2011] is essentially a \sim 50 km resolution version of AM2.1, but using the cubed-sphere dynamical core, 32 vertical levels, the LM3 land model, and some modest re-tuning. c90-AM3 is identical to AM3 other than roughly doubled horizontal resolution; the “c90” notation signifies that each of the six faces comprising the model’s cubed-sphere grid consists of 90×90 grid cells. The standard AM3 resolution is c48. c48-HiRAM [Zhao, 2014] is a \sim 200 km resolution version of HiRAM (whose resolution is c180), with a reduction in the land-ocean entrainment parameter ratio as described in Zhao *et al.* [2009] and in Chapter 3 for AM2.1-UW. In postprocessing, data for c90-AM3 was horizontally interpolated to the same \sim 200 km grid as AM2.1, AM3, and c48-HiRAM; the interpolation for AM2.5 and HiRAM retains their near-native resolution.¹

Each model has a pair of control and +2 K simulations that follow the same experimental

¹These discrepancies in interpolation procedure across the models is an artifact of the simulations being performed at different times by groups with different model execution procedures. Ideally, one would re-do the postprocessing for each simulation in order to interpolate all simulations to a common grid.

Table 4.1: GFDL AGCMs used in this study. Columns, from left to right: model name; publication that documents the model; observational SST dataset and year range used to create the climatological annual cycle of SSTs; length of simulation, in years. Top level value, if given, indicates topmost pressures to which the data was interpolated in addition to the standard levels shared by all models: 1000, 925, 850, 700, 600, 500, 400, 300, 250, 200, 150, 100, 70, 50, 30, 20, and 10 hPa. High-top models also include an additional 775 hPa tropospheric level; the other additional levels are 7, 5, 3, 2, and 1 hPa.

Model	Reference	SST data	Duration	Top
AM2.1	<i>GFDL Atmospheric Model Development Team</i> [2004]	<i>Reynolds et al.</i> [2002], 1981-1999	30	
AM2.1-UW	This thesis, Chapter 3		30	
AM2.5	<i>Delworth et al.</i> [2011]		20	1
AM3	<i>Donner et al.</i> [2011]	<i>Hurrell et al.</i> [2008], 1981-2000	30	1
c90-AM3	None		10	1
HiRAM	<i>Zhao et al.</i> [2009]	<i>Rayner et al.</i> [2003], 1981-2005	17	
c48-HiRAM	<i>Zhao</i> [2014]		15	

design as described in Chapter 3, although among models there are differences in their duration and the underlying SST dataset and averaging period across the models (Table 4.1).² We have tested the sensitivity to these differences by repeating the control and +2 K simulations in AM2.1 with each SST fields used by other models. The Sahel precipitation responses are similar in each case, and we assume this holds for the other models.

4.2.2 CMIP5 models and simulations

We examine the “amip” and “amip4K” CMIP5 experiments in ten AGCMs for which the necessary data is available in the GFDL local repository of CMIP5 data (Table 4.2). These simulations use a timeseries of observed SSTs from the *Hurrell et al.* [2008] dataset spanning 1979-2008. Atmospheric composition is also time-varying, with the same inputs as in the

²For expediency, in HiRAM we use an available +2.04 K (rather than exactly 2 K) SST perturbation simulation. In AM3, aerosol emissions (rather than burdens) are prescribed at near-present-day climatological values, due to that model’s online treatment of aerosols.

coupled “historical” CMIP5 simulation.³ In the +4 K simulation, 4 K is added uniformly to this timeseries of SSTs.

We do not expect the fact that SSTs and atmospheric composition are time-varying for the CMIP5 models to appreciably alter their response to imposed SST warming compared to the GFDL models. Of greater concern is the 2 vs. 4 K SST warming magnitude. We present the responses per K imposed warming to mitigate this difference, but the nonlinear response of Sahel rainfall to the imposed SST shown in Chapter 3 for AM2.1 and AM2.1-UW imply that this is an imperfect solution. Comparison of the GFDL and CMIP5 model results should be undertaken with this caveat in mind.

Table 4.2: CMIP5 AGCMs used in this study. Columns, from left to right: model name, modeling institution, horizontal resolution of output data analyzed, and topmost pressure level to which data was interpolated. Resolution refers to the data in the CMIP5 archive in the Tropics, which is not necessarily the same as the model’s native horizontal resolution. Top level value, if given, indicates topmost pressures to which the data was interpolated in addition to the standard levels shared by all models: 1000, 925, 850, 700, 600, 500, 400, 300, 250, 200, 150, 100, 70, 50, 30, 20, and 10 hPa. The additional levels are 7, 5, 3, 2, 1, 0.4, 0.2, and 0.1 hPa.

Model	Institution	Resolution	Top
BCC-CSM1	Beijing Climate Center	$2.8^\circ \times 2.8^\circ$	
CNRM-CM5	Centre National de Recherches Meteorologiques	$1.4^\circ \times 1.4^\circ$	
FGOALS-G2	Institute of Atmospheric Physics, Chinese Academy of Sciences	$2.8^\circ \times 2.8^\circ$	
IPSL-CM5A-LR	Institut Pierre-Simon Laplace	$1.9^\circ \times 3.75^\circ$	
IPSL-CM5B-LR	Institut Pierre-Simon Laplace	$1.9^\circ \times 3.75^\circ$	
MIROC5	Agency for Marine-Earth Science and Technology	$1.4^\circ \times 1.4^\circ$	
MPI-ESM-LR	Max Planck Institute for Meteorology	$1.9^\circ \times 1.9^\circ$	0.1
MPI-ESM-MR	Max Planck Institute for Meteorology	$1.9^\circ \times 1.9^\circ$	0.1
MRI-CGCM3	Meteorological Research Institute	$1.2^\circ \times 1.1^\circ$	0.4
NCAR-CCSM4	National Corporation for Atmospheric Research	$0.9^\circ \times 1.25^\circ$	

³BCC-CSM1 and NCAR-CCSM4 are among the CMIP5 models identified by *Zhou et al. [2015]* as exhibiting an erroneous zonal oscillation in the TOA downwelling shortwave radiation. This does not affect the Sahel rainfall climatologies or responses in any immediately identifiable way.

4.2.3 MSE budget computations

The available CMIP5 data comprises timeseries of pressure-interpolated, monthly averages and lacks the specific mass of ice water and geopotential height. Therefore, we use non-frozen MSE, $h \equiv c_p T + gz + L_v q$ as the energy tracer, with geopotential height computed from the temperature and specific humidity fields using the hypsometric equation, accounting for virtual temperature effects. To facilitate comparison between the GFDL and CMIP5 ensembles, we use the same computations and monthly, pressure-interpolated data for the GFDL models also. Comparison in AM2.1 of the budget quantities computed using the adjusted, high frequency data on model-native coordinates and the solid ice component as in Chapter 3 versus the more approximate method here indicate qualitative insensitivity to these differences, but quantitative differences are not negligible.

4.2.4 Model independence and statistical implications

Unlike other portions of this thesis, wherein identifying physical mechanisms underlying model responses is of greater concern than their statistical properties, statistical significance is centrally important in attempts to identify predictive relationships across models regarding the Sahel rainfall response. Of the seven GFDL models analyzed, three are pairs that differ primarily only in horizontal resolution (AM2.1 and AM2.5, AM3 and c90-AM3, HiRAM and c48-HiRAM), two are identical except for the convective parameterization (AM2.1 and AM2.1-UW), and of the three “base” models (AM2.1, AM3 and HiRAM), AM3 and HiRAM were developed directly from AM2.1. In our subjective judgment, this warrants reducing the effective degrees of freedom by two. Of the ten CMIP5 models, two pairs of models come from the same institution (Institut Pierre-Simon Laplace and Max Planck Institute), and we therefore choose to reduce the degrees of freedom by two.

For the computation of correlations across models (which start at two less degrees of freedom than the number of samples), this leaves three degrees of freedom for the GFDL

ensemble, six degrees of freedom for the CMIP5 ensemble, and eleven degrees of freedom for the combined GFDL and CMIP5 ensemble. With these effective sample sizes, for correlations to be significant at the $p = 0.05$ level requires correlation coefficient values of 0.878, 0.707, and 0.553 for the GFDL, CMIP5, and combined ensembles, respectively (using a two-sided test).

4.2.5 Region definition

As in Chapter 3, we analyze the Sahel wet-season of July-August-September and define the Sahel region as 10-20°N, 18°W-40°E. This extends slightly into the Atlantic Ocean and the Red Sea. While we employ each model's native land mask to exclude these bodies of water, results are insensitive to whether or not the land mask is applied (not shown). As such, no land mask is used for the observational data. The observational data we use is described in Section 4.4.

4.3 GFDL and CMIP5 model results

4.3.1 Overall hydrological responses

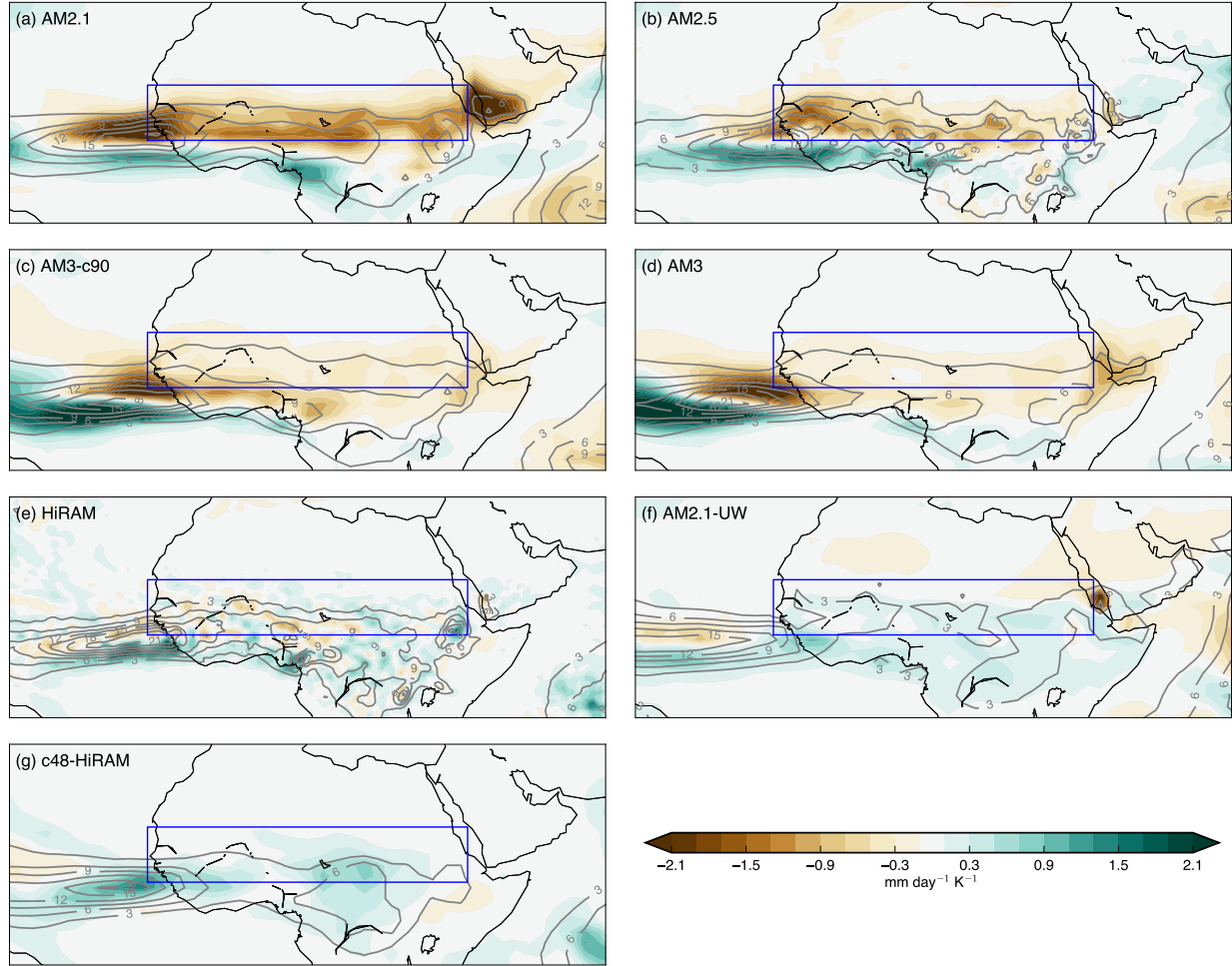


Figure 4.1: (Shaded contours) difference in precipitation per unit SST warming between simulation with uniform 2 K SST warming and present-day control simulation, units $\text{mm day}^{-1} \text{K}^{-1}$, and (grey contours) precipitation in the control simulation, with contours starting at 3 mm day^{-1} and with a 3 mm day^{-1} interval, in each of the seven GFDL models. The models are ordered (a) to (g) based on their precipitation response from most negative (AM2.1) to most positive (c48-HiRAM).

Figure 4.1 shows the precipitation response to 2 K SST warming in the GFDL models. The responses span a wide range, including severe drying (AM2.1), moderate drying (AM2.5, c90-AM3, and AM3), little response (HiRAM), modest wettening (AM2.1-UW), and moderate wettening (c48-HiRAM). On average, precipitation is reduced by $0.2 \text{ mm day}^{-1} \text{ K}^{-1}$, or $6\% \text{ K}^{-1}$, from 3.4 mm day^{-1} in the control. In the four models with region-mean drying, the precipitation reductions span the whole width of the Sahel and are larger in the south where rainfall is also climatologically greater. The rainfall response of HiRAM is muted throughout the region. Precipitation increases fairly uniformly over the southern Sahel in AM2.1-UW, while for c48-HiRAM the increases are zonally concentrated in the central Sahel, coinciding with greater climatological precipitation values in that location. Robust across all models is increased precipitation along the southern flank of the Atlantic ITCZ.

Table 4.3 lists the Sahel region-mean P and $P - E$ in the GFDL model control simulations and their response to 2 K SST warming. Relative to precipitation, the evaporation responses are more modest, from -0.2 to $+0.1 \text{ mm day}^{-1} \text{ K}^{-1}$ (not shown), leading each model's $P - E$ response to largely track its P response [Roderick *et al.*, 2014], excepting AM2.1-UW. In each higher resolution model variant, control simulation rainfall in the Sahel is greater than the lower resolution counterpart, but there is no clear relationship between model resolution and the precipitation response to SST warming.⁴

Figure 4.2 shows the precipitation responses to 4 K SST warming in the CMIP5 models. In all ten CMIP5 models, precipitation decreases in the Sahel, ranging from -0.1 (IPSL-CM5A-LR) to $-0.3 \text{ mm day}^{-1} \text{ K}^{-1}$ (CNRM-CM5). Except for MRI-CGCM3, all CMIP5 models also exhibit the increased precipitation with SST warming along the southern flank of the Atlantic ITCZ discussed previously for the GFDL models. Also consistent with the GFDL models, precipitation reductions within the Sahel tend to be predominantly in the south, with NCAR-CCSM4 as an exception.

⁴All nine members of the c48-HiRAM perturbed physics ensemble presented in Zhao [2014] are drier in the control (2.4 to 3.3 mm day^{-1}) and wetter the region more ($+5$ to $+22\%$) than HiRAM (not shown).

Table 4.3: Sahel region-mean precipitation (P) and precipitation minus evaporation ($P - E$) in the GFDL model control simulations and their response in the +2 K simulations, in mm day^{-1} . Fractional precipitation change is also listed, in percent. \pm values for the control fields denote one standard deviation. Note these are not normalized by the imposed SST magnitude.

Model	P	δP	$(\delta P)/P$	$P - E$	$\delta(P - E)$
AM2.1	4.0 ± 0.7	-1.6	-40%	1.7 ± 0.6	-1.3
AM2.5	4.6 ± 0.4	-1.0	-21%	2.0 ± 0.3	-0.8
c90-AM3	3.5 ± 0.4	-0.6	-17%	0.8 ± 0.3	-0.5
AM3	2.8 ± 0.4	-0.4	-15%	0.5 ± 0.3	-0.2
HiRAM	3.9 ± 0.2	+0.0	+0%	1.8 ± 0.2	-0.0
AM2.1-UW	2.7 ± 0.1	+0.2	+6%	0.3 ± 0.1	-0.1
c48-HiRAM	2.5 ± 0.4	+0.4	+15%	0.9 ± 0.2	+0.2

One curious precipitation feature that occurs in the control simulations in a majority of GFDL and CMIP5 models is a local maximum over the Red Sea or just to the east; these include AM2.1, AM2.5, CNRM-CM5, AM3, HiRAM, AM2.1-UW, CNRM-CM5, FGOALS-G2, MPI-ESM-MR, MIROC5, MPI-ESM-LR, and NCAR-CCSM4. In observations, there is no distinct local maximum in precipitation over the Red Sea in observations, although in some datasets the local maximum over the Ethiopian Highlands extends somewhat over the Red Sea (e.g. Figure 1 of *Cook* [1997] or Figure 4 of *Maidment et al.* [2014]). NCAR-CCSM4 has the largest bias in this region (in another idiosyncrasy, it also shows no orographic precipitation over the Ethiopian Highlands). In addition, in all of these models, precipitation decreases sharply with warming over this spurious local maximum. We have not determined the reasons behind this feature or whether it plays any meaningful role in the broader regional response to warming.

Unlike the GFDL models, the precipitation response does not scale with its climatological value. The control simulation region-mean precipitation varies over a wider range in the CMIP5 models than in the GFDL models. BCC-CSM1-1, IPSL-CM5B-LR, MRI-CGCM3, and FGOALS-G2, (1.0, 1.4, 1.6, and 2.0 mm day^{-1} , respectively) have less region-mean precipitation than the driest GFDL model (c48-HiRAM, 2.5 mm day^{-1}), while CNRM-CM5 and MIROC5 (4.8 and 5.5 mm day^{-1} , respectively) have more precipitation than the wettest

GFDL model (AM2.5, 4.6 mm day⁻¹). Of the two pairs of models from the same institutions, the Max Planck Institute models are very similar in both climatology and response to SST warming, whereas the IPSL-CM5A-LR and IPSL-CM5B-LR responses differ appreciably.

Table 4.4: CMIP5 AGCM responses to 4 K SST warming. Note that these are not normalized by the imposed SST change.

Model	<i>P</i>	δP	$(\delta P)/P$
CNRM-CM5	4.8	-1.1	-24%
FGOALS-G2	2.1	-1.0	-49%
MPI-ESM-MR	2.9	-0.9	-30%
MIROC5	5.4	-0.9	-16%
MRI-CGCM3	1.6	-0.8	-50%
MPI-ESM-LR	2.7	-0.7	-26%
IPSL-CM5B-LR	1.4	-0.6	-44%
NCAR-CCSM4	3.6	-0.6	-17%
BCC-CSM1	1.0	-0.4	-37%
IPSL-CM5A-LR	2.7	-0.3	-13%

Combining the GFDL and CMIP5 results, Sahel rainfall decreases with SST warming in fourteen of the seventeen models analyzed. The two models that wetten the region, AM2.1-UW and c48-HiRAM, are not production models that have been tuned for TOA radiative balance. While this does not have an immediately obvious physical imprint on the Sahel rainfall response to warming, the implication is that production-class models (which also excludes c90-AM3) all respond with drying, or at most no change (HiRAM). These results also provide further context for the uniqueness of AM2.1. In its standard configuration, precipitation is reduced in the Sahel with +2 K warming more than any other GFDL model or any CMIP5 model subjected to a larger +4 K warming. Moreover, replacing RAS with UW as its convective parameterization causes AM2.1 to go from having the most negative to the second-most positive precipitation response of all models.

4.3.2 Dynamical and MSE budget term responses

Figure 4.3 shows the control and perturbation Sahel region-mean profiles of the time-mean horizontal and vertical MSE advection in the GFDL models.⁵ For horizontal advection, c48-HiRAM is an outlier in the magnitude of its positive values in the lower troposphere, but otherwise the models are consistent: MSE divergence peaking in the lower troposphere and steadily decreasing towards zero in the mid- to upper-troposphere. The vertical advection profiles are also largely consistent, again with c48-HiRAM an outlier. Perturbed with 2 K SST warming, at nearly all levels above the boundary layer and below \sim 200 hPa the models respond with shared sign: anomalous MSE divergence by the horizontal flow and anomalous MSE convergence by the divergent flow. Moreover, from inspection both responses appear to track the precipitation responses, which we will return to below.

Figure 4.4 shows the control and perturbation Sahel region-mean profiles of the time-mean horizontal and meridional MSE advection profiles. Comparison of the control profiles verifies that the total horizontal MSE advection is dominated by the meridional advection, especially from the surface through the mid-troposphere; zonal advection is appreciable primarily in the upper troposphere, where the Tropical Easterly Jet acts to converge MSE into the region (not shown). As in the GFDL ensemble, the overall structure is quite consistent across the models. As is the case for precipitation, the responses show more heterogeneity, but apart from the boundary layer the the dry air advection is largely enhanced with SST warming. That the meridional advection response is more consistent than the total horizontal advection response corroborates our focus on the interactions with the Sahara. Moreover, the anomalous dry air advection generally peaks in the lower free-troposphere and rapidly taper off above – in sharp contrast to the deep increases in AM2.1, and this is consistent with AM2.1’s unmatched precipitation reductions.

⁵Comparing the AM2.1 and AM2.1-UW curves in Figures 4.3 and 4.5 with their counterparts in Chapter 3 (Figures 3.5 and 3.6, respectively) provides a sense of the information loss due to interpolation from model-native vertical coordinates to pressure levels. This is most pronounced in the boundary layer. Note also that the horizontal axis spacing is also different within each pair of figures.

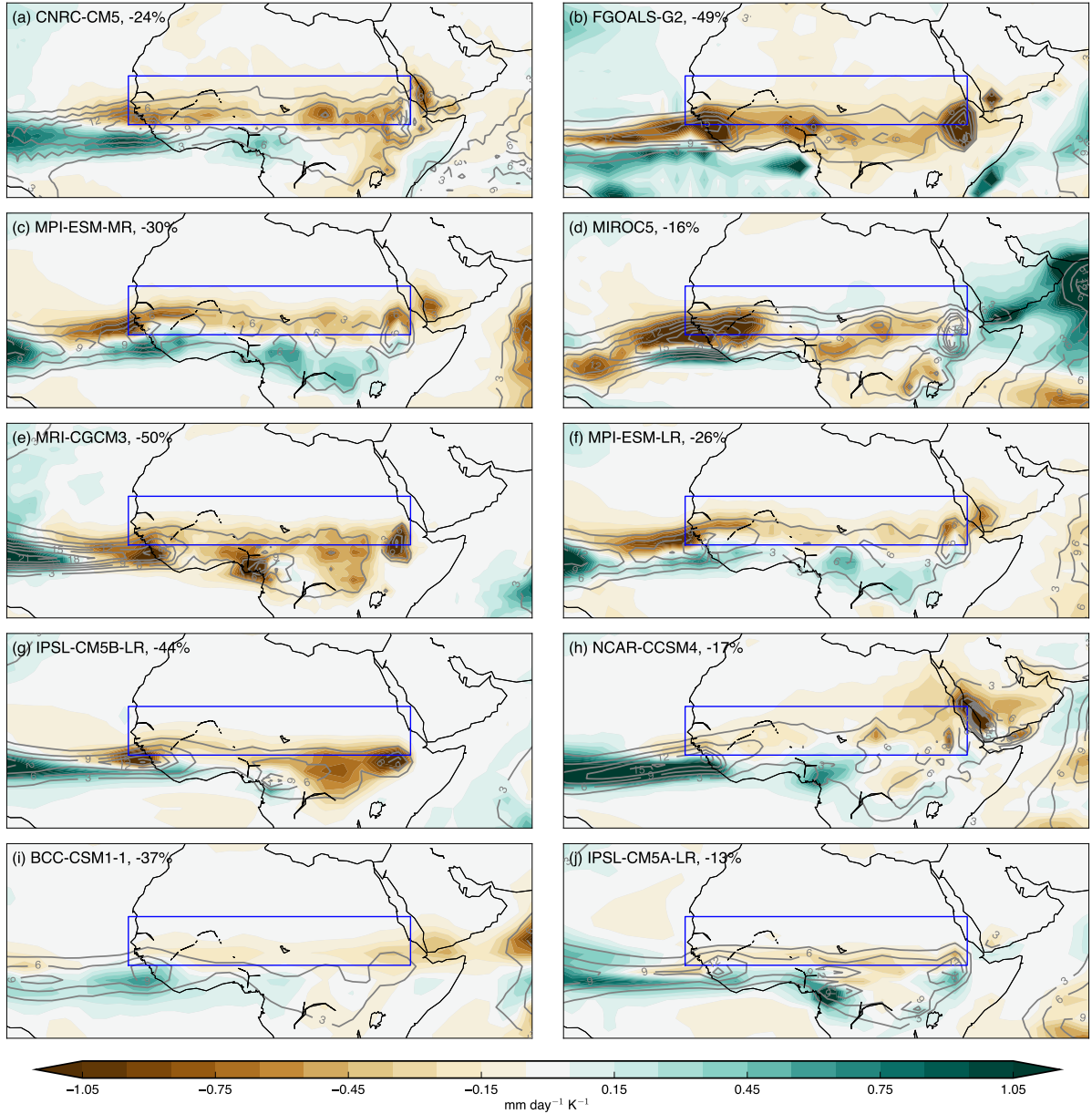


Figure 4.2: (Shaded contours) difference in precipitation per unit SST warming between simulation with uniform 4 K SST warming and present-day control simulation, units $\text{mm day}^{-1} \text{K}^{-1}$, and (grey contours) precipitation in the control simulation, with contours starting at 3 mm day^{-1} and with a 3 mm day^{-1} interval, in each of the ten CMIP5 models. The models are ordered from (a) to (j) from most negative to least negative precipitation response. The Sahel region-mean fractional precipitation change (total, not per unit warming) is printed within each panel. Note that the color spacing is half that of Figure 4.1. The printed values in the top-left are the fractional precipitation change in the Sahel, without normalization by the SST change.

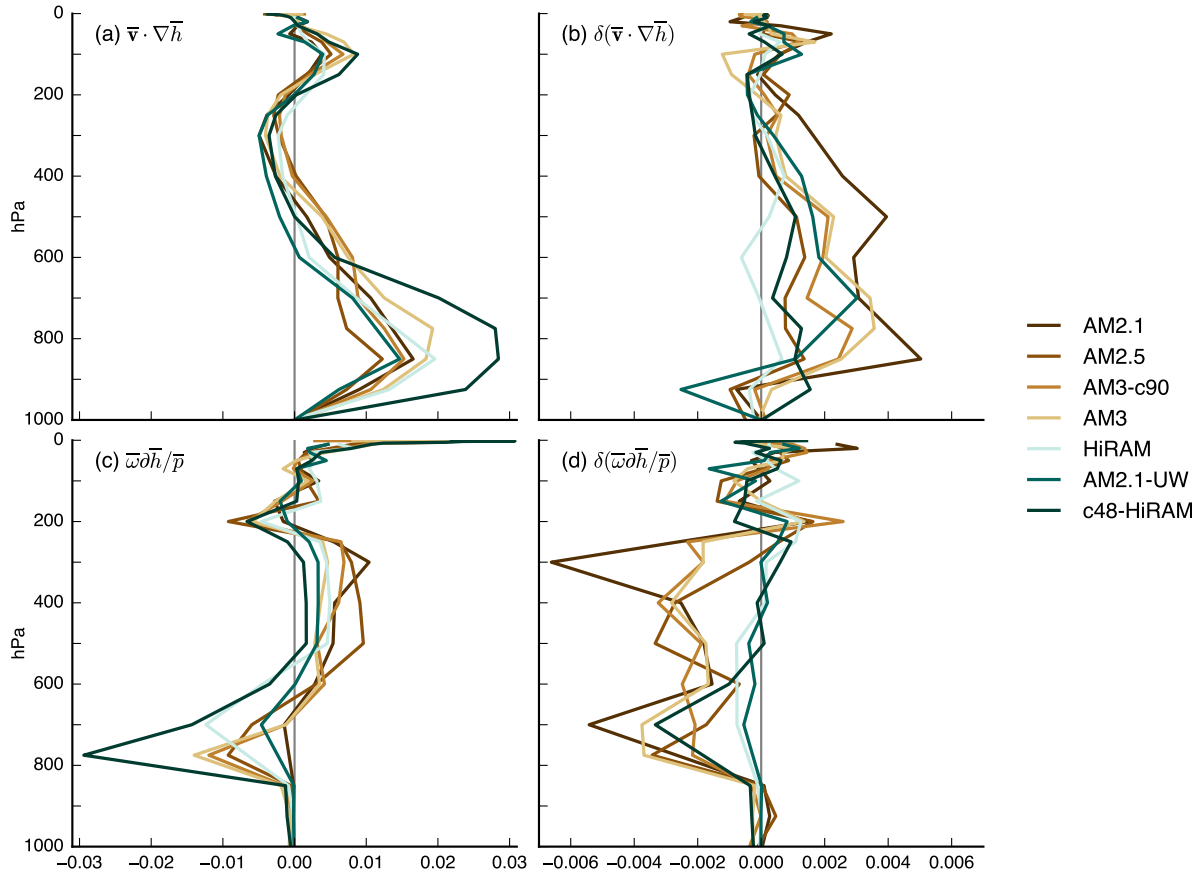


Figure 4.3: Sahel region-mean profiles of time-mean (left column) horizontal and (right column) vertical MSE advection in (top row) the control simulations and (bottom row) in response to 2 K SST warming in the GFDL models, in $\text{J kg}^{-1} \text{ s}^{-1}$. The color of each curve corresponds to the model's Sahel region-mean precipitation response to 4 K SST warming; the darkest green being the least negative, and the darkest brown being the most negative, response. These are not normalized by the imposed SST warming. Note the smaller horizontal axis spacing in the right column.

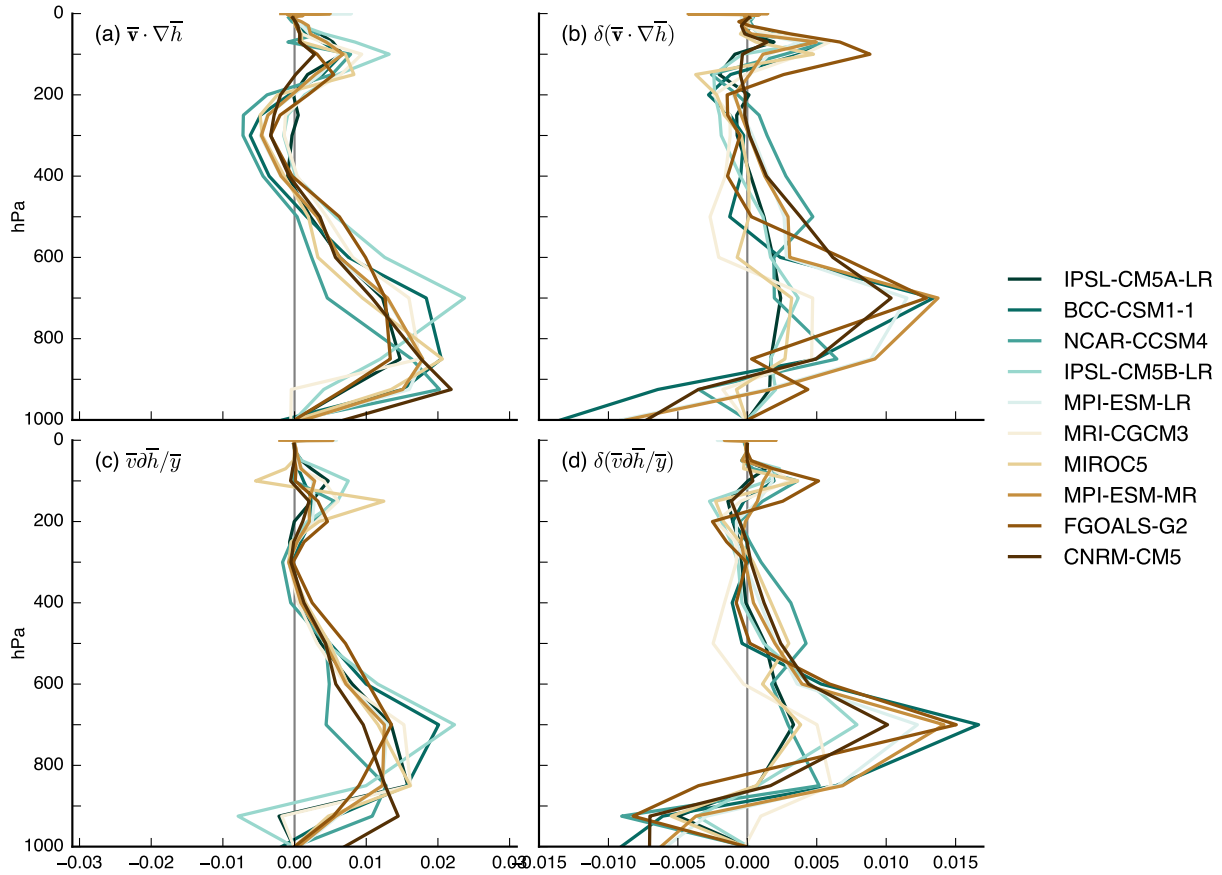


Figure 4.4: Sahel region-mean profiles of time-mean (left column) horizontal and (right column) meridional MSE advection in (top row) the control simulations and (bottom row) in response to 2 K SST warming in the CMIP5 models, in $\text{J kg}^{-1} \text{s}^{-1}$. The color of each curve corresponds to the model's Sahel region-mean precipitation response to 4 K SST warming; the darkest green being the least negative, and the darkest brown being the most negative, response. These are not normalized by the imposed SST warming. The horizontal axis spacing in the left column is the same as in Figure 4.3 but not in the right column.

Figure 4.5 shows the Sahel region-mean profiles of vertical pressure velocity in the control simulation and in response to SST warming and the moist static stability in the control simulation for each GFDL model. Figure 4.6 shows the same for the CMIP5 models. The control ascent profiles span from strong ascent throughout the troposphere (e.g. AM2.5 and CNRM-CM5) to much more bottom-heavy (e.g. c48-HiRAM and BCC-CSM1-1). In both sets of models, there is more spread among the control simulations in the vertical velocity than the moist static stability. All models exhibit decreased ascent over some portion of the mid- to upper-troposphere, and in most this extends over most of the free troposphere. Almost all also exhibit the dipole structure documented in Chapter 3 for both AM2.1 variants, with the free tropospheric descent directly above anomalous ascent in the boundary layer. The depth of the anomalous ascent layer varies greatly, however, from \sim 150 to \sim 400 hPa in thickness.

Several Sahel region-mean TOA radiative terms exhibit consistent responses across the models (not shown). Shallowing and suppression of moist convection across the models and the concomitant cloud loss causes the shortwave cloud radiative effect to become more positive in all models ($+1.5$ to $+15.9$ W m^{-2} for GFDL; $+0.8$ to $+19.0$ W m^{-2} for CMIP5) and the longwave cloud radiative effect to become less positive in all models except HiRAM (-6.6 to $+1.0$ W m^{-2} for GFDL; -5.0 to -13.1 W m^{-2} for CMIP5). The relative magnitudes of the longwave and shortwave flux responses varies, such that the net cloud radiative effect response is not of consistent sign (-0.2 to $+11.4$ W m^{-2} for GFDL; -4.4 to $+8.2$ W m^{-2} for CMIP5), although averaged within either ensemble or across models it is positive. Clear-sky net TOA radiation almost necessarily decreases in all models (-10.5 to -1.9 W m^{-2} for GFDL; -14.6 to -6.7 W m^{-2} for CMIP5), as the warmed surface and troposphere emit more longwave radiation that escapes to space (this exceeds the increase in LW trapping due to increased water vapor). The mixed response of net CRE combined with the robustly negative clear sky net TOA radiative flux results in decreased all-sky TOA radiation into the Sahel in all models except AM2.1, HiRAM, and AM2.1-UW (-7.7 to $+3.7$ W m^{-2} for

GFDL; -17.0 to -5.9 W m^{-2} for CMIP5).

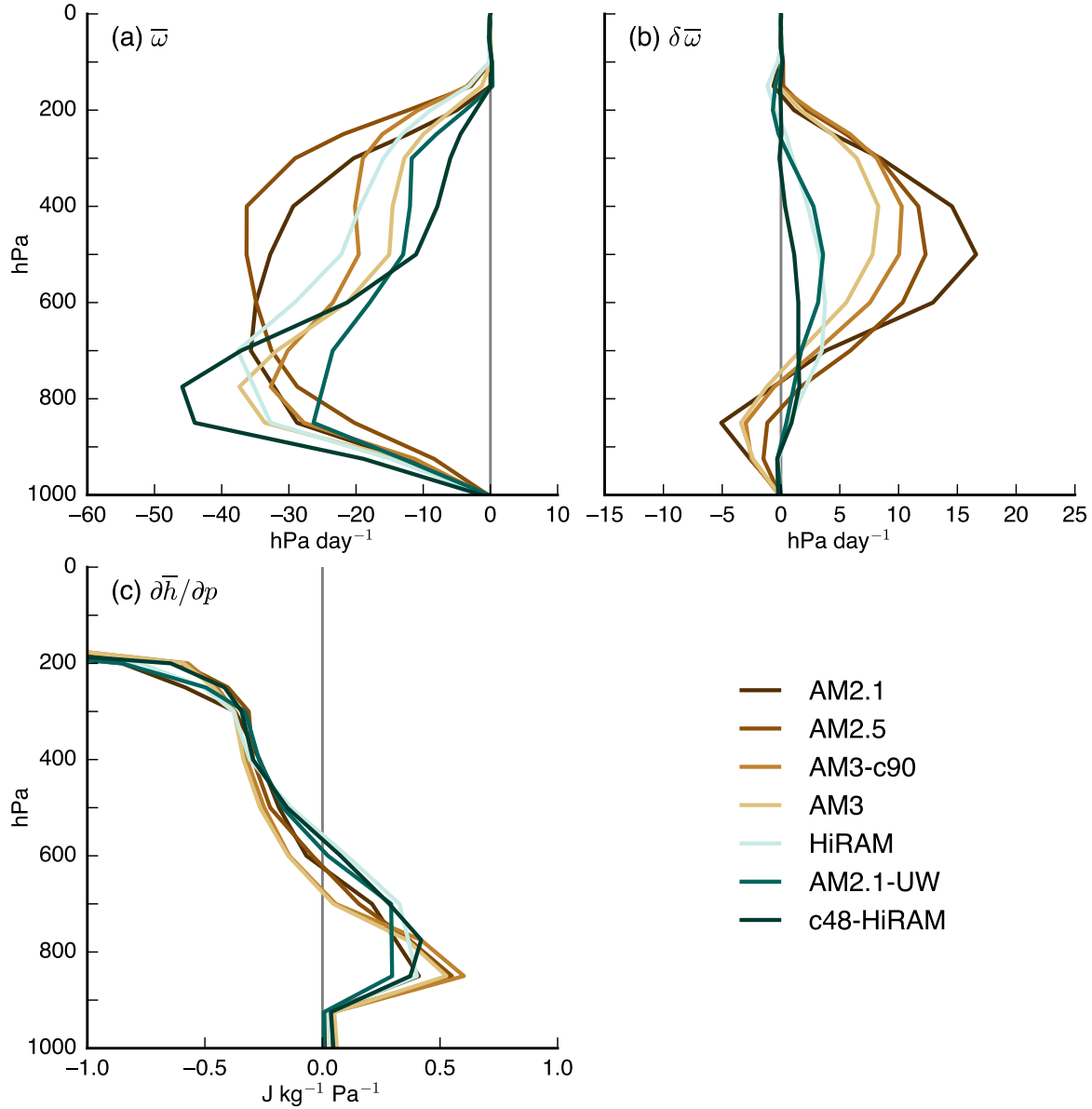


Figure 4.5: Sahel region-mean profiles of (a) vertical velocity in the control simulation, (b) the response of vertical velocity to the 2 K SST warming, and (c) moist static stability in the control simulation. The color of each curve corresponds to the model's Sahel region-mean precipitation response to 2 K SST warming.

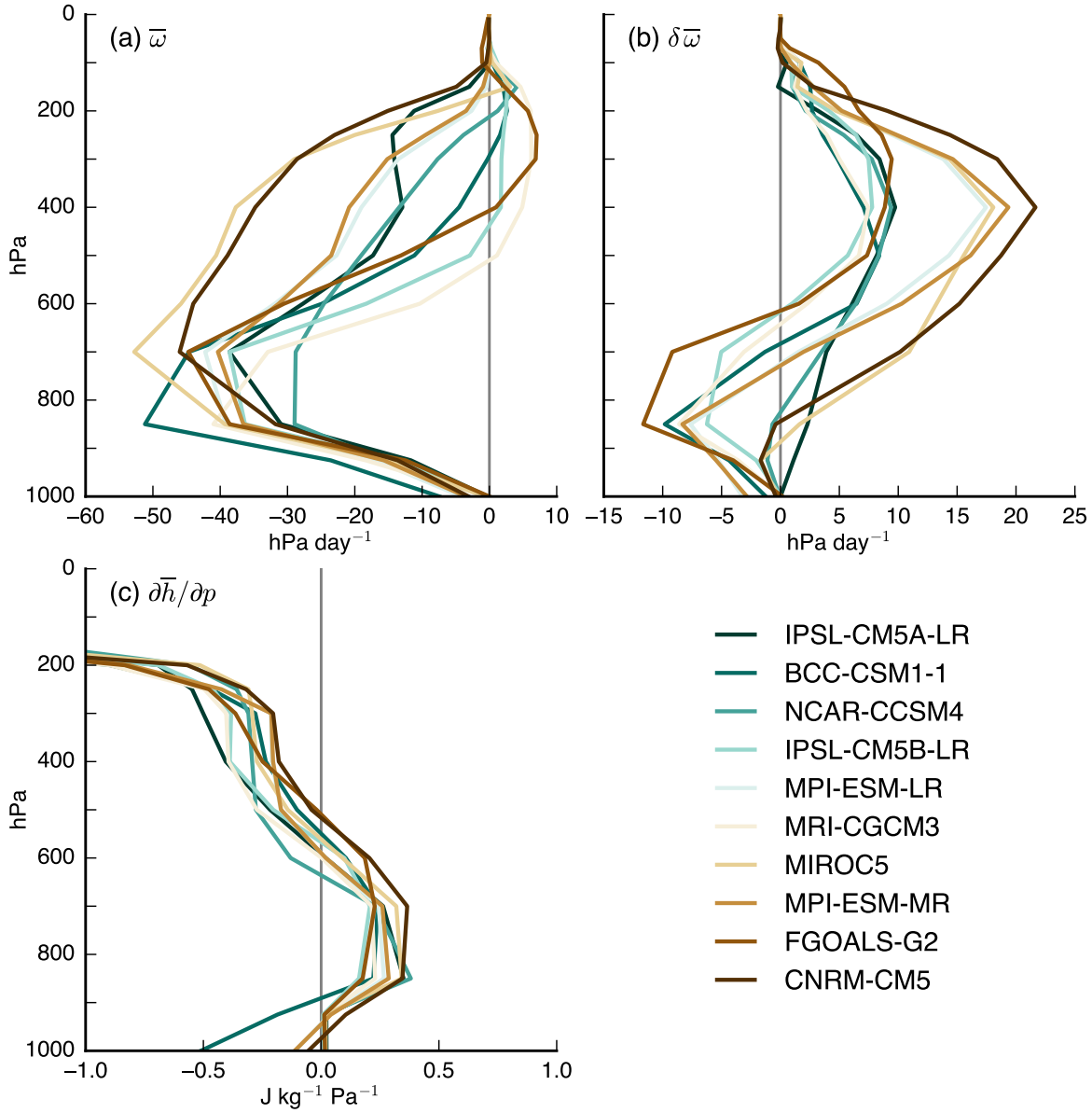


Figure 4.6: (Same as Figure 4.5, but for the CMIP5 models.) Sahel region-mean profiles of (a) vertical velocity in the control simulation, (b) the response of vertical velocity to the 4 K SST warming, and (c) moist static stability in the control simulation. The color of each curve corresponds to the model's Sahel region-mean precipitation response to 4 K SST warming; the darkest green being the least negative, and the darkest brown being the most negative, response, in absolute (rather than fractional) terms.

In summary, a consistent set of responses is shared by almost all models – ascent profile shallowing causing anomalous MSE convergence by the time-mean divergent circulation, an enhanced meridional MSE gradient contributing to increased MSE divergence by the horizontal flow, cloud loss causing reduced shortwave shading and longwave trapping, and reduced clear- and all-sky net TOA radiation.

4.3.3 Towards quantitative predictors of model precipitation responses

From Figure 4.5, it can be gleaned that the precipitation response in the GFDL models scales not only with the response of ω (panel b) in the free troposphere but also with the control simulation value of ω in the upper troposphere (panel a): models with top-heavy ascent profiles (AM2.1 and AM2.5) dry the most with SST warming, and those with bottom-heavy profiles (AM2.1-UW and c48-HiRAM) wetter with SST warming. Moreover, this is broadly consistent with the mechanism set forth in Chapter 3, wherein deeper climatological convection yields greater meridional MSE gradient enhancement and thus greater drying of the Sahel. Can this picture yield a quantitative predictor of the precipitation response?

As a preliminary step, Figure 4.7 shows the responses of precipitation and ω at 500 hPa per K SST warming for each GFDL and CMIP5 model. Across the GFDL models, the precipitation response is almost perfectly anti-correlated with the anomalous subsidence at 500 hPa. For the CMIP5 models, this qualitative relationship holds, but the correlation is weaker, $r = -0.56$, and given the sample size this is not statistically significant. That precipitation is more sensitive to SST change in the GFDL than CMIP5 ensembles is consistent with the saturation of the AM2.1 precipitation response shown in Chapter 3. Combining the GFDL and CMIP5 models, the correlation is $r = -0.91$, which is statistically significant. At face value, this bodes well for attempts to understand the precipitation response through the dynamical subsidence response through the mechanisms involving the anomalous horizontal advection described above. However, this overall correlation is dominated by the GFDL

models, and the lack of significant correlation for the CMIP5 ensemble is ominous. Also, if the precipitation responses are normalized by the control simulation values (based on the general hypothesis that the variability scales with the mean value), the correlation for GFDL remains nearly perfect ($r = 0.99$) but the CMIP5 correlation reverses entirely, $r = 0.53$ (not shown).

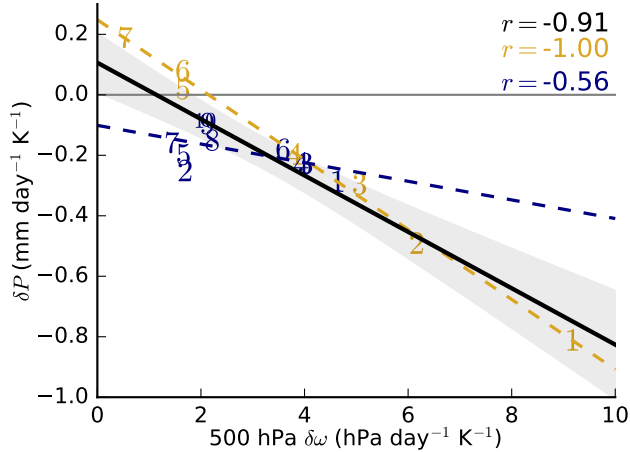


Figure 4.7: Scatterplot of Sahel region-mean (vertical axis) precipitation change as a function of (horizontal axis) ω change at 500 hPa, both expressed per unit of imposed SST warming ($\text{mm day}^{-1} \text{K}^{-1}$ and hPa day^{-1} , respectively). In this and subsequent scatterplots, each point corresponds to a single model, colored goldenrod for GFDL and navy for CMIP5, and with the number corresponding to the Sahel precipitation response ranking within that ensemble, with numbers increasing from most negative to most positive. The curve and text with the corresponding curve are the best fit line and correlation coefficient for that ensemble. The black line and text are the linear best fit for the combined GFDL and CMIP5 data, with shading denoting the 95% confidence interval of the fit.

Figure 4.8 is an analogous scatterplot of the precipitation response, in this case as a function of the horizontal advection response at 500 hPa. The overall relationships are similar as for the ω response, with a fairly strong correlation across the GFDL models but less so for CMIP5, but they exhibit greater spread, such that none of the correlations are statistically significant. This result holds more broadly: for all of the response that we have examined to date, the mid-tropospheric ω response is the only one with a significant correlation, despite all broadly conforming with the dynamical arguments posed above.

Figure 4.9 shows the precipitation response as a function of the Sahel region-mean OLR

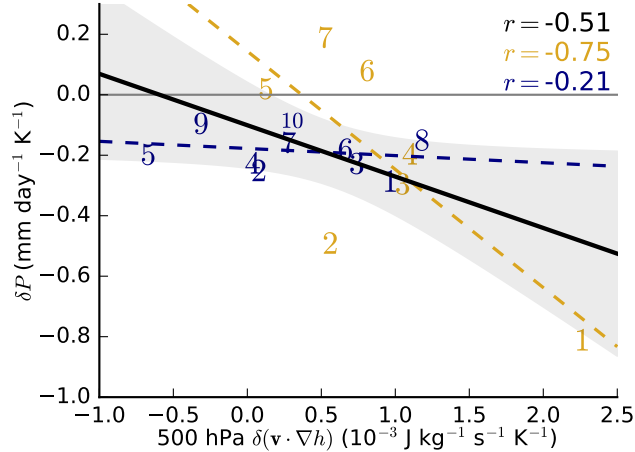


Figure 4.8: Scatterplot of Sahel region-mean (vertical axis) precipitation change as a function of (horizontal axis) horizontal MSE advection change at 500 hPa. See Figure 4.7 for further description.

in the control simulation. Deeper convection yields higher cloud tops, which being at colder temperatures emit less radiation. The expectation, therefore, is that the control simulation OLR is correlated with the precipitation response: a deeper circulation will have smaller OLR and will also have a more negative precipitation response. This generally holds, but again AM2.1 is an outlier, the GFDL models are more sensitive per unit SST change than the CMIP5 models, and the correlations are not statistically significant.

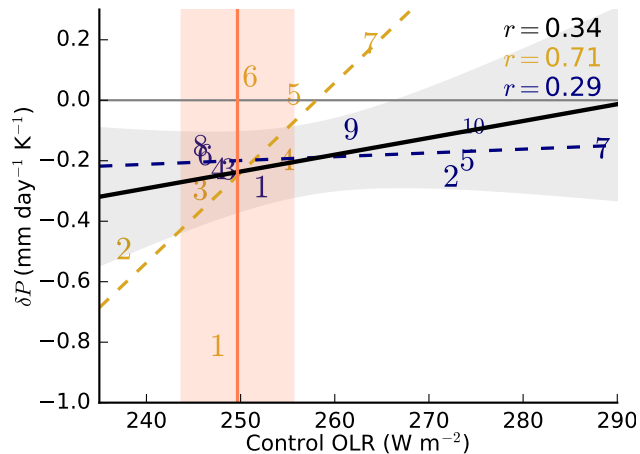


Figure 4.9: Scatterplot of Sahel region-mean (vertical axis) precipitation change as a function of (horizontal axis) control simulation OLR. Vertical line with shading is the observational estimate from CERES with a 95% confidence interval.

For climatological fields, the strongest relationship we have found with the precipitation response is with the net TOA radiative flux. Figure 4.10 shows the corresponding scatterplot. Greater net energy input into the Sahelian atmosphere in the control simulation is associated ($r = -0.83$) with a more negative precipitation response to uniform 2 K SST warming. AM2.1 is an outlier, with only the third highest control net TOA radiation but the most severe drying response. But the correlation is weaker across the CMIP5 models, and for the combined ensemble, it too is statistically insignificant.

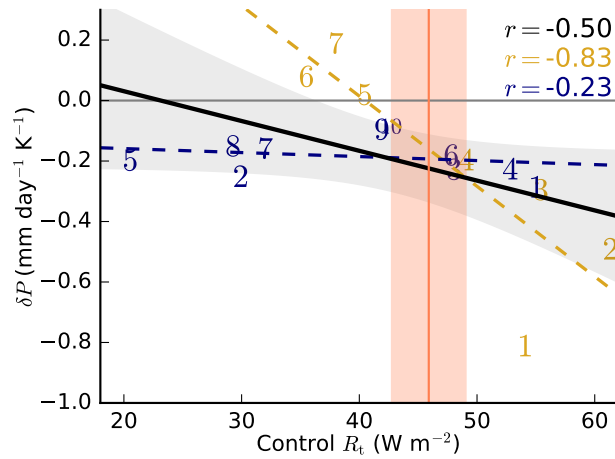


Figure 4.10: Same as Figure 4.9, except using the control simulation net TOA radiation as the horizontal axis.

4.4 Observations and reanalyses

Anticipating future progress in identifying a robust predictor of model Sahel rainfall responses, this section considers the observational facet of developing an emergent constraint for future Sahel rainfall: comparison of model control simulation hydrological values with observations, spread in Sahel MSE budget fields among reanalysis datasets and the potential link to the convective parameterization, the utility of satellite observations as constraints, and the realism of modeled cloud radiative variations.

4.4.1 Hydrological values in control simulations

Although the forced precipitation response does not *a priori* relate to its control value, fidelity in the climatological values to observations adds to the overall confidence one places in a model. Table 4.5 lists the Sahel region-mean precipitation in each of six gridded observational datasets, which collectively include both local rain-gauge and satellite measurements. Averages are shown over each product's full range and for the common period to all six, namely 2000-2009. The model climatologies, spanning 2.5–4.6 mm day⁻¹ for GFDL and 1.0–5.5 mm day⁻¹ for CMIP5, bracket the observational range of 3.0–3.6 mm day⁻¹. Of the GFDL models, only c90-AM3 is within this range, and of the CMIP5 models, only MPI-ESM-MR and NCAR-CCSM4 (3.0 and 3.6 mm day⁻¹, respectively) are within this range.

Table 4.5: Sahel July-August-September region-mean precipitation (P) in six observational datasets, in mm day⁻¹. The years available for each product are listed, as are averages over the full available range and for the period common to all products, 2000-2009.

Product	Year range	P	P 2000-2009	Reference
TRMM	2000-2009	3.6	3.6	Huffman <i>et al.</i> [2007]
GPCP	1979-2013	3.5	3.2	Adler <i>et al.</i> [2003]
U. Delaware	1900-2010	3.4	3.2	Legates and Willmott [1990]
PREC/L	1948-2014	3.2	3.2	Chen <i>et al.</i> [2002]
CMAP	1979-2014	3.1	3.1	Xie and Arkin [1997]
CRU	1901-2013	3.1	3.0	Harris <i>et al.</i> [2014]

Table 4.6 lists the Sahel JAS evapotranspiration in the LandFlux-EVAL observational gridded data product [Mueller *et al.*, 2013], which combines *in situ* data, land model simulations, and reanalysis products. The results vary from 1.5 to 2.1 mm day⁻¹, depending on which of the three input data types is included and whether extending beyond 1995, after which much less data is available. Compared to precipitation, model spread is smaller and aligns more closely with the observational range. To the extent that the region is in a moisture-limited evaporative regime, it is to be expected that the range of evapotranspiration values across models be smaller than that of precipitation, since the former generally varies linearly with the latter, although why the simulated E values are closer to observations than the simulated P values is not immediately clear.

Table 4.6: Sahel region-mean evaporation in the LandFlux-EVAL observational dataset [Mueller *et al.*, 2013], in mm day⁻¹. Averages are shown separately for the periods 1989-1995 and 1989-2005, as data availability drops substantially in 1995. The left column denotes what types of data are used for the estimate: diagnostic (i. e. measurement-based), land models, reanalyses, or all three.

Input data	1989-1995	1989-2005
All	1.7	1.6
Diagnostic	1.8	2.1
Land models	1.7	1.5
Reanalyses	1.7	1.5

4.4.2 Ascent profiles in reanalyses

Chapter 3 demonstrates that the Sahel MSE budget fields are highly sensitive to the convective parameterization in at least one AGCM. Though they assimilate observational data from multiple sources, reanalyses also ultimately rely on a convective parameterization in their underlying dynamical model. *Zhang et al.* [2008] find large discrepancies among three reanalyses in their representation of shallow meridional circulations in multiple tropical regions, including West Africa, and speculate that differences in the convective parameterization, in particular their sensitivity to dry air intrusions, are a key factor.

We analyze three reanalyses products: ERA-Interim [Dee *et al.*, 2011] averaged over 1979-2013, NASA-MERRA [Rienecker *et al.*, 2011] averaged over 1979-2011, and NCEP-CFSR [Saha *et al.*, 2010] averaged over 1979-2013. Figure 4.11 shows their Sahel region-mean ascent profiles. All three exhibit ascent throughout the troposphere that peaks near \sim 800 hPa. This ascent maximum is greatest in magnitude in NCEP-CFSR and smallest in ERA-Interim (approximately -47, -36, and -32 hPa day⁻¹ in NCEP-CFSR, MERRA, and ERA-Interim, respectively). In the upper troposphere, MERRA exhibits the greatest ascent, followed by ERA-Interim and then NCEP-CFSR. MERRA's ascent is greater than ERA-Interim's at nearly every level, indicating a stronger overall divergent circulation in MERRA, while NCEP-CFSR's relatively large ascent values in the lower troposphere and small values in the upper troposphere amount to a more bottom-heavy circulation. The average of the three reanalyses largely resembles ERA-Interim, though with a larger magnitude peak in ascent

near 800 hPa (not shown).

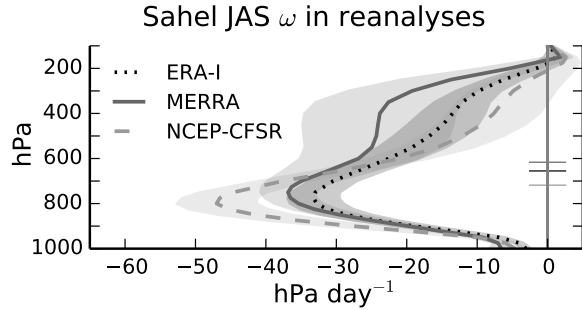


Figure 4.11: Sahel region-mean profile of vertical velocity in three reanalysis products. Shaded range denotes ± 1 standard deviation. Horizontal lines on the vertical axis denote the vertical centroid over the 100-1000 hPa range of the corresponding dataset.

In comparison with the GFDL and CMIP5 models, NCEP-CFSR is roughly as bottom-heavy as the most bottom-heavy profiles (c48-HiRAM, BCC-CSM1-1, c.f. Figures 4.5 and 4.6, respectively), but there are several models (AM2.1, AM2.5, CNRM-CM5, and MIROC5) that are more top-heavy than any of the reanalyses. Moreover, these models with relatively top-heavy climatological ascent profiles relative to the reanalyses are among those in which SST warming causes the strongest anomalous descent in the free troposphere and precipitation decrease. This is broadly consistent with our argument that deeper climatological convection tends to generate greater drying responses to warming, although as mentioned above the lack of statistical significance in the ascent-precipitation responses relationship means there are other important factors.

Another potential caveat is that the reanalyses themselves rely on a convective parameterization to generate their vertical velocity profiles – for example, MERRA, which generates the least bottom-heavy profile, uses, like AM2.1, the Relaxed Arakawa Schubert convective parameterization; ERA-Interim and NCEP-CFSR use the simplified Arakawa-Schubert and *Tiedtke* [1989] schemes, respectively. The sensitivity of AM2.1 to the convective parameterization shown in Chapter 3 suggests that the reanalyses therefore may not provide a truly reliable constraint. As discussed in Chapter 3, the especially bottom-heavy ascent profiles in c48-HiRAM and AM2.1-UW likely stem from the UW convection scheme being less active.

In the standard, \sim 50 km resolution version of HiRAM, this is compensated by convection resolved at the grid scale, which can be quantified e.g. by the ratio of convective to total (convective plus large-scale) precipitation in the Sahel during JAS, which is 0.17 in HiRAM, 0.70 in c48-HiRAM, and 0.95 in AM2.1.

4.4.3 Climatological TOA radiative fluxes

Figures 4.9 and 4.10 include the present-day Sahel region-mean values of OLR and net TOA radiation, respectively, from the Clouds and Earth Radiant Energy System (CERES) Energy Balanced and Filled (EBAF) Edition 2.8 dataset [Loeb *et al.*, 2009], averaged over 2000-2013. If taken as an emergent constraint, the observational value tells a different story using the two radiative quantities. The OLR value from CERES is roughly in the middle of the GFDL models, and AM2.1 is among the closest to the observational value. In contrast, for TOA radiation, while AM3 and c180-HiRAM are near the upper and lower edges of the observational range, AM2.1, AM2.1-UW, c48-HiRAM, and c90-AM3 are each well separated from the observational value. The disagreement holds for cloudy-sky OLR also (not shown), and we suspect for the other cloudy- and clear-sky components.

Although the net TOA radiation is better correlated across GFDL models with the precipitation response, OLR is the more direct proxy for convective depth, which is the quantity for which we have posited a physical mechanism linking it to the precipitation response. Ultimately, notwithstanding the significance of the correlations across models, using the TOA radiative fluxes as an emergent observational constraint requires further investigation of this sensitivity. (Although the observational range for both fields largely coincides with the intersection of the GFDL and CMIP5 correlations, this does not occur for other TOA radiative fields such as net CRE – it is therefore most likely an interesting coincidence; not shown).

4.4.4 Relationships between precipitation and cloud radiative properties

The smallness of the Sahel region-mean net TOA radiation response in AM2.1 to 2 K SST warming results from cancellation between increased shortwave absorption due to cloud loss and increased clear-sky longwave emission by the hotter surface and hotter, drier atmosphere. Because the convection is sufficiently shallow that the shortwave shading exceeds the longwave trapping, a decrease in cloud cover accompanying a decrease in precipitation will increase the net TOA radiative flux (and conversely for increased precipitation). This effectively increases the efficiency of MSE divergence by the divergent circulation – or, if the convection is sufficiently shallow, reduces the efficiency of the MSE convergence. This is the opposite of deep convecting regions, in which clouds trap radiation overall, thereby reducing the effective gross moist stability [Bretherton *et al.*, 2006]. Over land, however, the surface hydrological factors complicate matters: if reduced cloud cover allows more net radiation to impinge on the surface, it will heat the surface, potentially enhancing the original drying signal.

We use extended AMIP simulations in AM2.1, AM3, and HiRAM, respectively spanning 1870-1999, 1870-2005, and 1979-2009 and with 10, 3, and 2 ensemble members each (values presented are ensemble means). Unlike the CMIP5 `amip` specification, in these simulations the atmospheric composition is fixed at present-day values – only the SSTs and sea ice vary in time.

Figure 4.12 shows JAS Sahel averages net CRE from CERES-EBAF vs. precipitation from the CRU version 3.22 observational dataset [Harris *et al.*, 2014] for the period 2000-2013. Each dot denotes a single year, and the overlaid black line is the linear best fit, with its slope and the Pearson correlation coefficient printed in each panel. We have not removed any long-term linear trend that may be present in these fields, which could in principle affect the results. The net cloud radiative effect becomes slightly less positive as rainfall increases, at -0.8 W m^{-2} per mm day^{-1} . This is the residual of larger but canceling shortwave and

longwave relationships with rainfall (-4.5 and $+3.7 \text{ W m}^{-2}$ per mm day^{-1} , respectively).

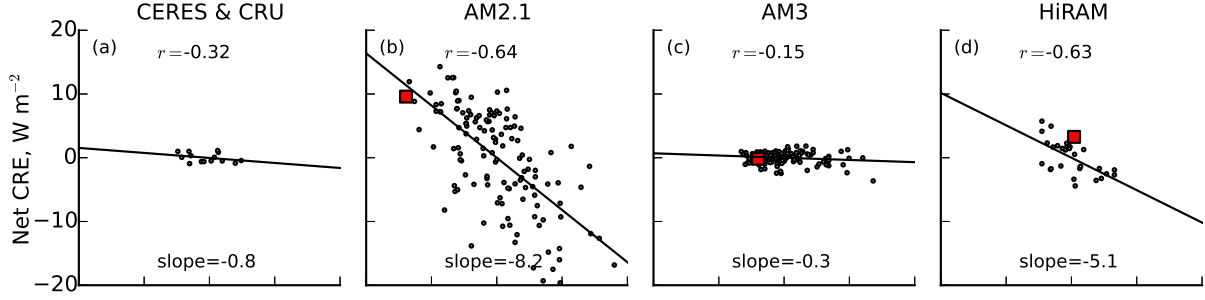


Figure 4.12: Sahel region-mean (vertical axis) net CRE, in W m^{-2} , as a function of (horizontal axis) precipitation, in mm day^{-1} , in (a) CERES-EBAF and CRU observational data, and AMIP simulations in (b) AM2.1, (c) AM3, and (d) HiRAM. Each dot represents a single year, and red squares in (b)-(c) denote the equilibrium response in the 2 K SST warming simulation. The horizontal axis spans -2 to $+2 \text{ mm day}^{-1}$ in all panels.

Figure 4.12 also shows the AMIP simulations. The CRE-precipitation slope values are -8.2 , -0.3 , and -5.1 W m^{-2} per mm day^{-1} in AM2.1, AM3, and HiRAM respectively. For AM2.1, this far exceeds the observational value. red squares in the model panels signify the response in the $+2 \text{ K}$ simulations. That they lie near the linear fits from the AMIP runs implies that the same mechanisms are acting in the forced equilibrium responses and the interannual variability.

Figure 4.13 decomposes the precipitation-net CRE relationship into SW and LW components. The LW CRE-precipitation slope using observations is 3.7 W m^{-2} per mm day^{-1} , slightly lower than AM2.1 and lower still than AM3 and HiRAM (4.5 , 9.8 , and 6.0 W m^{-2} per mm day^{-1} , respectively). The corresponding relationships for SW are -4.5 W m^{-2} per mm day^{-1} in observations and -12.7 , -10.2 , -11.1 W m^{-2} per mm day^{-1} in AM2.1, AM3, and HiRAM, respectively. So in all three models the shortwave shading by clouds varies at more than double the rate per unit precipitation change than observations, with AM2.1 the worst by a modest amount. However, AM2.1's modest LW slope causes the net to be severely negative, whereas the LW and SW variations largely cancel in AM3 and, to a lesser extent, HiRAM. The equilibrium 2 K warming responses in AM2.1 and AM3 in the SW and LW components are both smaller in magnitude than the interannual variability would

suggest, and this cancels for the net CRE-precipitation response.

Based on these results, all else equal, the excess radiation per unit precipitation loss in AM2.1 can be expected to reach the surface and feedback on the drying. To a lesser extent, the same would be expected in HiRAM, yet HiRAM's precipitation response is weak, consistent with an interpretation that these cloud radiative variations feed back on precipitation variations rather than cause them.

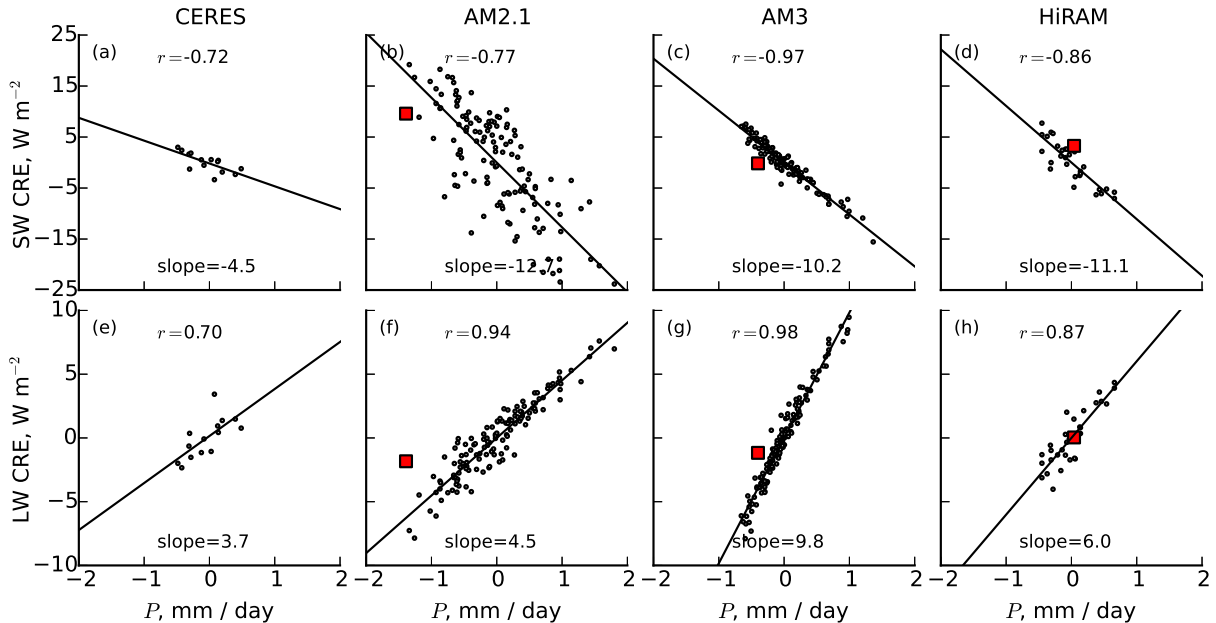


Figure 4.13: Sahel region mean (vertical axis, top row) SW CRE and (vertical axis, bottom row) LW CRE, in W m^{-2} , as a function of (horizontal axis) precipitation, in mm day^{-1} , in (a) CERES-EBAF and CRU observational data, and AMIP simulations in (b) AM2.1, (c) AM3, and (d) HiRAM. Each dot represents a single year, and red squares in (b)-(c) denote the equilibrium response in the 2 K SST warming simulation.

Figure 4.14 shows the relationships between Sahel precipitation and the net all-sky TOA radiative flux. The relationships between rainfall and clear-sky downward TOA flux are fairly consistent across models and observations: the observations, AM2.1, AM3, and HiRAM have slopes 4.5, 4.2, 7.5, and 5.7 W m^{-2} per mm day^{-1} , respectively (not shown). As a result, the excessive cloud radiative covariance with precipitation in AM2.1 causes the all-sky precipitation-TOA radiation relationship to be of the wrong sign compared to observations. The observations, AM3, and HiRAM adhere to classical expectations: precipitation and

TOA radiative flux are positively correlated. The observed slope is $3.7 \text{ W m}^{-2} \text{ mm day}^{-1-1}$. The equilibrium responses to SST warming generally agree less well with the interannual relationship than for net CRE, due to increased clear-sky OLR driven by the mean warming.

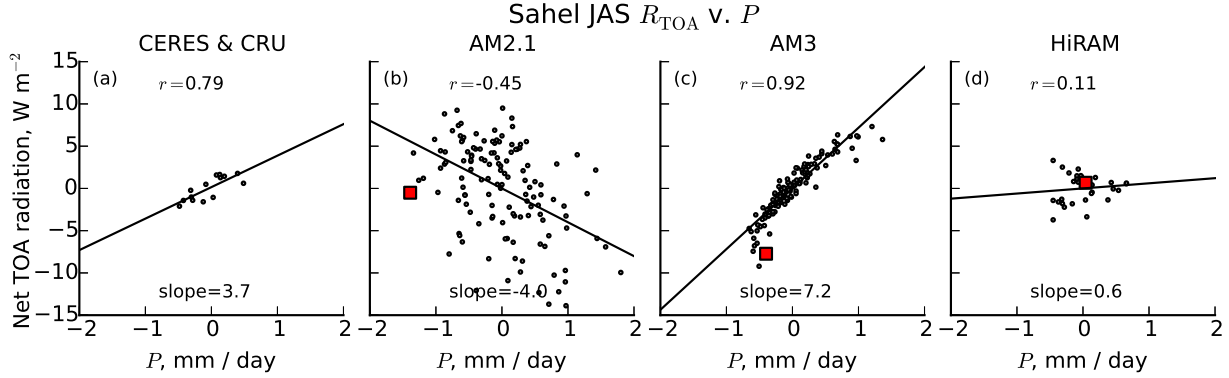


Figure 4.14: Sahel region-mean JAS net all-sky TOA radiative flux as a function of precipitation.

4.5 Discussion

We do not fully understand why the CMIP5 and GFDL ensembles exhibit differing quantitative relationships among the various fields presented. In particular, that the Sahel precipitation and tropospheric vertical velocity responses are not statistically significantly correlated in the CMIP5 models – compared to a near-perfect correlation in the GFDL ensemble – hamstrings efforts to develop a quantitative emergent constraint. We suspect that the greater heterogeneity in control climate state in the region across the CMIP5 models plays a role. In some models, e.g. BCC-CSM1-1 and IPSL-CM5B-LR, the control simulation is so dry that the region as we have defined its borders is fully arid rather than semi-arid, in which case the governing dynamics may be quite different. For example, while the evaporation and precipitation responses to SST warming are correlated across the GFDL models at $r = 0.95$, in the CMIP5 models there is effectively no relationship between the two fields ($r = 0.09$). A tight correspondence between evaporation and precipitation is one of the hallmarks of semi-arid regions. However, we have experimented with excluding certain CMIP5 models

based on climatological fields and have not found correlations to be easily improved.

The end-of-21st century Sahel rainfall change in the CMIP5 RCP8.5 simulations spans roughly -1 to $+2.5$ mm day $^{-1}$, with a positive multi-model mean [c.f. Figure 1 of *Park et al., 2015*]. Across all 17 CMIP5 and GFDL AGCMs analyzed, the span of Sahel rainfall responses to SST warming (ignoring the difference in SST warming magnitude) is -1.4 to $+0.4$ mm day $^{-1}$, or 1.8 mm day $^{-1}$, i.e. roughly half of the spread in the full 21st century simulation, with a negative multi-model mean. Assuming linearity in the response to uniform SST warming and all other perturbations, the fact that mean SST warming generally dries the Sahel implies that the combined effect of all other 21st century perturbations act to increase precipitation in the Sahel (otherwise the RCP8.5 ensemble would not be appreciably wetter on average than the uniform warming ensemble). This is consistent with prior reports of the general wetting influence of both the pattern of future SSTs and of increasing atmospheric CO₂ concentrations. For example, CM3, the CMIP5 coupled model using AM3 as its atmospheric component, wetters the Sahel in the 21st century under the high-emissions RCP8.5 scenario [*Biasutti, 2013*], despite AM3's drying response to mean warming.

For a given change in the meridional MSE gradient, the resulting horizontal MSE advection anomaly depends on the climatological horizontal wind. To the extent that the large-scale flow is predominantly rotational, which would be expected to hold more in the upper free troposphere than near the surface, it is likely less sensitive to the underlying convective parameterization – at least this is the case for AM2.1 and AM2.1-UW, between which in the Sahel in the control simulation vertical motion differs greatly but the horizontal wind much less so. A priority for future work, therefore, is characterizing the horizontal MSE advection fields in multiple reanalysis datasets.

4.6 Summary

Four of seven GFDL AGCMs and ten of ten CMIP5 AGCMs respond to uniform SST warming with reduced wet-season precipitation in the Sahel. All seventeen AGCMs respond in the Sahel with an increased meridional MSE gradient and divergence of MSE by horizontal advection and reduced free-tropospheric ascent. For most this sits above anomalous boundary layer ascent, indicating a shallowing (and drying) of the convection. Net TOA radiation also either responds modestly or decreases in all cases.

These consistent qualitative features bolster the credibility of the general arguments set forth in Chapter 3, namely that the increased meridional MSE gradient that arises with mean SST warming acts to increase the horizontal advection of dry, low-MSE air from the Sahara into the Sahel, thereby suppressing moist convection in the Sahel. At the same time, issues of data availability and accuracy notwithstanding, none of the attempted measures from the climatological simulations are correlated sufficiently well with the precipitation response as to merit the basis for an emergent constraint. The present-day climatological ascent profiles in three reanalysis products exhibit some discrepancies but are all largely bottom-heavy, such that, among others, AM2.1's more top-heavy is well removed from the likely real-world range. Satellite retrievals of present-day TOA radiative fluxes provide mixed guidance regarding which models are outside of the observational range for the present-day climatology. But in terms of interannual variability, CERES-EBAF combined with precipitation observations demonstrate that AM2.1 exhibits an excessive feedback on precipitation variations through the accompanying cloud radiative variations.

Though an unambiguous, quantitative observational constraint remains out of reach, we believe that these results substantially improve the overall understanding of and confidence in the effects of mean SST warming on the Sahel and that ample room exists to improve and extend these efforts on both the model and observational sides. Moreover, AM2.1 emerges as an outlier in a number of ways, including its excessively top-heavy ascent profile and the

cloud feedback that will excessively feed back on any drying signal. Thus, we are cautiously optimistic that more definitive constraints are attainable in the near term and will, more likely than not, rule out drying on the scale that it occurs in AM2.1.

Acknowledgments

We thank Fanrong Zeng and Larry Horowitz of GFDL for performing the extended AMIP simulations in AM2.1 and AM3, respectively. We thank Leo Donner, Isaac, Held, and Ming Zhao for scientific guidance. Data for GPCP, TRMM, CERES, and all three reanalyses comes from the GFDL obs4MIPs repository [*Teixeira et al.*, 2014]. CMAP, PREC/L, and U. of Delaware precipitation data were accessed from the NOAA Earth System Research Laboratory (ESRL) Physical Sciences Division (PSD) online repository of gridded climate datasets.

Chapter 5

Sahel rainfall: beyond uniform 2 K

Abstract

Prior studies have demonstrated the sensitivity of rainfall in the African Sahel to sea surface temperature variations in simulations of paleoclimates, the modern observational period, and future anthropogenically-forced warming, and prior chapters in this thesis demonstrate the competing factors of increased dry air advection from the Sahara Desert versus the overall wettening influences of mean warming. Here we further refine this conceptual picture and apply it to select outstanding topics through further idealized SST perturbation simulations that target different aspects of the global SST distribution.

When SSTs are warmed in only the Indo-Pacific warm pool in AM2.1 and AM3, the Sahel responds with drying comparable to the global SST warming simulations, which we interpret (following prior studies) through the response of free tropospheric dry static stability to enhanced deep convection. When SST anomalies corresponding to the full, mean, or spatial pattern components of either greenhouse gas or aerosol forcing, discrepancies among AM2.1, AM3, and HiRAM in the Sahel's response are driven by the mean component, including for the aerosol despite the general focus on their effect on SST spatial patterns. When AM2.1 and AM3 are forced with the observed timeseries of SSTs over the 20th century, both largely capture the observed Sahel rainfall decadal-scale variability on a fractional basis, with contributions from both spatial pattern and mean SST variations.

5.1 Introduction

Chapter 3 demonstrates that the precipitation response to uniform warming in AM2.1 is highly sensitive to the convective parameterization, but the overall energetic response is not: an enhanced meridional MSE gradient increases dry air advection into the Sahel, balanced in part by subsidence-driven MSE convergence. Chapter 4 demonstrates that this overarching energetic response is consistent across seven GFDL and ten CMIP5 AGCMs and generates decreased rainfall in 14 out of 17 of the AGCMs. In this penultimate chapter, we further refine this conceptual picture and apply it to other outstanding questions regarding the Sahel’s response to SST perturbations. We address three questions, one per section (Sections 5.2–5.4), each comprising background information, methodology, and results.

5.2 Localized SST perturbations

Does the impact of uniform SST warming on Sahel rainfall stem inherently from the global-scale thermal and hydrological changes, or does it reflect instead mechanisms relating to one or more particularly effective regions?

5.2.1 Background

Prior modeling studies suggest that Sahel rainfall is insensitive to hemispherically symmetric extratropical SST warming but is suppressed by overall warming of the tropics [Lu and Delworth, 2005; Park *et al.*, 2015]. This is commonly interpreted through qualitative appeals to the “upped-ante” mechanism [Giannini, 2016, and references therein]: warming in the tropical upper troposphere is amplified with respect to the lower troposphere and surface, increasing the dry static stability. All else being equal, this reduces the buoyancy of parcels ascending to these levels, thereby inhibiting their convective rainfall (although if low-level moisture increases sufficiently, this “upped convective ante” can be met and convective pre-

cipitation can actually *increase* with warming). The question then becomes: what portion of tropics-wide SST warming is most important for Sahel rainfall?

One approach would be systematically splitting the global ocean into small regions and imposing the same SST perturbation in each (loosely speaking, computing a Green's function). *Barsugli and Sardeshmukh* [2002] attempt something similar by systematically applying SST anomalies in a GCM over overlapping regions within the Indo-Pacific basin to understand teleconnections. An alternative to this labor-intensive approach is to target specific regions for localized SST perturbations based on physical arguments plausibly linking them to the Sahel. As discussed in Chapter 1, the tropical free-tropospheric lapse rate reflects the precipitation-weighted SSTs rather than their tropical mean value, due to the highly efficient communication of surface conditions aloft by convection. In the QTCM intermediate-complexity model, rainfall responses are similar in simulations with doubled CO₂ and with the tropical mean tropospheric temperature change from the doubled CO₂ run imposed only within the model's convection scheme [*Chou and Neelin*, 2004].

5.2.2 Methodology

We present results from simulations in AM2.1 and AM3 in which SSTs are warmed by 2 K only in the core of the Indo-Pacific warm pool, defined following *Vecchi et al.* [2006] as 5°S-5°N, 80-160°E. To effect upper tropospheric heating in this region directly without altering SSTs, we also present results if simulations in which a 2.4×10^{-6} kg m⁻² burden of black carbon aerosol is added over the Indo-Pacific warm pool in the model level corresponds to roughly 300 hPa.¹ Black carbon absorbs insolation, thereby heating the layer without altering SST gradients. To assess the sensitivity to the size of the heated region, two simulations were performed with different warm pool domains: 10°S-10°N, 90-150° and 5°S-5°N, 105-

¹This are effectively regionally confined versions of the simulations discussed by *Ming et al.* [2010] and *Persad et al.* [2012], but unlike the modified version of AM2.1 used by those studies and *Hill and Ming* [2012] that includes aerosol indirect effects for stratiform clouds, these simulations use the standard AM2.1 version without aerosol indirect effects.

125°E. These simulations and a corresponding control simulation span 17 years, the first discarded as spin-up. The control simulation climate is not identical to that described previously, due to the two sets of simulations being performed at different times with slightly different versions of the model code (in addition to differences in simulation duration). There is no indication that this affects the results appreciably.

5.2.3 Results

Figure 5.1 shows the precipitation responses in AM2.1 and AM3 to 2 K SST warming of the Indo-Pacific warm pool. In both models, rainfall in the Sahel decreases with similar magnitudes (-33% or -1.3 mm day^{-1} in AM2.1; -13% or -0.4 mm day^{-1} in AM3) and spatial structure as in the simulations with uniform 2 K SST warming. In AM2.1, reductions in P , E , and $P - E$, and the convective rainfall fraction P_{conv}/P are each $\sim 2/3$ of those in the uniform warming experiment. Other consistent responses between the warm pool and full warming simulations include local surface warming relative to surrounding regions, reduced shortwave cloud shading, and reduced ascent (not shown).

Like the full SST warming case, drying spans nearly the entire Sahel and east into the Arabian Peninsula and west into the northern flank of the Atlantic ITCZ. In contrast, increased precipitation spanning the Gulf of Guinea coast and the southern flank of the Atlantic ITCZ that occurs in the full warming case is absent when only the warm pool is warmed, implying that they are responding primarily to local SST changes.

We speculate that the enhanced Indo-Pacific convection acts as a triggering mechanism: deep convection in the Sahel is inhibited by the increased static stability. Because of the Sahel's proximity to the Sahara desert, the commensurate anomalous MSE convergence is balanced by increased dry horizontal advection from the Sahara, leading directly to the previously described drying response. Though stabilization of the upper troposphere occurs throughout the tropics (not shown), in no other region is precipitation reduced as much as the Sahel and its direct vicinity (ignoring regions in the direct vicinity of the SST warming),

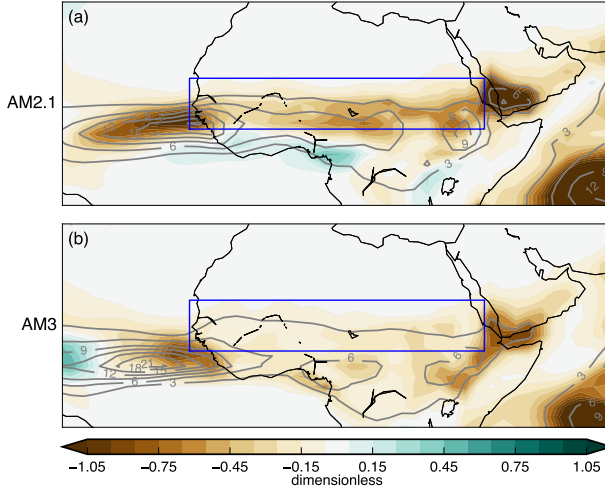


Figure 5.1: Precipitation change in (top) AM2.1 and (bottom) AM3 in response to 2 K SST warming applied only in the Indo-Pacific warm pool. The precipitation response is normalized by the model’s Sahel region-mean control precipitation. Grey contours denote precipitation in the control simulation, in mm day^{-1} . The large precipitation declines in the southeastern most portion of the plotted domain reflect convection near the warm pool being pulled towards the warmed SSTs.

consistent with the crucial influence of the Sahara Desert and with the arguments by *Su and Neelin* [2002] that the effect of anomalous convective heating on remote regions depends on the character of the latter’s climatological circulation.

Figure 5.2 shows the precipitation responses in the Indo-Pacific warm pool black carbon simulations. In the larger region case, precipitation is unambiguously suppressed throughout the Sahel. In the smaller region case, the response is weaker overall, and precipitation actually slightly increases in the far west. In the Sahel region-mean, precipitation decreases by 13 and 5% in the larger and smaller region simulations, respectively. Precipitation is also somewhat lower in the control simulation corresponding to these simulations than in the other control simulation (3.2 and 4.0 mm day^{-1} , respectively).

In summary, these results imply that the remote Indo-Pacific warming induces largely the same set of mechanisms as does the uniform ocean warming, and thereby lend credence to the claim that the increased dry static stability effected by enhanced oceanic convection is the primary influence on Sahelian rainfall arising from mean SST warming. An experiment

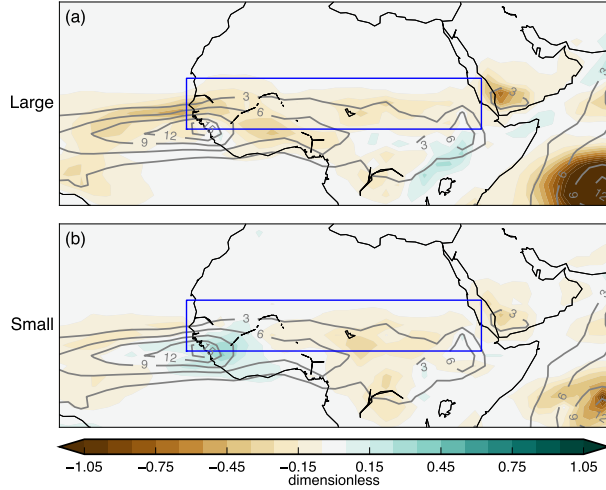


Figure 5.2: Precipitation change in AM2.1 in response to black carbon imposed over (top) large and (bottom) small region over the Indo-Pacific warm pool. The precipitation response is normalized by the model’s Sahel region-mean control precipitation. Grey contours denote precipitation in the control simulation, in mm day^{-1} .

in AM2.1 in which the warm pool is cooled by -2 K likewise captures the salient features of the Sahel hydrological response of its uniform counterpart (not shown).

The analysis presented of the black carbon simulations should be interpreted at the level of proof-of-concept for the argument that tropical upper-tropospheric warming acts to dry the Sahel. We leave for future work more detailed comparison of the Sahel precipitation sensitivity to warm pool SST warming vs. the direct upper tropospheric heating as well as sensitivity tests to the height and concentration of the imposed absorbing aerosol layer.

5.3 Responses to SST spatial patterns

How does the precipitation response to uniform SST change differ from the response to changes in SST spatial patterns, and how does each vary across models?

5.3.1 Background

In addition to the discrepancies in response to uniform SST warming that we have focused on, the future of Sahel rainfall is also clouded by uncertainty due to the response to SST spatial patterns. In addition to any uncertainty due to the direct responses to changes in forcing agents, this also stems from the different SST pattern that each coupled model generates. It would therefore be useful to impose the same patterned SST perturbation field, with and without any mean SST signal removed, in multiple AGCMs.

What are the mechanisms for each ocean basin? Meridional shifts of the West African monsoon rainfall have been associated with meridional gradients in tropical Atlantic SSTs [Lamb, 1978a,b; Giannini *et al.*, 2013], with high precipitation associated with SSTs being anomalously warm in the northern, and cold in the southern, tropical Atlantic. Extratropical Atlantic SSTs, including variations associated with the Atlantic Multidecadal Oscillation, also imprint upon the Sahel [Zhang and Delworth, 2005]. However, in some instances these Atlantic SST variations, while effective at moving the Atlantic ITCZ, do not appreciably alter the continental convection in northern Africa [Palmer, 1986; Bader and Latif, 2003; Lu and Delworth, 2005; Skinner *et al.*, 2012]. A regional model responds to the late-21st century SST anomalies taken from different coupled models largely the same as it does to uniform Atlantic SST warming [Patricola and Cook, 2011]. From the CQE perspective, warming of SSTs in the Gulf of Guinea would weaken the meridional near-surface MSE gradient that fuels the monsoon, thereby inhibiting rainfall in the Sahel [Eltahir and Gong, 1996; Hurley and Boos, 2013]. It has been argued that warming in the Atlantic more generally suppresses rainfall in the Sahel by simply making the ocean comparatively more hospitable to moist convection [Giannini *et al.*, 2003]

For the Indian Ocean, a large upper tropospheric temperature signal emerges in reanalysis data over the Sahel that originates from the deeper and larger Indian monsoon [Nie *et al.*, 2010; Boos and Hurley, 2013], and the Indian monsoon onset has been argued to control the timing of the West African Monsoon onset through a westward propagating disturbance

[Flaounas *et al.*, 2011]. Warming of the Indian Ocean is thought to have contributed appreciably to the 20th century drought [Giannini *et al.*, 2003; Bader and Latif, 2003], potentially through an anomalous Walker cell with ascent over the warmed Indian Ocean waters and subsidence over Africa [Lu and Delworth, 2005]. Based on the argument that condensational heating over India induces a Rossby wave [Matsuno, 1966; Gill, 1980] that then subsides over northern Africa [Rodwell and Hoskins, 1996, 2001], it has been suggested that variations in the intensity of the Indian monsoon have been and will be an important controlling factor on rainfall in the Sahel [Lu, 2009].

For the Pacific Ocean, the impact of ENSO on Sahel rainfall (reduced precipitation during positive El Niño events) is generally interpreted through the aforementioned increased static stability arguments. The pathways of influence for the Pacific Ocean include the El Niño-Southern Oscillation, including through a Kelvin wave originating from E. Pacific precipitation anomalies [Palmer, 1986].

5.3.2 Methodology

We repeat in AM3 and HiRAM the simulations presented in Chapter 2 with the full, mean, or spatial pattern components of greenhouse gas or aerosol SST anomalies. Briefly, the aerosol SSTs comprise 1.1 K tropical-mean cooling that is concentrated in the northern hemisphere, while the greenhouse gas SSTs comprise 2.0 K tropical-mean warming that is polar-amplified but more hemispherically symmetric than the aerosol SST. The imposed SST perturbations are identical across the models for each experiment.² In three additional simulations, the aerosol SSTs anomalies are applied in only one of the Atlantic, Indian, or Pacific oceans. Simulation duration is 17, 21, and 16 years for AM2.1, AM3, and HiRAM, respectively, each

²Inadvertently, for these simulations the AM2.1 control simulation to which the SST anomalies were added uses time-varying observational SSTs over the range 1982-1998 rather than a climatological annual cycle; we do not expect this to alter the results appreciably, although the response to the mean greenhouse gas SST warming, which is 2.04 K, is somewhat smaller in magnitude than the 2 K response presented in Chapter 3. Also, as was the case in Chapter 4 for the uniform 2 K SST warming simulations in various GFDL models, the underlying observational SST dataset and averaging period differs across the models.

with the first year discarded as spin-up. As in prior simulations discussed in this thesis, all of these simulations include fixed, present-day atmospheric composition the same as in the control.

5.3.3 Results

Figure 5.3 shows the precipitations responses in the aerosol SST anomaly full, mean, and spatial pattern simulations. Each of AM2.1, AM3, and HiRAM respond to the aerosol spatial pattern SST anomalies with similar magnitude drying in the Sahel (-0.8 , -0.6 , and -0.7 mm day^{-1} , respectively). Consistent with Chapter 4 and the wide range SST simulations, the mean cooling component strongly increases Sahel rainfall in AM2.1 ($+1.9 \text{ mm day}^{-1}$), slightly in AM3 ($+0.2 \text{ mm day}^{-1}$), and not at all in HiRAM ($+0.0 \text{ mm day}^{-1}$). Consequently, the response to the full SSTs is dominated in AM2.1 by the wettening effect of mean cooling ($+0.7 \text{ mm day}^{-1}$) but in AM3 and HiRAM by the drying influence of the SST spatial pattern (-0.4 and -0.5 mm day^{-1} , respectively).

Figure 5.4 shows the precipitation response to the full aerosol SST anomaly field applied individually to the Atlantic, Indian, and Pacific basins. The Atlantic SST anomalies unambiguously dry the Sahel (-1.4 , -0.5 , and -1.0 mm day^{-1} in AM2.1, AM3, and HiRAM, respectively). Conversely, the Pacific SST anomalies wetten the Sahel ($+2.8$, $+1.3$, and $+0.9 \text{ mm day}^{-1}$), as do the Indian ocean SST anomalies to a lesser extent ($+1.3$, $+0.1$, and $+0.4 \text{ mm day}^{-1}$). In AM2.1, the Pacific and Indian oceans' respective wettening effects are concentrated in the eastern and western Sahel. Given the Pacific's greater proportion of total ocean area, it is reasonable to attribute its wettening effect largely to its imprint on the tropical mean SSTs. Moreover, the response in AM2.1 to the Pacific SST anomalies is concentrated in the northeastern Sahel and southern Arabian Peninsula wherein, as described in Chapter 3, 2 K SST warming induces essentially runaway drying and warming.

The effect on precipitation of the aerosol SST spatial pattern is more pronounced in absolute terms over the adjacent Atlantic ITCZ, especially its northern flank, than in the

Sahel, although this scales to some extent with the differences in climatological precipitation. In AM3 and HiRAM, this bears the signature of a southward shift in the full and spatial pattern cases, but in the Atlantic-only SST anomaly case the response is more uniformly (and greater magnitude) drying. As described in Chapter 3, uniform SST warming also drives strong drying of the Atlantic ITCZ northern flank. Qualitatively, these responses are akin to the two mechanisms argued by *Giannini* [2016] to dominate Sahel rainfall variations: suppression by mean warming and/or by a tropical Atlantic SST meridional dipole with relative cooling of the northern hemisphere Atlantic.

Figure 5.5 shows the precipitation responses in the full, mean, and spatial patterns simulations for the greenhouse gas SST anomalies. The precipitation response to the full greenhouse gas SST anomaly field is -1.0 , -0.3 , and $x.x$ in AM2.1, AM3, and HiRAM, respectively. As is the case for the aerosol SSTs, the precipitation response to the spatial pattern component ($+0.9$, 0.3 , and 0.6 mm day^{-1} for AM2.1, AM3, and HiRAM, respectively) is more consistent across models than to the mean component (-1.0 , $(\backslash)0.3$, and $+0.0 \text{ mm day}^{-1}$ for AM2.1, AM3, and HiRAM, respectively). The spatial pattern of polar-amplified SST warming, which warms high latitudes relative to the tropics, causes increased precipitation in the Sahel. This is qualitatively consistent with the argument made by *Park et al.* [2015] that Arctic-amplified SST warming induces increased precipitation in the Sahel as part of a broader northward shift of the ITCZ.

The Sahel rainfall responses to the mean/spatial pattern decomposition of SST anomaly fields appears largely linear, insofar as there are no instances of the response to a full field differing qualitatively from the sum of the responses to its components (either mean plus spatial pattern or, for aerosols, the individual ocean basins). This is consistent with the broadly linear responses of the zonal mean circulation and energetic fields in AM2.1 in these simulations presented in Chapter 2. The response to the aerosol SST ocean basin decomposition exhibits more nonlinearity. For AM2.1, the sum of the precipitation responses to the ocean basin simulations is $+2.7 \text{ mm day}^{-1}$, much larger than the full aerosol SST

anomaly simulation response of $+0.7 \text{ mm day}^{-1}$. For AM3 and HiRAM, the ocean basin sum is also more positive than the full response, such that in both models the former is positive and the latter negative ($+0.8 \text{ vs. } -0.4 \text{ mm day}^{-1}$ in AM3; $+0.3 \text{ vs. } -0.5 \text{ mm day}^{-1}$ in HiRAM). The reasons for this are still to be determined, but the consistency in sign hint at a potentially identifiable underlying physical mechanism.

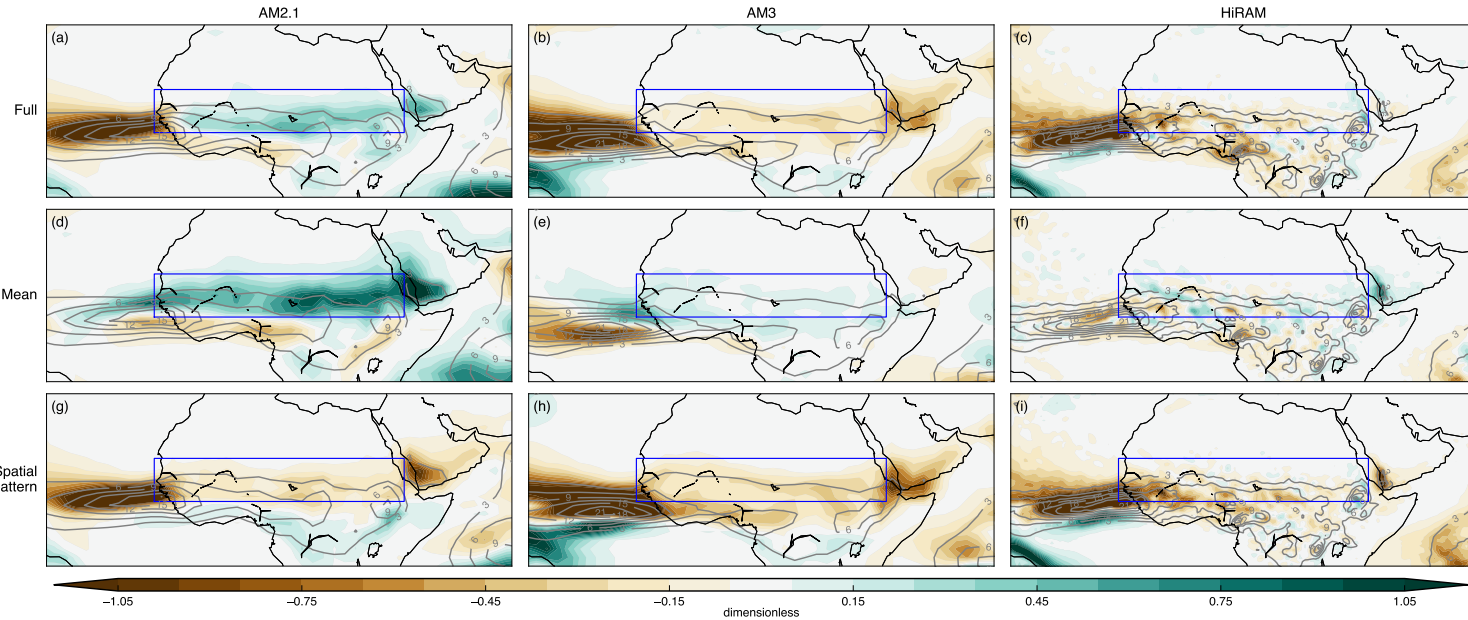


Figure 5.3: Precipitation change in (left column) AM2.1, (center column) AM3, and (right column) HiRAM in response to SST anomalies corresponding to the (top row) full, (center row) tropical mean component applied uniformly, or (bottom row) the spatial pattern component, i.e. the full field minus the tropical mean, of the aerosol SST anomalies. The precipitation response is normalized by the model's Sahel region-mean control precipitation. Grey contours denote precipitation in the control simulation, in mm day^{-1} . Because of slight differences in simulation duration and boundary conditions, the control precipitation contours differ slightly between these simulations and the control simulations presented in Chapter 3.

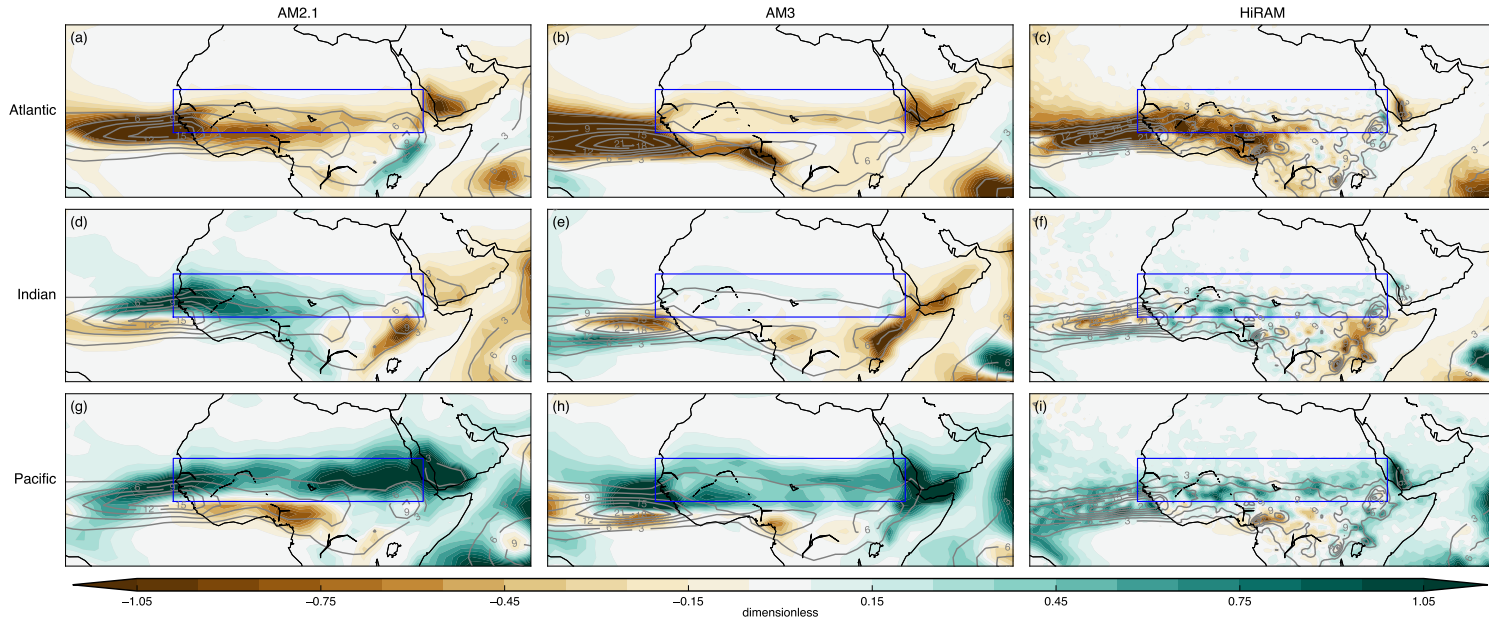


Figure 5.4: [Same as Figure 5.3, but for the response to the full aerosol SST anomaly field applied to individual ocean basins.] Precipitation change in (left column) AM2.1, (center column) AM3, and (right column) HiRAM in response to the aerosol SST anomaly field applied in only the (top row) Atlantic, (center row) Indian, or (bottom row) Pacific ocean. The precipitation response is normalized by the model's Sahel region-mean control precipitation. Grey contours denote precipitation in the control simulation, in mm day^{-1} . Because of slight differences in simulation duration and boundary conditions, the control precipitation contours differ slightly between these simulations and the control simulations presented in Chapter 3.

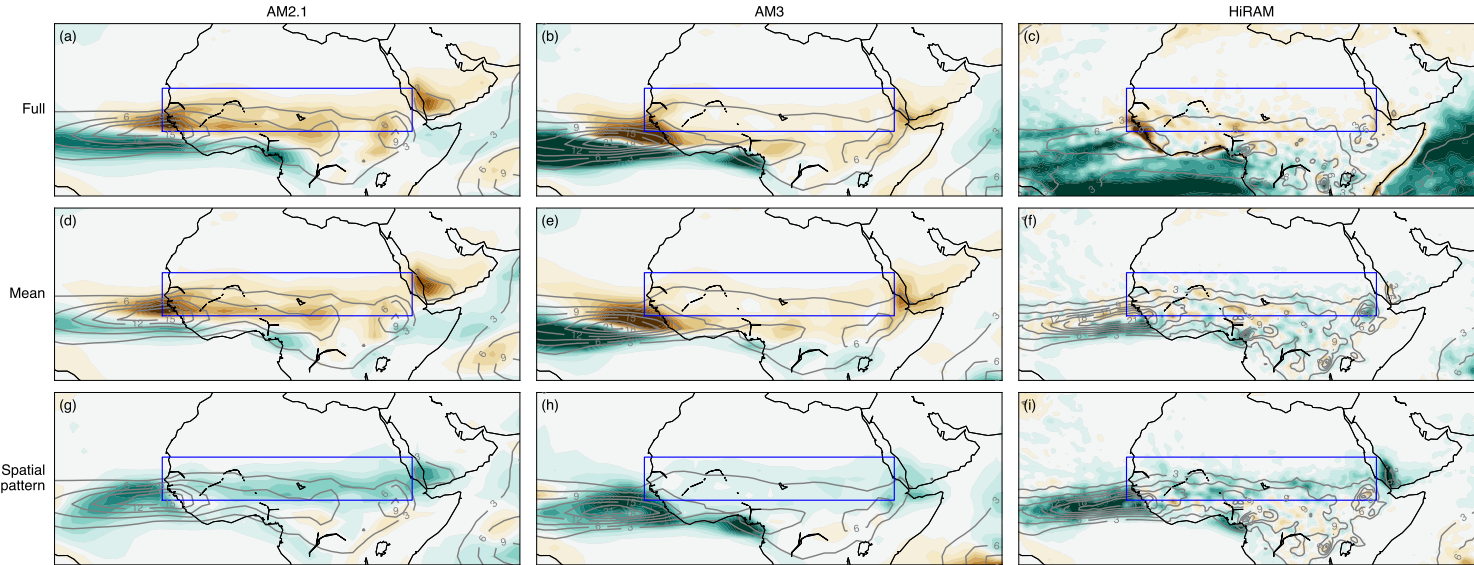


Figure 5.5: [Same as Figure 5.3, but for the greenhouse gas SST anomalies.] Precipitation change in (left column) AM2.1, (center column) AM3, and (right column) HiRAM in response to SST anomalies corresponding to the (top row) full, (center row) tropical mean component applied uniformly, or (bottom row) the spatial pattern component, i.e. the full field minus the tropical mean. The precipitation response is normalized by the model's Sahel region-mean control precipitation. Grey contours denote precipitation in the control simulation, in mm day^{-1} . Because of slight differences in simulation duration and boundary conditions, the control precipitation contours differ slightly between these simulations and the control simulations presented in Chapter 3.

5.4 Simulations of 20th century variations

What are the relative roles of the mean and spatial pattern components of SSTs in observed decadal-scale Sahel rainfall variability?

5.4.1 Background

Much of the existing literature on observed 20th century Sahel rainfall variations focuses primarily on SST spatial patterns, especially in the Atlantic Ocean. But given observed global mean surface warming over the century approaching 1 K, combined with acute sensitivity to mean SST warming in AM2.1 and other models, it is not self evident that spatial patterns have been dominant.

5.4.2 Methodology

We use extended AMIP simulations in AM2.1 and AM3 and standard AMIP simulations in HiRAM and the CMIP5 models, all originally presented in Chapter 4. Note that for the HiRAM and CMIP5 models, atmospheric composition is time-varying, whereas in the long-running AM2.1 and AM3 simulations, it is fixed at present-day values; *Dong and Sutton* [2015] argue based on single-forcing GCM simulations that the recovery from drought over the past 30 years largely derives from the direct influence of increased greenhouse gas concentrations. The number of ensemble members available to average over is 10, 3, and 2 respectively for AM2.1, AM3, and HiRAM. We also compare the model simulated decadal-scale precipitation variability to observations using the Climate Research Unit (CRU) TS3.22 dataset of precipitation, spanning 1900-2013. We apply a five-year running average to suppress interannual variability and highlight the longer decadal-scale phenomena of interest.

We compute the approximate contributions of the mean and spatial pattern components of global SSTs to anomalous precipitation in each year as follows. For each year, the July-August-September global-mean surface air temperature over ocean is used to linearly scale

each model's response to 2 K SST warming. The spatial pattern contribution is then assumed to be the residual between the total precipitation anomaly and this mean contribution. One drawback of this relatively simplistic methodology is that any unforced natural variability gets subsumed into the spatial pattern component.

The long-term mean precipitation in the Sahel varies substantially among models, and this constant offset can make comparisons of variability more difficult. At the same time, these climatological differences may also come to bear on the variability, based on the arguments in Chapter 3 linking the response to SST warming to the climatological circulation depth. As such, we present results with and without normalization. Averages for normalization are taken over 1979-1999, the period shared across all of the simulations and the observations.

5.4.3 Results

Figure 5.6 shows the timeseries of Sahel region-mean precipitation in the CRU observations and in the AMIP simulations in AM2.1, AM3, and HiRAM. Both AM2.1 and AM3 broadly capture the multidecadal variability in Sahel rainfall on a fractional basis over the entire 20th century. In raw terms, AM2.1 has a larger mean precipitation than AM3, and the multidecadal variability scales with the mean value (at least in these two models), leading the two to collapse nearly onto each other when normalized by the mean value. HiRAM captures the overall trend of increased precipitation from a minimum in the early 1980s onward, but with insufficient magnitude.

In AM2.1, the extreme 5-year average precipitation deviations from the mean are -1.3 and $+1.7 \text{ mm day}^{-1}$ in 1991 and 1952 respectively, and the corresponding global ocean mean temperature values are -0.4 and $+0.5$ for a 0.9 K range. In comparison, the difference in Sahel precipitation between the $+0.5$ and -0.5 K simulations in AM2.1 is 1.7 mm day^{-1} , which scaled to 0.9 K would amount to 1.6 mm day^{-1} . In other words, the span of ensemble-mean Sahel JAS precipitation variations associated with global mean temperature in AM2.1

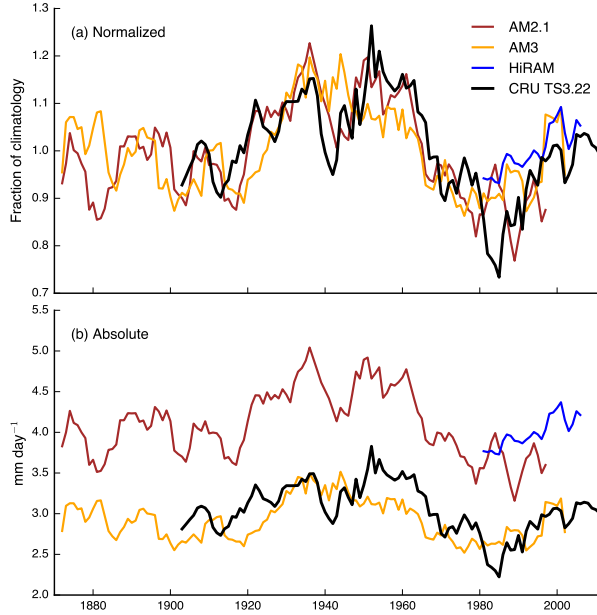


Figure 5.6: Time series of Sahel region-mean precipitation in the (thick black curve) CRU TS 3.22 observational dataset and in the AMIP simulations in (brown curve) AM2.1, (orange curve) AM3, and (blue curve) HiRAM, either (a) normalized by the time-mean precipitation (unitless) or (b) without normalization (mm day^{-1}).

is larger than half of the total span. In the CRU TS3.22 surface temperature data, July-August-September global mean surface temperature varies, in terms of the difference between the maximum and minimum global mean JAS temperatures in individual years, by 0.55 K, over the period 1901-2013 (0.32 K above the climatology in 2005; 0.23 K below the climatology in 1912). In comparison, the actual extreme values of Sahel JAS precipitation in the CRU data are -1.3 and $+1.7 \text{ mm day}^{-1}$ (1984 and 1950, respectively), for a total range of 3.0 mm day^{-1} .

One implication of these results is that, if the real-world sensitivity to global mean SST is similar to AM2.1 and AM3, then the observed variability in Sahel rainfall has had a non-negligible contribution from mean SST change. On the other hand, if the real-world sensitivity is more like HiRAM's, then spatial patterns are entirely to blame. (And, if the real-world is most like AM2.1-UW and c48-HiRAM, the mean warming will have had a potentially discernible wetting influence.) In terms of attribution, this extended-AMIP methodology with unchanging atmospheric composition and observed SSTs is agnostic to

the cause (anthropogenic or natural) of the temperature variations; moreover the relative contributions by the long-term warming signal induced by anthropogenic forcing and by internal variability to decadal variations in global mean temperature remains an area of vigorous research [e.g. *Trenberth*, 2015].

Figure 5.7 shows the Sahel region-mean timeseries of JAS rainfall in the CMIP5 AMIP simulations, (note the much shorter 1979-2008 timespan). The differences in time-mean precipitation are even more pronounced than across the GFDL models. As is the case for the GFDL models, all of the CMIP5 models capture the overall wetting over this span but generally with insufficient magnitude relative to the observations.

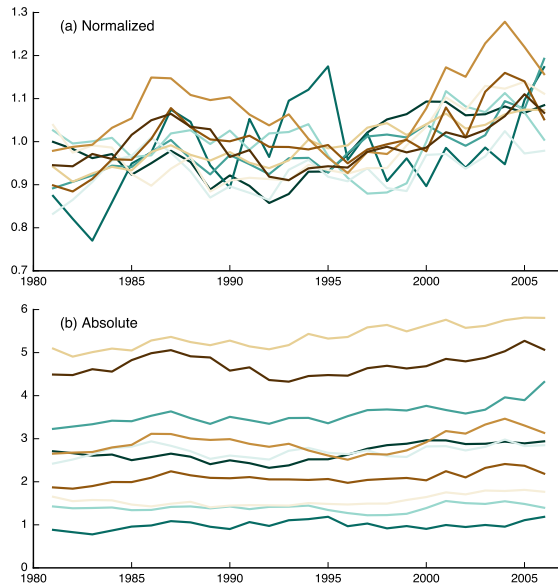


Figure 5.7: Time series of Sahel region-mean precipitation in the “amip” simulations in the ten CMIP5 AGCMs, (a) normalized by the time-mean precipitation (unitless) or (b) without normalization (mm day^{-1}). Each model’s curve is colored according to the legend in Figure X of Chapter 4.

5.5 Discussion

5.5.1 Local SST warming

The sensitivity of our warm pool warming simulation to the region boundaries and SST perturbation magnitude should be further examined. The region extends appreciably into the Indian Ocean, and warming of the Indian Ocean has been posited by prior authors as a direct drying influence on the Sahel.

Repeating the warm pool SST warming experiment in AM2.1-UW could provide a unique test of the drying influence of increased dry static stability. We have argued that its wettening response in the Sahel to uniform SST warming derives from the overall moistening of the boundary layer, which would not occur in this configuration. Meanwhile, we are conceptualizing the modest increase in precipitation in AM2.1-UW (and c48-HiRAM) as the result of the wettening influences of overall warming slightly outweighing the drying influences unique to the Sahel; the former are presumably absent in the case of Indo-Pacific warming.

5.5.2 Roles of SST mean and spatial pattern

The precipitation response in the AM2.1 aerosol full anomaly simulation [c. f. Figure 5(a)] bears a strong similarity to the response to 10 ka orbital precession in AM2.1, both for fixed SSTs and with a 50 m depth mixed-layer ocean [Smyth *et al.*, 2016]. In particular, precipitation increases over the Sahel, in contrast to the sharp precipitation reduction in the adjacent Atlantic ITCZ and the zonal-mean southward shift of the ITCZ due to the northern hemisphere-centric cooling. The same behavior – increased precipitation in the Sahel despite southward displacement of the zonal mean ITCZ – is present in the 10 ka orbital precession simulations, wherein it is much more counterintuitive: prevailing wisdom regarding the response of tropical precipitation to meridional energy gradients would lead to the intuition that the ITCZ would shift north in the 10 ka experiment, wherein the boreal

summer insolation gradient is enhanced.

The results regarding the relative importance of the mean and pattern components of SSTs are agnostic to the cause of the SST variations, i. e. whether anthropogenically forced or natural variability. On the one hand, the fact that the spatial pattern component of aerosol SST anomalies robustly causes Sahel drying in the three AGCMs supports the claim made by numerous studies that aerosol-induced Northern Hemisphere cooling acts to reduce precipitation in the Sahel. On the other hand, the full aerosol SST anomalies cause increased precipitation in the Sahel in AM2.1, due to the overpowering effect of its response to mean SST cooling. As noted in Chapter 2, ultimately these SST anomalies arise in a mixed-layer ocean model, and a dynamically active ocean may yield appreciably different patterns in the response (although the overall meridional gradient would be expected regardless).

5.5.3 Observed and simulated 20th century variability

How will the impact of mean SST warming change as climate changes? One potential means of determining this would be to modify the methodology we utilize for the AMIP simulation for application to the coupled 21st century simulations in CMIP5. If Sahel region-mean annual- or decadal-mean Sahel region-mean precipitation is plotted against global mean temperature in those simulations, eventually the models will diverge (given the large spread in Sahel precipitation in the RCP simulations). At what point does that occur? How does that relationship compare to the wide range SST experiments, e. g. in the RCP simulations with GFDL-CM3 vs. AM3? And how does the response in the 21st century simulations compare to the scaled sum of the responses to the 4 K and $4\times\text{CO}_2$ prescribed SST simulations? Given each coupled model's transient climate response, one could determine the fractional CO_2 change per unit global mean SST change, and then sum the responses of the CO_2 simulation scaled to that value with the SST warming simulation scaled to 1 K, although the latter is complicated by the saturation above $\sim 1\text{-}2$ K discussed above. Nevertheless, comparison of these responses to the precipitation responses per K global mean SST increase

in the RCPs could provide a measure of the influence of the relative factors, including the spatial pattern of SSTs and forcing agents other than CO₂

Supposing a model can reproduce the observed decadal-scale variations in Sahel rainfall when forced by the timeseries of observed SSTs, intuitively this would lend confidence in its response to other perturbations. But if the 20th century variations largely reflect the influence of SST spatial patterns, then it is possible that models will diverge in their responses moving forward as the mean warming signal becomes larger. In particular, if the AMIP simulations were extended using SSTs extending closer to the present and/or with the SSTs taken from an RCP simulation, presumably the model responses will diverge as the mean warming signal grows larger. An explicit test of these arguments would be to create separate timeseries of the monthly-resolved mean and spatial patterns of the SST field, and run the models with these timeseries as the boundary condition.

Acknowledgments

We thank Zhaoyi Shen for performing the black carbon simulations. We thank Leo Donner, Ming Zhao, and Isaac Held for scientific guidance.

Chapter 6

Conclusions

6.1 Summary

Using simulations in multiple comprehensive AGCMs and comparisons with observations, this thesis attempts to identify mechanisms by which perturbations to sea surface temperatures alter tropical energetic and hydrological fields, with an emphasis on separating those changes associated with changes in the tropical- or global-mean SST value from those associated with changes in the spatial pattern of SSTs. After motivating the problem and reviewing the relevant theory – most importantly, the column-integrated moist static energy budget – in Chapter 1, the tropical SST-precipitation-MSE budget links are investigated in the zonal mean framework (Chapter 2) and the Sahel region of Africa (Chapters 3-5).

Chapter 2 uses equilibrium SST anomaly fields derived from a mixed-layer ocean-AGCM perturbed with anthropogenic burdens of aerosols or greenhouse gases, each field then split into mean and spatial pattern components, to investigate the response of zonal-mean energy transports and their relation to meridional shifts of the ITCZ. For SST anomalies due to either forcing agent, the anomalous energy transports are largely consistent with expectations from prior literature; for example, poleward energy transport is generally increased with greenhouse gas warming [e.g. *Hwang and Frierson, 2010*], while the preferential cooling of the northern hemisphere by aerosols induces compensating northward energy transport and a southward shift of the ITCZ [e.g. *Ming and Ramaswamy, 2011*]. While changes in the Hadley cell mass flux contribute some fraction of the anomalous energy fluxes, away from the cell edges the (often neglected) Hadley cell GMS response is generally of at least comparable

importance, if not dominant. By combining the estimate for Hadley cell GMS of *Held* [2001] with thermodynamic scaling of lower-tropospheric moisture change with surface temperature [*Held and Soden*, 2006], we develop the “stable-get-stabler” scaling for the GMS response to SST changes: because of the fractional increase in specific humidity per degree warming, near-surface moisture and thus MSE will increase more where moisture is climatologically high; thus, approximating GMS as the difference between lower level MSE at the ITCZ and locally, mean SST warming increases GMS more in climatologically dry regions where it is already large. This dependence of the thermodynamically-controlled changes in GMS at a given latitude on the climatological humidity difference between the given latitude and the ITCZ yields a heuristic argument for the well-documented tight correlation between ITCZ displacements and anomalous cross-equatorial energy fluxes: near the ITCZ (which is generally near the equator), changes to the circulation – and with them, the position of the ITCZ – are simply the more viable means of yielding an anomalous energy flux.

The remaining chapters focus on the African Sahel. Using an adjustment procedure that ensures closure of column budgets of conserved tracers, Chapter 3 presents a precise accounting of the MSE budget in the Sahel in control and uniform 2 K SST warming simulations in two versions of AM2.1 varying solely in their convective parameterization. Replacing the default, Relaxed Arakawa-Schubert convective parameterization with the University of Washington convective parameterization causes the Sahel precipitation response to SST warming to change fundamentally, from a 40% decrease to a 6% increase. With both parameterizations, the MSE difference between the Sahel and the Sahara is enhanced with warming, which acted upon by prevailing northerly flow yields increased advective MSE divergence in the Sahel. This gradient is enhanced more in RAS than in UW throughout the free troposphere, which we hypothesize results from the deeper prevailing convection in RAS transporting increased moisture over a greater depth. In the mid-troposphere, because the moist static stability is small, balancing the anomalous horizontal dry air advection requires sharp subsidence. With UW, these mechanisms act with much weaker magnitudes

such that they are apparently outweighed by the general wettening influences of overall warming. In simulations over a wide range of SSTs, this overall energetic response to SST warming persists in both model variants, indicating that it arises from large-scale fields not sensitive to the convective parameterization, but the precipitation response in UW and RAS remain of opposite sign, implying that convective processes nevertheless still play a key role in its hydrological imprint. Thus, focusing solely on either component is insufficient to fully understand the overall behavior.

In an attempt to develop an emergent observational constraint on the Sahel rainfall response to warming, Chapter 4 extends the analysis of Chapter 3 to control and 2 K warming simulations in five other GFDL AGCMs and to CMIP5 uniform 4 K SST warming simulations in ten AGCMs from eight other modeling institutions and to satellite estimates of TOA radiative fluxes and reanalysis estimates of MSE budget quantities. An enhanced meridional MSE gradient, anomalous free-tropospheric descent, increased horizontal advective MSE divergence, and anomalous vertical advective MSE convergence in the Sahel are robust across all models in response to uniform SST warming, and this leads to reduced precipitation in 14 out of 17 of the AGCMs. AM2.1 is an outlier not only in the magnitude of its drying but also in its lack of an appreciable reduction in the net TOA radiative flux, which occurs in nearly every other model as part of the MSE budget response. Among the GFDL models, the precipitation response is almost perfectly correlated with the anomalous descent in the mid-troposphere, which in turn is well correlated with the climatological ascent profile, consistent with the arguments presented in Chapter 3. However, across the ten CMIP5 models, the precipitation response is not well correlated with either the climatological or perturbation ascent, which hamstrings attempts to use the climatological convective depth as an emergent constraint. Complications arise on the observational side also, including, for purely satellite-based observational proxies for convective depth, sensitivity of the models' accuracy relative to the likely observational range based on the choice of the convective depth proxy. Reanalyses suggest that several of the models that dry most severely with

warming have climatological ascent profiles that are too top-heavy, which in our formulation would exacerbate their drying response. Comparing interannual variability in observations and extended AMIP simulations in a subset of the GFDL models, variations in the cloud radiative properties are too strong per unit precipitation in AM2.1, and this likely creates a positive feedback on drying or wettening.

Chapter 5 addresses three other outstanding questions regarding the relationship among SSTs and the Sahelian MSE budget and precipitation field.

- In simulations in AM2.1 and AM3 with warming confined to the Indo-Pacific warm pool, precipitation decreases over the Sahel with nearly the same magnitude and character as in the case of uniform ocean warming over the entire globe. This provides anecdotal support for the claim [e. g. *Giannini*, 2016] that increased free-tropospheric dry static stability is the primary drying influence on the Sahel with warming.
- In the full, mean, and spatial pattern simulations of Chapter 2 repeated in AM3 and HiRAM, discrepancies among the three models in the Sahel rainfall response to either the greenhouse gas or aerosol SSTs stem primarily from the mean component: all three models dry the Sahel in response to the spatial pattern component of aerosol-induced SST anomalies, but in AM2.1 this is outweighed by the strong wettening influence of the mean cooling component. Therefore, even for SST anomalies with coherent, large-magnitude SST spatial structure, interpreting AGCM responses requires accounting for their response to the mean component of the SST change.
- In extended AMIP simulations in AM2.1 and AM3 with the observed timeseries of SSTs over the entire 20th century, both models capture qualitatively the main decadal-scale variations in Sahel rainfall compared to observations, in particular the maximum in the 1950s and 1960s giving way to the severe drought in the 1970s and 1980s and the subsequent partial rainfall recovery. Based on the time series of global mean SST, mean SST varies with a magnitude that contributes up to 1 mm day^{-1} variation in AM2.1.

The CMIP5 AMIP simulations are also broadly consistent with the 1979-2008 overall recovery in precipitation, although for both sets of models absolute precipitation values vary widely.

6.2 Implications, limitations, and future work

As noted in Chapter 1, we deliberately focus on the response to SST perturbations, sidestepping to the extent possible the issue of the direct response to forcings that occurs on a faster timescale than does the SST adjustment. The perturbed SST simulations presented act as idealized perturbations intended to isolate particular mechanisms of interest. This is useful only to the extent that the fast, direct response and the slow, SST-mediated responses are separable (the same issue as for the decomposition into mean and spatial pattern components of the SST anomaly fields done in Chapters 2 and 5). Because of these timescales, imposing SST perturbations that (however idealized) represent the effect of some forcing agent without that forcing agent itself being perturbed is less physically self-consistent than is the other way, i. e. holding SSTs fixed and examining the direct response to the perturbed forcing agent that would precede any SST-mediated response. Perhaps the most appropriate methodology moving forward would therefore be taking the difference between (1) simulations with both SSTs and the forcing agent perturbed and (2) simulations with control SSTs and the forcing agent perturbed. That way, the fast, direct response is included in both the control and perturbation simulations.

6.2.1 Zonal mean

The biggest outstanding issue from Chapter 2 is understanding why the GMS “stable-get-stabler” scaling fails for the greenhouse gas case. In their study of changes in the width of the Hadley cell ascent branch over a wide range of climates in the idealized moist GCM, *Byrne and Schneider [2016]* find that GMS does not behave in accordance with the “stable-

get-stabler” scaling. Given this result in a more idealized model, it may be fruitful to assess the scaling more systematically in an idealized framework, which would enable more clear delineation of the minimal sufficient conditions under which the scaling holds.

Several of the Hadley cell GMS results in *Hill et al.* [2015] were noted by *Chou et al.* [2013], although in that study GMS is defined on a latitude-longitude basis rather than for the zonal mean circulation and imposes an analytically defined vertical velocity profile at each gridpoint that corresponds to deep convection. They demonstrate that GMS thus defined increases with warming robustly in CMIP3 and CMIP5 21st century simulations, and that this reflects deepening of the divergent circulation and therefore increased dry static energy export aloft that exceeds the increase in latent energy convergence near the surface due to increased moisture. The direct thermodynamic changes alone without accounting for the deepening of the circulation would actually yield decreased GMS. The GMS response also largely reinforces the existing spatial pattern of GMS (see their Figures 3 and 4). Unlike the zonal mean GMS that is smallest near the ITCZ and increases toward the subtropics, GMS in the latitude-longitude framework is largest where convection is deepest. This is because the convective outflow can be assumed to occur in essentially all directions: in the zonal mean context the meridional energy fluxes are signed, and this isotropic behavior causes northward and southward components to largely cancel.

The studies of *Kraus* [1977b,a] argue for the co-location of the ITCZ with the energy flux equator, present an analytical model for the ITCZ position throughout the annual cycle under this assumption, and argue based on observations for a southward shift of the zonal mean ITCZ based on anomalous northward energy transport contributing to 1970s drought in the Sahel and other northern hemisphere subtropical regions on the margin of the ITCZ seasonal migration. But they have been woefully under cited in the modern literature on the energetic framework for ITCZ displacements – insofar as Google Scholar citation tracking is accurate, not one of the papers addressing the ITCZ energetic framework from a theoretical perspective reference them. The precise form of their analytical model, which is purely

diffusive, is not entirely justifiable, and their subsequent derivation of analytical solutions in terms of Legendre polynomials is not especially physically enlightening, but these were nonetheless pioneering works that merit much greater notoriety than they have received.

An overall weakening of the Hadley cells with warming would manifest as a scaling down of the circulation over the whole cells, whereas the largest anomalies in our simulations are near the equator. Also, the mass flux anomalies, though centered within the winter hemisphere cell, do extend into the summer hemisphere cell. This would imply an equatorward ITCZ shift throughout the annual cycle. This contrasts the findings of *Dwyer et al.* [2014], who show in CMIP5 models that the tropical precipitation annual cycle amplitude robustly increases in 21st century simulations, driven primarily by the mean warming signal (based on a uniform 3 K SST warming simulation). *Bischoff and Schneider* [2014] also find increased seasonal ITCZ migrations with global warming in an idealized moist GCM, which they attribute to increased cross-equatorial energy transport. From the *Bischoff and Schneider* [2014] framework, the apparent equatorward shift in our simulations could occur if the net energetic input near the equator increases sufficiently to counteract the increased cross-equatorial energy transport. Potential future work could entail more careful analysis of our results based on these other perspectives in order to reconcile seemingly incongruous results.

Applying the analyses from Chapter 2 to the full/mean/spatial pattern suite in AM3 and HiRAM could provide more context regarding which of the results are robust and which are idiosyncratic to AM2.1 – an issue made more concerning by that model’s singular behavior with regard to the Sahel’s response to SST perturbations. The wide SST range simulations may also be useful, if for example the scaling performs better at smaller magnitude SST changes.

A more satisfying approach to the zonal mean energy transport calculations than inferring the transient eddy term as a residual would be to explicitly compute it. This residual methodology is for expediency and to ensure exact closure of the MSE budget. We have

begun the process of re-formulating the budget adjustment method presented in Chapter 3 for these purposes.

6.2.2 The Sahel

The character of the convection and MSE budget changes steadily in the meridional, and this complicates the interpretation of regional averages. Although averaged over the entire Sahel the meridional advection is a leading order term in the vertically integrated MSE and moisture budgets, within the more convective southern Sahel the canonical tropical convection zone balance exists between the source terms and the convergence. Conversely, in the north the convergence term is small and changes to the net energetic source term is balanced by horizontal advection. But the climatological precipitation distribution extends appreciably into the northern Sahel, as do the reductions in precipitation with ocean warming, thereby limiting the utility of considering the northern and southern halves independently. Models commonly displace the entire West African Monsoon circulation meridionally relative to one another and to observations, or even for a single model with different treatments of moist convection [Marshall *et al.*, 2013; Birch *et al.*, 2014].

It would be interesting to assess how well the meridional overturning circulation in the eastern Sahel adheres to the CQE framework. As noted in Chapter 1, climatological precipitation in the Sahel is to first order zonally symmetric, but many studies [e.g. Nie *et al.*, 2010] focus solely on the western Sahel, presumably to restrict to longitudes directly north of the Gulf of Guinea wherein a classical monsoon circulation can most likely be found. It could be that the meridional overturning circulation does indeed differ markedly in the east and west, in which case the drying influence of the Sahara Desert acts to homogenize precipitation zonally in the Sahel through its overwhelming drying influence. At the same time a relatively robust result across CMIP5 future simulations (much more so than the region-mean precipitation change) is a zonal dipole, with drying in the west and increased precipitation in the east [Biasutti, 2013].

Work in a more idealized setting could be informative, for example the idealized moist GCM of *Frierson et al.* [2006] modified from its standard aquaplanet configuration to include a subtropical continent. As regards the effect of SST spatial patterns, an imposed SST profile based on the superposition of analytic functions, each representing the most robust and/or most important patterns associated with global warming (namely mean warming and Arctic amplification). Their relative magnitudes could then be varied and the effect on summer monsoon precipitation over the subtropical continent examined. The longwave absorber could also be modified.

Because the direct, non-SST-mediated response to a perturbed forcing agent occurs on a faster timescale than the SST-mediated response, it is somewhat contrived to examine the latter in isolation, since in reality it would occur after the former. One potential means of teasing out the relative roles of the mean warming, SST spatial patterns, and direct forcing response would be joint analysis of the `amip4xC02` and `amipFuture` simulations in the CMIP5 archive. The response in the `amip4K` simulations could be scaled to match the mean SST warming in the `amipFuture` simulations, and their difference (assuming linearity) could be considered to be the spatial pattern component of the SSTs. Separately, each model's climate transient climate response (TCR, i. e. the global mean temperature change at the time of CO₂ doubling in an 1% year⁻¹ CO₂ increase simulation) could be used to estimate the amount of SST warming per unit CO₂ increase. All else being equal, models that warm slower (i. e. have lower TCR) would be expected to be more affected by the direct, fast response relative to the slow, SST-mediated response, per unit combined SST-and-CO₂ change.

Bibliography

- Adam, O., T. Bischoff, and T. Schneider (2016a), Seasonal and Interannual Variations of the Energy Flux Equator and ITCZ. Part I: Zonally Averaged ITCZ Position, *J. Climate*, 29(9), 3219–3230, doi:10.1175/JCLI-D-15-0512.1.
- Adam, O., T. Bischoff, and T. Schneider (2016b), Seasonal and interannual variations of the energy flux equator and ITCZ. Part II: Zonally varying shifts of the ITCZ, *J. Climate*, doi:10.1175/JCLI-D-15-0710.1.
- Adler, R. F., G. J. Huffman, A. Chang, R. Ferraro, P.-P. Xie, J. Janowiak, B. Rudolf, U. Schneider, S. Curtis, D. Bolvin, A. Gruber, J. Susskind, P. Arkin, and E. Nelkin (2003), The Version-2 Global Precipitation Climatology Project (GPCP) Monthly Precipitation Analysis (1979–Present), *J. Hydrometeor*, 4(6), 1147–1167, doi:10.1175/1525-7541(2003)004<1147:TVGPCP>2.0.CO;2.
- Allen, M. R., and W. J. Ingram (2002), Constraints on future changes in climate and the hydrologic cycle, *Nature*, 419(6903), 224–232, doi:10.1038/nature01092.
- Arakawa, A., and W. H. Schubert (1974), Interaction of a Cumulus Cloud Ensemble with the Large-Scale Environment, Part I, *J. Atmos. Sci.*, 31(3), 674–701, doi:10.1175/1520-0469(1974)031<0674:IOACCE>2.0.CO;2.
- Back, L., K. Russ, Z. Liu, K. Inoue, J. Zhang, and B. Otto-Bliesner (2013), Global Hydrological Cycle Response to Rapid and Slow Global Warming, *J. Climate*, 26(22), 8781–8786, doi:10.1175/JCLI-D-13-00118.1.
- Back, L. E., and C. S. Bretherton (2006), Geographic variability in the export of moist static

energy and vertical motion profiles in the tropical Pacific, *Geophys. Res. Lett.*, 33(17), L17,810, doi:10.1029/2006GL026672.

Bader, J., and M. Latif (2003), The impact of decadal-scale Indian Ocean sea surface temperature anomalies on Sahelian rainfall and the North Atlantic Oscillation, *Geophys. Res. Lett.*, 30(22), 2169, doi:10.1029/2003GL018426.

Barsugli, J. J., and P. D. Sardeshmukh (2002), Global Atmospheric Sensitivity to Tropical SST Anomalies throughout the Indo-Pacific Basin, *J. Climate*, 15(23), 3427–3442, doi:10.1175/1520-0442(2002)015<3427:GASTTS>2.0.CO;2.

Berg, A., B. R. Lintner, K. Findell, S. I. Seneviratne, B. van den Hurk, A. Ducharne, F. Chéruy, S. Hagemann, D. M. Lawrence, S. Malyshev, A. Meier, and P. Gentine (2014), Interannual Coupling between Summertime Surface Temperature and Precipitation over Land: Processes and Implications for Climate Change, *J. Climate*, 28(3), 1308–1328, doi:10.1175/JCLI-D-14-00324.1.

Biasutti, M. (2013), Forced Sahel rainfall trends in the CMIP5 archive, *J. Geophys. Res. Atmos.*, 118(4), 1613–1623, doi:10.1002/jgrd.50206.

Biasutti, M., and A. H. Sobel (2009), Delayed Sahel rainfall and global seasonal cycle in a warmer climate, *Geophys. Res. Lett.*, 36(23), L23,707, doi:10.1029/2009GL041303.

Biasutti, M., I. M. Held, A. H. Sobel, and A. Giannini (2008), SST Forcings and Sahel Rainfall Variability in Simulations of the Twentieth and Twenty-First Centuries, *J. Climate*, 21(14), 3471–3486, doi:10.1175/2007JCLI1896.1.

Biasutti, M., A. H. Sobel, and S. J. Camargo (2009), The Role of the Sahara Low in Summertime Sahel Rainfall Variability and Change in the CMIP3 Models, *Journal of Climate*, 22(21), 5755–5771, doi:10.1175/2009JCLI2969.1.

- Birch, C. E., D. J. Parker, J. H. Marsham, D. Copsey, and L. Garcia-Carreras (2014), A seamless assessment of the role of convection in the water cycle of the West African Monsoon, *J. Geophys. Res. Atmos.*, 119(6), 2013JD020,887, doi:10.1002/2013JD020887.
- Bischoff, T., and T. Schneider (2014), Energetic Constraints on the Position of the Intertropical Convergence Zone, *J. Climate*, 27(13), 4937–4951, doi:10.1175/JCLI-D-13-00650.1.
- Bischoff, T., and T. Schneider (2015), The Equatorial Energy Balance, ITCZ Position, and Double-ITCZ Bifurcations, *J. Climate*, 29(8), 2997–3013, doi:10.1175/JCLI-D-15-0328.1.
- Boé, J., A. Hall, and X. Qu (2009), Current GCMs' Unrealistic Negative Feedback in the Arctic, *J. Climate*, 22(17), 4682–4695, doi:10.1175/2009JCLI2885.1.
- Bony, S., G. Bellon, D. Klocke, S. Sherwood, S. Fermepin, and S. Denvil (2013), Robust direct effect of carbon dioxide on tropical circulation and regional precipitation, *Nature Geosci*, 6(6), 447–451, doi:10.1038/ngeo1799.
- Boos, W. R. (2011), Thermodynamic Scaling of the Hydrological Cycle of the Last Glacial Maximum, *J. Climate*, 25(3), 992–1006, doi:10.1175/JCLI-D-11-00010.1.
- Boos, W. R., and J. V. Hurley (2013), Thermodynamic Bias in the Multimodel Mean Boreal Summer Monsoon, *J. Climate*, 26(7), 2279–2287, doi:10.1175/JCLI-D-12-00493.1.
- Bretherton, C. S., J. R. McCaa, and H. Grenier (2004), A New Parameterization for Shallow Cumulus Convection and Its Application to Marine Subtropical Cloud-Topped Boundary Layers. Part I: Description and 1d Results, *Mon. Wea. Rev.*, 132(4), 864–882, doi:10.1175/1520-0493(2004)132<0864:ANPFSC>2.0.CO;2.
- Bretherton, C. S., P. N. Blossey, and M. E. Peters (2006), Interpretation of simple and cloud-resolving simulations of moist convection–radiation interaction with a mock-Walker circulation, *Theor. Comput. Fluid Dyn.*, 20(5-6), 421–442, doi:10.1007/s00162-006-0029-7.

Brovkin, V., and M. Claussen (2008), Comment on "Climate-Driven Ecosystem Succession in the Sahara: The Past 6000 Years", *Science*, 322(5906), 1326–1326, doi:10.1126/science.1163381.

Byrne, M. P., and P. A. O'Gorman (2013), Land–Ocean Warming Contrast over a Wide Range of Climates: Convective Quasi-Equilibrium Theory and Idealized Simulations, *J. Climate*, 26(12), 4000–4016, doi:10.1175/JCLI-D-12-00262.1.

Byrne, M. P., and P. A. O'Gorman (2013), Link between land-ocean warming contrast and surface relative humidities in simulations with coupled climate models, *Geophys. Res. Lett.*, 40(19), 5223–5227, doi:10.1002/grl.50971.

Byrne, M. P., and T. Schneider (2016), Energetic constraints on the width of the intertropical convergence zone, *J. Climate*, doi:10.1175/JCLI-D-15-0767.1.

Caballero, R., and P. L. Langen (2005), The dynamic range of poleward energy transport in an atmospheric general circulation model, *Geophys. Res. Lett.*, 32(2), L02,705, doi:10.1029/2004GL021581.

Caldwell, P. M., C. S. Bretherton, M. D. Zelinka, S. A. Klein, B. D. Santer, and B. M. Sanderson (2014), Statistical significance of climate sensitivity predictors obtained by data mining, *Geophys. Res. Lett.*, 41(5), 1803–1808, doi:10.1002/2014GL059205.

Chadwick, R. (2016), Which Aspects of CO₂ Forcing and SST Warming Cause Most Uncertainty in Projections of Tropical Rainfall Change over Land and Ocean?, *J. Climate*, 29(7), 2493–2509, doi:10.1175/JCLI-D-15-0777.1.

Chadwick, R., I. Boutle, and G. Martin (2013), Spatial Patterns of Precipitation Change in CMIP5: Why the Rich Do Not Get Richer in the Tropics, *J. Climate*, 26(11), 3803–3822, doi:10.1175/JCLI-D-12-00543.1.

Charney, J., P. H. Stone, and W. J. Quirk (1975), Drought in the Sahara: A Biogeophysical Feedback Mechanism, *Science*, 187(4175), 434–435, doi:10.1126/science.187.4175.434.

Charney, J., W. J. Quirk, S. Chow, and J. Kornfield (1977), A Comparative Study of the Effects of Albedo Change on Drought in Semi–Arid Regions, *J. Atmos. Sci.*, 34(9), 1366–1385, doi:10.1175/1520-0469(1977)034<1366:ACSOTE>2.0.CO;2.

Charney, J. G. (1975), Dynamics of deserts and drought in the Sahel, *Q.J.R. Meteorol. Soc.*, 101(428), 193–202, doi:10.1002/qj.49710142802.

Chen, M., P. Xie, J. E. Janowiak, and P. A. Arkin (2002), Global Land Precipitation: A 50-yr Monthly Analysis Based on Gauge Observations, *J. Hydrometeor*, 3(3), 249–266, doi:10.1175/1525-7541(2002)003<0249:GLPAYM>2.0.CO;2.

Chiang, J. C. H., and A. R. Friedman (2012), Extratropical Cooling, Interhemispheric Thermal Gradients, and Tropical Climate Change, *Annual Review of Earth and Planetary Sciences*, 40(1), 383–412, doi:10.1146/annurev-earth-042711-105545.

Chou, C., and J. D. Neelin (2001), Mechanisms limiting the southward extent of the South American Summer Monsoon, *Geophys. Res. Lett.*, 28(12), 2433–2436, doi:10.1029/2000GL012138.

Chou, C., and J. D. Neelin (2003), Mechanisms Limiting the Northward Extent of the Northern Summer Monsoons over North America, Asia, and Africa*, *J. Climate*, 16(3), 406–425, doi:10.1175/1520-0442(2003)016<0406:MLTNEO>2.0.CO;2.

Chou, C., and J. D. Neelin (2004), Mechanisms of Global Warming Impacts on Regional Tropical Precipitation, *J. Climate*, 17(13), 2688–2701, doi:10.1175/1520-0442(2004)017<2688:MOGWIO>2.0.CO;2.

Chou, C., J. D. Neelin, and H. Su (2001), Ocean-atmosphere-land feedbacks in an idealized monsoon, *Q.J.R. Meteorol. Soc.*, 127(576), 1869–1891, doi:10.1002/qj.49712757602.

Chou, C., J. D. Neelin, C.-A. Chen, and J.-Y. Tu (2009), Evaluating the “Rich-Get-Richer” Mechanism in Tropical Precipitation Change under Global Warming, *J. Climate*, 22(8), 1982–2005, doi:10.1175/2008JCLI2471.1.

Chou, C., T.-C. Wu, and P.-H. Tan (2013), Changes in gross moist stability in the tropics under global warming, *Clim Dyn*, 41(9-10), 2481–2496, doi:10.1007/s00382-013-1703-2.

Collins, M., R. Knutti, J. Arblaster, J.-L. Dufresne, T. Fichefet, P. Friedlingstein, X. Gao, W. J. Gutowski, T. Johns, G. Krinner, M. Shongwe, C. Tebaldi, A. J. Weaver, and M. Wehner (2013), Long-term Climate Change: Projections, Commitments and Irreversibility, in *Climate Change 2013: The Physical Science Basis. Contribution of Working Group I to the Fifth Assessment Report of the Intergovernmental Panel on Climate Change*, pp. 1029–1136, Cambridge University Press, Cambridge, United Kingdom and New York, NY, USA, doi:10.1017/CBO9781107415324.024.

Cook, K. H. (1994), Mechanisms by Which Surface Drying Perturbs Tropical Precipitation Fields, *J. Climate*, 7(3), 400–413, doi:10.1175/1520-0442(1994)007<0400:MBWSDP>2.0.CO;2.

Cook, K. H. (1997), Large-Scale Atmospheric Dynamics and Sahelian Precipitation, *J. Climate*, 10(6), 1137–1152, doi:10.1175/1520-0442(1997)010<1137:LSADAS>2.0.CO;2.

Cook, K. H. (1999), Generation of the African Easterly Jet and Its Role in Determining West African Precipitation, *J. Climate*, 12(5), 1165–1184, doi:10.1175/1520-0442(1999)012<1165:GOTAEJ>2.0.CO;2.

Dee, D. P., S. M. Uppala, A. J. Simmons, P. Berrisford, P. Poli, S. Kobayashi, U. Andrae, M. A. Balmaseda, G. Balsamo, P. Bauer, P. Bechtold, A. C. M. Beljaars, L. van de Berg, J. Bidlot, N. Bormann, C. Delsol, R. Dragani, M. Fuentes, A. J. Geer, L. Haimberger, S. B. Healy, H. Hersbach, E. V. Hólm, L. Isaksen, P. Kållberg, M. Köhler, M. Matricardi, A. P. McNally, B. M. Monge-Sanz, J.-J. Morcrette, B.-K. Park, C. Peubey, P. de Rosnay,

C. Tavolato, J.-N. Thépaut, and F. Vitart (2011), The ERA-Interim reanalysis: configuration and performance of the data assimilation system, *Q.J.R. Meteorol. Soc.*, *137*(656), 553–597, doi:10.1002/qj.828.

Delworth, T. L., A. J. Broccoli, A. Rosati, R. J. Stouffer, V. Balaji, J. A. Beesley, W. F. Cooke, K. W. Dixon, J. Dunne, K. A. Dunne, J. W. Durachta, K. L. Findell, P. Ginoux, A. Gnanadesikan, C. T. Gordon, S. M. Griffies, R. Gudgel, M. J. Harrison, I. M. Held, R. S. Hemler, L. W. Horowitz, S. A. Klein, T. R. Knutson, P. J. Kushner, A. R. Langenhorst, H.-C. Lee, S.-J. Lin, J. Lu, S. L. Malyshev, P. C. D. Milly, V. Ramaswamy, J. Russell, M. D. Schwarzkopf, E. Shevliakova, J. J. Sirutis, M. J. Spelman, W. F. Stern, M. Winton, A. T. Wittenberg, B. Wyman, F. Zeng, and R. Zhang (2006), GFDL's CM2 Global Coupled Climate Models. Part I: Formulation and Simulation Characteristics, *J. Climate*, *19*(5), 643–674, doi:10.1175/JCLI3629.1.

Delworth, T. L., A. Rosati, W. Anderson, A. J. Adcroft, V. Balaji, R. Benson, K. Dixon, S. M. Griffies, H.-C. Lee, R. C. Pacanowski, G. A. Vecchi, A. T. Wittenberg, F. Zeng, and R. Zhang (2011), Simulated Climate and Climate Change in the GFDL CM2.5 High-Resolution Coupled Climate Model, *J. Climate*, *25*(8), 2755–2781, doi:10.1175/JCLI-D-11-00316.1.

deMenocal, P., J. Ortiz, T. Guilderson, J. Adkins, M. Sarnthein, L. Baker, and M. Yarusinsky (2000), Abrupt onset and termination of the African Humid Period:: rapid climate responses to gradual insolation forcing, *Quaternary Science Reviews*, *19*(1–5), 347–361, doi:10.1016/S0277-3791(99)00081-5.

Derbyshire, S. H., I. Beau, P. Bechtold, J.-Y. Grandpeix, J.-M. Piriou, J.-L. Redelsperger, and P. M. M. Soares (2004), Sensitivity of moist convection to environmental humidity, *Q.J.R. Meteorol. Soc.*, *130*(604), 3055–3079, doi:10.1256/qj.03.130.

Dima, I. M., and J. M. Wallace (2003), On the Seasonality of the Hadley Cell, *J. Atmos. Sci.*, *60*(12), 1522–1527, doi:10.1175/1520-0469(2003)060<1522:OTSOTH>2.0.CO;2.

Dong, B., and R. Sutton (2015), Dominant role of greenhouse-gas forcing in the recovery of Sahel rainfall, *Nature Clim. Change*, *5*(8), 757–760, doi:10.1038/nclimate2664.

Donner, L. J. (1993), A Cumulus Parameterization Including Mass Fluxes, Vertical Momentum Dynamics, and Mesoscale Effects, *J. Atmos. Sci.*, *50*(6), 889–906, doi:10.1175/1520-0469(1993)050<0889:ACPIMF>2.0.CO;2.

Donner, L. J., C. J. Seman, R. S. Hemler, and S. Fan (2001), A Cumulus Parameterization Including Mass Fluxes, Convective Vertical Velocities, and Mesoscale Effects: Thermo-dynamic and Hydrological Aspects in a General Circulation Model, *J. Climate*, *14*(16), 3444–3463, doi:10.1175/1520-0442(2001)014<3444:ACPIMF>2.0.CO;2.

Donner, L. J., B. L. Wyman, R. S. Hemler, L. W. Horowitz, Y. Ming, M. Zhao, J.-C. Golaz, P. Ginoux, S.-J. Lin, M. D. Schwarzkopf, J. Austin, G. Alaka, W. F. Cooke, T. L. Delworth, S. M. Freidenreich, C. T. Gordon, S. M. Griffies, I. M. Held, W. J. Hurlin, S. A. Klein, T. R. Knutson, A. R. Langenhorst, H.-C. Lee, Y. Lin, B. I. Magi, S. L. Malyshev, P. C. D. Milly, V. Naik, M. J. Nath, R. Pincus, J. J. Poshay, V. Ramaswamy, C. J. Seman, E. Shevliakova, J. J. Sirutis, W. F. Stern, R. J. Stouffer, R. J. Wilson, M. Winton, A. T. Wittenberg, and F. Zeng (2011), The Dynamical Core, Physical Parameterizations, and Basic Simulation Characteristics of the Atmospheric Component AM3 of the GFDL Global Coupled Model CM3, *J. Climate*, *24*(13), 3484–3519, doi:10.1175/2011JCLI3955.1.

Donohoe, A., J. Marshall, D. Ferreira, and D. Mcgee (2013), The Relationship between ITCZ Location and Cross-Equatorial Atmospheric Heat Transport: From the Seasonal Cycle to the Last Glacial Maximum, *J. Climate*, *26*(11), 3597–3618, doi:10.1175/JCLI-D-12-00467.1.

Dwyer, J. G., M. Biasutti, and A. H. Sobel (2012), Projected Changes in the Seasonal Cycle

of Surface Temperature, *Journal of Climate*, 25(18), 6359–6374, doi:10.1175/JCLI-D-11-00741.1.

Dwyer, J. G., M. Biasutti, and A. H. Sobel (2014), The Effect of Greenhouse Gas-Induced Changes in SST on the Annual Cycle of Zonal Mean Tropical Precipitation, *J. Climate*, 27(12), 4544–4565, doi:10.1175/JCLI-D-13-00216.1.

Eltahir, E. A. B., and C. Gong (1996), Dynamics of Wet and Dry Years in West Africa, *J. Climate*, 9(5), 1030–1042, doi:10.1175/1520-0442(1996)009<1030:DOWADY>2.0.CO;2.

Emanuel, K. (2007), Quasi-equilibrium dynamics of the tropical atmosphere, in *The Global Circulation of the Atmosphere*, pp. 186–218.

Emanuel, K. A. (1995), On Thermally Direct Circulations in Moist Atmospheres, *J. Atmos. Sci.*, 52(9), 1529–1534, doi:10.1175/1520-0469(1995)052<1529:OTDCIM>2.0.CO;2.

Fasullo, J. T., and K. E. Trenberth (2012), A Less Cloudy Future: The Role of Subtropical Subsidence in Climate Sensitivity, *Science*, 338(6108), 792–794, doi:10.1126/science.1227465.

Faulk, S., J. Mitchell, and S. Bordoni (2016), Dynamical constraints on the ITCZ extent in planetary atmospheres, *J. Atmos. Sci.*, Submitted.

Flannaghan, T. J., S. Fueglistaler, I. M. Held, S. Po-Chedley, B. Wyman, and M. Zhao (2014), Tropical temperature trends in Atmospheric General Circulation Model simulations and the impact of uncertainties in observed SSTs, *J. Geophys. Res. Atmos.*, 119(23), 2014JD022365, doi:10.1002/2014JD022365.

Flaounas, E., S. Janicot, S. Bastin, R. Roca, and E. Mohino (2011), The role of the Indian monsoon onset in the West African monsoon onset: observations and AGCM nudged simulations, *Clim Dyn*, 38(5-6), 965–983, doi:10.1007/s00382-011-1045-x.

Folland, C. K., T. N. Palmer, and D. E. Parker (1986), Sahel rainfall and worldwide sea temperatures, 1901–85, *Nature*, 320(6063), 602–607, doi:10.1038/320602a0.

Frierson, D. M. W. (2007), The Dynamics of Idealized Convection Schemes and Their Effect on the Zonally Averaged Tropical Circulation, *J. Atmos. Sci.*, 64(6), 1959–1976, doi:10.1175/JAS3935.1.

Frierson, D. M. W., and Y.-T. Hwang (2012), Extratropical Influence on ITCZ Shifts in Slab Ocean Simulations of Global Warming, *J. Climate*, 25(2), 720–733, doi:10.1175/JCLI-D-11-00116.1.

Frierson, D. M. W., I. M. Held, and P. Zurita-Gotor (2006), A Gray-Radiation Aquaplanet Moist GCM. Part I: Static Stability and Eddy Scale, *J. Atmos. Sci.*, 63(10), 2548–2566, doi:10.1175/JAS3753.1.

Frierson, D. M. W., Y.-T. Hwang, N. S. Fučkar, R. Seager, S. M. Kang, A. Donohoe, E. A. Maroon, X. Liu, and D. S. Battisti (2013), Contribution of ocean overturning circulation to tropical rainfall peak in the Northern Hemisphere, *Nature Geoscience*, 6(11), 940–944, doi:10.1038/ngeo1987.

Gallego, D., P. Ordóñez, P. Ribera, C. Peña-Ortiz, and R. García-Herrera (2015), An instrumental index of the West African Monsoon back to the nineteenth century, *Q.J.R. Meteorol. Soc.*, 141(693), 3166–3176, doi:10.1002/qj.2601.

Gentine, P., A. A. M. Holtslag, F. D'Andrea, and M. Ek (2013), Surface and Atmospheric Controls on the Onset of Moist Convection over Land, *J. Hydrometeor*, 14(5), 1443–1462, doi:10.1175/JHM-D-12-0137.1.

GFDL Atmospheric Model Development Team (2004), The New GFDL Global Atmosphere and Land Model AM2–LM2: Evaluation with Prescribed SST Simulations, *J. Climate*, 17(24), 4641–4673, doi:10.1175/JCLI-3223.1.

Giannini, A. (2010), Mechanisms of Climate Change in the Semiarid African Sahel: The Local View, *J. Climate*, 23(3), 743–756, doi:10.1175/2009JCLI3123.1.

Giannini, A. (2016), 40 Years of Climate Modeling: The Causes of Late-20th Century Drought in the Sahel, in *The End of Desertification?*, edited by R. Behnke and M. Mortimore, Springer Earth System Sciences, pp. 265–291, Springer Berlin Heidelberg, dOI: 10.1007/978-3-642-16014-1_10.

Giannini, A., R. Saravanan, and P. Chang (2003), Oceanic Forcing of Sahel Rainfall on Interannual to Interdecadal Time Scales, *Science*, 302(5647), 1027–1030, doi:10.1126/science.1089357.

Giannini, A., S. Salack, T. Lodoun, A. Ali, A. T. Gaye, and O. Ndiaye (2013), A unifying view of climate change in the Sahel linking intra-seasonal, interannual and longer time scales, *Environ. Res. Lett.*, 8(2), 024,010, doi:10.1088/1748-9326/8/2/024010.

Gill, A. E. (1980), Some simple solutions for heat-induced tropical circulation, *Q.J.R. Meteorol. Soc.*, 106(449), 447–462, doi:10.1002/qj.49710644905.

Guan, K., B. Sultan, M. Biasutti, C. Baron, and D. B. Lobell (2015), What aspects of future rainfall changes matter for crop yields in West Africa?, *Geophys. Res. Lett.*, 42(19), 2015GL063,877, doi:10.1002/2015GL063877.

Hadley, G. (1735), Concerning the Cause of the General Trade-Winds, *Philosophical Transactions of the Royal Society of London*, 39(436-444), 58–62, doi:10.1098/rstl.1735.0014.

Hales, K., J. D. Neelin, and N. Zeng (2006), Interaction of Vegetation and Atmospheric Dynamical Mechanisms in the Mid-Holocene African Monsoon, *J. Climate*, 19(16), 4105–4120, doi:10.1175/JCLI3833.1.

Hall, A., and X. Qu (2006), Using the current seasonal cycle to constrain snow

albedo feedback in future climate change, *Geophys. Res. Lett.*, 33(3), L03,502, doi:10.1029/2005GL025127.

Halley, E. (1686), An Historical Account of the Trade Winds, and Monsoons, Observable in the Seas between and Near the Tropicks, with an Attempt to Assign the Phisical Cause of the Said Winds, *Philosophical Transactions of the Royal Society of London*, 16(179-191), 153–168, doi:10.1098/rstl.1686.0026.

Harris, I., P. Jones, T. Osborn, and D. Lister (2014), Updated high-resolution grids of monthly climatic observations – the CRU TS3.10 Dataset, *Int. J. Climatol.*, 34(3), 623–642, doi:10.1002/joc.3711.

Hastenrath, S., and P. Lamb (1977), Some Aspects of Circulation and Climate over the Eastern Equatorial Atlantic, *Mon. Wea. Rev.*, 105(8), 1019–1023, doi:10.1175/1520-0493(1977)105<1019:SAOCAC>2.0.CO;2.

He, J., B. J. Soden, and B. Kirtman (2014), The robustness of the atmospheric circulation and precipitation response to future anthropogenic surface warming, *Geophys. Res. Lett.*, 41(7), 2014GL059,435, doi:10.1002/2014GL059435.

Held, I. M. (2001), The Partitioning of the Poleward Energy Transport between the Tropical Ocean and Atmosphere, *J. Atmos. Sci.*, 58(8), 943–948, doi:10.1175/1520-0469(2001)058<0943:TPOTPE>2.0.CO;2.

Held, I. M., and B. J. Hoskins (1985), Large-scale eddies and the general circulation of the troposphere, in *Advances in geophysics.*, vol. 28, pp. 3–31.

Held, I. M., and A. Y. Hou (1980), Nonlinear Axially Symmetric Circulations in a Nearly Inviscid Atmosphere, *J. Atmos. Sci.*, 37(3), 515–533, doi:10.1175/1520-0469(1980)037<0515:NASCIA>2.0.CO;2.

Held, I. M., and a. B. J. Soden (2000), Water Vapor Feedback and Global Warming, *Annual Review of Energy and the Environment*, 25(1), 441–475, doi:10.1146/annurev.energy.25.1.441.

Held, I. M., and B. J. Soden (2006), Robust Responses of the Hydrological Cycle to Global Warming, *J. Climate*, 19(21), 5686–5699, doi:10.1175/JCLI3990.1.

Held, I. M., T. L. Delworth, J. Lu, K. L. Findell, and T. R. Knutson (2005), Simulation of Sahel drought in the 20th and 21st centuries, *PNAS*, 102(50), 17,891–17,896, doi:10.1073/pnas.0509057102.

Held, I. M., M. Zhao, and B. Wyman (2007), Dynamic Radiative–Convective Equilibria Using GCM Column Physics, *Journal of the Atmospheric Sciences*, 64(1), 228–238, doi:10.1175/JAS3825.11.

Hill, S., and Y. Ming (2012), Nonlinear climate response to regional brightening of tropical marine stratocumulus, *Geophys. Res. Lett.*, 39(15), L15,707, doi:10.1029/2012GL052064.

Hill, S. A., Y. Ming, and I. M. Held (2015), Mechanisms of Forced Tropical Meridional Energy Flux Change, *J. Climate*, 28(5), 1725–1742, doi:10.1175/JCLI-D-14-00165.1.

Hou, A. Y., and R. S. Lindzen (1992), The Influence of Concentrated Heating on the Hadley Circulation, *J. Atmos. Sci.*, 49(14), 1233–1241, doi:10.1175/1520-0469(1992)049<1233:TIOCHO>2.0.CO;2.

Hu, Y., D. Li, and J. Liu (2007), Abrupt seasonal variation of the ITCZ and the Hadley circulation, *Geophys. Res. Lett.*, 34(18), L18,814, doi:10.1029/2007GL030950.

Huffman, G. J., D. T. Bolvin, E. J. Nelkin, D. B. Wolff, R. F. Adler, G. Gu, Y. Hong, K. P. Bowman, and E. F. Stocker (2007), The TRMM Multisatellite Precipitation Analysis (TMPA): Quasi-Global, Multiyear, Combined-Sensor Precipitation Estimates at Fine Scales, *J. Hydrometeor*, 8(1), 38–55, doi:10.1175/JHM560.1.

Hurley, J. V., and W. R. Boos (2013), Interannual Variability of Monsoon Precipitation and Local Subcloud Equivalent Potential Temperature, *J. Climate*, 26(23), 9507–9527, doi:10.1175/JCLI-D-12-00229.1.

Hurrell, J. W., J. J. Hack, D. Shea, J. M. Caron, and J. Rosinski (2008), A New Sea Surface Temperature and Sea Ice Boundary Dataset for the Community Atmosphere Model, *J. Climate*, 21(19), 5145–5153, doi:10.1175/2008JCLI2292.1.

Hwang, Y.-T., and D. M. W. Frierson (2010), Increasing atmospheric poleward energy transport with global warming, *Geophys. Res. Lett.*, 37(24), L24,807, doi:10.1029/2010GL045440.

Im, E.-S., R. L. Gianotti, and E. A. B. Eltahir (2014), Improving the Simulation of the West African Monsoon Using the MIT Regional Climate Model, *J. Climate*, 27(6), 2209–2229, doi:10.1175/JCLI-D-13-00188.1.

Indo-Asian News Service (2010), India cheers as monsoon arrives; hopes of better farm output raised, *Hindustan Times*.

Inoue, K., and L. E. Back (2015), Gross Moist Stability Assessment during TOGA COARE: Various Interpretations of Gross Moist Stability, *J. Atmos. Sci.*, 72(11), 4148–4166, doi:10.1175/JAS-D-15-0092.1.

Johnson, N. C., and S.-P. Xie (2010), Changes in the sea surface temperature threshold for tropical convection, *Nature Geoscience*, 3(12), 842–845, doi:10.1038/ngeo1008.

Kang, S. M., and I. M. Held (2011), Tropical precipitation, SSTs and the surface energy budget: a zonally symmetric perspective, *Clim Dyn*, 38(9-10), 1917–1924, doi:10.1007/s00382-011-1048-7.

Kang, S. M., I. M. Held, D. M. W. Frierson, and M. Zhao (2008), The Response of the

ITCZ to Extratropical Thermal Forcing: Idealized Slab-Ocean Experiments with a GCM, *J. Climate*, 21(14), 3521–3532, doi:10.1175/2007JCLI2146.1.

Kang, S. M., D. M. W. Frierson, and I. M. Held (2009), The Tropical Response to Extratropical Thermal Forcing in an Idealized GCM: The Importance of Radiative Feedbacks and Convective Parameterization, *J. Atmos. Sci.*, 66(9), 2812–2827, doi:10.1175/2009JAS2924.1.

Kang, S. M., C. Deser, and L. M. Polvani (2013), Uncertainty in Climate Change Projections of the Hadley Circulation: The Role of Internal Variability, *J. Climate*, 26(19), 7541–7554, doi:10.1175/JCLI-D-12-00788.1.

Kidson, J. W., and R. E. Newell (1977), African rainfall and its relation to the upper air circulation, *Quarterly Journal of the Royal Meteorological Society*, 103(437), 441–456, doi:10.1002/qj.49710343705.

Knutson, T. R., and S. Manabe (1995), Time-Mean Response over the Tropical Pacific to Increased CO₂ in a Coupled Ocean-Atmosphere Model, *J. Climate*, 8(9), 2181–2199, doi:10.1175/1520-0442(1995)008<2181:TMROTT>2.0.CO;2.

Knutti, R., D. Masson, and A. Gettelman (2013), Climate model genealogy: Generation CMIP5 and how we got there, *Geophysical Research Letters*, 40(6), 1194–1199, doi:10.1002/grl.50256.

Koster, R. D., P. A. Dirmeyer, Z. Guo, G. Bonan, E. Chan, P. Cox, C. T. Gordon, S. Kanae, E. Kowalczyk, D. Lawrence, P. Liu, C.-H. Lu, S. Malyshev, B. McAvaney, K. Mitchell, D. Mocko, T. Oki, K. Oleson, A. Pitman, Y. C. Sud, C. M. Taylor, D. Verseghy, R. Vasic, Y. Xue, and T. Yamada (2004), Regions of Strong Coupling Between Soil Moisture and Precipitation, *Science*, 305(5687), 1138–1140, doi:10.1126/science.1100217.

Kraus, E. B. (1977a), Subtropical Droughts and Cross-Equatorial En-

ergy Transports, *Mon. Wea. Rev.*, 105(8), 1009–1018, doi:10.1175/1520-0493(1977)105<1009:SDACEE>2.0.CO;2.

Kraus, E. B. (1977b), The Seasonal Excursion of the Intertropical Convergence Zone, *Mon. Wea. Rev.*, 105(8), 1052–1055, doi:10.1175/1520-0493(1977)105<1052:TSEOTI>2.0.CO;2.

Kröpelin, S., D. Verschuren, and A.-M. Lézine (2008a), Response to Comment on "Climate-Driven Ecosystem Succession in the Sahara: The Past 6000 Years", *Science*, 322(5906), 1326–1326, doi:10.1126/science.1163483.

Kröpelin, S., D. Verschuren, A.-M. Lézine, H. Eggermont, C. Cocquyt, P. Francus, J.-P. Cazet, M. Fagot, B. Rumes, J. M. Russell, F. Darius, D. J. Conley, M. Schuster, H. v. Suchodoletz, and D. R. Engstrom (2008b), Climate-Driven Ecosystem Succession in the Sahara: The Past 6000 Years, *Science*, 320(5877), 765–768, doi:10.1126/science.1154913.

Lamb, P. J. (1978a), Case Studies of Tropical Atlantic Surface Circulation Patterns During Recent Sub-Saharan Weather Anomalies: 1967 and 1968, *Mon. Wea. Rev.*, 106(4), 482–491, doi:10.1175/1520-0493(1978)106<0482:CSOTAS>2.0.CO;2.

Lamb, P. J. (1978b), Large-scale Tropical Atlantic surface circulation patterns associated with Subsaharan weather anomalies, *Tellus*, 30(3), 240–251, doi:10.1111/j.2153-3490.1978.tb00839.x.

Legates, D. R., and C. J. Willmott (1990), Mean seasonal and spatial variability in gauge-corrected, global precipitation, *Int. J. Climatol.*, 10(2), 111–127, doi:10.1002/joc.3370100202.

Lesins, G., T. J. Duck, and J. R. Drummond (2012), Surface Energy Balance Framework for Arctic Amplification of Climate Change, *Journal of Climate*, 25(23), 8277–8288, doi:10.1175/JCLI-D-11-00711.1.

Lindzen, R. S., and S. Nigam (1987), On the Role of Sea Surface Temperature Gradients in Forcing Low-Level Winds and Convergence in the Tropics, *J. Atmos. Sci.*, 44(17), 2418–2436, doi:10.1175/1520-0469(1987)044<2418:OTROSS>2.0.CO;2.

Lintner, B. R., P. Gentine, K. L. Findell, and G. D. Salvucci (2015), The Budyko and complementary relationships in an idealized model of large-scale land–atmosphere coupling, *Hydrol. Earth Syst. Sci.*, 19(5), 2119–2131, doi:10.5194/hess-19-2119-2015.

Loeb, N. G., B. A. Wielicki, D. R. Doelling, G. L. Smith, D. F. Keyes, S. Kato, N. Manalo-Smith, and T. Wong (2009), Toward Optimal Closure of the Earth’s Top-of-Atmosphere Radiation Budget, *J. Climate*, 22(3), 748–766, doi:10.1175/2008JCLI2637.1.

Losada, T., B. Rodriguez-Fonseca, E. Mohino, J. Bader, S. Janicot, and C. R. Mechoso (2012), Tropical SST and Sahel rainfall: A non-stationary relationship, *Geophys. Res. Lett.*, 39(12), L12,705, doi:10.1029/2012GL052423.

Lough, J. M. (1986), Tropical Atlantic Sea Surface Temperatures and Rainfall Variations in Subsaharan Africa, *Mon. Wea. Rev.*, 114(3), 561–570, doi:10.1175/1520-0493(1986)114<0561:TASSTA>2.0.CO;2.

Lu, J. (2009), The dynamics of the Indian Ocean sea surface temperature forcing of Sahel drought, *Clim Dyn*, 33(4), 445–460, doi:10.1007/s00382-009-0596-6.

Lu, J., and T. L. Delworth (2005), Oceanic forcing of the late 20th century Sahel drought, *Geophys. Res. Lett.*, 32(22), L22,706, doi:10.1029/2005GL023316.

Ma, J., and S.-P. Xie (2012), Regional Patterns of Sea Surface Temperature Change: A Source of Uncertainty in Future Projections of Precipitation and Atmospheric Circulation, *J. Climate*, 26(8), 2482–2501, doi:10.1175/JCLI-D-12-00283.1.

Maidment, R. I., D. Grimes, R. P. Allan, E. Tarnavsky, M. Stringer, T. Hewison, R. Roebeiling, and E. Black (2014), The 30 year TAMSAT African Rainfall Climatology And

Time series (TARCAT) data set, *J. Geophys. Res. Atmos.*, 119(18), 2014JD021,927, doi:10.1002/2014JD021927.

Manabe, S., and R. T. Wetherald (1975), The Effects of Doubling the CO₂ Concentration on the climate of a General Circulation Model, *J. Atmos. Sci.*, 32(1), 3–15, doi:10.1175/1520-0469(1975)032<0003:TEODTC>2.0.CO;2.

Marshall, J., A. Donohoe, D. Ferreira, and D. McGee (2013), The ocean's role in setting the mean position of the Inter-Tropical Convergence Zone, *Clim Dyn*, 42(7-8), 1967–1979, doi:10.1007/s00382-013-1767-z.

Marsham, J. H., N. S. Dixon, L. Garcia-Carreras, G. M. S. Lister, D. J. Parker, P. Knippertz, and C. E. Birch (2013), The role of moist convection in the West African monsoon system: Insights from continental-scale convection-permitting simulations, *Geophys. Res. Lett.*, 40(9), 1843–1849, doi:10.1002/grl.50347.

Masson, D., and R. Knutti (2011), Climate model genealogy, *Geophysical Research Letters*, 38(8), n/a–n/a, doi:10.1029/2011GL046864.

Matsuno, T. (1966), Quasi-Geostrophic Motions in the Equatorial Area, *Journal of the Meteorological Society of Japan. Ser. II*, 44(1), 25–43.

McCrory, R. R., D. A. Randall, and C. Stan (2014), Simulations of the West African Monsoon with a Superparameterized Climate Model. Part I: The Seasonal Cycle, *J. Climate*, 27(22), 8303–8322, doi:10.1175/JCLI-D-13-00676.1.

Merlis, T. M., T. Schneider, S. Bordoni, and I. Eisenman (2013a), Hadley Circulation Response to Orbital Precession. Part I: Aquaplanets, *J. Climate*, 26(3), 740–753, doi:10.1175/JCLI-D-11-00716.1.

Merlis, T. M., T. Schneider, S. Bordoni, and I. Eisenman (2013b), Hadley Circulation Re-

sponse to Orbital Precession. Part II: Subtropical Continent, *J. Climate*, 26(3), 754–771, doi:10.1175/JCLI-D-12-00149.1.

Merlis, T. M., T. Schneider, S. Bordoni, and I. Eisenman (2013c), The Tropical Precipitation Response to Orbital Precession, *J. Climate*, 26(6), 2010–2021, doi:10.1175/JCLI-D-12-00186.1.

Merlis, T. M., W. Zhou, I. M. Held, and M. Zhao (2016), Surface temperature dependence of tropical cyclone-permitting simulations in a spherical model with uniform thermal forcing, *Geophys. Res. Lett.*, 43(6), 2016GL067,730, doi:10.1002/2016GL067730.

Milly, P. C. D., and A. B. Shmakin (2002), Global Modeling of Land Water and Energy Balances. Part I: The Land Dynamics (LaD) Model, *J. Hydrometeor*, 3(3), 283–299, doi:10.1175/1525-7541(2002)003<0283:GMOLWA>2.0.CO;2.

Ming, Y., and V. Ramaswamy (2009), Nonlinear Climate and Hydrological Responses to Aerosol Effects, *Journal of Climate*, 22(6), 1329–1339, doi:10.1175/2008JCLI2362.1.

Ming, Y., and V. Ramaswamy (2011), A Model Investigation of Aerosol-Induced Changes in Tropical Circulation, *Journal of Climate*, 24(19), 5125–5133, doi:10.1175/2011JCLI4108.1.

Ming, Y., V. Ramaswamy, L. J. Donner, and V. T. J. Phillips (2006), A New Parameterization of Cloud Droplet Activation Applicable to General Circulation Models, *J. Atmos. Sci.*, 63(4), 1348–1356, doi:10.1175/JAS3686.1.

Ming, Y., V. Ramaswamy, L. J. Donner, V. T. J. Phillips, S. A. Klein, P. A. Ginoux, and L. W. Horowitz (2007), Modeling the Interactions between Aerosols and Liquid Water Clouds with a Self-Consistent Cloud Scheme in a General Circulation Model, *J. Atmos. Sci.*, 64(4), 1189–1209, doi:10.1175/JAS3874.1.

Ming, Y., V. Ramaswamy, and G. Persad (2010), Two opposing effects of absorbing

aerosols on global-mean precipitation, *Geophysical Research Letters*, 37(13), n/a–n/a, doi:10.1029/2010GL042895.

Mitchell, J. F. B., C. A. Wilson, and W. M. Cunningham (1987), On CO₂ climate sensitivity and model dependence of results, *Q.J.R. Meteorol. Soc.*, 113(475), 293–322, doi:10.1002/qj.49711347517.

Mitchell, J. L. (2008), The drying of Titan's dunes: Titan's methane hydrology and its impact on atmospheric circulation, *J. Geophys. Res.*, 113(E8), E08,015, doi:10.1029/2007JE003017.

Moorthi, S., and M. J. Suarez (1992), Relaxed Arakawa-Schubert. A Parameterization of Moist Convection for General Circulation Models, *Mon. Wea. Rev.*, 120(6), 978–1002, doi:10.1175/1520-0493(1992)120<0978:RASAPO>2.0.CO;2.

Mueller, B., M. Hirschi, C. Jimenez, P. Ciais, P. A. Dirmeyer, A. J. Dolman, J. B. Fisher, M. Jung, F. Ludwig, F. Maignan, D. G. Miralles, M. F. McCabe, M. Reichstein, J. Sheffield, K. Wang, E. F. Wood, Y. Zhang, and S. I. Seneviratne (2013), Benchmark products for land evapotranspiration: LandFlux-EVAL multi-data set synthesis, *Hydrol. Earth Syst. Sci.*, 17(10), 3707–3720, doi:10.5194/hess-17-3707-2013.

Neelin, J. D. (2007), Moist dynamics of tropical convection zones in monsoons, teleconnections, and global warming, in *The Global Circulation of the Atmosphere*, pp. 267–301, Princeton University Press.

Neelin, J. D., and I. M. Held (1987), Modeling Tropical Convergence Based on the Moist Static Energy Budget, *Mon. Wea. Rev.*, 115(1), 3–12, doi:10.1175/1520-0493(1987)115<0003:MTCBOT>2.0.CO;2.

Neelin, J. D., and N. Zeng (2000), A Quasi-Equilibrium Tropical Circulation Model-Formulation*, *Journal of the atmospheric sciences*, 57(11), 1741–1766.

Neelin, J. D., C. Chou, and H. Su (2003), Tropical drought regions in global warming and El Niño teleconnections, *Geophys. Res. Lett.*, 30(24), 2275, doi:10.1029/2003GL018625.

Nicholson, S. E. (1985), Sub-Saharan Rainfall 1981–84, *J. Climate Appl. Meteor.*, 24(12), 1388–1391, doi:10.1175/1520-0450(1985)024<1388:SSR>2.0.CO;2.

Nicholson, S. E. (2009), A revised picture of the structure of the “monsoon” and land ITCZ over West Africa, *Clim Dyn*, 32(7-8), 1155–1171, doi:10.1007/s00382-008-0514-3.

Nicholson, S. E. (2013), The West African Sahel: A Review of Recent Studies on the Rainfall Regime and Its Interannual Variability, *International Scholarly Research Notices*, 2013, e453,521, doi:10.1155/2013/453521.

Nie, J., W. R. Boos, and Z. Kuang (2010), Observational Evaluation of a Convective Quasi-Equilibrium View of Monsoons, *Journal of Climate*, 23(16), 4416–4428, doi:10.1175/2010JCLI3505.1.

O’Gorman, P. A., and T. Schneider (2008), The Hydrological Cycle over a Wide Range of Climates Simulated with an Idealized GCM, *J. Climate*, 21(15), 3815–3832, doi:10.1175/2007JCLI2065.1.

Palmer, T. N. (1986), Influence of the Atlantic, Pacific and Indian Oceans on Sahel rainfall, *Nature*, 322(6076), 251–253, doi:10.1038/322251a0.

Park, J.-Y., J. Bader, and D. Matei (2015), Northern-hemispheric differential warming is the key to understanding the discrepancies in the projected Sahel rainfall, *Nat Commun*, 6, 5985, doi:10.1038/ncomms6985.

Patricola, C. M., and K. H. Cook (2011), Sub-Saharan Northern African climate at the end of the twenty-first century: forcing factors and climate change processes, *Clim Dyn*, 37(5-6), 1165–1188, doi:10.1007/s00382-010-0907-y.

Persad, G. G., Y. Ming, and V. Ramaswamy (2012), Tropical Tropospheric-Only Responses to Absorbing Aerosols, *Journal of Climate*, 25(7), 2471–2480, doi:10.1175/JCLI-D-11-00122.1.

Peters, M. E., Z. Kuang, and C. C. Walker (2008), Analysis of Atmospheric Energy Transport in ERA-40 and Implications for Simple Models of the Mean Tropical Circulation, *J. Climate*, 21(20), 5229–5241, doi:10.1175/2008JCLI2073.1.

Plumb, R. A., and A. Y. Hou (1992), The Response of a Zonally Symmetric Atmosphere to Subtropical Thermal Forcing: Threshold Behavior, *J. Atmos. Sci.*, 49(19), 1790–1799, doi:10.1175/1520-0469(1992)049<1790:TROAZS>2.0.CO;2.

Privé, N. C., and R. A. Plumb (2007), Monsoon Dynamics with Interactive Forcing. Part I: Axisymmetric Studies, *J. Atmos. Sci.*, 64(5), 1417–1430, doi:10.1175/JAS3916.1.

Raymond, D. J. (2000), Thermodynamic control of tropical rainfall, *Q.J.R. Meteorol. Soc.*, 126(564), 889–898, doi:10.1002/qj.49712656406.

Raymond, D. J., S. L. Sessions, A. H. Sobel, and Ž. Fuchs (2009), The Mechanics of Gross Moist Stability, *J. Adv. Model. Earth Syst.*, 1(3), 9, doi:10.3894/JAMES.2009.1.9.

Rayner, N. A., D. E. Parker, E. B. Horton, C. K. Folland, L. V. Alexander, D. P. Rowell, E. C. Kent, and A. Kaplan (2003), Global analyses of sea surface temperature, sea ice, and night marine air temperature since the late nineteenth century, *J. Geophys. Res.*, 108(D14), 4407, doi:10.1029/2002JD002670.

Reynolds, R. W., N. A. Rayner, T. M. Smith, D. C. Stokes, and W. Wang (2002), An Improved In Situ and Satellite SST Analysis for Climate, *J. Climate*, 15(13), 1609–1625, doi:10.1175/1520-0442(2002)015<1609:AIISAS>2.0.CO;2.

Rienecker, M. M., M. J. Suarez, R. Gelaro, R. Todling, J. Bacmeister, E. Liu, M. G. Bosilovich, S. D. Schubert, L. Takacs, G.-K. Kim, S. Bloom, J. Chen, D. Collins, A. Conaty,

- A. da Silva, W. Gu, J. Joiner, R. D. Koster, R. Lucchesi, A. Molod, T. Owens, S. Pawson, P. Pegion, C. R. Redder, R. Reichle, F. R. Robertson, A. G. Ruddick, M. Sienkiewicz, and J. Woollen (2011), MERRA: NASA's Modern-Era Retrospective Analysis for Research and Applications, *J. Climate*, 24(14), 3624–3648, doi:10.1175/JCLI-D-11-00015.1.
- Roderick, M. L., F. Sun, W. H. Lim, and G. D. Farquhar (2014), A general framework for understanding the response of the water cycle to global warming over land and ocean, *Hydrol. Earth Syst. Sci.*, 18(5), 1575–1589, doi:10.5194/hess-18-1575-2014.
- Rodríguez-Fonseca, B., E. Mohino, C. R. Mechoso, C. Caminade, M. Biasutti, M. Gae-tani, J. Garcia-Serrano, E. K. Vizy, K. Cook, Y. Xue, I. Polo, T. Losada, L. Druyan, B. Fontaine, J. Bader, F. J. Doblas-Reyes, L. Goddard, S. Janicot, A. Arribas, W. Lau, A. Colman, M. Vellinga, D. P. Rowell, F. Kucharski, and A. Volodioire (2015), Variability and Predictability of West African Droughts: A Review on the Role of Sea Surface Temperature Anomalies, *J. Climate*, 28(10), 4034–4060, doi:10.1175/JCLI-D-14-00130.1.
- Rodwell, M. J., and B. J. Hoskins (1996), Monsoons and the dynamics of deserts, *Q.J.R. Meteorol. Soc.*, 122(534), 1385–1404, doi:10.1002/qj.49712253408.
- Rodwell, M. J., and B. J. Hoskins (2001), Subtropical Anticyclones and Summer Monsoons, *J. Climate*, 14(15), 3192–3211, doi:10.1175/1520-0442(2001)014<3192:SAASM>2.0.CO;2.
- Romps, D. M. (2008), The Dry-Entropy Budget of a Moist Atmosphere, *J. Atmos. Sci.*, 65(12), 3779–3799, doi:10.1175/2008JAS2679.1.
- Romps, D. M. (2014), An Analytical Model for Tropical Relative Humidity, *J. Climate*, 27(19), 7432–7449, doi:10.1175/JCLI-D-14-00255.1.
- Romps, D. M. (2015), MSE Minus CAPE is the True Conserved Variable for an Adiabatically Lifted Parcel, *J. Atmos. Sci.*, 72(9), 3639–3646, doi:10.1175/JAS-D-15-0054.1.

Romps, D. M., and Z. Kuang (2010), Do Undiluted Convective Plumes Exist in the Upper Tropical Troposphere?, *J. Atmos. Sci.*, 67(2), 468–484, doi:10.1175/2009JAS3184.1.

Saha, S., S. Moorthi, H.-L. Pan, X. Wu, J. Wang, S. Nadiga, P. Tripp, R. Kistler, J. Woollen, D. Behringer, H. Liu, D. Stokes, R. Grumbine, G. Gayno, J. Wang, Y.-T. Hou, H.-Y. Chuang, H.-M. H. Juang, J. Sela, M. Iredell, R. Treadon, D. Kleist, P. Van Delst, D. Keyser, J. Derber, M. Ek, J. Meng, H. Wei, R. Yang, S. Lord, H. Van Den Dool, A. Kumar, W. Wang, C. Long, M. Chelliah, Y. Xue, B. Huang, J.-K. Schemm, W. Ebisuzaki, R. Lin, P. Xie, M. Chen, S. Zhou, W. Higgins, C.-Z. Zou, Q. Liu, Y. Chen, Y. Han, L. Cucurull, R. W. Reynolds, G. Rutledge, and M. Goldberg (2010), The NCEP Climate Forecast System Reanalysis, *Bull. Amer. Meteor. Soc.*, 91(8), 1015–1057, doi:10.1175/2010BAMS3001.1.

Salmon, R., I. M. Held, J. Fields, and J.-L. Thiffeault (2001), *The General circulation of the atmosphere : 2000 program in Geophysical Fluid Dynamics*, Woods Hole Oceanographic Institution, Woods Hole, MA.

Scheff, J., and D. M. W. Frierson (2014), Scaling Potential Evapotranspiration with Greenhouse Warming, *J. Climate*, 27(4), 1539–1558, doi:10.1175/JCLI-D-13-00233.1.

Scheff, J., and D. M. W. Frierson (2015), Terrestrial Aridity and Its Response to Greenhouse Warming across CMIP5 Climate Models, *J. Climate*, 28(14), 5583–5600, doi:10.1175/JCLI-D-14-00480.1.

Schneider, E. K. (1977), Axially Symmetric Steady-State Models of the Basic State for Instability and Climate Studies. Part II. Nonlinear Calculations, *J. Atmos. Sci.*, 34(2), 280–296, doi:10.1175/1520-0469(1977)034<0280:ASSSMO>2.0.CO;2.

Schneider, T., T. Bischoff, and G. H. Haug (2014), Migrations and dynamics of the intertropical convergence zone, *Nature*, 513(7516), 45–53, doi:10.1038/nature13636.

Seeley, J. T., and D. M. Romps (2015), Why does tropical convective available potential energy (CAPE) increase with warming?, *Geophys. Res. Lett.*, 42(23), 2015GL066199, doi:10.1002/2015GL066199.

Seeley, J. T., and D. M. Romps (2016), Tropical cloud buoyancy is the same in a world with or without ice, *Geophys. Res. Lett.*, 43(7), 2016GL068583, doi:10.1002/2016GL068583.

Seth, A., S. A. Rauscher, M. Rojas, A. Giannini, and S. J. Camargo (2010), Enhanced spring convective barrier for monsoons in a warmer world?, *Climatic Change*, 104(2), 403–414, doi:10.1007/s10584-010-9973-8.

Shaevitz, D. A., and A. H. Sobel (2004), Implementing the Weak Temperature Gradient Approximation with Full Vertical Structure, *Mon. Wea. Rev.*, 132(2), 662–669, doi:10.1175/1520-0493(2004)132<0662:ITWTGA>2.0.CO;2.

Shanahan, T. M., N. P. McKay, K. A. Hughen, J. T. Overpeck, B. Otto-Bliesner, C. W. Heil, J. King, C. A. Scholz, and J. Peck (2015), The time-transgressive termination of the African Humid Period, *Nature Geosci.*, 8(2), 140–144, doi:10.1038/ngeo2329.

Shaw, T. A., and A. Voigt (2015), Tug of war on summertime circulation between radiative forcing and sea surface warming, *Nature Geosci.*, 8(7), 560–566, doi:10.1038/ngeo2449.

Shekhar, R., and W. R. Boos (2016), Improving energy-based estimates of monsoon location in the presence of proximal deserts, *Journal of Climate*, p. Submitted.

Sherwood, S., and Q. Fu (2014), A Drier Future?, *Science*, 343(6172), 737–739, doi:10.1126/science.1247620.

Shevliakova, E., S. W. Pacala, S. Malyshev, G. C. Hurtt, P. C. D. Milly, J. P. Caspersen, L. T. Sentman, J. P. Fisk, C. Wirth, and C. Crevoisier (2009), Carbon cycling under 300 years of land use change: Importance of the secondary vegetation sink, *Global Biogeochem. Cycles*, 23(2), GB2022, doi:10.1029/2007GB003176.

Simmons, A. J., and D. M. Burridge (1981), An Energy and Angular-Momentum Conserving Vertical Finite-Difference Scheme and Hybrid Vertical Coordinates, *Mon. Wea. Rev.*, **109**(4), 758–766, doi:10.1175/1520-0493(1981)109<0758:AEAAMC>2.0.CO;2.

Singh, M. S., and P. A. O’Gorman (2012), Upward Shift of the Atmospheric General Circulation under Global Warming: Theory and Simulations, *J. Climate*, **25**(23), 8259–8276, doi:10.1175/JCLI-D-11-00699.1.

Singh, M. S., and P. A. O’Gorman (2013), Influence of entrainment on the thermal stratification in simulations of radiative-convective equilibrium, *Geophys. Res. Lett.*, **40**(16), 4398–4403, doi:10.1002/grl.50796.

Skinner, C. B., M. Ashfaq, and N. S. Diffenbaugh (2012), Influence of Twenty-First-Century Atmospheric and Sea Surface Temperature Forcing on West African Climate, *J. Climate*, **25**(2), 527–542, doi:10.1175/2011JCLI4183.1.

Smyth, J., S. A. Hill, and Y. Ming (2016), Simulated response of the African monsoon and tropical precipitation to orbital precession, New Orleans, LA.

Sobel, A. (2010), Raised bar for rain, *Nature Geosci.*, **3**(12), 821–822, doi:10.1038/ngeo1025.

Sobel, A. H. (2007), Simple models of ensemble-averaged tropical precipitation and surface wind, given the sea surface temperature, in *The Global Circulation of the Atmosphere*, pp. 219–251, Princeton University Press.

Sobel, A. H., J. Nilsson, and L. M. Polvani (2001), The Weak Temperature Gradient Approximation and Balanced Tropical Moisture Waves*, *Journal of the atmospheric sciences*, **58**(23), 3650–3665.

Sobel, A. H., I. M. Held, and C. S. Bretherton (2002), The ENSO signal in tropical tropospheric temperature., *Journal of climate*, **15**(18).

Su, H., and J. D. Neelin (2002), Teleconnection Mechanisms for Tropical Pacific Descent Anomalies during El Niño*, *J. Atmos. Sci.*, 59(18), 2694–2712, doi:10.1175/1520-0469(2002)059<2694:TMFTPD>2.0.CO;2.

Tanaka, M., B. C. Weare, A. R. Navato, and R. E. Newell (1975), Recent African rainfall patterns, *Nature*, 255(5505), 201–203, doi:10.1038/255201a0.

Taylor, C. M., A. Gounou, F. Guichard, P. P. Harris, R. J. Ellis, F. Couvreux, and M. De Kauwe (2011), Frequency of Sahelian storm initiation enhanced over mesoscale soil-moisture patterns, *Nature Geosci.*, 4(7), 430–433, doi:10.1038/ngeo1173.

Taylor, K. E., R. J. Stouffer, and G. A. Meehl (2012), An Overview of CMIP5 and the Experiment Design, *Bulletin of the American Meteorological Society*, 93(4), 485–498, doi:10.1175/BAMS-D-11-00094.1.

Teixeira, J., D. Waliser, R. Ferraro, P. Gleckler, T. Lee, and G. Potter (2014), Satellite Observations for CMIP5: The Genesis of Obs4mips, *Bull. Amer. Meteor. Soc.*, 95(9), 1329–1334, doi:10.1175/BAMS-D-12-00204.1.

Thorncroft, C. D., N. M. J. Hall, and G. N. Kiladis (2008), Three-Dimensional Structure and Dynamics of African Easterly Waves. Part III: Genesis, *J. Atmos. Sci.*, 65(11), 3596–3607, doi:10.1175/2008JAS2575.1.

Tiedtke, M. (1989), A Comprehensive Mass Flux Scheme for Cumulus Parameterization in Large-Scale Models, *Mon. Wea. Rev.*, 117(8), 1779–1800, doi:10.1175/1520-0493(1989)117<1779:ACMFSF>2.0.CO;2.

Tokioka, T., K. Yamazaki, A. Kitoh, and T. Ose (1988), The Equatorial 30-60 day Oscillation and the Arakawa-Schubert Penetrative Cumulus Parameterization, *Journal of the Meteorological Society of Japan. Ser. II*, 66(6), 883–901.

Trenberth, K. E. (1991), Climate Diagnostics from Global Analyses: Conservation of Mass in ECMWF Analyses, *J. Climate*, 4(7), 707–722, doi:10.1175/1520-0442(1991)004<0707:CDFGAC>2.0.CO;2.

Trenberth, K. E. (2015), Has there been a hiatus?, *Science*, 349(6249), 691–692, doi:10.1126/science.aac9225.

Trenberth, K. E., and D. P. Stepaniak (2003), Covariability of Components of Poleward Atmospheric Energy Transports on Seasonal and Interannual Timescales, *J. Climate*, 16(22), 3691–3705, doi:10.1175/1520-0442(2003)016<3691:COCPA>2.0.CO;2.

Vecchi, G. A., and B. J. Soden (2007), Effect of remote sea surface temperature change on tropical cyclone potential intensity, *Nature*, 450(7172), 1066–1070, doi:10.1038/nature06423.

Vecchi, G. A., B. J. Soden, A. T. Wittenberg, I. M. Held, A. Leetmaa, and M. J. Harrison (2006), Weakening of tropical Pacific atmospheric circulation due to anthropogenic forcing, *Nature*, 441(7089), 73–76, doi:10.1038/nature04744.

Vellinga, M., M. Roberts, P. L. Vidale, M. S. Mizielinski, M.-E. Demory, R. Schieemann, J. Strachan, and C. Bain (2016), Sahel decadal rainfall variability and the role of model horizontal resolution, *Geophys. Res. Lett.*, 43(1), 2015GL066,690, doi:10.1002/2015GL066690.

Voigt, A., and T. A. Shaw (2015), Circulation response to warming shaped by radiative changes of clouds and water vapour, *Nature Geosci*, 8(2), 102–106, doi:10.1038/ngeo2345.

Walker, C. C., and T. Schneider (2005), Response of idealized Hadley circulations to seasonally varying heating, *Geophys. Res. Lett.*, 32(6), L06,813, doi:10.1029/2004GL022304.

Webster, P. (1987), The Elementary Monsoon, in *Monsoons*, pp. 3–32, Wiley-Interscience, Chichester.

Wu, Z. (2003), A shallow CISK, deep equilibrium mechanism for the interaction between large-scale convection and large-scale circulations in the Tropics., *Journal of the atmospheric sciences*, 60(2).

Wyant, M. C., C. S. Bretherton, J. T. Bacmeister, J. T. Kiehl, I. M. Held, M. Zhao, S. A. Klein, and B. J. Soden (2006), A comparison of low-latitude cloud properties and their response to climate change in three AGCMs sorted into regimes using mid-tropospheric vertical velocity, *Climate Dynamics*, 27(2-3), 261–279, doi:10.1007/s00382-006-0138-4.

Xie, P., and P. A. Arkin (1997), Global Precipitation: A 17-Year Monthly Analysis Based on Gauge Observations, Satellite Estimates, and Numerical Model Outputs, *Bull. Amer. Meteor. Soc.*, 78(11), 2539–2558, doi:10.1175/1520-0477(1997)078<2539:GPAYMA>2.0.CO;2.

Xie, S.-P., C. Deser, G. A. Vecchi, J. Ma, H. Teng, and A. T. Wittenberg (2010), Global Warming Pattern Formation: Sea Surface Temperature and Rainfall*, *Journal of Climate*, 23(4), 966–986, doi:10.1175/2009JCLI3329.1.

Yoshimori, M., and A. J. Broccoli (2008), Equilibrium Response of an Atmosphere–Mixed Layer Ocean Model to Different Radiative Forcing Agents: Global and Zonal Mean Response, *J. Climate*, 21(17), 4399–4423, doi:10.1175/2008JCLI2172.1.

Zeng, N., J. D. Neelin, K.-M. Lau, and C. J. Tucker (1999), Enhancement of Interdecadal Climate Variability in the Sahel by Vegetation Interaction, *Science*, 286(5444), 1537–1540, doi:10.1126/science.286.5444.1537.

Zhang, C., D. S. Nolan, C. D. Thorncroft, and H. Nguyen (2008), Shallow Meridional Circulations in the Tropical Atmosphere, *J. Climate*, 21(14), 3453–3470, doi:10.1175/2007JCLI1870.1.

Zhang, G. J. (1994), Effects of Cumulus Convection on the Simulated Monsoon Circulation

in a General Circulation Model, *Mon. Wea. Rev.*, 122(9), 2022–2038, doi:10.1175/1520-0493(1994)122<2022:EOCCOT>2.0.CO;2.

Zhang, R., and T. L. Delworth (2005), Simulated Tropical Response to a Substantial Weakening of the Atlantic Thermohaline Circulation, *J. Climate*, 18(12), 1853–1860, doi:10.1175/JCLI3460.1.

Zhang, R., and T. L. Delworth (2006), Impact of Atlantic multidecadal oscillations on India/Sahel rainfall and Atlantic hurricanes, *Geophys. Res. Lett.*, 33(17), L17,712, doi:10.1029/2006GL026267.

Zhao, M. (2014), An Investigation of the Connections among Convection, Clouds, and Climate Sensitivity in a Global Climate Model, *J. Climate*, 27(5), 1845–1862, doi:10.1175/JCLI-D-13-00145.1.

Zhao, M., I. M. Held, S.-J. Lin, and G. A. Vecchi (2009), Simulations of Global Hurricane Climatology, Interannual Variability, and Response to Global Warming Using a 50-km Resolution GCM, *J. Climate*, 22(24), 6653–6678, doi:10.1175/2009JCLI3049.1.

Zhou, L., M. Zhang, Q. Bao, and Y. Liu (2015), On the incident solar radiation in CMIP5 models, *Geophys. Res. Lett.*, 42(6), 2015GL063,239, doi:10.1002/2015GL063239.